Application of High Impedance Surfaces to Improve Radiofrequency Coil Performance for 7-Tesla Magnetic Resonance Imaging

Der Fakultät für Ingenieurwissenschaften,
Abteilung Elektrotechnik und Informationstechnik
der Universität Duisburg-Essen

zur Erlangung des akademischen Grades

Doktor der Ingenieurwissenschaft (Dr.-Ing.)

genehmigte Dissertation

von

Zhichao Chen
aus
Datong, China

Gutachter: Prof. Dr. sc. techn. Daniel Erni
Gutachter: Prof. Dr.-Ing. Klaus Solbach
mündlichen Prüfung: 15.12.2016

Abstract

In modern medicine Magnetic Resonance Imaging (MRI) has been widely used for the detection of diseases, like brain tumor, breast cancer or heart disease, to name a few. In order to improve the image quality, the concept of high-field and ultra-high-field imaging has been intensively investigated over the last three decades. However, associated with the increased magnetic field strength various problems and challenges occur. The inhomogeneous B1-field distribution and decreased penetration depth into the subject to be imaged are two critical issues.

The concept of High Impedance Surface (HIS) has been successfully applied in a number of antenna applications. The most relevant achievements are an improved radiation efficiency especially for low profile antennas and a decreased mutual coupling between adjacent antennas or antenna ports. In this thesis an approach to improve the B1 distribution of radiofrequency (RF) coils in terms of homogeneity and penetration depth by utilizing a HIS shield is presented.

First, fundamental investigations are carried out to verify the concept of using a shield with large surface impedance, which is modeled here by a Surface Impedance Boundary Condition (SIBC), to enhance the B1 distribution of RF coils. Different SIBCs are considered and their effects on the electromagnetic (EM) field of RF coils are studied. Next, the shield with a large surface impedance is realized by a periodic HIS structure, where two approaches (multi-layer uni-planar and mushroom-like topologies) are introduced in the lattice design of the HIS structure. The proposed HIS structures are evaluated via their reflection phase and dispersion diagram, which are based on unit cell simulation; as well as the bandgap property based on transmission line (TL) models. Then, the realized HIS shield based on the uni-planar topology is applied to the RF coils, and the concept of using HIS shield to improve the B1 distribution is confirmed through full-wave simulations and experimental results. Additionally, we consider another important parameter for a multi-channel dipole coil array consisting of several array elements-the coupling characteristic of the coil array, especially between the neighboring elements (the worst case scenario). The last chapter provides a brief summary and discussion, as well as an outlook of the future work.

Preface

In modern medicine *Magnetic Resonance Imaging* (MRI) has been widely used for detection of diseases, e.g. brain tumor, breast cancer, heart disease, etc. In order to improve the image quality, the concept of high-field and ultra-high-field imaging have been intensively investigated over the last few decades. However, associated with the increased magnetic field strength, various problems and challenges occur. The inhomogeneous B_1 field distribution and decreased penetration depth inside the subject to be imaged are two critical issues.

In this thesis an approach to improve the B_1 distribution in terms of homogeneity and penetration depth by utilizing a *High Impedance Surface* (HIS) shield is presented. First, a fundamental research is carried out to verify the concept of using a shield with a large surface impedance, which is modeled by a *Surface Impedance Boundary Condition* (SIBC), to enhance the B_1 distribution of *Radio Frequency* (RF) coils. Next, the shield with a large surface impedance is realized by a periodic HIS structure, where two approaches are introduced in the lattice design of the HIS structure. Finally, the realized HIS shield is applied to the RF coils, and the concept of using HIS shield to improve the B_1 distribution is confirmed through full-wave simulations and experimental results.

The present work is partially comprised of my published journal contributions and conference papers. These works were produced solely by myself and the co-authors participated as scientific advisors. For the sake of readability, I chose not to cite text paragraphs and figures taken from the original publications.

Finally, I would like to thank those people that have been always very supportive during all these years. In particular, Prof. Dr. sc. techn. Daniel Erni, Prof. Dr.-Ing. Klaus Solbach, Dr.-Ing. Andreas Rennings, Dr.-Ing. Simon Otto and all the colleagues from Laboratory for General and Theoretical Electrical Engineering (ATE), University of Duisburg-Essen and Laboratory for High Frequency Engineering (HFT), University of Duisburg-Essen. Further, my deepest gratitude goes to my parents and my family for their limitless support and love.

10, June, 2016
Zhichao Chen

Contents

Chapter 1

Introduction

In modern medicine magnetic resonance imaging (MRI) has become an important method for detection of diseases, e.g. brain tumor, breast cancer, heart disease, etc., and has been widely accepted due to its noninvasive imaging modality. On one hand, diverse techniques concerning pulse sequence, radio frequency (RF) field, image contrast, patient safety, etc., have been developed for MRI. On the other hand, engineers and scientist never stopped from seaching and merging new techniques to improve the image quality of MRI. The concept of high impedance surface (HIS) has been successfully applied in a number of antenna applications, in terms of increasing the antenna efficiency, suppressing the mutual coupling, etc,. In this thesis, the potential of applying the HIS concept to MRI in order to improve the RF coil performance is exploited. The primary purpose of this chapter is to provide a brief overview of MRI and a story line for the reader of this thesis.

1.1 A Brief Overview of Magnetic Resonance Imaging

In this section a brief overview of magnetic resonance imaging (MRI), such as the historical development of MRI, the working principles of an MRI system, the safety consideration, is provided.

1.1.1 A Brief Historical Survey of MRI

Magnetic resonance imaging is a relatively new discipline, which originates from the application of nuclear magnetic resonance (NMR) to radiological imaging. Due to its flexibility and sensitivity to a broad range of tissue properties, along with its relative safety in comparison to other radiotherapies, e.g., X-ray imaging [1], MRI has become a powerful and widely accepted imaging modality in today's biomedical science applications.

The concept of nuclear magnetic resonance can be traced back to the discovery of the spin nature of proton, which was firstly confirmed by the Stern-Gerlach experiment in the early 1920's [2]. Based on the prior work of Stern and Gerlach, Rabi and his coworkers developed the investigation of the interaction between the hydrogen molecules and an external magnetic field in the 1930's [3, 4]. By passing a stream of hydrogen molecules through a strong and constant magnetic field and measuring the deflection of the beam, they observed that the electromagnetic energy was absorbed by the molecules at a certain frequency, which is the so-called Larmor frequency [5]. In 1946, Bloch and Purcell successfully measured the nuclear magnetic resonance (NMR) in bulk material, independently and in different ways. Bloch predicted that the nuclear magnetization of the water sample could be rotated away from its equilibrium state and precess around the applied constant magnetic field with the Larmor frequency. The electrical signal induced by this precessing magnetization could be detected by an appropriately placed copper coil in the radio frequency (RF) range, and he succeeded [6]. Meanwhile, Purcell observed the same phenomenon by directly measuring the small absorption of RF energy by a block of paraffin [7]. The NMR phenomenon that magnetic nuclei absorb or irradiate electromagnetic energy from an external magnetic field where they are precessing at a certain frequency, is acknowledged as the essence of MRI. For this work, Bloch and Purcell were both awarded with the Nobel Prize for Physics in 1952.

By the mid-1950's the basic physics of NMR had been well elucidated and some primitive commercial instruments were available [8]. In 1961, Shoolery introduced the first commercial high-resolution NMR spectrometer—the Varian A-60. The potential of NMR in medical applications began to be explored since 1971, when Damadian found out that tumors and normal tissue can be distinguished by different relaxation times and that this difference could be used to diagnose cancer [9]. In 1973, Lauterbur presented the principles of MRI and achieved the first 2D image of a water-filled object [10]. By using a "Zeugmatography" process, as he called it, he carried out the first cross-sectional image of a living mouse in January 1974 [11]. In the late 1970's, more key techniques were developed to deliver efficient and rapid imaging, e.g., using 2D NMR technique together

with Fourier transform for acquisition of MR images by Ernst [12], and using a so-called "echo-planar" technique to dramatically shorten the scan times by Mansfield [13]. The first 1.5 T clinical MR system was installed in 1983 by Bottomley [14]. Over the last three decades, a plenty of MRI techniques, e.g., EPI [15], FLASH MRI [16], SMASH [17], SENSE [18], GRAPPA [19], etc., have been discovered and developed. Being supported by the more and more mature and advanced imaging techniques, the MRI market has been growing exponentially. Although the most commercial MRI scanns are performed at 1.5 T and 3 T, higher fields such as 7 T, 9.4 T and even higher, are currently explored because of their increased sensitivity and resolution [20, 21, 22]. Recently, promising results have been shown in whole-body imaging at 7 T [23, 24, 25, 26, 27]. In the near future 7 T MRI is very likely to be considered for clinical diagnostics.

1.1.2 Working Principles of MRI

MRI makes use of the magnetic properties of certain atomic nuclei. When an object is placed in a strong and constant magnetic field (B_0), nuclei in the object precess around this external field and reveal a net magnetization along the direction of B_0. By applying an additional perpendicular magnetic RF field (B_1) with respect to B_0, the net magnetization is tilted away from the direction of B_0 with a certain angle. Once the B_1 field is removed, the net magnetic moment begin to realign with B_0, which is referred as relaxation. During the relaxation process, the nuclei lose energy by emitting their own RF signal, which can be detected by the receiving coils. The emitted signals differ from tissue to tissue, and this difference contributes to the image contrast.

1.1.2.1 Spins and Magnetization

It has been previously mentioned that MRI is based on the interaction of a nuclear spin with an external magnetic field, namely B_0. The spin of a nucleus creates a magnetic moment, which has an orientation as the nuclear rotation axis, and produces its own tiny magnetic field in the surroundings. In a neutral environment the magnetic moments of nuclei point in a random direction, and thus, reveal no overall magnetic effect. In the presence of an external magnetic field, the interaction of the nuclear own field and the external field induces a torque. This torque attempts to turn the magnetic moment of the nucleus into alignment with the external field, parallel or anti-parallel. However, the magnetic moment does not simply align with the external field but instead precesses around the direction of the field, as depicted in Fig. 1.1(a). A well-known example is the precession of a gyroscope: before a spinning gyroscope finally falls in a gravitational field, it precesses around the gravity with a certain velocity [cf. Fig. 1.1(b)] [5]. The frequency at which the nucleus precesses around the external magnetic field is known as the Larmor frequency, which is defined by the Larmor equation as follows:

$$\omega_0 = \gamma \cdot B_0, \tag{1.1.1}$$

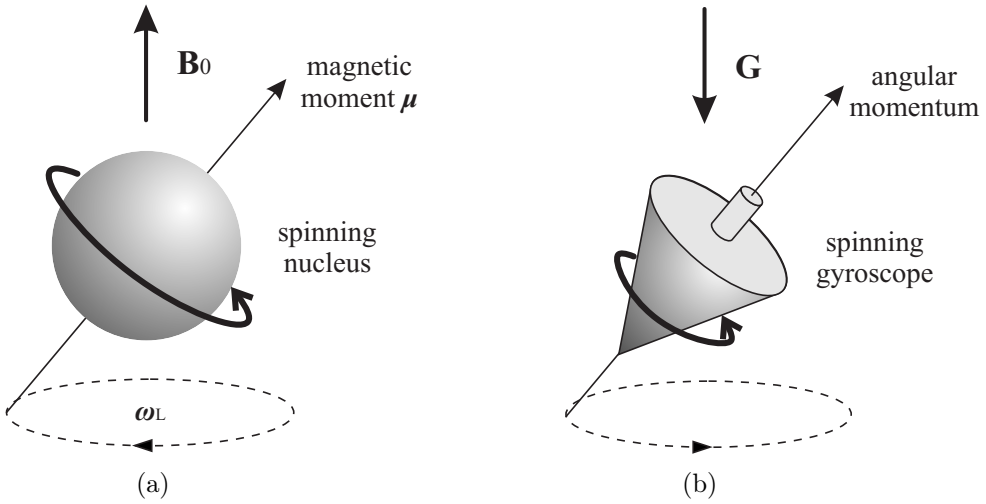

Figure 1.1: Illustration of (a) the precession of a spinning nucleus in the presence of an external magnetic field B_0, and (b) a spinning gyroscope precessing around gravity.

where ω_0 is the Larmor frequency in megahertz [MHz], B_0 is the magnetic flux density of the external field in tesla [T], and γ is the gyromagnetic ratio[1]. Note that the Larmor frequency is proportional to the strength of the external magnetic field.

Similar to the magnetic moment for a single nucleus, the bulk magnetization, denoted by M, characterizes the magnetic moment of all the nuclei in the sample. At equilibrium, nuclei precess around B_0 with random phases, as shown in Fig. 1.2(a). From a macroscopic perspective, the transverse components of their magnetic moments cancel out and produce no transverse magnetization. However, in the longitudinal direction a greater proportion of nuclei are oriented toward (parallel to) the external magnetic field than against (anti-parallel to) it becasue the nuclei in parallel alignment possess a minimum energy state [5, 28]. As a result, a small longitudinal net magnetization M_0 which has an orientation as the B_0 arises.

1.1.2.2 Spin Excitation and Relaxation

As mentioned before, each nucleus with nonzero spin generates a magnetic moment, and all the nuclei in the sample produce a net magnetization along the direction of the external magnetic field. However, this small net magnetization is too weak to generate a detectable MR signal. In order to produce an MR signal that can be directly detected, the net magnetization has to be tipped away from the external field direction so that a transverse component of the net magnetization vector (NMV) is produced [cf. Fig. 1.2(b)]. This can be achieved by applying a transverse oscillating magnetic field, known as B_1, to the sample at the Larmor frequency. The resulting transverse magnetization then precesses around the original external field (B_0) at Larmor frequency, emitting a detectable signal.

[1]The gyromagnetic ratio is a constant specific to a particular nucleus and is defined as the precessional frequency of a nucleus as the external magnetic field strength being 1 T.

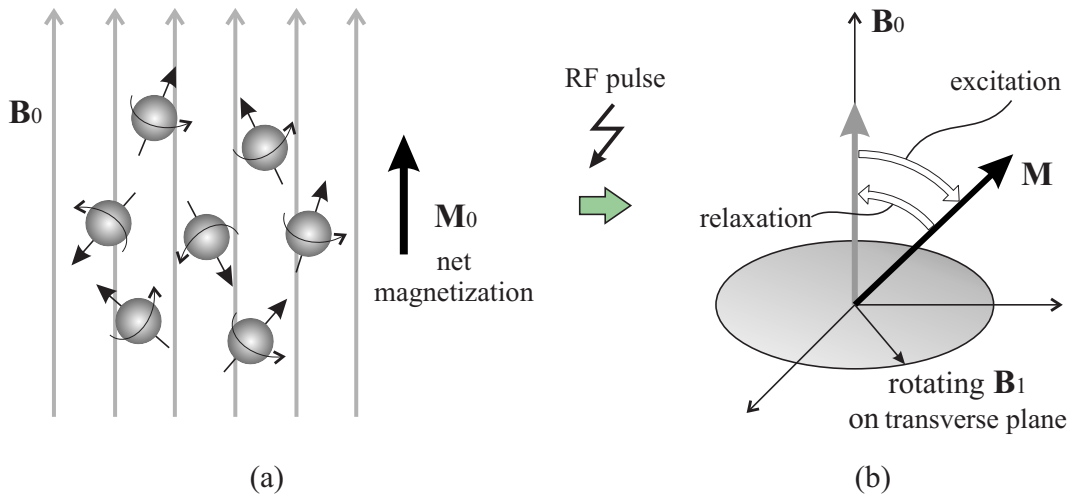

Figure 1.2: (a) In the presence of an external magnetic field B_0, the spinning nuclei precess around B_0 with random phases, producing no transverse magnetization. However, slightly more spins align parallel to B_0, and thus a small longitudinal net magnetization M_0 arises. (b) By applying an RF pulse the net magnetization is tipped away from the longitudinal direction, so that a transverse component of the net magnetization vector is produced. This process is called spin excitation. Conversely, the process where the net magnetization realign with B_0 is referred as spin relaxation.

Since the Larmor frequencies of most nuclei fall in the radio frequency (RF) range, this process is normally termed as RF excitation.

Right after the RF excitation, the transverse magnetization still precesses about B_0 and emits MR signal to the receiver coil. However, the transverse magnetization and the resulting MR signal rapidly decay due to the spin relaxation process [5, 28]. There are two independent relaxation processes: longitudinal relaxation and transverse relaxation. For the longitudinal relaxation the nuclei lose energy through interactions with neighboring nuclei and molecules (spin-lattice interaction), and the magnetization vector realigns to B_0 with a time constant T_1. For this reason, the longitudinal relaxation is also known as T_1 relaxation. Different from the longitudinal relaxation, the transverse relaxation the nuclei do not dissipate energy to their surroundings but instead exchange energy with each other (spin-spin interaction) due to the lost of phase coherence, or so-called dephasing. Dephasing arises in two ways: First, energy is exchanged between spins as a result of local variation in the magnetic field produced by each spin. Second, intrinsic inhomogeneities of the external field B_0 and differences in magnetic susceptibility among the tissues themselves contribute to dephasing as well. The aforementioned two dephasing processes occur with the time constant T_2 and T_2^*, respectively. T_1 and $\mathrm{T}_2/\mathrm{T}_2^*$ differ among various tissues and therefore can be exploited to produce signal contrast on MR images [5, 28, 29, 30].

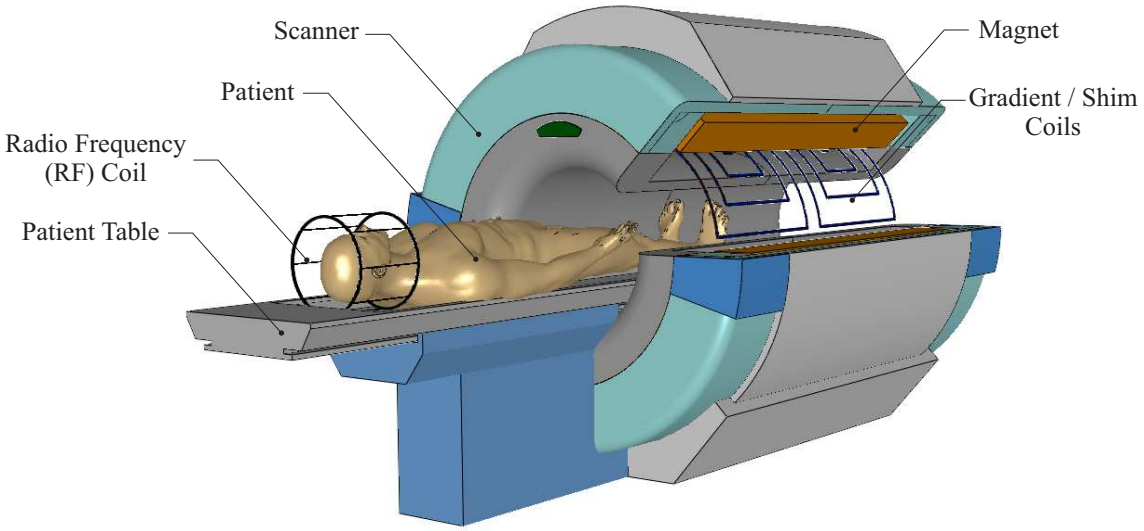

Figure 1.3: The major components of an MRI scanner in cutaway view.

1.1.2.3 Contrast and Pulse Sequence

A sufficient contrast in an MR image is necessary for clinical diagnostics. The image contrast is determined by the intrinsic features of biological tissues, such as proton density, T_1 and T_2 times. Depending on which of these features is emphasized in the imaging process, various imaging methods (proton density-weighted images, T_1-weighted images and T_2-weighted images) and pulse sequences are developed. In principle an MR pulse sequence is a series of RF pulses, gradient applications and intervening time periods, which controls the RF excitation, the gradient magnetic fields, and the signal acquisitions. A wide variety of sequences are utilized for particular applications to provide optimal image quality. The commonly used pulse sequences are spin echo (SE) sequence, the inversion recovery (IR) sequence, the gradient echo (GRE) sequence, and some variants thereof [5, 29, 31, 32].

1.1.3 Components of an MRI System

A modern MRI system basically consists of four main components: a primary magnet which generates a strong and constant magnetic field, B_0; gradient coils and shim coils which adjust the spatial variations in B_0; RF coils which transmit and receive the MR signal; and a computer system which is responsible for data acquisition and processing.

1.1.3.1 Primary Magnet

Most primary magnets used for MRI are of three types: permanent, resistive and superconductive [28, 33]. Permanent MRI magnets use permanently magnetized iron, which is usually bent into a C-form so that the two poles are parallel to each other. Resistive

MRI magnets generate an uniform magnetic field inside a solenoid coil which is made of standard conductors and has a considerable electrical resistance. Both permanent and resistive MRI scanners are limited to low-field applications, primarily open MRI and extremity MRI [28]. Similar to resistive magnets, superconductive MRI magnets also use a solenoid shaped coil, but made of alloys, which become superconducting when cooled down to about 10 K. Then the coil carries large electrical currents with negligible resistance, producing a strong and stable magnetic field. The coil is kept below this temperature by being immersed in a bath of liquid helium [33].

1.1.3.2 Gradient and Shim Coils

It is important for MRI that the B_0 field shall be kept as homogeneous as possible during the imaging. However, the environment where the scanner is located, the manufacturing imperfections in the primary magnet, the susceptibility differences within the object to be imaged, etc., all result in the inhomogeneity of the B_0 field. Shim coils are used to produce compensatory magnetic fields to correct the spatial variations in the B_0 field [30].

Gradient coils are used to produce linear spatial variations in the main magnetic field along all three directions (x, y, z). This variation in the magnetic field permits localization of image slices as well as phase encoding and frequency encoding. The gradient coil design for z direction (parallel to B_0) is usually based on Helmholtz pair coils, while the gradient coils for x and y directions typically have paired saddle coils configuration [30]. Due to its property, gradient coils sometimes also serve as shim coils to adjust for linear variations of B_0 field.

1.1.3.3 RF Coils

The RF coils of an MRI system broadcast the RF signal to the object to be imaged and receive the emitted signal during the relaxation process. From the perspective of functionality, RF coils are designed either for transmission (transmitter) or reception (receiver), or for both purposes (transceiver). The RF coils are produced in a variety of geometries and can be generally classified as volume coils, surface coils, intracavity coils and phased array coils. Volume coils completely enclose the region of interest and produce a quite uniform B_1 field inside, e.g., saddle coil and birdcage coil. Surface coils are mostly placed adjacent to the tissues, and have a penetration depth on the order of the coil radius [34]. For certain particular target organs, intracavity coils, which are inserted into body cavities, are used to improve image quality [28]. Recently, phased array coils consisting of several independently fed coil elements have revealed promising results both for transmission and reception, especially in ultra-high field (UHF) imaging. Because such phased array coils could improve the B_1 homogeneity by controlling the excitation of each coil element, and provide a high spatial resolution within a larger field of view (FoV). More information and details concerning the RF coil designs can be found in [34, 35, 36].

Besides the aforementioned RF coils which generate a localized B_1 field near to coils, Brunner et al. proposed another novel way to generate a B_1 field in the form of circularly polarized traveling waves within the bore of the MRI scanner [37, 38]. This approach was intended to provide a more uniform B_1 field with a larger coverage of samples, which makes it a promising candidate for whole-body imaging at considerably high magnetic field strengths [37]. Many research groups have been inspired by this concept, and in [39] an RF antenna system consisting of multiple ring structures was presented. These ring structures are based on the concept of composite right-/left-handed (CRLH) metamaterials [40], and can be fully integrated inside the bore housing.

1.1.3.4 Computer System

An MRI system involves an enormous amount of hardware, control units, data processing, etc. The computer system controls and coordinates all the processes ranging from moving the patient table to data acquisition and processing.

1.1.4 Safety Considerations in MRI

Based on the current knowledge the MRI is believed to pose no harmful bioeffects or risks to people, animals, or biological samples. However, there are potential safety issues as the field strength rises to UHF regime ($B_0 \geq 7$ T). One consideration is about the excessive RF power deposition inside the tissue, which can be described in terms of specific absorption rate (SAR). Due to the higher Larmor frequency and increased inhomogeneity of B_1 field, critical local SAR can arise inside the tissue, creating so-called "hot spots". Besides, other physiological side-effects, including dizziness, nausea, headache, light flashes, etc., have been noticed due to the high magnetic field strength [41, 42, 43].

1.2 A Brief Overview of High Impedance Surface (HIS)

Speaking of high impedance surface (HIS), one has to firstly introduce the concept of periodic structures. Under the interaction with electromagnetic waves, interesting features and phenomena of periodic structures have been observed and studied. Depending on the domain of application, various terminologies could be found in literature, such as photonic crystals [44], frequency selective surfaces (FSS) [45], photonic band gaps [46], and high impedance surfaces (HIS) [47], etc. These various terminologies can be classified under a wide category with the name of electromagnetic bandgap (EBG) structures [48].

1.2.1 Electromagnetic Bandgap (EBG) Structure

In general, electromagnetic bandgap structures are periodic objects which prevent the propagation of bounded electromagnetic surface waves in certain frequency bands [48, 49, 50]. Related to its bandgap feature, EBG structures also possess some other special properties, such as in-phase reflection phase property and high surface impedance. Therefore, at a specific frequency the EBG structure can be functionally considered as a HIS. With these special properties, the EBG structures have found numerous applications in the antenna field, such as increasing the antenna gain, reducing the mutual coupling between array elements, bulding efficient low profile antennas, beam steering, etc. [47, 51, 52, 53, 54, 55].

Recently, the EBG surfaces have been placed behind the radio frequency (RF) coils in order to improve the coil performance in ultra-high field MRI applications [56]. With an appropriate design, where the magnetic resonant frequency is located inside the bandgap of the EBG structure, the undesired surface current on the EBG structure can be suppressed in comparison to the conventional metallic shielding plate.

1.2.2 Classification of EBG Structure

According to the geometric configuration, the EBG structures can be classified as one-dimensional, two-dimensional and three-dimensional EBGs. Here we provide a brief introduction and a couple of common examples for each kind of EBG structure.

Corrugated surfaces [57, 61] [cf. Fig. 1.4(a)] and defected ground planes [58, 62, 63] [cf. Fig. 1.4(b)] are two examples of one-dimensional EBG. A corrugated surface is basically a metal slab, where a series of vertical slots with a depth of quarter-wavelength are etched, as depicted in Fig. 1.4(a). The short circuit at the bottom of the slab is transformed by the quarter-wavelength slots into an open circuit at the top surface, where a high impedance is achieved. The height of the slab can be reduced by filling the slots with high-dielectric materials. Being another example of one-dimensional EBG, a defected ground plane introduces various slots and cuts on a complete metallic plate to achieve specific purposes, e.g., in filter applications.

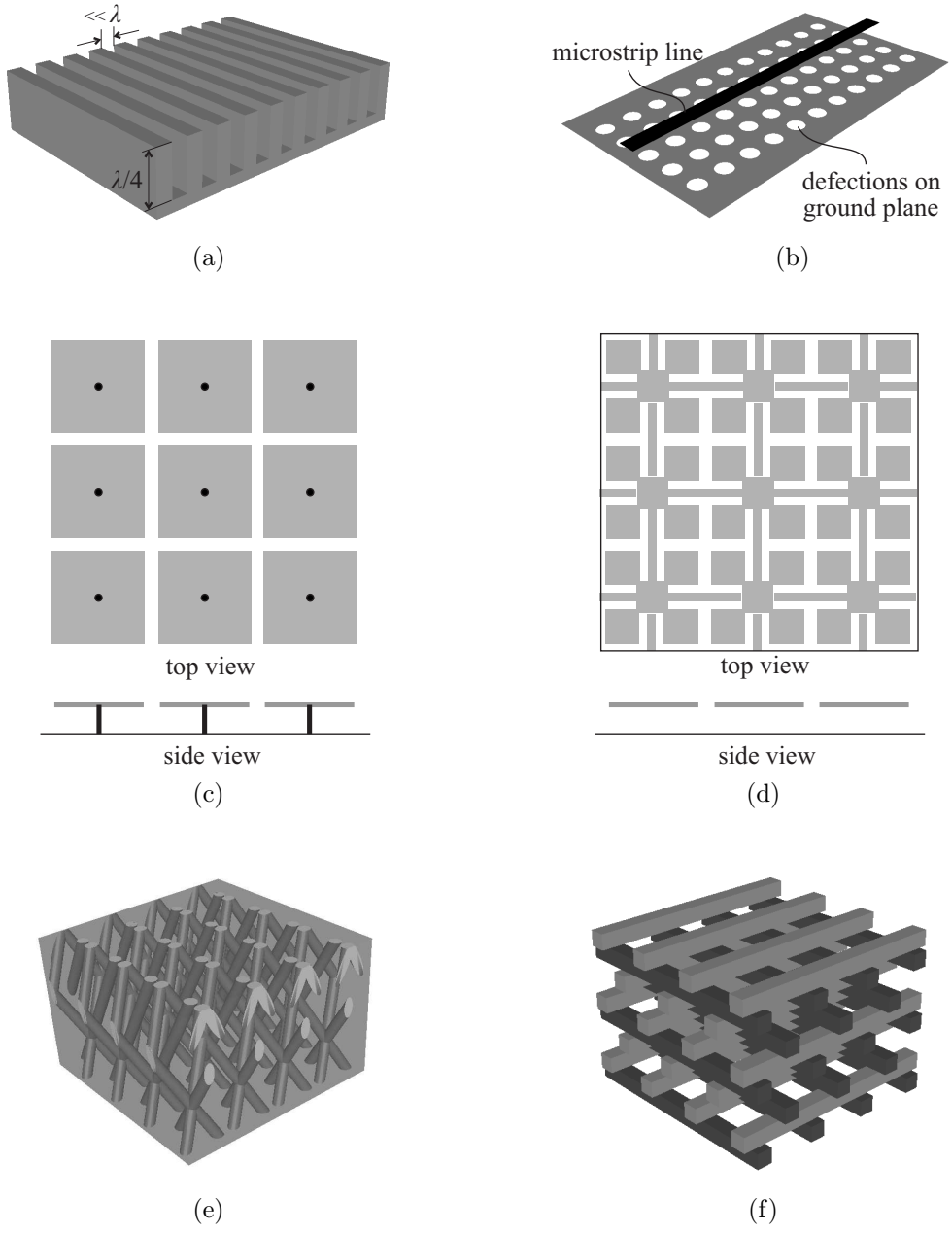

Figure 1.4: One-dimensional EBG structures: (a) a corrugated surface [57] and (b) a defected ground plane below a microstrip line [58]. Two-dimensional EBG structures: (c) a mushroom-like EBG surface [47] and (d) an uni-planar EBG surface [53]. Three-dimensional EBG structures: (e) a Yablonovitch face-centered-cubic structure [59] and (f) a woodpile dielectric structure [60].

Among the various 2D EBG designs, the mushroom-like [47] [cf. Fig. 1.4(c)] and uni-planar [53] EBG structures [cf. Fig. 1.4(d)] are the most well-known examples. A mushroom-like EBG structure normally consists of a lattice of metal plates, which are connected to a solid metal sheet by vertical conducting vias. For an uni-planar EBG the lattice of metal plates are connected by thin microstrip lines on the same layer instead of being connected to a solid metal sheet by the vertical vias. The solid metal sheet has essential effects on the EBG characteristics, and can be included or removed depending on the specific circumstances [64]. This chapter focuses mainly on the 2D EBG structures.

In practice, 3D EBG structures are mainly applied to applications in gigahertz and terahertz range. Various manufacturing techniques have been used to fabricate 3D EBG structures [59, 60, 65, 66]. In [59] a 3D EBG crystal was created by drilling sets of parallel holes with certain angles between each set in a block of dielectric material [cf. Fig. 1.4(e)]. An alternative approach was presented in [60], where the 3D EBG structure is formed from orthogonal layers of parallel bars with rectangular cross section [cf. Fig. 1.4(f)].

1.3 Organization of this Dissertation

The main contribution of this thesis is to investigate the feasibility to improve the RF coil performance for 7 T MRI by using a high-impedance-surface (HIS) RF shield. The RF shield, typically made of metal, is normally placed behind the RF coil to prevent the interaction with the bore components of the MRI scanner. Besides the shielding functionality, here we exploit the possibility to improve the coil performance by using an RF shield with novel characteristics.

In Chapter 2, the RF shield is characterized by a surface impedance boundary condition (SIBC), where different surface impedances are defined. A fundamental investigation of the effect of different shields on the electromagnetic (EM) fields generated by the RF coils is carried out in a systematic manner. Particularly, Section 2.1 provides the definition of the surface impedance which characterizes the shielding plate and defines the categories of the surface impedance to be examined in the forthcoming sections. In Section 2.2 and Section 2.3, EM field analysis of dipole and loop coils is carried out based on full-wave simulation for different surface impedance boundaries, respectively. For each coil type (dipole and loop) two simulation models are considered: an ideal impressed current model for two-dimensional analysis and a real dipole/loop structure for three-dimensional analysis. It is demonstrated, that the RF shield with high surface impedance provides an improved magnetic field distribution for dipole and loop coils compared to the conventional metal shield.

To realize the RF shield with a high surface impedance, two compact HIS/EBG designs for 7 T MRI application (300 MHz) are presented in Chapter 3. In antenna applications the terminology of electromagnetic bandgap (EBG) structure is perhaps more widely and well known. In certain frequency bands EBG structures prevent the propagation of electromagnetic surface waves and exhibit a high surface impedance, hence they can be functionality considered as a HIS. In Chapter 3 we firstly provide a brief introduction to the HIS/EBG structure, including the definition, characterization of well-known examples of a HIS/EBG structure. Subsequently, two compact two-dimensional HIS/EBG surface designs based on uni-planar and mushroom-like concepts will be presented. The proposed EBG structures will be evaluated via their reflection phase and dispersion diagram, which are based on unit cell simulation; as well as the bandgap property based on transmission line (TL) models. Additionally, a thorough geometry parameter study of the compact EBG structures will be performed. In the beginning phase of the research project (Deutsche Forschungsgemeinschaft, DFG under the grant SO 457/8-1), preliminary investigations concerning the EBG designs and the application of EBGs for single RF coil has been carried out by Gameel Saleh [67, 68].

With the HIS structures presented in Chapter 3, the performance of the RF coils backed by real HIS shield will be investigated in Chapter 4. Due to the absence of the vertical conducting vias the compact uni-planar EBG is easier to fabricate in comparison to the mushroom-like EBG. Here we utilize the realized HIS shield based on the uni-planar concept for the proposed investigation. The field characteristics of the considered RF coils

(dipole and loop) will be firstly investigated based on full-wave simulation, and further validated by experimental results. Additionally, the effect of the separation distance between the HIS shield and the dipole/loop coil element is well studied. Besides the investigation based on single coil element, an eight-channel dipole coil backed by a HIS shield is presented. Compared to the conventional metal shield, the B_1 distribution of the considered coils is significantly improved by the HIS shield, both in terms of field homogeneity and penetration depth.

For UHF MRI ($B_0 \geq 7$ T) an RF coil array consisting of several array elements is often used to improve the imaging quality. In Chapter 5 we consider another important parameter for such a dipole coil array consisting of several array elements — the coupling characteristic of the coil array, especially between the directly neighboring elements (worst case). Firstly, the coupling mechanism of several well-established dipole coil elements [69, 70, 71] is investigated by applying a characteristic mode analysis and full-wave simulation. Different dipole elements reveal diverse magnetic field distributions and coupling characteristics. Based on the results from coupling investigation, a multi-channel dipole coil consisting of different dipole coil element is proposed, which achieves an optimal compromise between the field distribution and the coupling characteristic. Additionally, a fundamental investigation is carried out to evaluate how the coupling mechanism is affected by the RF shield which is characterized by its surface impedance. This fundamental investigation reveals a new approach to modify the coupling characteristics of the dipole coil elements for UHF MRI.

The last chapter provides a brief summary and discussion, as well as an outlook of the future works.

Chapter 2

Electromagnetic Field Analysis of RF Coils with Surface Impedance Characterized Shields

Being an essential component of magnetic resonance imaging (MRI) systems, diverse radio frequency (RF) coils have been studied and developed over decades. With the advent of ultra-high field (UHF) imaging ($B_0 \geq$7 T), the conventional RF coils challenge the limits of design and performance due to the higher magnetic resonance frequencies. Among the arising issues for UHF MRI, a spatially inhomogeneous B_1 field and increased peak SAR are most critical for whole-body imaging [20, 72]. As one solution, multi-channel RF coils based on several longitudinally oriented stripline coil elements have been successfully applied in UHF MRI [69, 72, 73, 74, 75, 76, 77, 78]. For the localized body regions surface coils are preferable to be utilized due to the superior signal-to-noise ratio [34, 79], especially for the receive (Rx) case. According to specific applications several surface coil elements can be combined to cover a larger region of interest [26]. In order to prevent the interaction with the bore components of the MRI scanner, such as the gradient/shim coils and the cryostat's shell, a metallic plate, which is commonly called RF shield, is usually placed behind the RF coil element. In this chapter the shield behind the RF coil is characterized by a surface impedance boundary condition (SIBC) [80, 81]. The effect of different shields on the electromagnetic (EM) fields generated by the RF coils is investigated in a systematic manner by considering various surface impedances categorized in terms of its magnitude and phase [82]. Particularly, Section 2.1 provides the definition of the surface impedance which characterizes the shielding plate and defines the categories of the surface impedance to be examined in the forthcoming sections. In Section 2.2 and Section 2.3, EM field analysis of dipole and loop RF coils are carried out based on full-wave simulation for different surface impedance boundaries, respectively.

2.1 Surface Impedance Boundary Conditions (SIBCs)

This section gives a general definition of the surface impedance and defines the categories of the surface impedance to be considered in the forthcoming sections. In addition, a preliminary investigation on the effect of various SIBCs is performed based on a one-dimensional model. This fundamental one-dimensional investigation provides the theoretical backgrounds for our subsequent studies.

2.1.1 Concept of Surface Impedance

Surface impedance boundary conditions (SIBCs) are widely used to model the interface between two media where the main interest is focused only on one of them, and hence significantly simplify the simulation domain in electromagnetic problems. A half-space of isotropic medium can be approximated by a SIBC, where no fields exist behind the boundary (cf. Fig. 2.1).

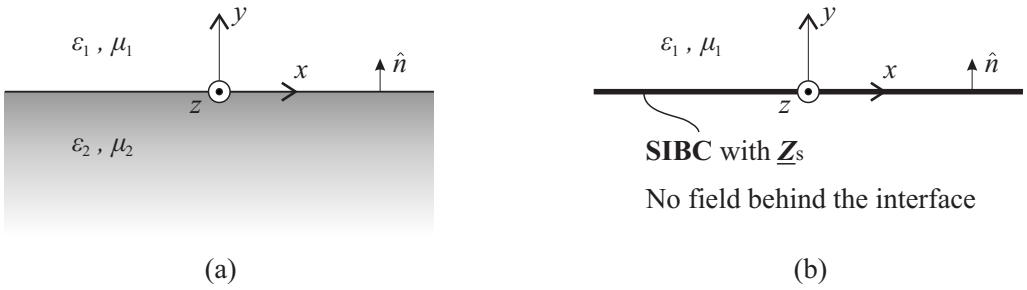

Figure 2.1: Illustration of the concept of surface impedance: a half-space filled with isotropic medium can be approximated by a SIBC with a corresponding surface impedance Z_s, where no fields exist behind the boundary.

Suppose the half-space region is large enough and the electromagnetic waves propagation inside the half-cpace can be described as plane waves, the surface impedance at the interface between two media can be defined by the tangential components of both the electric and magnetic fields [80]:

$$\mathbf{E}_t = Z_\mathrm{s} \cdot (\hat{\mathbf{n}} \times \mathbf{H}_t), \tag{2.1.1}$$

where the index t refers to the tangential components. Further, (2.1.1) can be expressed by the material parameters of the media which is to be modeled by the SIBC as

$$Z_\mathrm{s} = \sqrt{\frac{\underline{\mu}}{\underline{\epsilon}}} = \sqrt{\frac{\mu_0 \mu_\mathrm{r}}{\epsilon_0 \epsilon_\mathrm{r} - j\sigma/\omega}}, \tag{2.1.2}$$

where μ_r, ϵ_r and σ are the relative permeability, relative permittivity and electric conductivity, respectively. In COMSOL Multiphysics, the EM simulator utilized in this study, the impedance boundary condition is used on exterior boundaries representing the surface of an artificial domain outside the boundary. The surface impedance is defined based on the material parameters of the domain behind the SIBC. The detailed mathematical derivation for the equation of surface impedance can be found in [81, 83].

2.1.2 Categorized Surface Impedance

Trying to obtain a comprehensive insight into the effect of the corresponding SIBCs on the EM fields, three most representative cases of the surface impedance are considered:

(I) $\Re\left(Z_\mathrm{s}\right) \neq 0,\ \Im\left(Z_\mathrm{s}\right) = 0$: With σ set to zero, μ_r and ϵ_r being of the same sign, the complex surface impedance from (2.1.2) reads

$$Z_\mathrm{s} = \sqrt{\frac{\mu_0\mu_\mathrm{r}}{\epsilon_0\epsilon_\mathrm{r}}} = |Z_\mathrm{s}|\ e^{j0}. \tag{2.1.3}$$

(II) $\Re\left(Z_\mathrm{s}\right) = \Im\left(Z_\mathrm{s}\right) \neq 0$: By setting μ_r to one, ϵ_r to zero, the radicand is with 90° phase angle. Thus, the square root operation leads to equal real and imaginary parts of Z_s:

$$Z_\mathrm{s} = \sqrt{j\frac{\mu_0\mu_\mathrm{r}\omega}{\sigma}} = |Z_\mathrm{s}|\ e^{j\pi/4}. \tag{2.1.4}$$

(III) $\Re\left(Z_\mathrm{s}\right) = 0,\ \Im\left(Z_\mathrm{s}\right) \neq 0$: Similarly to the case (I), but with μ_r and ϵ_r being of the opposite signs, a purely imaginary surface impedance can be achieved:

$$Z_\mathrm{s} = \sqrt{\frac{\mu_0\mu_\mathrm{r}}{\epsilon_0\epsilon_\mathrm{r}}} = \sqrt{-\left|\frac{\mu_0\mu_\mathrm{r}}{\epsilon_0\epsilon_\mathrm{r}}\right|} = j\sqrt{\left|\frac{\mu_0\mu_\mathrm{r}}{\epsilon_0\epsilon_\mathrm{r}}\right|} = |Z_\mathrm{s}|\ e^{j\pi/2}. \tag{2.1.5}$$

In the categories defined above, the phase of the surface impedance varies from 0 to $\pi/2$. As given in Tab. 2.1, for each category only one material parameter is used to sweep the magnitude of surface impedance from a considerably small to a relatively large value with the remaining fixed. Thus, the SIBC can be simulated from perfect electrical conductor (PEC) to perfect magnetic conductor (PMC), approximately. In order to carry out the comparison in a fair manner, the magnitude of surface impedance for different cases is kept constant.

Table 2.1: Considered Surface Impedances

CASE I		CASE II		CASE III		
$\mu_r = 1,\ \sigma = 0$		$\mu_r = 1,\ \epsilon_r = 0$		$\mu_r = 1,\ \sigma = 0$		
ϵ_r	Z_s [Ω]	σ [S/m]	Z_s [Ω]	ϵ_r	Z_s [Ω]	$\lvert Z_s\rvert$ [Ω]
10^{-5}	$1.2{\cdot}10^5$	$1.67{\cdot}10^{-7}$	$(8.4{+}8.4\,\mathrm{j}){\cdot}10^4$	-10^{-5}	$1.2{\cdot}10^5$ j	$1.2{\cdot}10^5$
1	377	0.0167	266+266 j	-1	377 j	377
10	120	0.167	84+84 j	-10	120 j	120
10^5	1.2	1670	0.84+0.84 j	-10^5	1.2 j	1.2

2.1.3 Preliminary Investigation of Various SIBCs

According to the image theory [84], a PEC boundary in the vicinity of a current source can be removed by placing a virtual image current source, which is out-of-phase with respect to the original one; whereas for a PMC boundary an in-phase image current can be utilized to replace the PMC boundary. Theoretically, a PMC boundary represented by $Z_s = \infty$ could reinforce the absolute magnetic field above the original current source in comparison to a PEC boundary ($Z_s = 0\ \Omega$), since the magnetic field excited by the original and image currents add up constructively instead of destructively (if the distance from the current source to the boundary is electrically small).

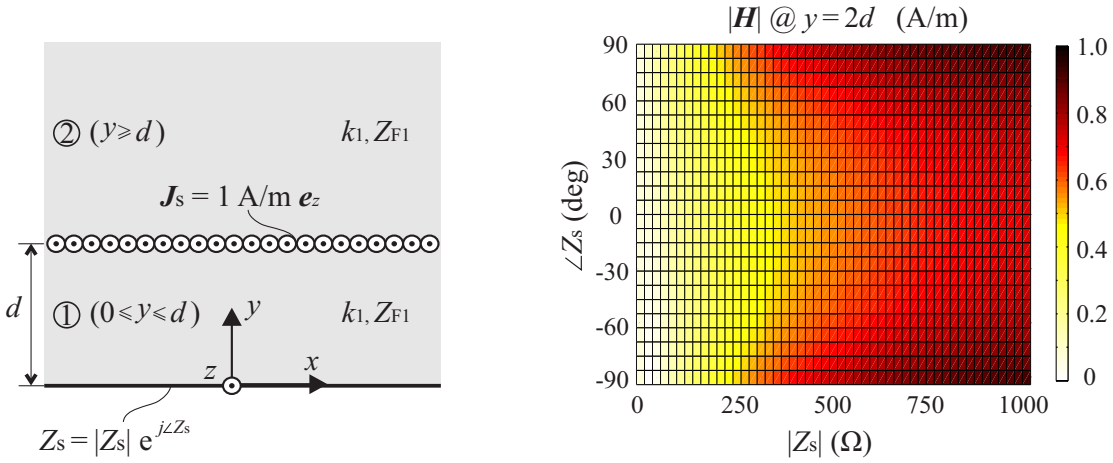

Figure 2.2: (a) One-dimensional model for analytical investigation: A surface current density J_s in z-direction is defined at $y = d$. The lower boundary at $y = 0$ is characterized by a complex surface impedance Z_s. (b) The computed absolute magnetic field at $y = 2d$ for different magnitudes and phases of the surface impedance Z_s.

In this section an analytical investigation is performed based on a simple one-dimensional model: the interface of two semi-infinite media coincides with the xz-plane, and is char-

acterized by a complex surface impedance Z_s. A surface current density J_s in z-direction is defined at a distance d from that surface impedance boundary [cf. Fig. 2.2(a)]. The excited electromagnetic field in the upper half-space can be expressed as follows:

$$\mathbf{H}_1(y) = \left(H_1^- \mathrm{e}^{+jk_1 y} - H_1^+ \mathrm{e}^{-jk_1 y}\right) \mathbf{e}_x, \qquad (0 \leq y \leq d) \tag{2.1.6}$$

$$\mathbf{E}_1(y) = -Z_{\mathrm{F}1} \left(H_1^- \mathrm{e}^{+jk_1 y} + H_1^+ \mathrm{e}^{-jk_1 y}\right) \mathbf{e}_z, \qquad (0 \leq y \leq d) \tag{2.1.7}$$

$$\mathbf{H}_2(y) = -H_2^+ \mathrm{e}^{-jk_1 y} \mathbf{e}_x. \qquad (y \geq d) \tag{2.1.8}$$

$$\mathbf{E}_2(y) = -Z_{\mathrm{F}1} H_2^+ \mathrm{e}^{-jk_1 y} \mathbf{e}_z. \qquad (y \geq d) \tag{2.1.9}$$

By evaluating the following boundary conditions:

$$\mathbf{e}_y \times (\mathbf{H}_2 - \mathbf{H}_1) = J_s \mathbf{e}_z, \qquad (y = d) \tag{2.1.10}$$

$$\mathbf{e}_y \times (\mathbf{E}_2 - \mathbf{E}_1) = \mathbf{0}, \qquad (y = d) \tag{2.1.11}$$

$$\mathbf{E}_1 = Z_\mathrm{s} \left(\mathbf{e}_y \times \mathbf{H}_1\right), \qquad (y = 0) \tag{2.1.12}$$

the unknown parameters (H_1^+, H_1^-, H_2^+) in (2.1.6) and (2.1.8) can be solved as a function of the given parameters (k_1, $Z_{\mathrm{F}1}$, d, J_s, Z_s). In Fig. 2.2(b) the absolute magnetic field $|\mathbf{H}|$ at $y = 2\,d$, $d = 2$ cm, is plotted for different magnitudes and phases of the surface impedance Z_s. It can be seen that the magnitude of the complex surface impedance has a stronger impact on the absolute magnetic field, indicated by a large-scale color change in horizontal direction [cf. Fig. 2.2(b)]; whereas the effect of the phase is comparatively weaker, especially for extremely small and large magnitudes. For the magnitude of surface impedance being around 350 Ω, the absolute magnetic field reveals a maximum phase selectivity.

For the analytical calculation, the effect of the lossy phantom and the dimension of the excitation is not taken into account, which is, however, crucial for MRI applications. These effects will be considered in the forthcoming section based on two- and three-dimensional finite element method (FEM) simulation models.

2.2 EM Field Analysis of Dipole Coil with SIBCs

In this section the EM field characteristics of a dipole coil will be investigated under different shielding scenarios (i.e., with various SIBCs) based on full-wave FEM simulation. Initially, the field analysis will be performed in a two-dimensional manner where the dipole coil element is modeled by a stripline shaped current sheet with an impressed surface current. Subsequently, a real dipole structure is utilized to carry out the three-dimensional simulation, with single and multi-channel arrangements.

2.2.1 Two-Dimensional Analysis with Impressed Current Model

Here a two-dimensional simulation model is established to investigate the EM field behavior based on the pre-classified SIBCs in Sec. 2.1. The excitation of the RF field is realized by an impressed surface current density of 1 A/m.

2.2.1.1 Two-dimensional Simulation Model

Fig. 2.3 shows the two-dimensional model with the corresponding geometry. The coordinate system is aligned in such a way that the x and y axis coincide in horizontal and vertical direction, respectively, and the z axis points outward the figure. Here, a 1.5 cm wide stripline shaped current sheet with an impressed surface current density of 1 A/m in z-direction is used as the excitation of the electromagnetic field. In order to emulate the human body for 7 Tesla MRI, a flat phantom ($\epsilon_\mathrm{r} = 58.2$, $\sigma = 0.92$ S/m, $\rho = 1000$ kg/m^3) with the dimension of 20 cm$\times$15 cm is placed 2 cm above the current sheet. The SIBC in -y direction, which models the shielding plate, is located 2 cm below the stripline. The remaining boundaries, which are separated 5 cm away from the outer surfaces of the phantom, are set as scattering boundary condition, which provides a sufficiently low reflection.

2.2.1.2 EM Field Distribution for Various SIBCs

Fig. 2.4 and Fig. 2.5 show the absolute magnetic and electric field distributions for the previously classified surface impedance from Tab. 2.1. The corresponding field distributions are normalized to the accepted power via the following equation:

$$P_\mathrm{in} = -\frac{1}{2}\Re\left\{\int_S \mathbf{E}\cdot\mathbf{J}_\mathrm{s}^*\,ds\right\}, \tag{2.2.1}$$

where $\mathbf{J}_\mathrm{s}$ and $\mathbf{E}$ is the impressed electric surface current density and the resulting electric field on the stripline shaped current sheet (cf. Fig. 2.3), respectively.

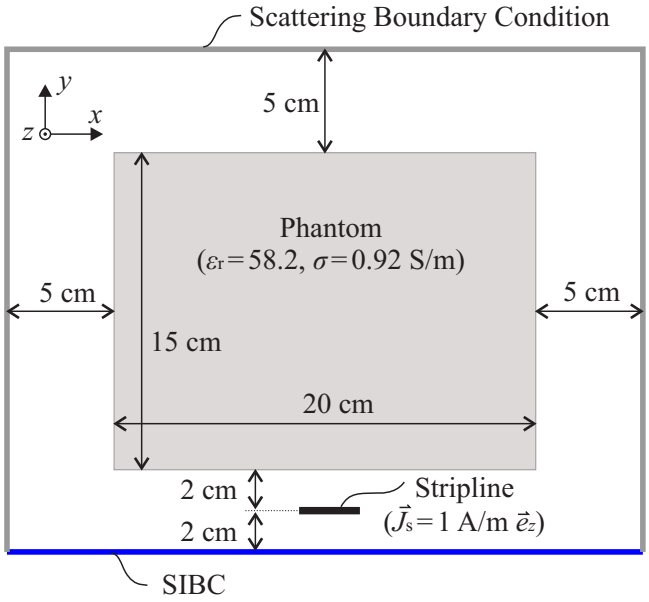

Figure 2.3: Two-dimensional simulation model for dipole coil: A 1.5 cm wide stripline with an impressed surface current density of 1 A/m in z-direction models the RF coil element. A flat phantom is placed 2 cm above the stripline. The lower boundary which serves as a shielding plate is set to a SIBC, while the remaining ones are scattering boundary conditions.

Basically, the SIBCs for different cases ($\Im(\mathrm{Z_s}) = 0$, $\Re(\mathrm{Z_s}) = \Im(\mathrm{Z_s})$ and $\Re(\mathrm{Z_s}) = 0$), which possess the same magnitude of surface impedance, behave in a very similar manner. However, for the case $\Re(\mathrm{Z_s}) = 0$, distinctive field behaviors [cf. Fig. 2.4(b-3) and Fig. 2.5(b-3)] can be observed in comparison to the other two cases. These exceptions will be scrutinized in the forthcoming section while addressing the concept of surface plasmon polarization. According to the magnetic and electric field distributions shown in Fig. 2.4 and Fig. 2.5, as the magnitude remains constant, the variation of real and imaginary parts has no obvious impact on the EM field distribution. More cases ($\mathrm{Z_s}$ with phase angle of 30° and 60°) have been investigated as well. The amplitude of surface impedance is swept in the same range as listed in Tab. 2.1. The field distributions are consistent with the two other cases (first two rows) in Fig. 2.4 and Fig. 2.5. The results are not shown here to avoid the redundancy. Thus, if the absolute electromagnetic field distribution is considered, the SIBC can be approximately characterized by the magnitude of a complex surface impedance. Avoiding the lengthiness of this work, the forthcoming investigations will be carried out only for the purely real surface impedance.

As the magnitude of surface impedance increases, the electric and magnetic fields both tend to expand in the horizontal direction, indicated by the outspread contour lines, while the vertical penetration of the absolute magnetic and electric field inside the phantom is only slightly increased. Another interesting tendency in vertical direction is that the area with strong magnetic field is "pushed" away from the SIBC by an increased surface impedance, whereas the situation for the electric field is contrary—the maximum electric field area tends to be "pulled" towards the SIBC.

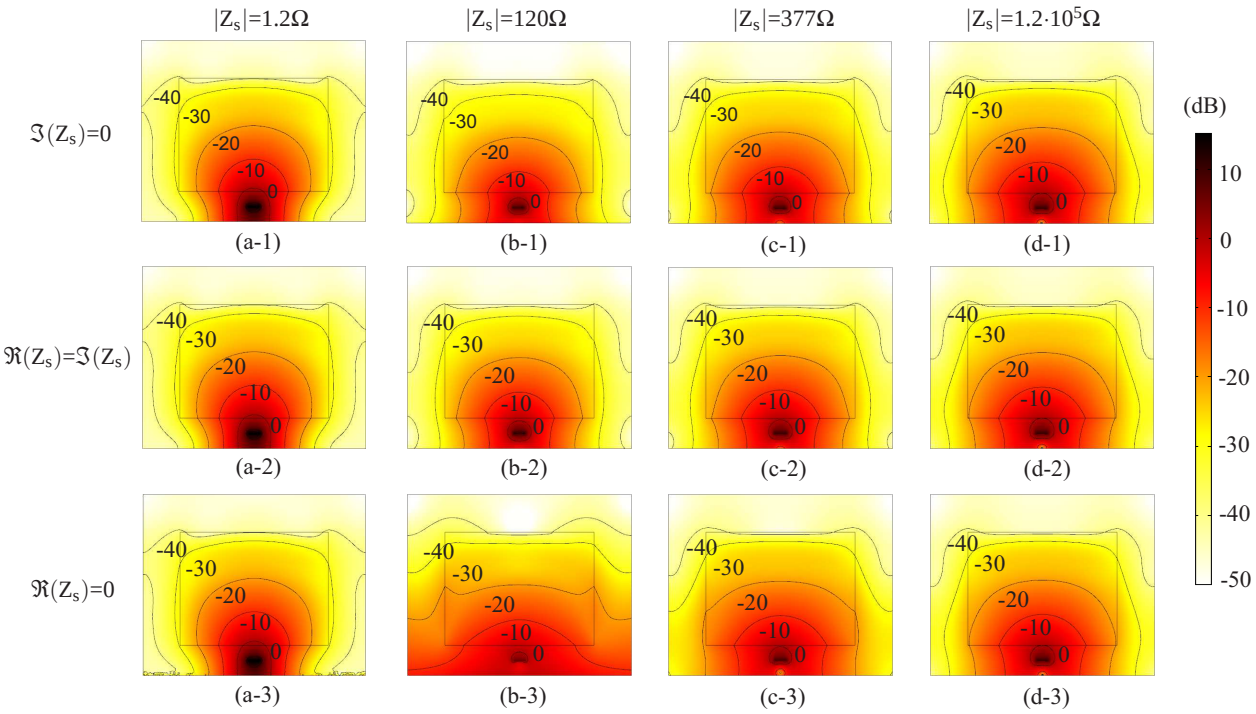

Figure 2.4: Simulated 2D absolute magnetic field distribution $|\mathbf{H}(x, y)|$ at 300 MHz of the stripline dipole based on the SIBCs given in Tab. 2.1. From top to bottom, the SIBC for the lower boundary of the model shown in Fig. 2.3 corresponds to the case of $\Im(Z_\mathrm{s}) = 0$, $\Re(Z_\mathrm{s}) = \Im(Z_\mathrm{s})$ and $\Re(Z_\mathrm{s}) = 0$, respectively. For each case the magnitude of surface impedance is swept from 1.2 Ω [Fig. (a-1), (a-2) and (a-3)] to $1.2{\cdot}10^5$ Ω [Fig. (d-1), (d-2) and (d-3)]. All the field distributions are normalized to the applied power and plotted in dB.

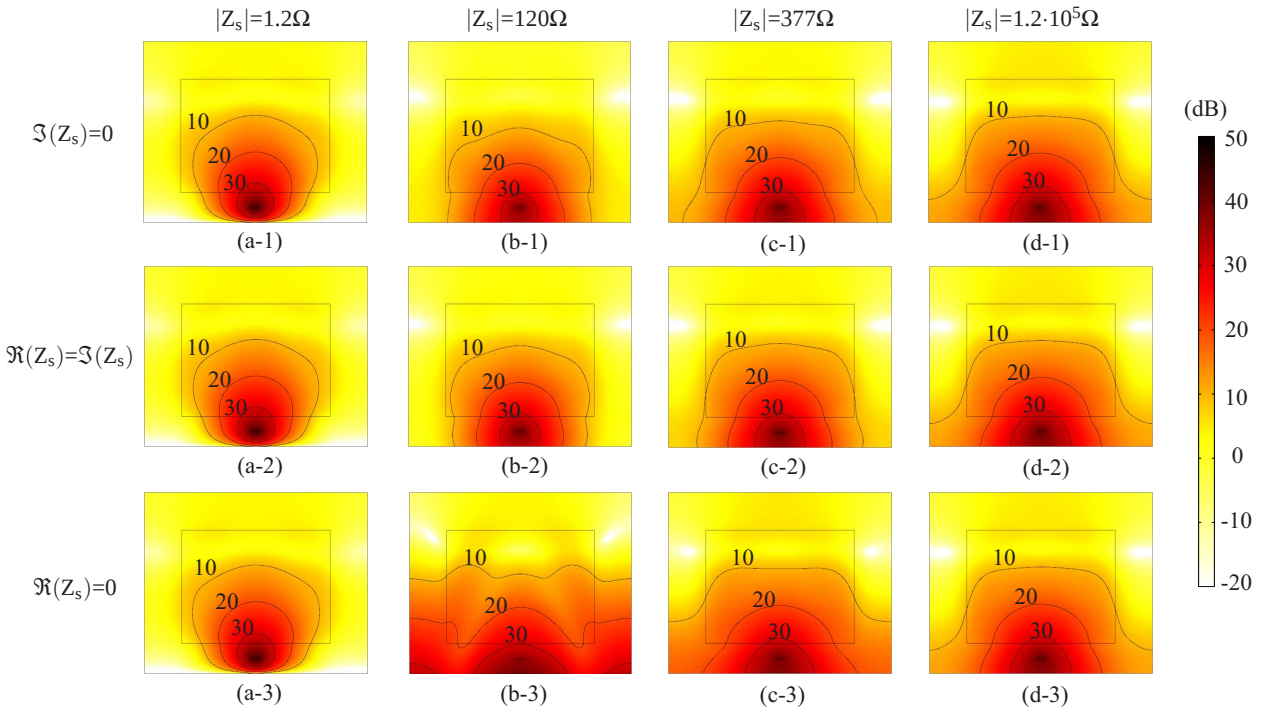

Figure 2.5: Simulated 2D absolute electric field distribution $|\mathbf{E}(x, y)|$ at 300 MHz of the stripline dipole based on the SIBCs given in Tab. 2.1. From top to bottom, the SIBC for the lower boundary of the model shown in Fig. 2.3 corresponds to the case of $\Im(Z_\mathrm{s}) = 0$, $\Re(Z_\mathrm{s}) = \Im(Z_\mathrm{s})$ and $\Re(Z_\mathrm{s}) = 0$, respectively. For each case the magnitude of surface impedance is swept from 1.2 Ω [Fig. (a-1), (a-2) and (a-3)] to $1.2{\cdot}10^5$ Ω [Fig. (d-1), (d-2) and (d-3)]. All the field distributions are normalized to the applied power and plotted in dB.

Here two extreme scenarios are considered: the PEC and the PMC, which refers to the SIBC with extremely small and large surface impedance, respectively. Due to the fact that the magnetic field vector is tangential to the PEC and normal to the PMC, if the shielding plate is assigned as a PEC, the magnetic field is mainly localized between the current sheet and the shielding plate. As the surface impedance approaches to infinity, denoting a PMC, the magnetic field lines are spread away from the central axis while impinging normally on the shielding plate, as shown in Fig. 2.6. As a result, the magnetic field beneath the current sheet is weakened and a broader magnetic field distribution in the horizontal direction is achieved. Since the PEC and PMC can be considered as a "short-circuited" and an "open" terminal, respectively, the voltage, here represents the electric field, at the terminal is proportional to the corresponding terminal (surface) impedance. Hence, the tangential electric field (i.e. the only component in our case) vanishes at the PEC boundary due to the zero surface impedance, whereas a large tangential electric field at the PMC boundary is supported by the infinitely large surface impedance.

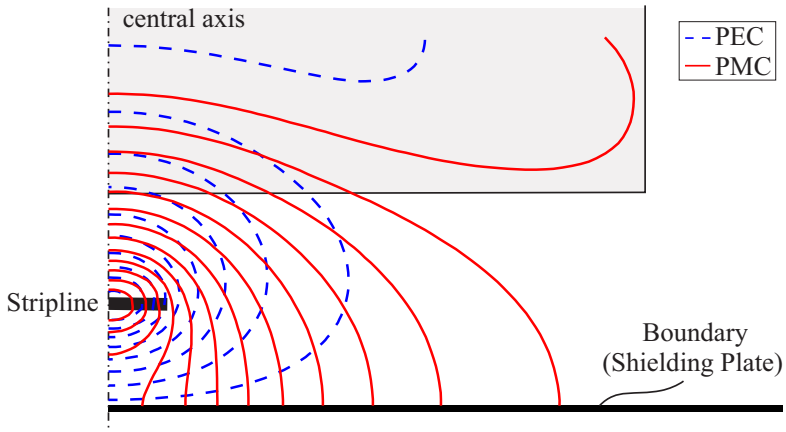

Figure 2.6: Magnetic field lines of the simulation model in Fig. 2.3 with the lower boundary set to PEC (dashed line) and PMC (solid line). The gray area represents the homogeneous flat phantom which is placed above the stripline.

The simulated surface impedances in this study (cf. Tab. 2.1) fall in between the two aforementioned limiting scenarios. The field pattern in Fig. 2.4 and Fig. 2.5 vary progressively from the case with an extremely small surface impedance to the case with a considerably large one.

2.2.1.3 Surface Plasmon Polarization

Surface plasmons are coherent collective electron oscillations that exist at the interface between any two materials where the real part of the dielectric function changes sign across the interface [85], [86]. Here in our case, one of the materials is air, and the other is simulated by the SIBC. In order to achieve a purely imaginary surface impedance, the relative permittivity is set to a negative value, which satisfies the existence condition of surface plasmon. The charge motion/oscillation in a surface plasmon excites electromagnetic fields, which are partially distributed in the air region. This excitation, including

the charge motion/oscillation and the associated electromagnetic field, is called a surface plasmon polariton [86].

For particular values of relative permittivity, here ϵ_r = -10, the surface plasmon polarization with a strong associated electromagnetic field is observed. For the other values of relative permittivity that we specified in this study, the effect of surface plasmon polarization is not observable. Further investigations about the surface plasmon polarization effect is not within the scope of this thesis.

2.2.2 Three-Dimensional Analysis with Real Dipole Structure

In this section, we establish two three-dimensional models and evaluate the effect of the applied SIBCs on the EM fields. Firstly, the evaluation is carried out based on a single coil element with a lumped port excitation. Subsequently, an eight-channel RF coil with circularly polarized magnetic field distribution is considered.

2.2.2.1 Single Coil Element

As the first step, the EM field analysis of a dipole element is performed for various SIBCs. Using the established three-dimensional simulation model, the magnetic field distribution of a dipole coil element is simulated and compared for different shielding scenarios. Based on the simulated field distribution, a numerical analysis is carried out.

2.2.2.1.1 Full-Wave Simulation Model

Fig. 2.7 shows the three-dimensional FEM simulation model. A symmetrically fed dipole coil element [69] which is terminated by two meanders [70] has been employed as an excitation. The total length of the coil element is 25 cm. The geometry of the meander remains unchanged in comparison to the original one in [70]. In order to fine-tune the current distribution on the dipole, high-dielectric substrates have been placed around the meander sections [87]. Similar to the two-dimensional model, a homogenous flat phantom is placed 2 cm above the dipole. The width, length and height of the phantom is set to 20 cm, 40 cm and 15 cm, respectively. The boundary 2 cm beneath the dipole coil element is assigned as a SIBC, whereas the remaining boundaries of the simulation box are set to scattering boundary conditions.

2.2.2.1.2 Effective Magnetic Field

In MRI applications, the specific absorption rate (SAR) inside the body is a critical limitation which should be minimized [43, 88]. Thus, the magnetic field distribution which is normalized to the square root of the maximum local SAR inside the phantom is of our great interest and is usually defined as the B_1 efficiency:

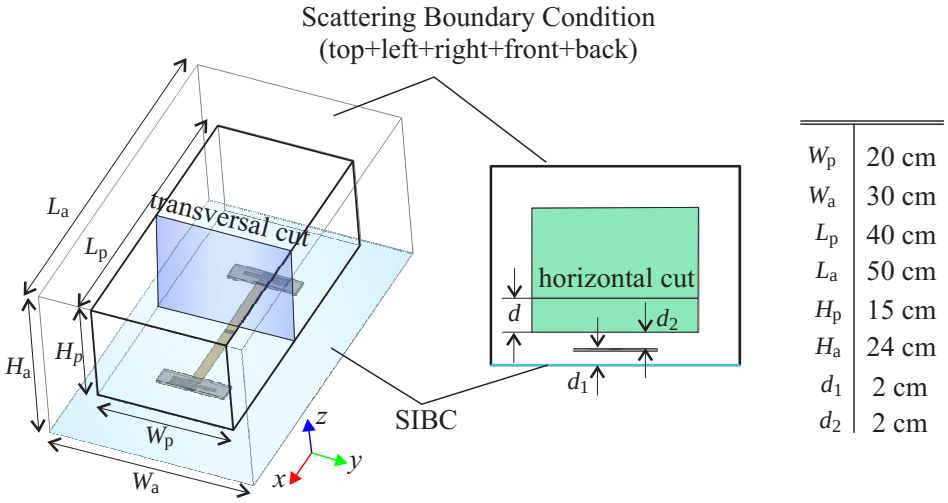

Figure 2.7: Simulation setup of the single RF coil element with the geometry data. The bottom of the simulation box is assigned as SIBCs, whereas the remaining walls are set to scattering boundary conditions.

$$\mathbf{B}_{1,\,\mathrm{eff}} = \frac{|\mathbf{B}_1|}{\sqrt{\max\left(SAR\right)}}. \tag{2.2.2}$$

The local SAR can be computed according to the following equation

$$SAR = \frac{\sigma|\mathbf{E}|^2}{2\rho}, \tag{2.2.3}$$

where ρ and σ is the density of matter and the electric conductivity of the tissue, respectively.

2.2.2.1.3 Simulation Results

In the previous section a two-dimensional model was utilized to investigate the EM field characteristics of a dipole coil based on different SIBCs. In order to validate the equivalence of the two- and three-dimensional model, the normalized magnetic field distributions ($B_{1,\,\mathrm{eff}}$) on the transverse plane are plotted in dB (cf. Fig. 2.8) for $\mathrm{Z_s} = 1.2\ \Omega$. An excellent agreement of the field distribution can be observed for the two- and three-dimensional models.

The normalized magnetic field distribution ($B_{1,\,\mathrm{eff}}$) in the transversal and horizontal planes of the three-dimensional model specified in Fig. 2.7 are investigated for different surface impedances as for the two-dimensional study in Sec. 2.2.1. Moreover, the horizontal field distribution are evaluated for different depths inside the phantom ($d = 1,\ 3,\ 5$ cm). The magnetic field distribution on the transversal and horizontal planes vary gradually according to the magnitude of surface impedance. Here only two extreme cases, where the

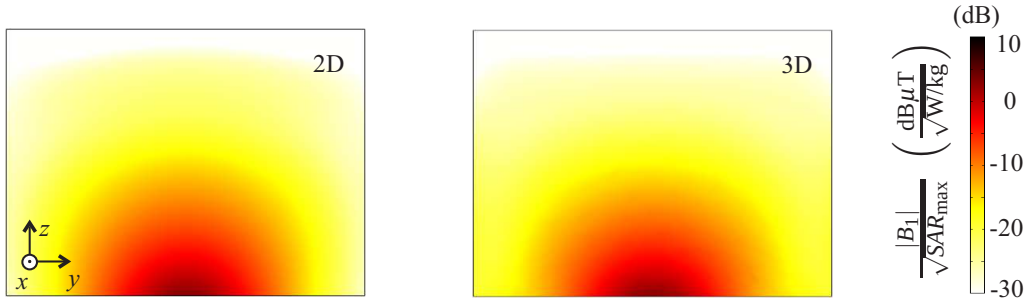

(a) (b)

Figure 2.8: Simulated absolute magnetic field distribution ($|\mathbf{B}_1|$) at 300 MHz on the transversal cut of the phantom with (a) the two-dimensional model depicted in Fig. 2.3 and (b) the three-dimensional model depicted in Fig. 2.7. The surface impedance is set to 1.2 Ω. The field distributions are normalized to the square root of peak *SAR* inside the phantom and plotted in dB.

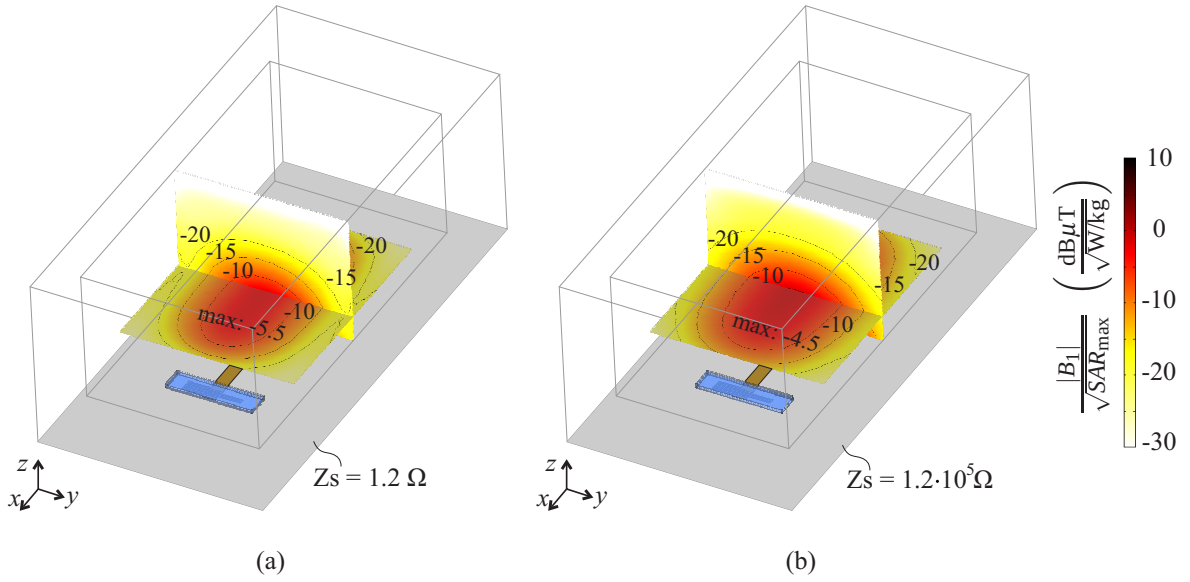

(a) (b)

Figure 2.9: Simulated absolute magnetic field distribution ($|\mathbf{B}_1|$) at 300 MHz on the transversal and horizontal cut (3 cm inside the phantom) with the three-dimensional full-wave model depicted in Fig. 2.7. Two cases—the surface impedance set to (a) 1.2 Ω and (b) $1.2{\cdot}10^5$ Ω—are compared. The field distributions are normalized to the square root of peak *SAR* and plotted in dB.

surface impedance is set to 1.2 Ω and $1.2{\cdot}10^5$ Ω, are compared in Fig. 2.9. It has been noticed that the relative horizontal field distribution for different depths inside phantom behave in a similar manner. Hence, Fig. 2.9 shows only the field distribution located 3 cm inside the phantom, i.e., 5 cm above the dipole.

As the magnitude of surface impedance increases, the maximal penetration of magnetic field inside phantom is slightly strengthened. Moreover, the magnetic field is distributed in a broader manner along the y-direction. For a small surface impedance (Fig. 2.9(a)), the

field is mainly concentrated near the z axis and a rapid field decay can be observed when reaching the sideward boundaries of the phantom. If the surface impedance approaches to a large value, the magnetic field tends to decay away from the central axis more gently, as shown in Fig. 2.9(b). Thus, an improved homogeneity of magnetic field distribution inside the phantom can be achieved by using a shielding plate with large surface impedance.

2.2.2.1.4 Numerical Analysis

For an RF coil the penetration depth and the homogeneity of the magnetic field inside the human body are two essential parameters to evaluate the performance of the coil. To some extent, the averaged penetrating ability of the magnetic field can be correlated to the mean value of the normalized magnetic field, which is defined by

$$B_{1,\,\mathrm{avg}} = \frac{\mathrm{mean}\,(|\mathbf{B}_1|)}{\sqrt{\max\,(SAR)}}. \tag{2.2.4}$$

The homogeneity of the magnetic field inside the phantom is then represented by the coefficient of variation (CoV) of the absolute magnetic field inside the phantom according to the following definition [89, 90]:

$$\mathrm{CoV}\,(|\mathbf{B}_1|) = \frac{\mathrm{std}\,(|\mathbf{B}_1|)}{\mathrm{mean}\,(|\mathbf{B}_1|)}, \tag{2.2.5}$$

where std stands for the standard deviation. A small CoV indicates a low variance of the examined variable. For a good RF coil, a sufficient penetration depth and, meanwhile, a homogenous magnetic field are desired. Hence, the $B_{1,\,\mathrm{avg}}$ and CoV of the absolute magnetic field in (2.2.4) and (5.2.1) should be maximized and minimized, respectively.

Based on the field data extracted from the central transversal cross section and the horizontal cross sections at different penetration depths, the corresponding $B_{1,\,\mathrm{avg}}$ and CoV $(|\mathbf{B}_1|)$ of the absolute magnetic field for various surface impedances are calculated and given in Tab. 2.2 and Tab. 2.3.

Table 2.2: Calculated Field Parameters for Different Surface Impedances on the Transversal Cut of the Phantom

Z_s $[\Omega]$	1.2	120	377	$1.2{\cdot}10^5$
$B_{1,\,\mathrm{avg}}[\frac{\mu\mathrm{T}}{\sqrt{\mathrm{W/kg}}}]$	0.1597	0.1787	0.1863	0.1976
CoV $(\|\mathbf{B}_1\|)$	1.1898	1.1442	1.1145	1.0812

Tab. 2.2 shows that with a larger magnitude of surface impedance, the averaged magnetic field over the transversal cross section is increased. Additionally, a smaller CoV $(|\mathbf{B}_1|)$ of the absolute magnetic field is obtained, indicating a more homogenous field distribution.

Table 2.3: Calculated Field Parameters for Different Surface Impedances and Penetration Depths (cf. Fig. 2.7) on the Horizontal Cuts of the Phantom

Z_s [Ω]	1.2	120	377	$1.2{\cdot}10^5$		
$B_{1,\,\mathrm{avg}}[\frac{\mu\mathrm{T}}{\sqrt{\mathrm{W/kg}}}]$	0.3576	0.4053	0.4205	0.4283	1 cm	d
	0.2291	0.2614	0.2725	0.2789	3 cm	
	0.1480	0.1704	0.1788	0.1838	5 cm	
CoV ($\lvert\mathbf{B}_1\rvert$)	0.7575	0.6805	0.6437	0.6237	1 cm	d
	0.5968	0.5609	0.5347	0.5211	3 cm	
	0.4839	0.4835	0.4580	0.4411	5 cm	

A consistent tendency can be observed in Tab. 2.3 for various penetration depths. By increasing the magnitude of surface impedance, a larger $B_{1,\,\mathrm{avg}}$ and a smaller CoV ($\lvert\mathbf{B}_1\rvert$) can be achieved. Additionally, the averaged magnetic field and the CoV both decrease with an increased penetration depth, where the field is naturally distributed in a more uniform and broader manner (cf. Fig. 2.4).

2.2.2.2 Multi-Channel RF Coil

For UHF MRI applications, instead of a single coil element, multi-channel RF coils are utilized for a better imaging quality [34, 91]. Here the EM field analysis of an eight-channel dipole coil is performed for various SIBCs. Apart from a homogeneous cylindrical phantom, a heterogeneous head model is also considered. Additionally, the impact of different SIBCs on the coupling level between the dipole elements is investigated.

2.2.2.2.1 Full-Wave Simulation Model

Fig. 2.10 depicts an eight-channel model with the same coil element as displayed in Fig. 2.7. The eight coil elements are uniformly arranged around a cylindrical phantom ($\epsilon_\mathrm{r} = 58.2$, $\sigma = 0.92$ S/m) with a radial separation of 2 cm between the coil element and the phantom. An octagonal prismatic simulation box is utilized here to adapt the particular arrangement of the coil elements. The lateral surface of the simulation box is assigned as SIBC, whereas the top and bottom interfaces are set to scattering boundary conditions.

For a multi-channel RF coil, the circularly polarized magnetic field, namely the B_1^+ field, inside the phantom is mostly considered [91, 92]. In order to excite a circularly polarized mode, the coil elements in our case are fed equally in magnitude and with a relative phase lag of 45°.

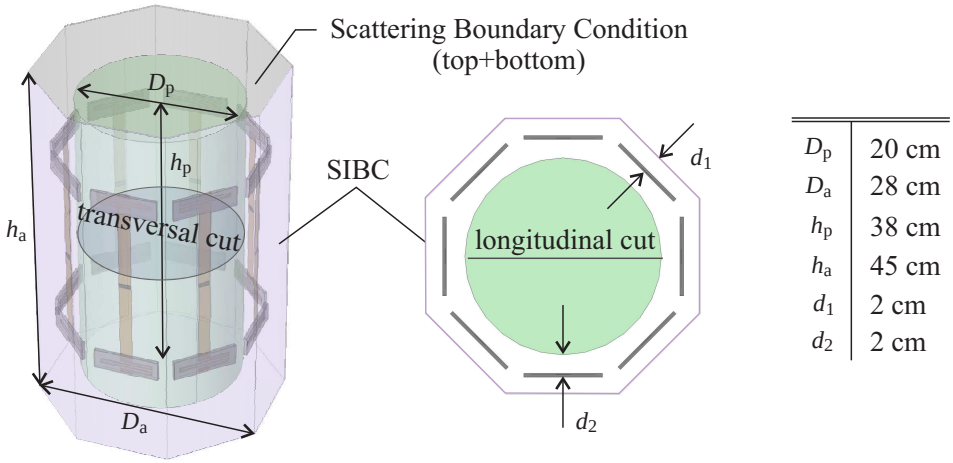

D_p	20 cm
D_a	28 cm
h_p	38 cm
h_a	45 cm
d_1	2 cm
d_2	2 cm

Figure 2.10: Simulation setup of the 8-channel RF coil including the geometry data. The lateral surfaces of the simulation box are assigned as SIBCs, whereas the top and bottom interfaces are set to scattering boundary conditions.

2.2.2.2.2 Simulation Results

The simulated $|B_1^+|$ field distributions of the multi-channel RF dipole coil (cf. Fig. 2.10) for various surface impedances are shown in Fig. 2.11. The B_1^+ distribution is normalized to the square root of the peak SAR inside the phantom. Here only two cases, a relative small and large surface impedance which corresponds to the PEC and PMC, respectively, are presented. A consistent tendency of the field distribution versus surface impedance can be observed, as in Fig. 2.9. By applying a shielding plate with a large surface impedance, the B_1^+ field distribution on the transversal cross section of the phantom is improved, in terms of homogeneity and penetration [cf. Fig. 2.11(a, b)]. With the surface impedance set to 1.2 Ω and $1.2{\cdot}10^5$ Ω, the CoV of the normalized $|B_1^+|$ field as defined in (2.2.2) on the transversal plane reads 0.31 and 0.28, respectively, indicating that the homogeneity of the B_1^+ field is improved by the SIBC with a large surface impedance. With the surface impedance set to 1.2 Ω and $1.2{\cdot}10^5$ Ω, the mean value of the normalized $|B_1^+|$ on the transversal plane reads 0.37 and 0.42 $\mu\mathrm{T}/\sqrt{\mathrm{W/kg}}$, respectively, indicating a stronger penetration ability of the B_1^+ field is obtained by using a SIBC with a large surface impedance. The field distribution on the longitudinal plane also reveals that a shielding plate with a large surface impedance could effectively improve the penetration depth of the magnetic field excited by the dipole coil in comparison to the one with an extremely small surface impedance [cf. Fig. 2.11(c, d)].

Additionally, a heterogeneous human head model has been utilized to validate the effect of the applied SIBCs on the $|B_1^+|$ distribution. The arrangement and the excitation of coil elements are kept unchanged in comparison to the case with a homogeneous phantom, i.e., no particular RF shimming is performed. The $|B_1^+|$ distribution on the transverse cut of the head model is compared for two SIBCs—the surface impedance set to 1.2 Ω and $1.2{\cdot}10^5$ Ω. As displayed in Fig. 2.12, the coil shielded by a SIBC with large surface impedance provides a better $|B_1^+|$ distribution, both in terms of homogeneity and absolute

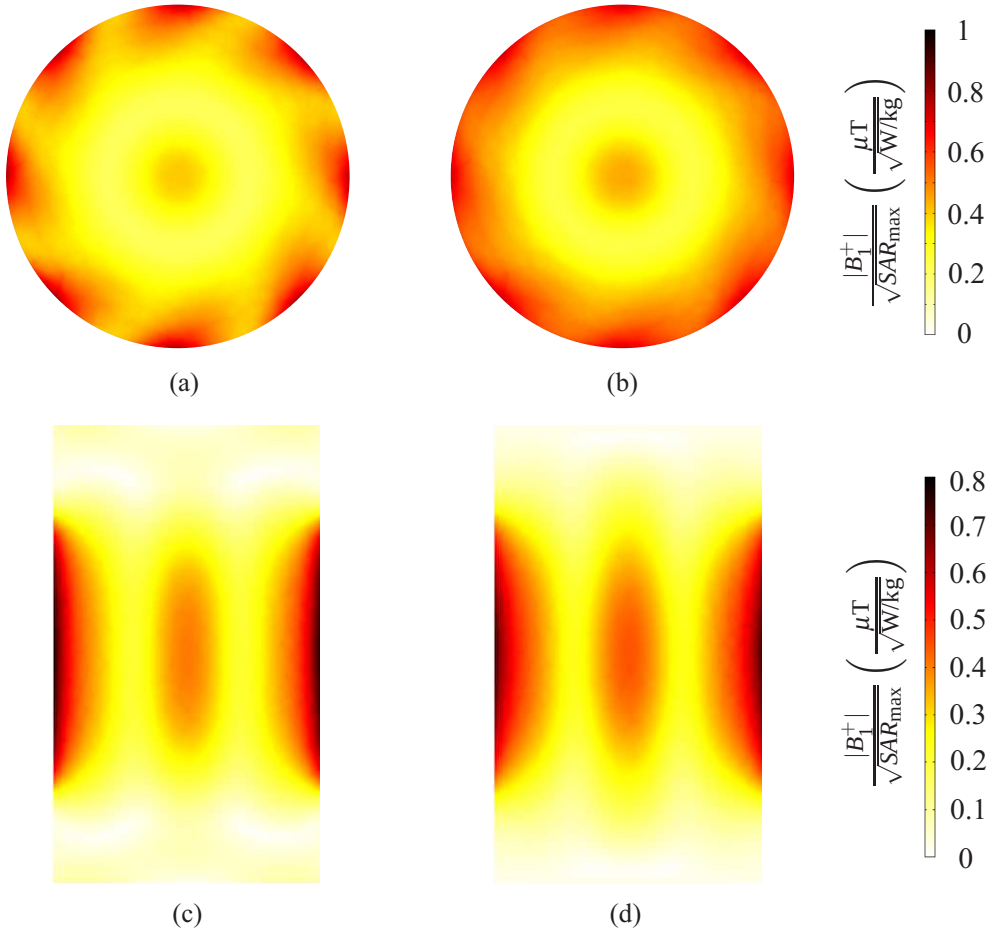

Figure 2.11: Simulated magnetic field distributions of the 8-channel RF coil depicted in Fig. 2.10 on (a, b) the transversal and (c, d) the longitudinal cut plane of the phantom at 300 MHz. Two cases—the surface impedance set to 1.2 Ω (a, c) and $1.2{\cdot}10^5$ Ω (b, d)—are compared. The field distributions are normalized to the square root of the peak SAR inside the phantom.

field strength.

2.2.3 Summary of Dipole Coil with SIBCs

In this section the RF shield of the dipole coil element for UHF MRI has been modeled by the surface impedance boundary condition (SIBC). According to the simulation results, if the absolute electromagnetic field distribution is considered, the SIBC can be approximately characterized by the magnitude of a complex surface impedance. For UHF MRI applications ($B_0 \geq 7$ T), the inhomogeneous and rapidly decaying B_1 field is a major challenge. The investigation carried out in this section has demonstrated the feasibility to improve the B_1 homogeneity and the absolute penetration depth on the transversal plane inside the phantom by utilizing an RF shield with high surface impedance behind the coil element. For an eight-channel RF dipole coil loaded with a homogeneous cylindrical

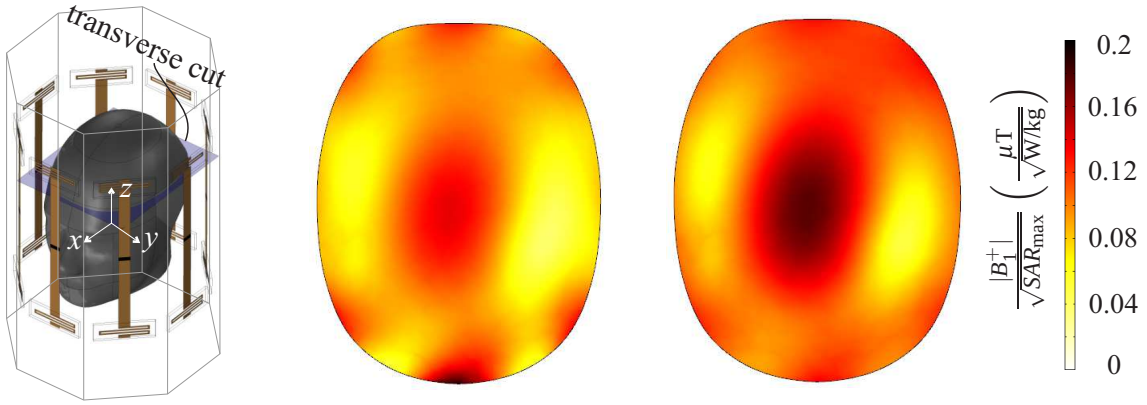

(a) (b) (c)

Figure 2.12: (a) Multi-channel RF coil with a heterogeneous head model and (b, c) the simulated $|\mathbf{B}_1^+|$ distributions at 300 MHz on the transverse cut (z=5 cm) for different SIBCs: (b) 1.2 Ω and (c) $1.2{\cdot}10^5$ Ω. The $|\mathbf{B}_1^+|$ distributions are normalized to the square root of peak SAR.

phantom, a 10% reduction on CoV of the transverse $|B_1^+|$ distribution, and a 13% increase on the averaged transverse $|B_1^+|$ can be achieved by using an RF shield with a high surface impedance ($1.2{\cdot}10^5$ Ω) comparing to the case with a small one (1.2 Ω).

2.3 EM Field Analysis of Loop Coil with SIBCs

In this section the EM field analysis of a stripline surface loop coil will be carried out for different shielding scenarios based on FEM simulations. Similar to the investigation for the dipole coil in Sec. 2.2, the field analysis will be firstly performed in a two-dimensional manner, and then verified by a three-dimensional model where a real loop structure is considered.

2.3.1 Two-Dimensional Analysis with Impressed Current Model

Here a two-dimensional simulation model is established to investigate the EM field behavior based on the pre-classified SIBCs in Sec. 2.1. As the excitation of the electromagnetic field, a stripline shaped current loop with an impressed surface current density of 1 A/m in φ-direction is utilized (cf. Fig. 2.13).

2.3.1.1 Two-dimensional Simulation Model

Fig. 2.13 depicts the two-dimensional model, which is rotationally symmetric around the z-axis. As the excitation of the electromagnetic field a 1.5 cm wide current loop with an impressed surface current density of 1 A/m in φ-direction has been utilized. The diameter of the current loop is set to 10 cm. Similar to the case of a dipole coil in the previous section, a homogeneous phantom ($\epsilon_\mathrm{r} = 58.2$, $\sigma = 0.92$ S/m, $\rho = 1000$ kg/m^3) with a diameter of 20 cm is placed 1 cm above the current loop. The SIBC in -z direction, which models the shielding plate, is located 1 cm below the current loop. The remaining boundaries, which are located 5 cm away from the outer surfaces of the phantom, are set to scattering boundary condition, which provides a sufficiently low reflection.

2.3.1.2 EM Field Distribution for Various SIBCs

Fig. 2.14 and Fig. 2.15 show the absolute magnetic and electric field distributions for the previously classified surface impedance from Tab. 2.1. Generally, the SIBCs in different categories ($\Im(Z_\mathrm{s}) = 0$, $\Re(Z_\mathrm{s}) = \Im(Z_\mathrm{s})$ and $\Re(Z_\mathrm{s}) = 0$) behave in a similar manner if the same magnitude of the corresponding surface impedance is assigned. The irregular field distribution in Fig. 2.14(b-3) and Fig. 2.15(b-3) are caused by the surface plasmons, which has been discussed in Sec. 2.2.1.3. As the magnitude of surface impedance increases, the magnetic field of the current loop reveals an extension in the horizontal direction, indicated by the outspread contour lines. And in the vertical direction a slightly strengthend penetration of the magnetic field inside the phantom is observed. However, in the region close to the center of the loop, the magnetic field in the case of a large surface impedance is remarkably stronger in comparison to the case of a small one. This can be explained by the fact that the normal magnetic field component is supported at the SIBC with a large surface impedance, whereas suppressed by the boundary with a small surface impedance.

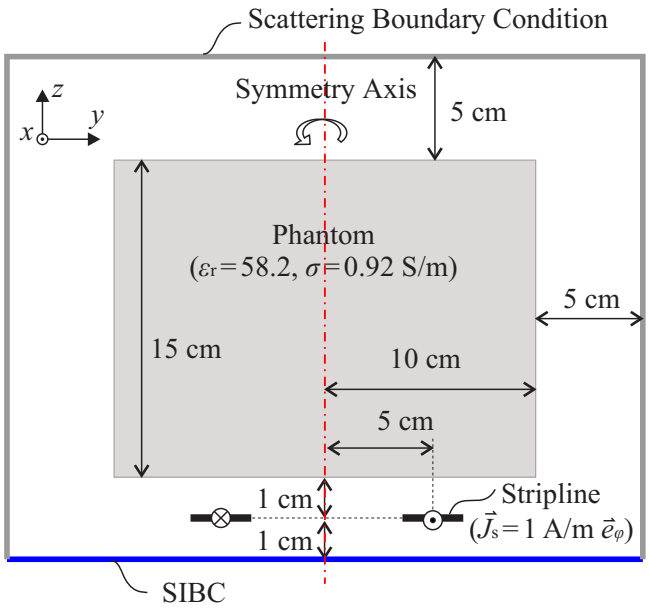

Figure 2.13: Two-dimensional simulation model for surface loop coil: A 1.5 cm wide current loop with an impressed surface current density of 1 A/m in φ-direction models the RF coil element. A homogeneous phantom is placed 1 cm above the current loop. The lower boundary which serves as a shielding plate is set to a SIBC, while the remaining are set to scattering boundary conditions.

With an increased surface impedance, the electric field also tends to expand in the horizontal direction. Meanwhile, the penetration depth of the absolute electric field in the vertical direction is slightly increased. Another interesting phenomenon is that the electric field is repelled by the SIBC with a small surface impedance [cf. Fig. 2.15(a)], whereas attracted by the SIBC with a large surface impedance [cf. Fig. 2.15(d)]. As a result, the maximum electric field spots for a small and a large surface impedance are located above and below the current loop, respectively. Hence, the maximum electric field inside the phantom for the case of a small surface impedance is relatively larger compared to the case of a large surface impedance.

2.3.2 Three-Dimensional Analysis with Real Loop Structure

In this section a three-dimensional model is established to evaluate the effect of different SIBCs on the performance of a surface coil. A series resonant loop structure based on periodic design [84] is proposed and utilized for the investigation.

2.3.2.1 Evaluation Parameter

For 7 Tesla RF coils operating in transmit mode, the local maximum of the specific absorption rate (peak SAR) is a critical parameter, which restricts the power that can be applied to the RF coil, and could cause RF safety issues if exceeding the allowed value

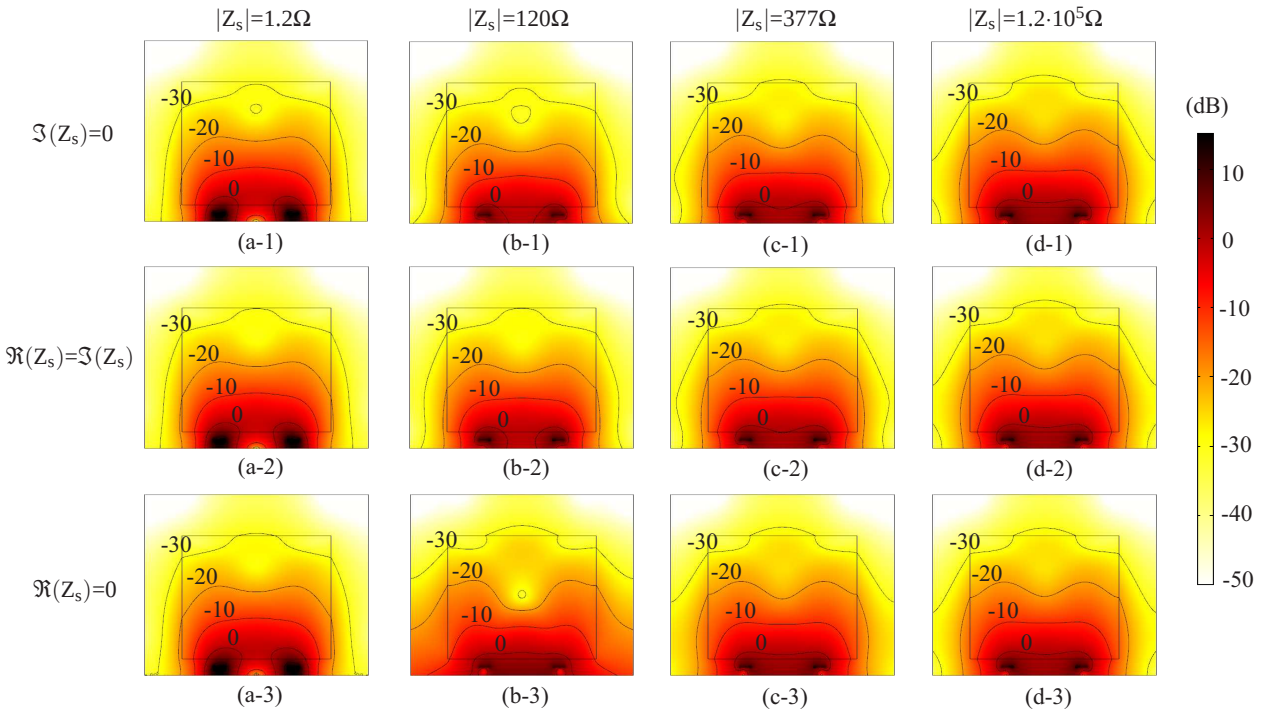

Figure 2.14: Simulated 2D absolute magnetic field distribution $|\mathbf{H}(x, y)|$ at 300 MHz of the current loop based on the SIBCs given in Tab. 2.1. From top to bottom, the SIBC for the lower boundary of the model shown in Fig. 2.13 corresponds to the case of $\Im(Z_s) = 0$, $\Re(Z_s) = \Im(Z_s)$ and $\Re(Z_s) = 0$, respectively. For each case the magnitude of surface impedance is swept from 1.2 Ω [Fig. (a-1), (a-2) and (a-3)] to $1.2{\cdot}10^5$ Ω [Fig. (d-1), (d-2) and (d-3)]. All the field distributions are normalized to the applied power and plotted in dB.

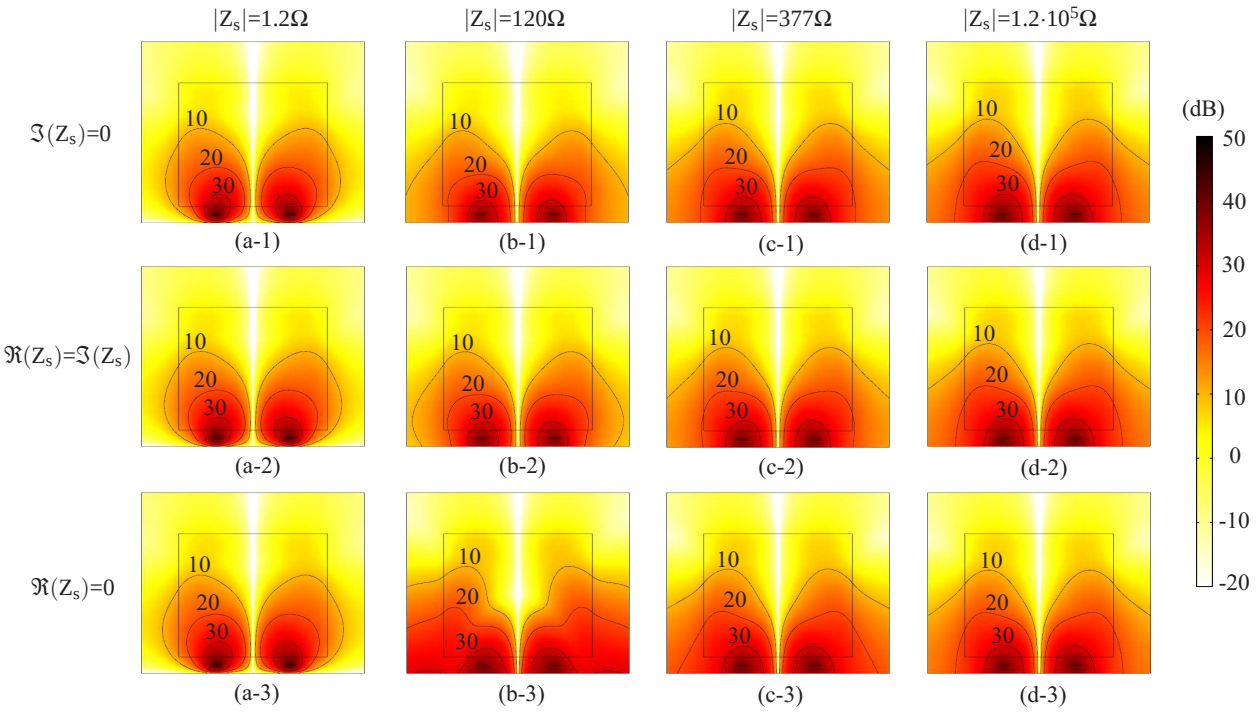

Figure 2.15: Simulated 2D absolute electric field distribution $|\mathbf{E}(x, y)|$ at 300 MHz of the current loop based on the SIBCs given in Tab. 2.1. From top to bottom, the SIBC for the lower boundary of the model shown in Fig. 2.13 corresponds to the case of $\Im(Z_s) = 0$, $\Re(Z_s) = \Im(Z_s)$ and $\Re(Z_s) = 0$, respectively. For each case the magnitude of surface impedance is swept from 1.2 Ω [Fig. (a-1), (a-2) and (a-3)] to $1.2{\cdot}10^5$ Ω [Fig. (d-1), (d-2) and (d-3)]. All the field distributions are normalized to the applied power and plotted in dB.

[34, 88, 93]. Under this consideration, here we utilize the previously defined B_1 efficiency in (2.2.2), where the absolute B_1 field is normalized to the square root of the peak SAR:

$$\mathbf{B}_{1,\,\mathrm{eff}} = \frac{|\mathbf{B}_1|}{\sqrt{\max(SAR)}}.$$

Being a widely used parameter to measure the performance of receiving RF coils, the SNR can be defined as follows by neglecting the power loss within the coil [94]:

$$\mathrm{SNR} = \frac{U_{\mathrm{S,\,peak}}}{\sqrt{2}U_{\mathrm{N,\,eff}}} = \frac{\omega V M_0 |\mathbf{B}_1|}{\sqrt{8kT\Delta f R_{\mathrm{L}}}} = \frac{\omega V M_0 |\mathbf{B}_1|}{\sqrt{16kT\Delta f P_{\mathrm{L}}}}. \tag{2.3.1}$$

The absolute B_1 field ($|\mathbf{B}_1|$) and the total power loss within the phantom (P_{L}) are computed by the EM simulator, here COMSOL Multiphysics. The remaining parameters in (2.3.1) are taken as constant and are listed in Tab. 2.4.

Table 2.4: Parameters for SNR Calculation

Symbol	Value	Description
ω	$1.866{\cdot}10^9$ rad/s	precession angular frequency at 7 T
V	1 mm^3	voxel volume
M_0	0.02288 A/m	magnetization at 7 T
k	$1.38{\cdot}10^{-23}$ J/K	Boltzmann's constant
T	300 K	temperature
Δf	1 Hz	receiver bandwidth

2.3.2.2 Real Periodic Loop Structure

The proposed periodic loop structure is basically a cascade of several unit cells which can be modelled by a series resonant circuit. The layout and the corresponding equivalent circuit of the unit cell are shown in Fig. 2.16. The top and bottom metallic layers are in the same width [W_1 in Fig. 2.16(a)] and printed on a Rogers RO3010 substrate ($\epsilon_r = 11.2$) with a thickness of 0.64 mm, which create a metal-insulator-metal (MIM) structure. The series inductance L_{top} and L_{bot} in the equivalent circuit [cf. Fig. 2.16(b)] are due to the current flow along the unit cell. The slit in the top layer and the overlap between top and bottom layers contributes to the C_{gap} and C_{mim}, respectively. The MIM capacitance C_{mim} has a dominant effect on the total capacitance compare to the C_{gap}. Thus, the equivalent circuit can be simplified to an ordinary series LC resonant circuit.

The closed loop structure can be formed by cascading more unit cells. The excitation of the loop is done by placing a lumped port between two adjacent unit cells on the top metal layer. The corresponding resonant frequency can be determined by the zero crossing of the

imaginary part of the port input impedance. At this resonant frequency a quite uniform current distribution along the loop can be achieved.

It has to be pointed out that the original loop structure has no shield behind it. By introducing a shield with specific surface impedance, the corresponding resonant frequency will be shifted due to the coupling between the loop and the shielding structure. For instance, if a PEC shield or so-called ground plane is introduced under the loop structure, the resonant frequency will be shifted to a higher frequency; if a PMC shield is placed under the loop structure, the resonant frequency is shifted slightly to a lower frequency.

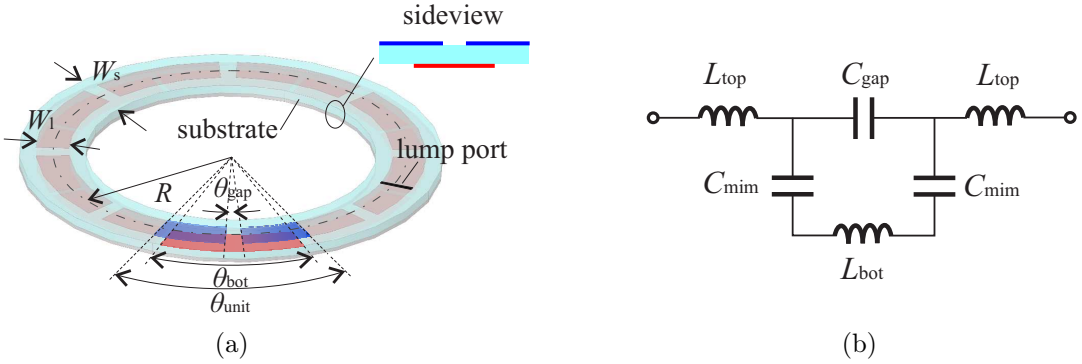

Figure 2.16: The proposed series resonant loop: (a) the unit cell of the series resonant loop structure with the geometry parameters and (b) the corresponding lumped-element equivalent circuit in a lossless case.

2.3.2.3 Simulation Setup with Real Loop Structure

The simulation setup for the investigation on the effect of different SIBCs based on the series resonant loop structure is depicted in Fig. 2.17. Here, only the SIBCs with extremely small and large surface impedance, which corresponds to the PEC and PMC boundary, respectively, are considered. The bottom boundary of the computational domain in -z direction serves as the RF shield (PEC or PMC), while the remaining are set to scattering boundary conditions. A cylindrical phantom ($\epsilon_r = 58.2$, $\sigma = 0.92$ S/m) with a diameter of 10 cm and a height of 15 cm is placed 10 mm above the surface coil. The parameters used to evaluate the coil performance (SNR and B_1 efficiency) are extracted along the central axis of the cylindrical phantom for the different shielding scenarios. Additionally, a parametric study is carried out to investigate the effect of the separation distance from the surface coil to the surface impedance boundary.

The loop structure has been tuned to achieve a series resonance at 300 MHz (Larmor frequency for 7 T MRI) for the PEC and PMC shields separately with different separation distances to the top surface of the loop (d = 5, 10, 15 mm). The corresponding geometry parameters are given in Tab. 4.1. The number of the cascading cells and the azimuth span of the unit cell (θ_{unit}) are kept identical for different shielding scenarios (PEC, PMC) and

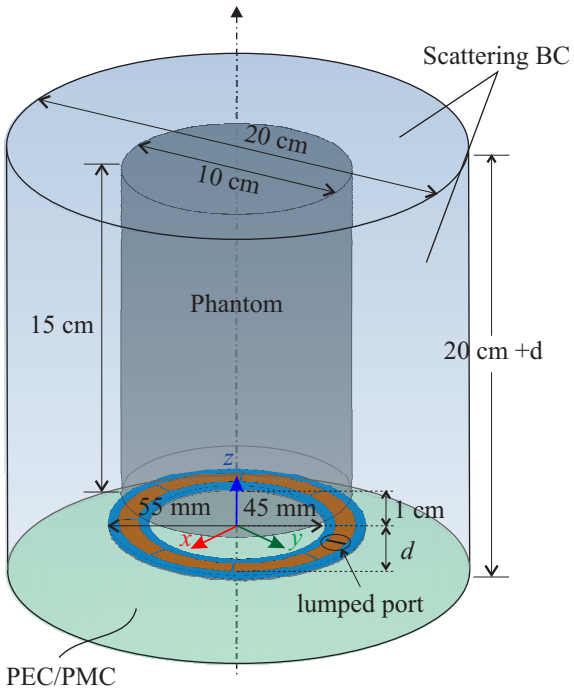

Figure 2.17: The 3D simualtion setup of the series loop loaded with a homogeneous cylindrical phantom for the investigation on the effect of different shielding scenarios. The bottom boundary of the computational domain in -z direction serves as the RF shield (PEC or PMC), while the remaining ones are scattering boundary conditions.

Table 2.5: Parameters of Series Loop with PEC and PMC Shields [cf. Fig. 2.16(a)]

Type of Shield	Nr. of cells	R [mm]	W_l [mm]	W_s [mm]	θ_unit [deg]	θ_bot [deg]	θ_gap [deg]	d [mm]
PEC	6	50.6	10	20	60	53.0	2.26	5
	6	50.6	10	20	60	36.0	2.26	10
	6	50.6	10	20	60	30.3	2.26	15
PMC	6	50.6	10	20	60	16.6	2.26	5
	6	50.6	10	20	60	18.3	2.26	10
	6	50.6	10	20	60	19.4	2.26	15

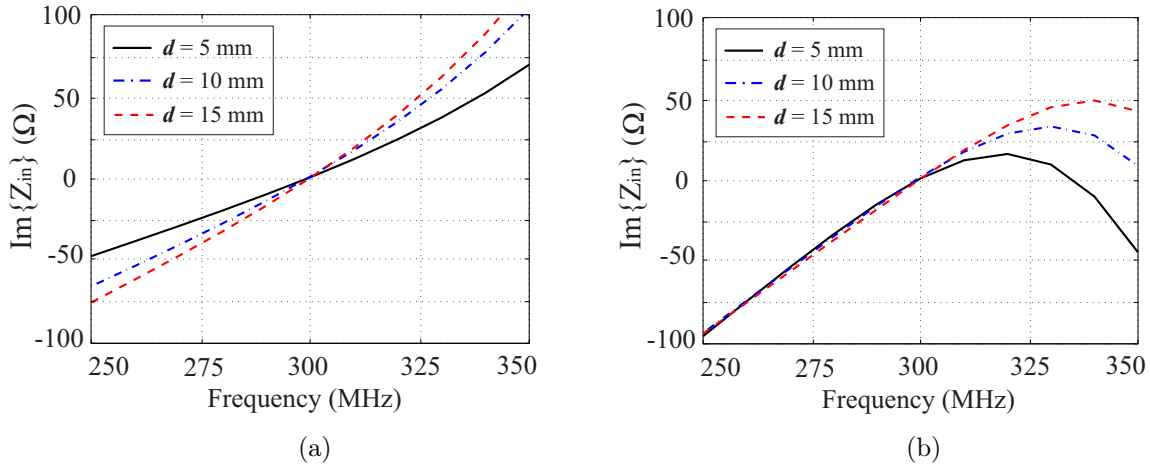

Figure 2.18: Imaginary part of the input impedance of the surface loop loaded with a homogeneous cylindrical phantom for (a) a PEC shield and (b) a PMC shield.

separation distances (d), only the azimuth span of the bottom metal layer in each unit cell (θ_{bot}) is adjusted.

From the reactance plot of the series resonant loop loaded with a homogeneous cylindrical phantom, the resonance frequency of the surface loop is verified by the zero-crossing of the imaginary part of the corresponding input impedance (cf. Fig. 2.18).

2.3.2.4 Influence on B_1 Efficiency and SNR

As can be seen from Fig. 2.19(a-c), the PMC shield generally provides an improvement on the B_1 efficiency compare to the PEC case. The improvement is significant for small penetration depths and degrades as the penetration depth further increases. For large penetration depths the B_1 efficiency and the *SNR* curves for the PEC and the PMC cases converge gradually. Note that the coil with PEC shield exhibits a local maximum in the B_1 efficiency at a certain penetration depth (optimal penetration depth), which depends on the particular design parameters [35], whereas for the PMC case the B_1 efficiency shows a monotone decrease. The optimal penetration depth for the PEC case tends to slightly decrease for an increased separation distance d. Additionally, as the separation distance from the surface coil to the PEC shield increases, an increment on B_1 efficiency can be observed, since the effect of the induced current on the shield is reduced. Due to the fact that no induced current is supported on the PMC boundary, the B_1 efficiency of the surface coil with a PMC shield is quite constant for the different separation distances.

The *SNR* shown in Fig. 2.19(d-f) behave in a similar but slightly different manner as the B_1 efficiency. In comparison to the PEC case, the coil with a PMC shield achieves an enhanced *SNR* for the region close to the bottom surface of the phantom. For larger penetration depth only a slight improvement can be observed. Again, the largest *SNR* improvement is obtained for the smallest separation distance.

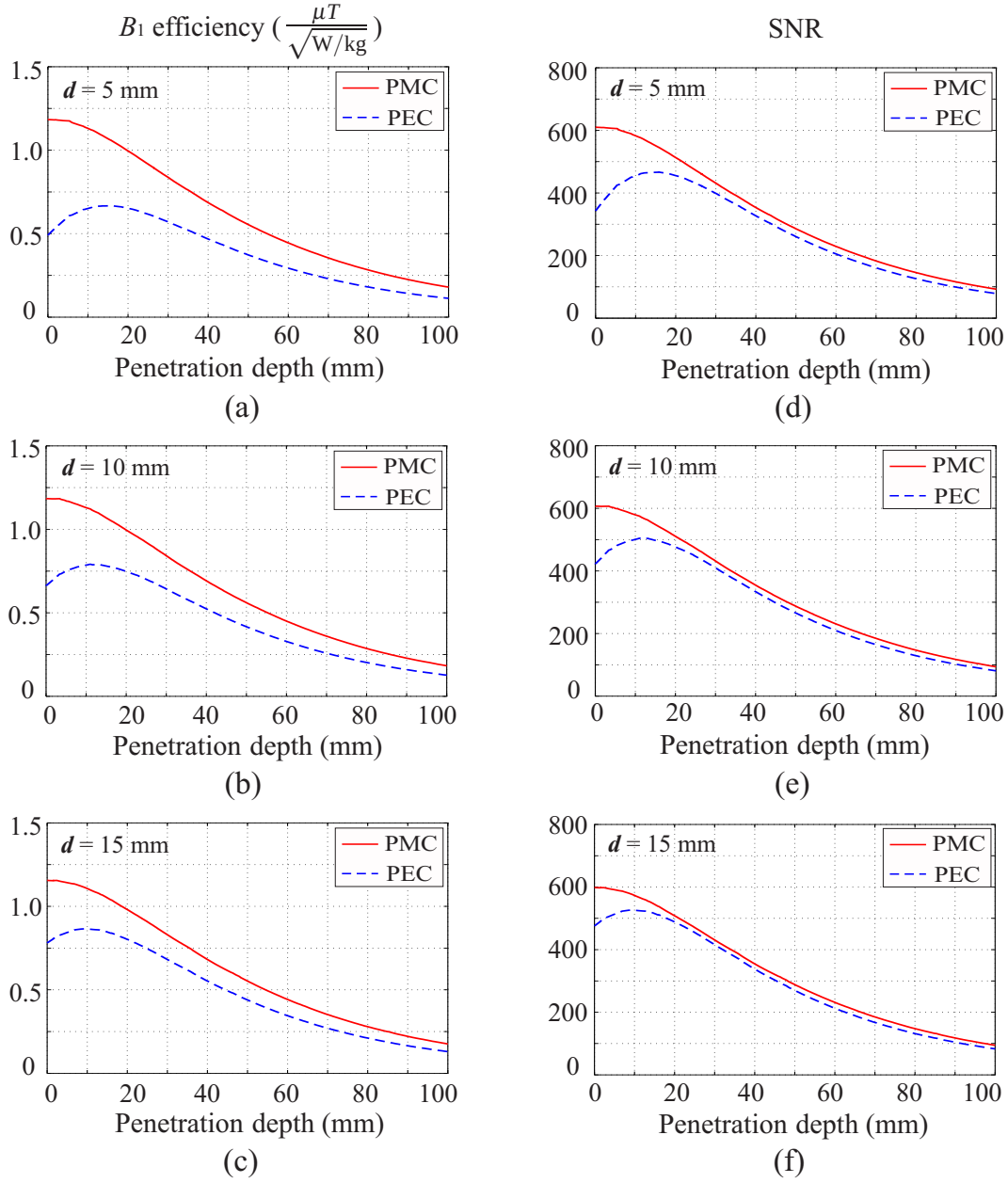

Figure 2.19: The B_1 efficiency (left column) and *SNR* (right column) of the impressed current model along the axis of the cylindrical phantom versus the penetration depth for different shielding scenarios (PMC and PEC) at 300 MHz. Different separation distance from the surface coil to the RF shields are considered: (a, d) $d = 5$ mm, (b, e) $d = 10$ mm, (c, f) $d = 15$ mm.

The improvement on B_1 efficiency and *SNR* can be explained by the corresponding magnetic field distribution shown in Fig. 2.20. Due to the fact that the normal component of the magnetic field, which is mainly excited by the loop, is supported at the surface of a PMC, whereas suppressed by a PEC boundary, the magnetic field in vicinity of the PMC shield is stronger in comparison to the case with a PEC shield (this area is outlined by a

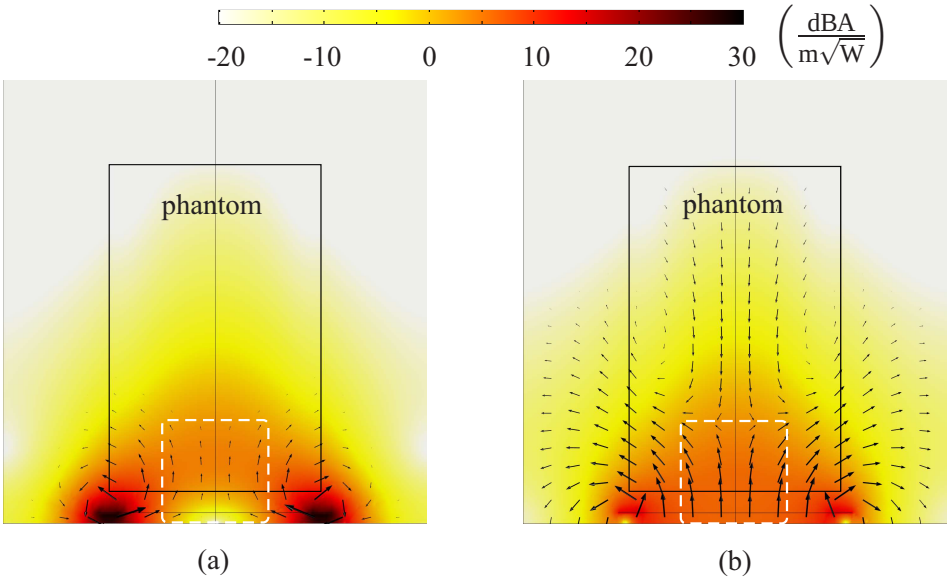

Figure 2.20: Simulated 3D absolute magnetic field distribution on the xz cut plane (cf. Fig. 2.17) for different shielding scenarios [(a) PEC and (b) PMC] at 300 MHz. The separation between the loop and the lower boundary is set to 5 mm. The corresponding absolute magnetic field is normalized to the square root of accepted power and plotted in dB.

dashed rectangle in Fig. 2.20). This superior field distribution extends into the phantom and enhances the coil performance. The more prominent improvement for the B_1 efficiency compared to the *SNR* is due to the different normalization bases in the definitions given in (2.3.2.1) and (2.3.1). Both parameters, the B_1 efficiency and the *SNR*, are proportional to the absolute B_1 field. The difference is that the B_1 efficiency is normalized to a "peak" basis—namely the peak *SAR*, whereas the *SNR* is normalized to a "sum" or "integral" basis—the total loss within the coil and the phantom. As mentioned previously, for the 7 T transmit case the peak *SAR* is more critical since it creates so-called 'hot spots' inside the body [88, 93] and limits the allowed RF power to be used for the B_1 field excitation. In contrast, for the reception, instead of the local maximum, the total loss within the coil and phantom produces the noise signal and affects the receive performance.

The *SAR* is proportional to the squared electric field magnitude. From the electric field distribution in Fig. 2.21 and Fig. 2.22 it is obvious that the electric field of a loop with a PEC shield tends to distributed *above* the coil due to the PEC boundary condition, whereas a loop with a PMC shield tends to focus the electric field *below* the coil. Therefore, the maximum electric field spots for a PMC shield and a PEC shield are located below and above the loop structure, respectively. As a result, the peak *SAR* inside the phantom for the case of a PMC shield is relatively smaller compared to the case of a PEC shield. After averaging the effect of the locally surpassing electric field is significantly weakend, and thus a smaller difference on the whole-body *SAR* (averaged over the whole phantom) is observed for the different shielding scenarios (PMC and PEC). In Fig. 2.23 the peak *SAR* and the whole-body *SAR* for PEC and PMC shields are normalized to the accepted

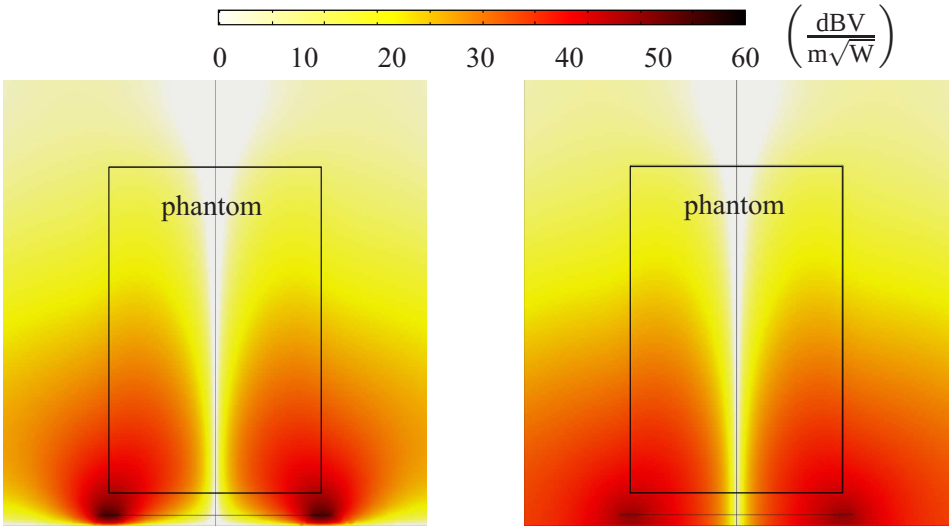

Figure 2.21: Simulated 3D absolute electric field distribution on the xz cut plane (cf. Fig. 2.17) for different shielding scenarios [(a) PEC and (b) PMC] at 300 MHz. The separation between the loop and the lower boundary is set to 5 mm. The corresponding absolute electric field is normalized to the square root of accepted power and plotted in dB.

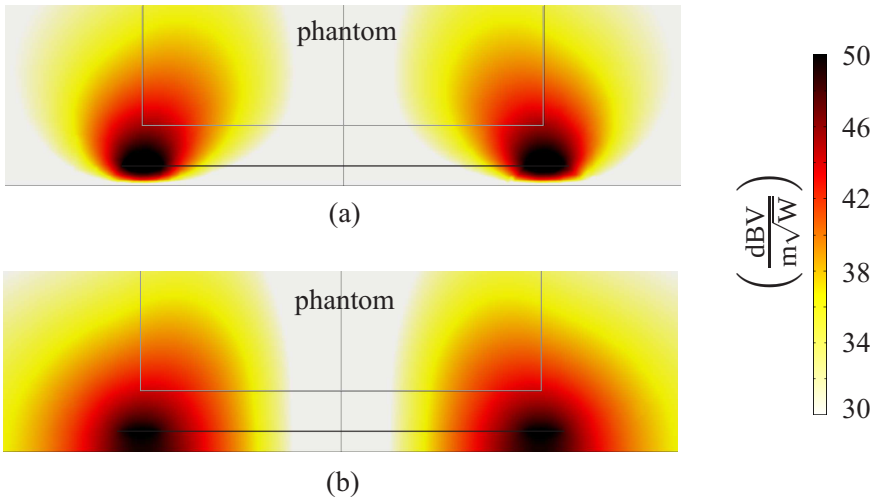

Figure 2.22: Simulated 3D absolute electric field distribution (shown in Fig. 2.21) in vicinity of the loop structure in zoomed view for different shielding scenarios [(a) PEC and (b) PMC].

power and plotted versus frequency. The peak SAR for the PEC shield is considerably larger than for the PMC shield. Hence, the predominant field distribution produced by the surface coil with a PMC shield reveals a significant improvement on the B_1 efficiency, which is normalized to the square root of the peak SAR. The whole-body SAR for the different shielding scenarios (PMC and PEC) are on a similar level. Thus the improvement on the SNR, which is normalized to the averaged SAR is not that significant.

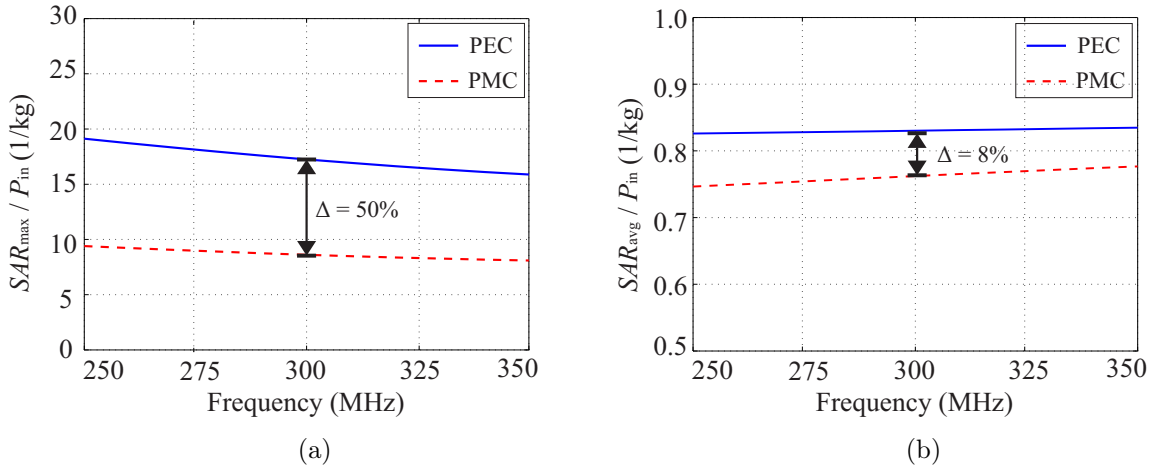

Figure 2.23: (a) The peak SAR and (b) the averaged SAR for PEC and PMC shields inside the phantom of the impressed current model depicted in Fig. 2.17.

2.3.3 Summary of Loop Coil with SIBCs

In this section the RF shield of a surface loop coil for UHF MRI has been modeled by the surface impedance boundary condition (SIBC). The EM field characteristic of the loop coil which is backed by different SIBCs has been evaluated based on two- and three-dimensional FEM simulation models. According to the obtained results, the SNR and B_1 efficiency of a 7 Tesla surface coil can be improved by utilizing an RF shield with high surface impedance. Two extreme and ideal cases, a PEC (small surface impedance) and a PMC (large surface impedance), have been systematically compared based on an ideal impressed current model and a series resonant loop structure. Due to the fact that the mainly excited normal component of the magnetic field is supported at a PMC surface, whereas suppressed by a PEC surface, the B_1 field in vicinity of the PMC shield is enhanced compared to the case with a PEC shield. The improvement degrades with larger penetration depth into the phantom. The result obtained here may inspire the design of a low-profile surface coil with an artificial magnetic conductor (AMC) as the RF shield in order to achieve enhanced SNR, and especially B_1 efficiency.

2.4 Summary of EM Field Analysis of RF Coils with SIBCs

In this chapter the shielding plate behind an RF coil is modeled by a surface impedance boundary condition (SIBC), which is characterized by the corresponding surface impedance on it. By considering various surface impedances (in terms of magnitude and phase) a fundamental investigation of the effect of different shields (SIBCs) on the electromagnetic fields generated by the RF coils is presented. It has been demonstrated that the transverse B_1 distribution of a dipole coil can be improved by utilizing an RF shield with high surface impedance in terms of the field homogeneity and the absolute penetration depth. For a surface loop coil, the B_1 field in vicinity of the RF shield with a large surface impedance is significantly enhanced compared to the case with a small surface impedance. As a result, the coil performance (SNR and B_1 efficiency) of a surface loop is considerably improved by the RF shield with a high surface impedance. The improvement degrades with larger penetration depth into the phantom and larger separation distance between the loop and the shield. In general, the presented fundamental investigation revealed a feasibility of improving the coil performance by using an RF shield with a high surface impedance.

Chapter 3

Realization of a High-Impedance-Surface (HIS)

In Chapter 2 it has been shown that the RF coil performance could be improved by using a SIBC with a large surface impedance. In this chapter we present two approaches for the realization of a high-impedance-surface (HIS). Perhaps the terminology of electromagnetic band gap (EBG) structure is more widely and well known. EBG structures are periodic objects which prevent the propagation of electromagnetic waves in certain frequency bands. An EBG structure exhibits a high surface impedance at a specific frequency, where it can be functionally considered as a HIS. The proposed approaches are based on mushroom-like and uni-planar EBG designs [47, 53]. For each approach the EBG structure is evaluated based on lattice analysis and finite-element model. Section 3.1 and Section 3.2 provide the characterization of EBG structures, along with several well-known and sophisticated EBG designs. In section 3.3 two compact EBG surfaces based on multi-layer technology for 7-T MRI application are proposed. The reflection phase and stop band properties of the presented EBG structures are investigated based on full-wave simulation and experimental results.

3.1 Characterization of EBG Structures

According to specific applications, diversified EBG structures have been designed, which exhibit unusual electromagnetic properties. In this section we illustrate how these interesting properties, e.g. in-phase reflection and frequency band gap, will be characterized by full-wave simulations.

3.1.1 Lumped-Element Circuit Model for EBG Structures

In order to more readily understand the operation mechanism of EBG structures, equivalent circuit models are widely. A well-known lumped LC model was originally proposed in [95], where the two-dimensional mushroom planar EBG surface was represented by a parallel LC circuit model [cf. Fig. 3.1(a)]. The capacitance is contributed by the electric coupling of the adjacent metal patches, while the inductance is due to the current following within the structure [cf. Fig. 3.1(b)]. This lumped circuit model is valid when the periodicity is small compared to the wavelength at the operation frequency.

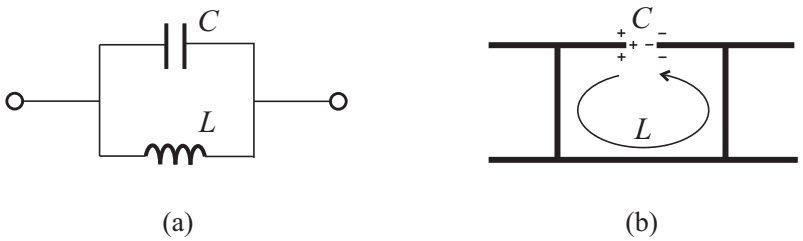

Figure 3.1: (a) Equivalent circuit model with lumped elements for EBG structures [95]. (b) Origin of the lumped elements of the equivalent circuit model for the case of a mushroom EBG structure.

Although this equivalent circuit model is intrinsically derived for a particular EBG structure (so-called mushroom EBG), the LC circuit model is also widely utilized for a broad range of 2D planar EBGs [47, 50]. The impedance of this parallel LC circuit, which refers to the surface impedance of the EBG structure, is given by

$$Z_{\mathrm{S}} = \frac{j\omega L}{1-\omega^2 LC} = jX_{\mathrm{S}}. \tag{3.1.1}$$

The corresponding resonance frequency, where the EBG structure operates as a high impedance surface, can be determined as following:

$$f_0 = \frac{1}{2\pi\sqrt{LC}}. \tag{3.1.2}$$

Around this resonance frequency the EBG structures reveal unique characteristics, such as in-phase reflection and frequency band gap properties.

3.1.2 In-Phase Reflection for Plane Wave Incidence

As one widely used parameter to describe the reflection property of a surface, its reflection coefficient is defined as the ratio of the reflected wave over the incident wave at the considered surface. The magnitude of the reflection coefficient describes how much energy transmitted by the incident wave is reflected back. The phase of reflection coefficient, namely the reflection phase, provides the phase information of the reflected wave with respect to the incident one. For a perfect electric conductor (PEC), the reflected electric fields process the same amplitude but the opposite sign compared to the incident fields, in order to satisfy the boundary condition that the tangential electric field has to be zero. Thus, the reflection coefficient for a PEC is -1, resulting in a reflection phase of $\pm 180°$. For another well-known analytical model, the perfect magnetic conductor (PMC), the reflected and incident electric fields have the same amplitudes and signs. As a result, the reflection coefficient for a PMC is $+1$, and the corresponding reflection phase is $0°$ [84].

Due to the special surface impedance characteristics, EBG structures exhibit an interesting reflection phase behavior. For an incident wave normally impinged on a surface, which is characterized by the corresponding surface impedance Z_s, the reflection coefficient of the surface is defined as

$$\Gamma = \frac{Z_\mathrm{s} - \eta}{Z_\mathrm{s} + \eta} = |\Gamma|\, \mathrm{e}^{+j\Phi}, \tag{3.1.3}$$

where η is the wave impedance of the medium in which the wave propagates. For a normally incident wave, the phase of the reflection coefficient in (3.1.3) at the considered surface with a surface impedance Z_s can be then calculated by [95]

$$\Phi = \Im\left\{\ln\left(\frac{Z_\mathrm{s} - \eta}{Z_\mathrm{s} + \eta}\right)\right\}. \tag{3.1.4}$$

From (3.1.1) and (3.1.4) the reflection phase behavior of the surface characterized by a surface impedance Z_s can be predicted as a function of frequency: at very low frequencies, the surface impedance is inductive (positive reactance X_s) and its magnitude is much smaller compared to the characteristic impedance of the medium $|Z_\mathrm{s}| \ll \eta$, and thus, the reflection coefficient can be approximated as -1 with a $180°$ reflection phase; at the resonance frequency f_0, the magnitude of the surface impedance is theoretically infinite, $|Z_\mathrm{s}| \gg \eta$, and thus, the reflection coefficient can be approximated as $+1$ with a $0°$ reflection phase; at higher frequencies, the surface impedance is capacitive (negative reactance X_s) and its magnitude decreases to a very low value $|Z_\mathrm{s}| \ll \eta$, and the reflection coefficient can be again approximated to -1 with a $-180°$ reflection phase[1]. The overall reflection

[1]The exact reflection phase is equal to the phase difference of the terms Z_s-η and $Z_\mathrm{s} + \eta$, which are conjugate complex with each other for a purely imaginary Z_s. Assuming the phase of the term $Z_\mathrm{s}+\eta$ is α, for low frequencies the reflection phase is then $(\pi\text{-}\alpha)\text{-}\,\alpha = \pi\text{-}2\alpha$. As the frequency approaches zero, the reflection phase approaches π. Analogously, for high frequencies the reflection phase is $(\pi+\alpha)\text{-}\,2\pi\text{-}\alpha = \text{-}\pi+2\alpha$. As the frequency approaches infinity, the reflection phase approaches $\text{-}\pi$.

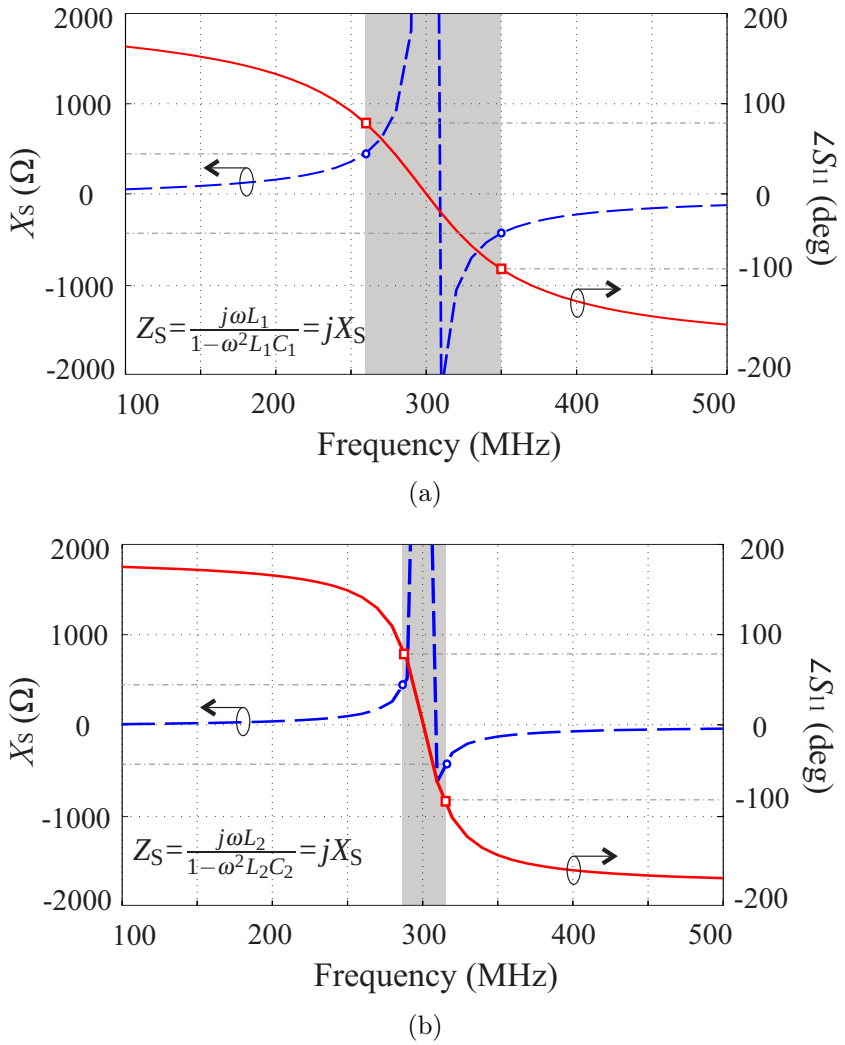

Figure 3.2: Simulated reflection phase of the effective surface impedance model with the corresponding impedance set to: (a) $L = 70$ nH and $C = 4$ pF, and (b) $L = 20$ nH and $C = 14$ pF. The grayly shaded region indicates the frequency band where the reflection phase falls within $\pi/2$ and $-\pi/2$.

phase continuously varies from 180° to −180° as frequency increases, and crosses through 0° at the resonance frequency.

Now we consider a surface which is characterized by the aforementioned lumped-element model. The reflection phase and the surface impedance of the surface are calculated according to (3.1.1) and (3.1.4), and plotted versus frequency in Fig. 3.2. Different LC combinations (case I: $L = 70$ nH and $C = 4$ pF, case II: $L = 20$ nH and $C = 14$ pF) are chosen in such a way that the same resonance frequency f_0 is achieved, and utilized to investigate the influence of different LC values on the reflection phase. The reflection phase approaches π at very low frequencies where the magnitude of the surface impedance is much smaller than the impedance of free space. At higher frequencies, the reflection phase slopes down and crosses through zero at the resonance frequency, where the effec-

tive impedance surface exhibits an infinitely large impedance. As the frequency further increases, the reflection phase reaches -π progressively. The observed phenomenon that the reflection phase falls within $\pi/2$ and -$\pi/2$ as the magnitude of the surface impedance exceeds the impedance of free space conforms to the conclusion in [47]. Additionally, a greater $\sqrt{L/C}$ ratio provides a larger in-phase bandwidth, where the reflection phase curve crosses through $\pi/2$ and -$\pi/2$ (cf. Fig. 3.2).

3.1.3 Frequency Band Gap for Surface Wave Propagation

Besides the in-phase reflection property, EBG structures also exhibit interesting properties for surface wave propagation. One of the popular concepts to evaluate the frequency band gap of EBG structures is based on the dispersion diagram. For a two-dimensional EBG structure, we assign a periodic boundary condition for each orientation, and specify a phase shift between the periodic boundaries along each orientation. By solving an eigenvalue problem for a specified phase shift, the eigen frequencies from different eigen modes can be computed. To fully and efficiently describe the natural resonance behavior of the two-dimensional EBG structure, a path along the boundary of the irreducible Brillouin zone [49, 96] is generated by defining the phase shift in a proper two-dimensional manner. The eigenmode simulation identifies the possible eigen frequencies for each point (phase shift) along the previously defined path. The relation between the specified phase shift and calculated eigen frequencies is plotted and referred to as the dispersion diagram. If in a certain frequency band no eigen frequencies (modes) are found, then it can be considered as a frequency band gap.

The lumped-element circuit model can be used to effectively predict the reflection phase, but not the band gap itself [47]. The radiation in the fast-wave regime (leaky waves which are not bound to the surface) and the dissipation loss in the EBG structure can not be properly modeled by the lumped-element circuit model [47]. In order to precisely describe the dispersion diagram of the EBG structure, eigen-mode simulations based on full-wave model are required. The dispersion approach will be utilized for the EBG designs in the forthcoming section.

Another commonly used approach to evaluate the band gap property of an EBG structure is the transmission parameter in driven-mode, where a surface wave is generated above the finite EBG array and the transmission coefficient of the propagating surface wave along the EBG surface is investigated.

Considering a surface characterized by a surface impedance based on the lumped-element circuit model (L = 70 nH and C = 4 pF), the transmission behavior of a propagating surface wave along the considered surface is demonstrated in Fig. 3.3. The surface, which is modeled by a parallel LC circuit, has a resonance frequency of 300 MHz, and is nested between two wave ports with TE and TM polarizations. For the TE (TM) polarization, the electric (magnetic) and magnetic (electric) field component is aligned tangential and vertical to the impedance surface, respectively. The excited surface wave is propagating between the two wave ports. For an inductive impedance surface (lower frequency range)

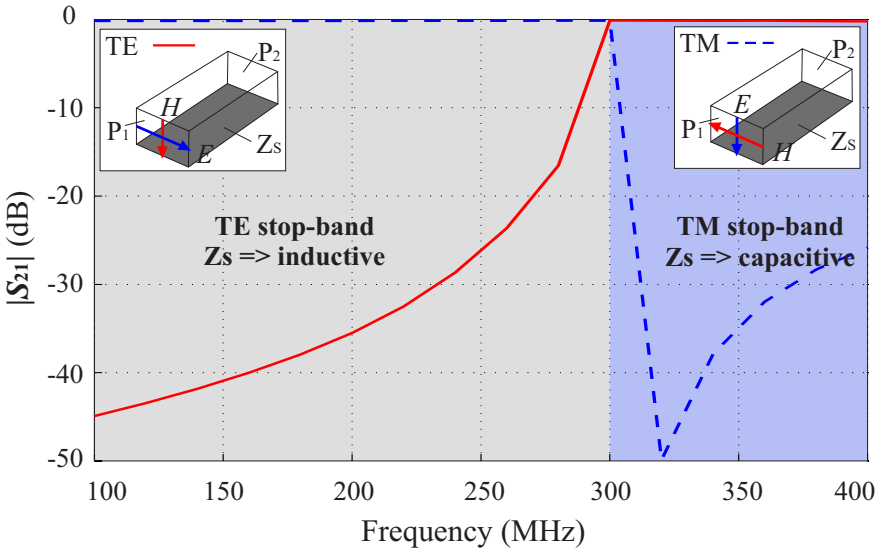

Figure 3.3: Simulated transmission coefficient of the effective surface impedance model ($L = 70$ nH and $C = 4$ pF) for TM polarization (magnetic field tangential to the impedance surface) and TE polarization (electric field tangential to the impedance surface).

the TE polarized surface wave is retarded, since the tangential electric field component is not supported [47]. As the frequency approaches the resonant frequency, here 300 MHz, the magnitude of the inductive surface impedance rapidly increases and the suppression of the TE surface wave is weakened. In contrast, the propagation of a TM surface wave is suppressed by a capacitive surface impedance (upper frequency range), whereas supported by an inductive surface (lower frequency range). The band gap effect decays with a decreasing magnitude of the surface impedance as the frequency increases (cf. Fig. 3.3).

3.2 Examples of EBG Designs

Here we present two EBG designs based on the well-established topologies (mushroom-like and uni-planar EBG), and utilize them to demonstrate the previously introduced characterization methods of EBG structures.

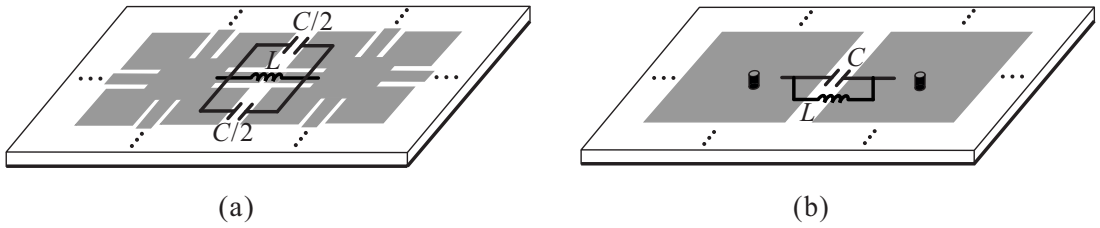

Figure 3.4: Conventional (a) uni-planar and (b) mushroom-like EBG surface with the corresponding equivalent LC model.

3.2.1 Uni-planar EBG Design

An uni-planar EBG structure consists of an uniformly distributed periodic metallic pattern printed on a dielectric material, in our case, a 3.2 mm-thick Arlon AD1000 ($\epsilon_r = 8$). Fig. 3.4(a) shows a classical uni-planar EBG surface [53], its working principle can be explained by a lumped LC model. The capacitance comes from the edge coupling between adjacent patches, whereas the inductance is provided by a thin microstrip line which connects the neighboring patches. In order to increase the inductance value, the microstrip line is usually inset into the patch.

3.2.1.1 Reflection Phase

The simulation model for the reflection phase investigation in HFSS, a FEM-based simulation tool, is depicted in Fig. 3.5. Two-dimensional periodic boundaries are applied in two transversal (x and y) directions. The top boundary in $+z$ direction is assigned as a so-called Floquet port, which excites a plane wave with controllable incident angle and TE or TM polarization. For the TE and TM incident case, the only electric and magnetic field component is set along the y-direction, respectively.

With the geometry parameters[2] given in Fig. 3.6(a) an in-phase reflection on the uni-planar EBG surface can be achieved around 1.16 GHz [cf. Fig. 3.6(a)]. Since the reflection phase at the EBG surface is identical in the case of a normal incident wave for a TE and

[2]Considering that the main purpose of this section is to demonstrate the characterization methods of EBG structures, the presented EBG structures are not tuned to achieve a resonance frequency of 297 MHz, which is the operation frequency for the 7 T MRI application. The geometry parameters of the top patch of the uni-planar EBG is kept unchanged as the ones utilized for the compact multi-layer uni-planar EBG design from Section 3.3. This is also true for the mushroom EBG case.

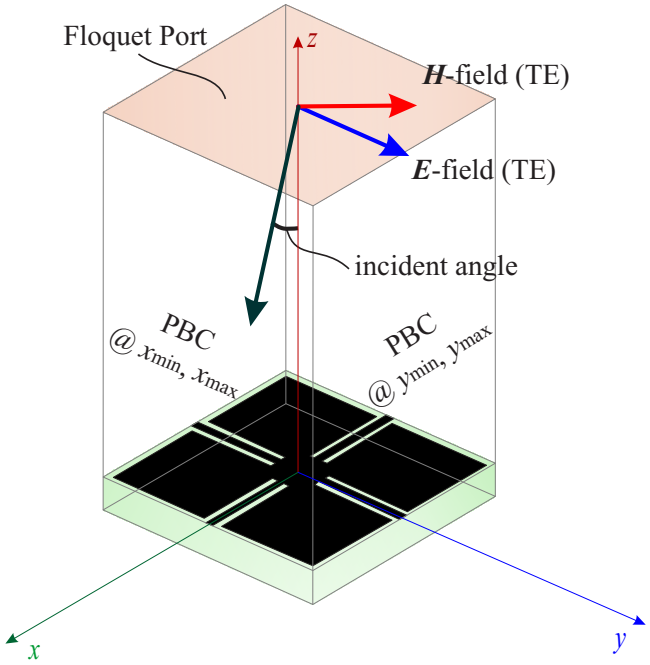

Figure 3.5: The simulation model for the reflection phase investigation. Two-dimensional periodic boundaries are applied in x and y directions. The top boundary in $+z$ direction is assigned as a Floquet port, which excites a plane wave with an adjustable incident angle.

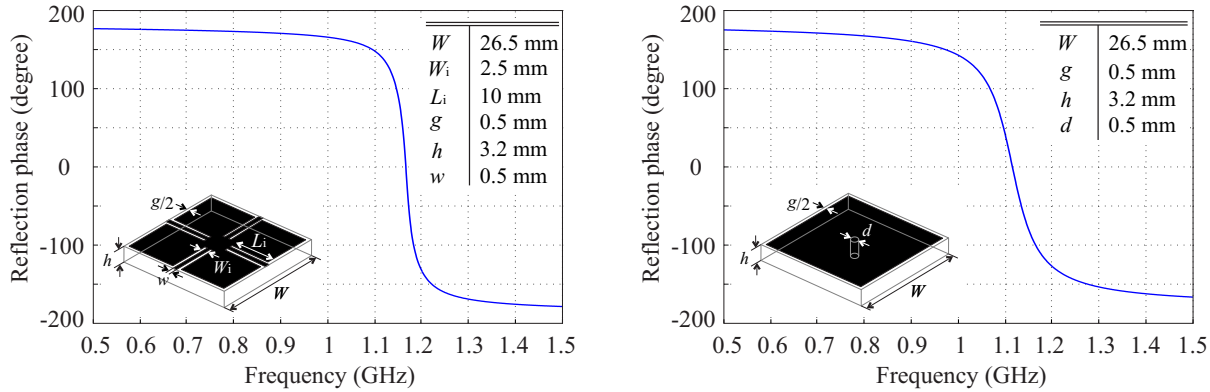

Figure 3.6: Simulated reflection phase at the top surface of (a) a uni-planar and (b) a mushroom EBG structure with the corresponding geometry parameters.

TM polarization, here we plot only the reflection phase for the TE polarization. At low frequencies the EBG surface exhibits a nearly 180° reflection phase. As the frequency approaches the resonance frequency, here 1.16 GHz, the reflection phase slopes downward and eventually crosses through zero at the resonance frequency. Beyond the resonance frequency the phase turns to -180° gradually and holds for higher frequencies.

3.2.1.2 Dispersion Diagram

To generate the two-dimensional dispersion diagram for the EBG lattice, a path which describes the irreducible Brillouin zone [97] is defined. The simulation model for the dispersion diagram is depicted in Fig. 3.7. Two-dimensional periodic boundaries are applied in two transversal (x and y) directions. The top boundary in $+z$ direction is assigned as a perfect matched layer (PML). For the eigen-mode approach the natural resonances of the considered structure are calculated and no source excitations are required. A path along the boundary of the irreducible Brillouin zone is generated by defining the phase shift in a proper two-dimensional manner. This path is specified by three points:

$$\begin{aligned} \Gamma &: \quad p_{\mathrm{x}} = 0^\circ, \qquad p_{\mathrm{y}} = 0^\circ, \\ X &: \quad p_{\mathrm{x}} = 180^\circ, \qquad p_{\mathrm{y}} = 0^\circ, \\ M &: \quad p_{\mathrm{x}} = 180^\circ, \qquad p_{\mathrm{y}} = 180^\circ, \end{aligned}$$

where p_{x} and p_{y} is the phase shift in x and y direction, respectively. From Γ to X, p_{x} increases from 0° to 180°, while p_{y} is 0°. From X to M, p_{x} is fixed to 180°, while p_{y} sweeps from 0° to 180°. From M to Γ, both p_{x} and p_{y} decrease from 180° to 0°.

The corresponding dispersion diagram of the uni-planar EBG surface is displayed in Fig. 3.8(a). A frequency band gap for surface wave propagation is observed between 0.6 GHz and 0.9 GHz, which is outlined by a grayly shaded rectangle. The lower limit of the band gap is the maximum eigen frequency of the first mode supported by the EBG surface, the upper limit is the frequency where the second mode crosses the light line. Within the corresponding band gap the propagation of surface waves above the EBG surface is suppressed. It is worth mentioning that the band gap obtained in the dispersion diagram does not necessarily coincide with the in-phase reflection band. Additionally, the resonance frequency, where the reflection phase curve crosses zero is not per se covered by this band gap.

3.2.2 Mushroom EBG Design

A mushroom-like EBG structure consists of a lattice of metal plates, which are connected to a solid metal sheet by vertical conducting vias, as shown in Fig. 3.4(b). A lumped LC model can also be used to explain its working principle. The capacitance comes from the edge coupling between adjacent patches, whereas the inductance is provided by the ground plane and the vertical conducting vias which connect the top and ground layers.

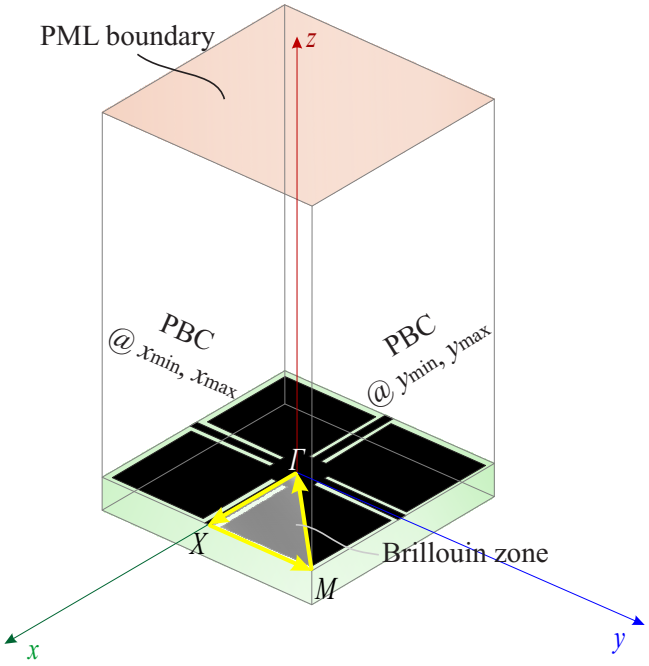

Figure 3.7: The simulation model for evaluation of the dispersion diagram. Two-dimensional periodic boundaries are applied in x and y directions. The top boundary in $+z$ direction is assigned as a perfect matched layer (PML). No excitation is applied for eigen-mode simulation. A path along the boundary of the irreducible Brillouin zone is generated by defining the phase shift in a proper two-dimensional manner. From Γ to X, p_x (phase shift in x direction) increases from 0° to 180°, while p_y (phase shift in y direction) is 0°. From X to M, p_x is fixed to 180°, while p_y sweeps from 0° to 180°. From M to Γ, both p_x and p_y decrease from 180° to 0°.

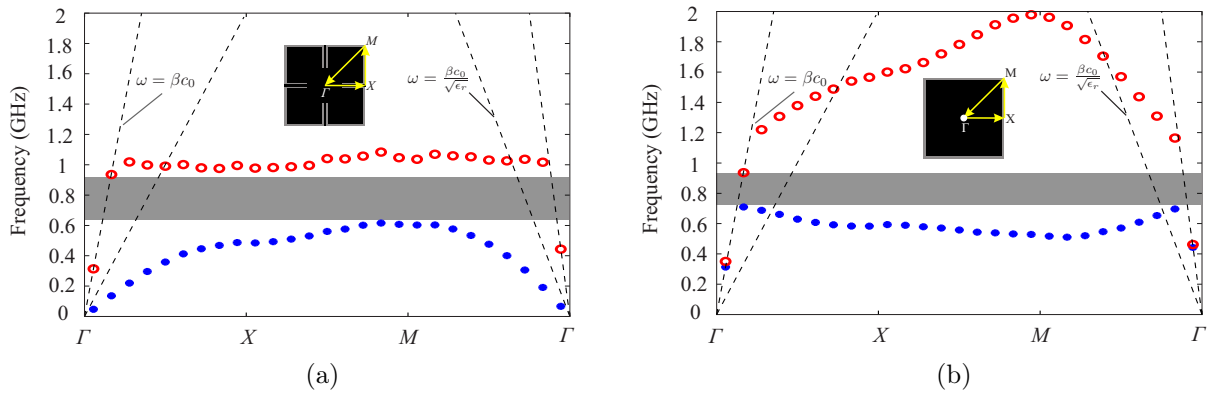

Figure 3.8: Simulated dispersion diagram of (a) a uni-planar and (b) a mushroom EBG structure with the corresponding geometry parameters given in Fig. 3.6 including the first two modes. The band gap between the first and second modes is outlined by the grayly shaded rectangle.

3.2.2.1 Reflection Phase

With the geometry parameters given in Fig. 3.6(b) an in-phase reflection on the msuhroom EBG surface can be achieved around 1.11 GHz [cf. Fig. 3.6(b)]. Similar to the uni-planar EBG design, EBG surface exhibits a nearly 180° and -180° reflection phase at lower and higher frequencies, respectively. At the resonance frequency, here 1.11 GHz, the reflection phase crosses through zero. Compared to the uni-planar EBG, the bandwidth where the reflection phase falls within 90° and -90° for the mushroom EBG is slightly larger. It can be seen that with a same lattice dimension, here 26.5 mm, the mushroom EBG exhibits a smaller resonance frequency and a larger bandwidth compared to the uni-planer EBG (cf. Fig. 3.6) [50].

3.2.2.2 Dispersion Diagram

The corresponding dispersion diagram of the mushroom EBG surface is displayed in Fig. 3.8(b). A frequency band gap for surface wave propagation is observed between 0.7 GHz and 0.9 GHz, which is outlined by a grayly shaded rectangle. The observed frequency band gap with a mushroom EBG is slightly narrower compare to the case of a uni-planar EBG. For both cases (uni-planar and mushroom EBGs) the frequency band gap for surface wave propagation does not coincide with the in-phase reflection band.

3.2.3 Summary of Examples of EBG Design

In this section two well-known topologies for the two dimensional EBG structures are introduced. The corresponding EBG design is characterized by its reflection phase and dispersion diagram, which are widely utilized in EBG designs. The given examples provide an overview of the research approach how an EBG structure is evaluated. Similar research approach will be used for the more compact EBG designs which will be introduced in the following section.

3.3 Compact HIS (EBG) Designs

The single-layer uni-planar and mushroom EBG structures with a lattice dimension of 26.5 mm given in the previous section have a resonance frequency around 1.1 GHz, which is too high for 7-T MRI. In order to bring the resonance frequency down to around 300 MHz, which is the Larmor frequency for 7-T MRI, the lattice dimension of the EBG surface has to be comparatively small with respect to the RF coils and the wavelength at the operation frequency. Diverse design schemes for the metal plates of EBG structures have been proposed to achieve a compact lattice dimension [98, 99, 100]. In this section we present two EBG structure designs with remarkable size reduction generally based on multi-layer technology. The uni-planar and mushroom-like concepts are applied to the proposed EBG designs.

3.3.1 Uni-Planar Concept

Firstly, a compact multi-layer EBG design based on uni-planar concept is presented [101]. The proposed EBG surface will be characterized by its reflection phase and band gap properties. Additionally, a parametric study on the geometry of the proposed EBG surface will be carried out based on full-wave simulations.

3.3.1.1 Multi-layer Uni-Planar EBG Structure

The proposed compact EBG structure introduces a floating metallic layer between the top layer, where the conventional uni-planar surface is printed, and the ground plane, as shown in Fig. 3.9(a). A metal-insulator-metal (MIM) capacitance is created by the overlap of the top and the additional floating layer. Hence, a more compact EBG structure can be achieved due to the enhanced total capacitance. In this case, the resonant frequency f_0 of the equivalent LC model shown in Fig. 3.9(b) can be calculated as follows:

$$f_0 = \frac{1}{2\pi\sqrt{L_{\text{line}}(C_{\text{gap}} + C_{\text{mim}})}} \tag{3.3.1}$$

As shown in Fig. 3.9(a), the stack-up encompasses a top and a bottom core substrate with a thickness of 152 μm and 3.2 mm, respectively, and a 38 μm thick prepreg film ($\epsilon_r \approx 2$) in between. The top and floating metallic layers are printed on the top core substrate, one side of the bottom core substrate is etched away and sticked to the prepreg film. Since the EBG structure contains no vias, the complexity and cost of fabrication could be effectively brought down. The metallic layout on the top layer of the proposed EBG structure is similar to the conventional uni-planar EBG, as depicted in Fig. 3.10(a). A thin microstrip line, which is inset into the path, connects the neighboring patches. The additional floating metallic layer is outlined by the white dashed lines.

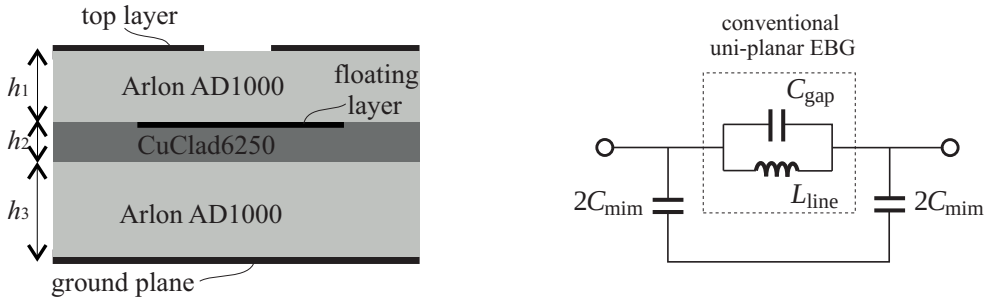

(a) (b)

Figure 3.9: (a) The proposed compact uni-planar EBG structure in side view, and (b) the corresponding equivalent circuit, where C_{mim} represents the MIM capacitance provided by the overlap of top and floating layers.

The geometry parameters of the EBG structure are determined in such a way that the magnetic resonant frequency of a 7 T MRI system (297 MHz) is covered by the stop-band, additionally, the dimension of the EBG lattice should be minimized. In this sense, a high-dielectric substrate, here Arlon AD1000[3], is prefered to miniaturize the lattice. Aiming to enhance the MIM capacitance [C_{mim} in Fig. 3.9(b)], the top core substrate should be as thin as possible. Additionally, the thickness of the bottom core substrate should be kept large to increase the inductance of the connecting mircostrip line [L_{line} in Fig. 3.9(b)]. With the optimal geometry data given in Fig. 3.10(b), an in-phase reflection and a surface wave band gap around 297 MHz can be achieved. The detailed results will be presented in the following content.

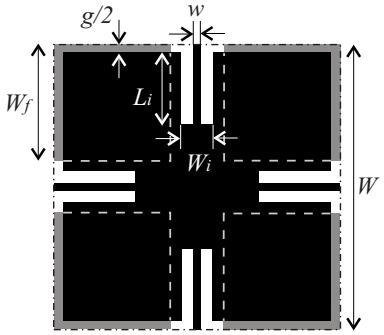

(a)

W	26.5 mm
W_{f}	12 mm
W_{i}	2.5 mm
w	0.5 mm
L_{i}	11 mm
g	0.5 mm

(b)

Figure 3.10: (a) Layout of the proposed compact uni-planar EBG structure in top view, and (b) the corresponding geometry parameters. The additional floating metallic layer is outlined by the white dashed lines.

[3]The dielectric constants of AD1000 vary with the thickness of the substrate. For the thickness of 0.152 mm and 3.2 mm, the dielectric constant is 8 and 10.9, respectively.

3.3.1.2 Characterization of the Uni-Planar EBG Design

The reflection phase for plane wave incidence and the surface wave stop-band are the two properties that are commonly used to characterize EBG structures [50]. In this section, the proposed EBG structure is characterized by the aforementioned two porperties based on full-wave simulations.

3.3.1.2.1 Reflection Phase

Fig. 3.11 shows the reflection phase at the top surface of the proposed EBG structure in the case of TM and TE polarization for different incident angles. The incident angle is defined as the angle between the propagation vector and the -z axis (cf. Fig. 3.5). The proposed compact uni-planar EBG structure exhibits a reflection phase close to 0° for a normal incidence at 297 MHz. As the incident angle increases, the resonant frequency (where the reflection phase is equal to zero) is slightly shifted to higher frequencies in the case of a TM polarization. Specifically, for 30° and 60° incident angles, the resonant frequencies are shifted to 300 MHz and 303 MHz, respectively [cf. Fig 3.11(b)]. In this case the tangential electric field component is getting smaller with an increased incident angle. Thus, the charge accumulation across the gap between adjacent EBG lattices is less sufficient and provides a smaller capacitance, which results in a higher resonant frequency. For a TE polarized incident wave, the variation on reflection phase due to different incident angles is negligible, since the inductance related to the tangential magnetic field, which depends on the incident angle, has minor effect on the resonant frequency in comparison to the large MIM capacitance. Therefore, the reflection phase of the proposed compact uni-planar EBG is more sensitive to TM polarized waves with different incident angles in comparison to TE polarized waves.

Additionally, as the incident angle increases, the bandwidth of the EBG structure tends to decrease for a TE polarization, whereas it increases for a TM polarization. This phenomenon can be explained in such a way that the tangential magnetic field component for a TE polarized plane wave is getting smaller with an increased incident angle, and thus the induced inductance L is reduced, resulting in a decreased L/C ratio, i.e., bandwidth [47]. Analogously, for a TM polarization the reduced tangential electric field component, which relates to the capacitance C, leads to a greater L/C ratio and thus an increased bandwidth.

3.3.1.2.2 Band Gap — Dispersion Diagram

The dispersion diagram of the proposed uni-planar EBG structure including the first two modes is given in Fig. 3.12. A surface wave stop-band between the first and second mode which covers the magnetic resonant frequency for 7 T MRI (297 MHz) is observed and denoted by the grayly shaded region. The gray and black dashed lines indicate the light line for air and the substrate of the EBG structure, respectively.

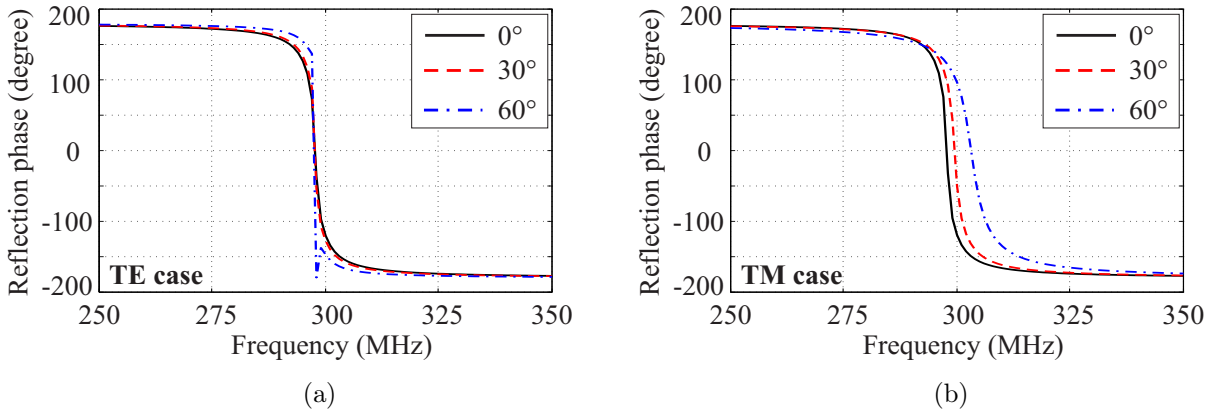

Figure 3.11: Simulated reflection phase of the multi-layer EBG structure in the case of (a) a TE polarization and (b) a TM polarization for different incident angles.

Firstly, the polarization characteristics of the involved modes are investigated. Fig. 3.13 shows the electric and magnetic field distributions on the considered EBG surfaces at the spectral point of dispersion diagram, where $p_x = 10°$ and $p_y = 0°$. In this case the propagation direction of surface waves is set in x direction. The first mode of the compact uni-planar EBG structure is a TM-like mode, indicated by the transversal magnetic field (red arrow) in y direction and the longitudinal electric field (blue arrow) in the propagation direction, here x direction [cf. Fig. 3.13(a)]. Since the adjacent lattices of the uni-planar EBG is connected through a thin microstrip line, the magnetic field is mainly focused around the microstrip lines. However, the polarization state of the second mode for the considered EBG is not absolutely distinct, since electric fields in both transversal and longitudinal directions are observed. Due to the fact that the magnetic field aligns in the propagation direction [cf. Fig. 3.13(b)], here we suppose the second mode from the dispersion diagram is a TE-like mode. It can be noticed that in addition to the transversal and longitudinal electric field components, for both EBG surfaces considerable normal electric filed is confined inside the MIM capacitor where the top patch and the floating metallic layer overlap.

For the uni-planar EBG a band gap from 250 MHz to 310 MHz which is denoted by the grayly shaded region in Fig. 3.12 is observed. The dispersion curve of first mode lies near the light line in the substrate at lower frequencies, here approximately up to 100 MHz. After this frequency, which is still much lower than the resonant frequency, the curve is bent over away from the light line. The maximum eigen frequency supported by the first mode appears roughly at the point M ($p_x = 180°$, $p_y = 180°$), which determines the lower boundary of the band gap. The second mode of the uni-planar EBG starts close by the resonance frequency determined by the reflection phase. The dispersion curve of the second mode does not follow the light line, but rapidly crosses the light line at a frequency which is slightly above the resonance frequency. Hence, the upper and lower boundaries of the band gap are not symmetrical with respect to the resonance frequency for the compact uni-planar EBG. The resonance frequency is located quite near by the upper boundary of the band gap. It can be noticed that the band gap obtained from dispersion diagram

does not necessarily occur at the same frequency band with in-phase reflection, where the reflection phase falls between 180° and -180°.

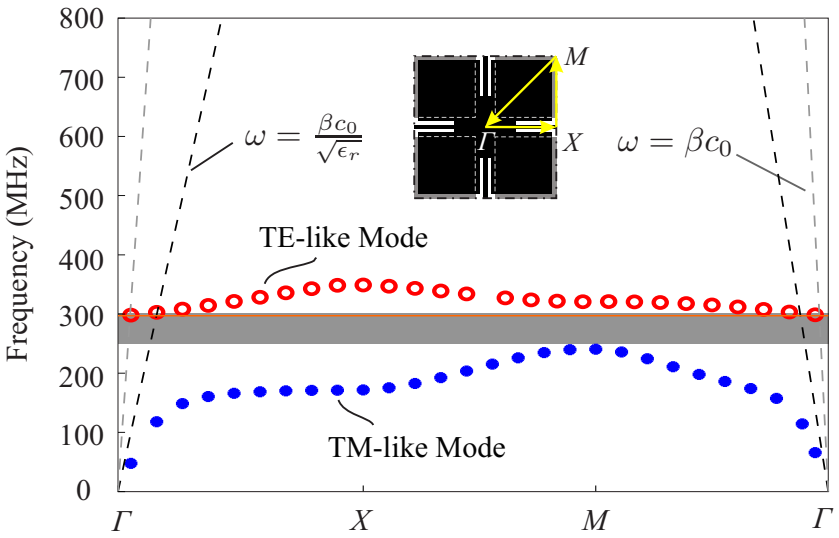

Figure 3.12: Simulated dispersion diagram of the multi-layer EBG structure including the first two modes. The stop-band between the first and second modes is denoted by the grayly shaded frequency band.

3.3.1.2.3 Band Gap — Transmission Behavior

Besides the dispersion diagram the band gap property of an EBG structure can also be evaluated by its transmission behavior. Two evaluation methods will be discussed: the suspended TL model and the co-planar TL model [98, 102, 103].

For a suspended TL model, the EBG structure is placed between an air-filled microstrip transmission line [cf. Fig. 3.14(a)]. The upper stripline is kept as wide as the EBG surface in order to create a quasi TEM wave above the EBG surface. The transmission behavior depends on the separation between the suspended stripline and the EBG surface. Here, two separation distances (d = 1 cm, 3 cm) will be considered.

The transmission coefficient of the TL model for the case of a compact uni-planar EBG is plotted in Fig. 3.15(a) for different separation distances between the suspended stripline and the EBG surface. For a small separation distance d = 1 cm two band gaps around 360 MHz and 430 MHz are observed. For a larger separation distance d = 3 cm the band gaps are located near 340 MHz and 435 MHz. Note that the band gap obtained based on transmission line model is not in agreement with the one from the dispersion diagram. The dispersion diagram describes the propagation characteristics of surface waves, which are tightly bound on the surface of EBG structure. In a suspended TL model a quasi transverse electromagnetic (TEM) wave is excited between the microstrip TL and the EBG structure. Therefore, different band gaps are observed from the transmission behavior and the dispersion diagram. The separation between the EBG and the stripline has an impact

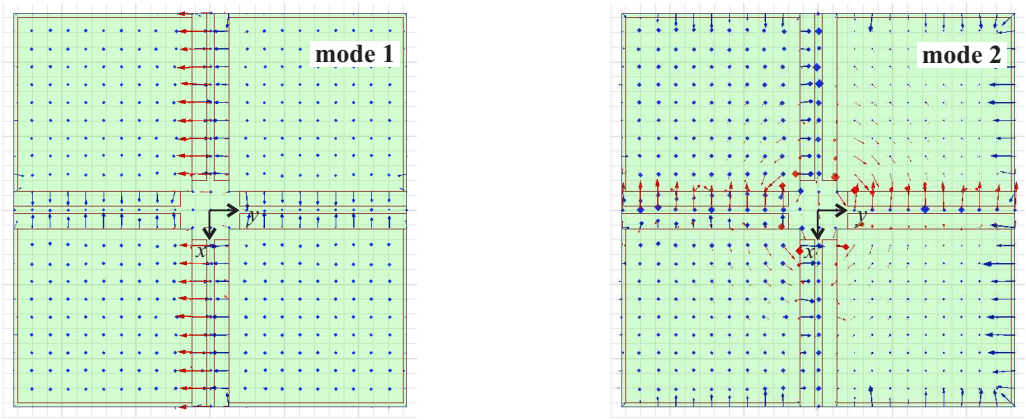

Figure 3.13: Electric field (blue arrow) and magnetic field (red arrow) distribution on the top surface of the uni-planar EBG at the spectral point of dispersion diagram $p_{\mathrm{x}} = 10°$, $p_{\mathrm{y}} = 0°$ (10° phase shift on x-direction).

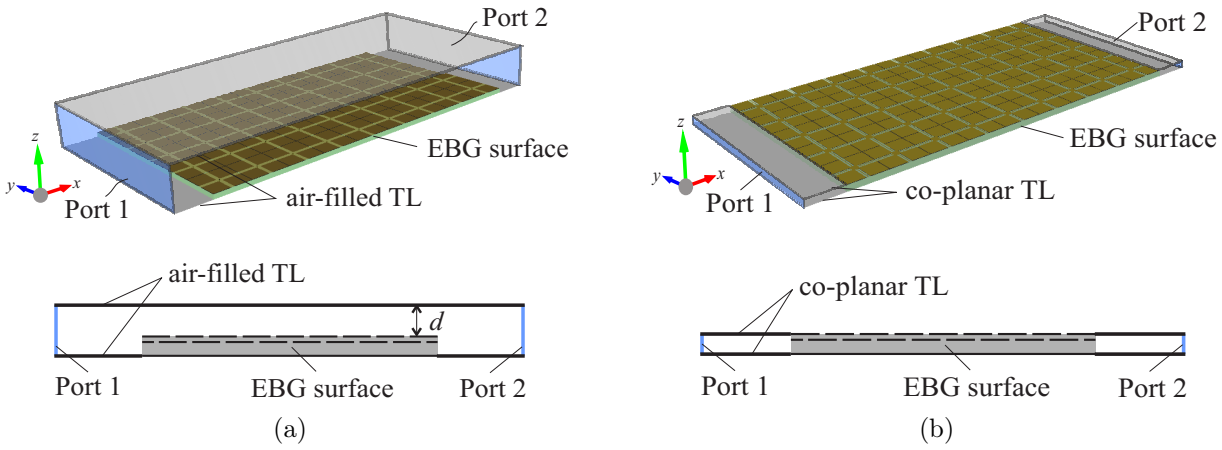

Figure 3.14: (a) The suspended transmission line model and (b) the co-planar transmission line model for the transmission characteristics investigation of the considered EBG surfaces based on finite-element model.

on the generated quasi TEM waves between the TL and the EBG structure, denoted by the shift of the band gaps for different separation distances.

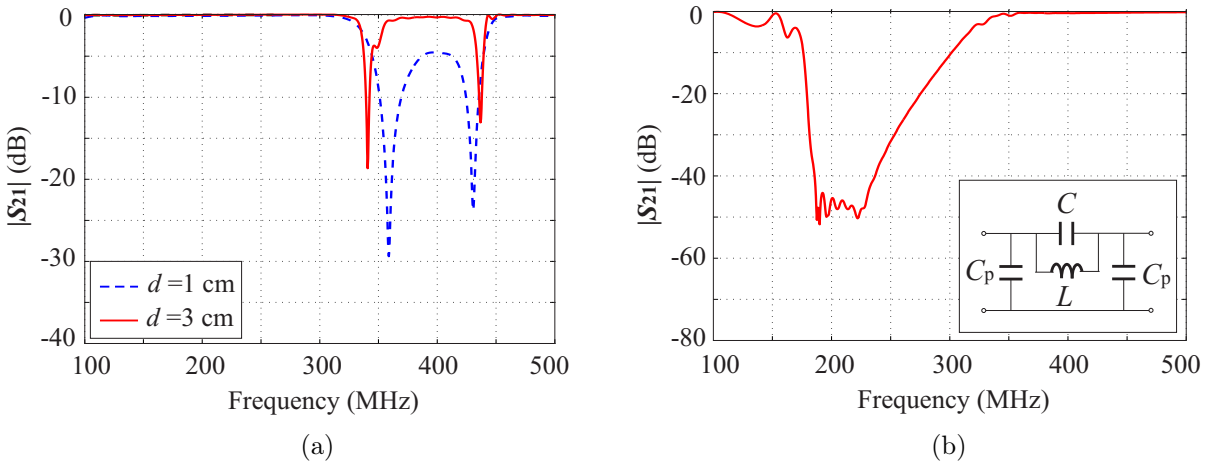

Figure 3.15: Simulated transmission coefficient of (a) a suspended TL model with a compact uni-planar EBG placed between the air-filled microstrip transmission line, and (b) a co-planar TL model with a compact uni-planar EBG embedded between two microstrip line sections.

As depicted in Fig. 3.14(b), in the co-planar TL model the EBG surface is embedded between two microstrip line (MSL) sections, where the top layer of the EBG structure and the microstrip are aligned in the same plane. Instead of generating a surface wave above the EBG structure in the suspended TL model, the co-planar TL model impresses a surface current on the top layer of the EBG structure.

The observed stop-band spans from 170 MHz to 320 MHz, which is roughly the same as the band gap in the Γ–X section of the dispersion diagram (cf. Fig. 3.12). Note that the dispersion diagram describes the surface wave propagation in a two-dimensional manner, whereas in the transmission line case the propagation in only one direction, here the x-direction (Γ–X), is considered. It can be seen that the co-planar TL model is more suitable for the evaluation of the stop-band property of the uni-planar EBGs.

3.3.1.2.4 Prototype and Measurement

With the geometry parameters given in Fig. 3.10(b), a 5×9 EBG array based on the uni-planar concept is fabricated and utilized for experimental investigation. The transmission behavior of the EBG structure is evaluated based on a suspended and a co-planar TL model. For the suspended TL model, the separation between the microstrip line and the EBG surface is approximately 3 cm. A tapered metallic section on each side of the TL model which merges the width of the TL to the junction with the probe cable is applied to facilitate the measurement [cf. 3.15(a)]. For the co-planar TL model, the tapered metallic section aligns in the same layer as the top surface of the EBG structure [cf. 3.15(b)].

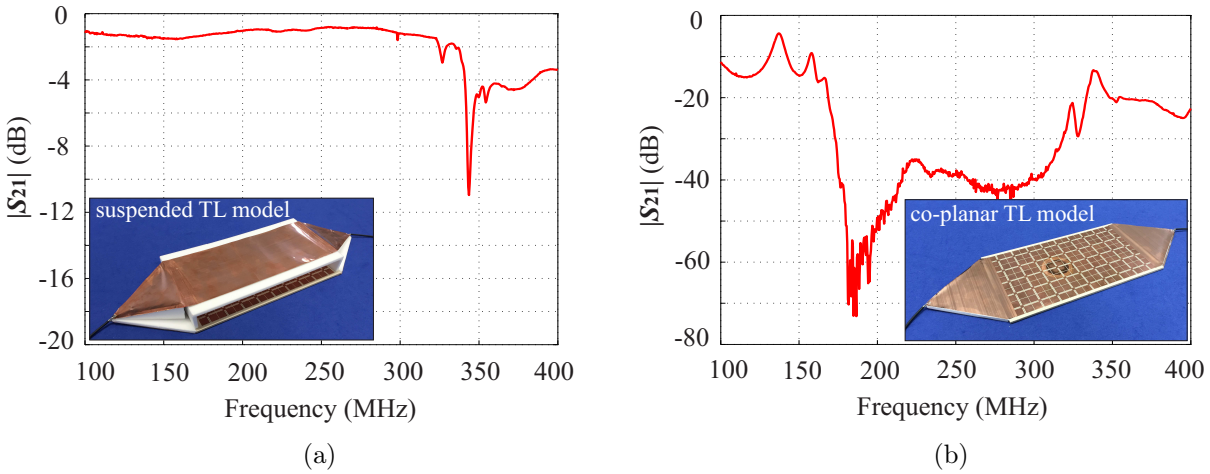

Figure 3.16: Measured transmission coefficient of (a) a suspended TL model with a compact uni-planar EBG placed between the air-filled microstrip transmission line, and (b) a co-planar TL model with a compact uni-planar EBG embedded between two microstrip line sections.

The measured transmission coefficient of a suspended TL model with a compact uni-planar EBG placed between the air-filled microstrip transmission line, and a co-planar TL model with a compact uni-planar EBG embedded between two microstrip line sections are displayed in Fig. 3.16.

Considering the frequency selectivity of the transmission curves, the measured and simulated results match to each other very well. With the suspended TL model [cf. Fig. 3.16(a)], the uni-planar EBG exhibits a low transmission coefficient at a higher frequency, here 350 MHz, in comparison with the designed resonance frequency (297 MHz). With the co-planar TL model [cf. Fig. 3.16(b)], a stop-band with a dynamic range of more than 30 dB spanning roughly from 170 MHz to 320 MHz can be observed for the uni-planar EBG. The degraded transmission behavior over the entire frequency range is attributed to the mismatch between the EBG structure together with the tapered metallic section and the 50 Ω probe cable.

3.3.1.3 Parametic Study

The physical dimensions of an EBG structure determine its electromagnetic properties. Here the effects of these parameters listed in Fig. 3.10(b) are investigated in order to obtain more insights for EBG designs. For each parameter, the reflection phase and dispersion diagram are compared to the original design.

3.3.1.3.1 Floating Patch Dimension: W_f

By decreasing the dimension of the floating patch (from 12 mm to 10 mm), the overlap of the top and floating layers decreases, and thus, the MIM capacitance will be reduced. As a

result, the resonance frequency is shifted to a higher region (from 297 MHz to 345 MHz), which can be seen in Fig. 3.17(a). Due to the decreased capacitance, the L/C ratio, i.e., the in-phase reflection bandwidth, is slightly increased, indicated by the less steep zero-crossing of the reflection phase curve. However, this minor difference is hardly noticeable from the reflection phase plot.

From the dispersion diagram we can observe that the dispersion curves of the first two simulated modes are shifted to higher frequency regions for an decreased dimension of the floating patch W_f (from 12 mm to 10 mm). It is worth noticing that the band gap between the first and second mode of the EBG structure with a smaller W_f is slightly larger compared to the original design. Although the band gap in the dispersion diagram does not coincide with the in-phase reflection band from the reflection phase plot, they do reveal a similar tendency for the same parameter variation.

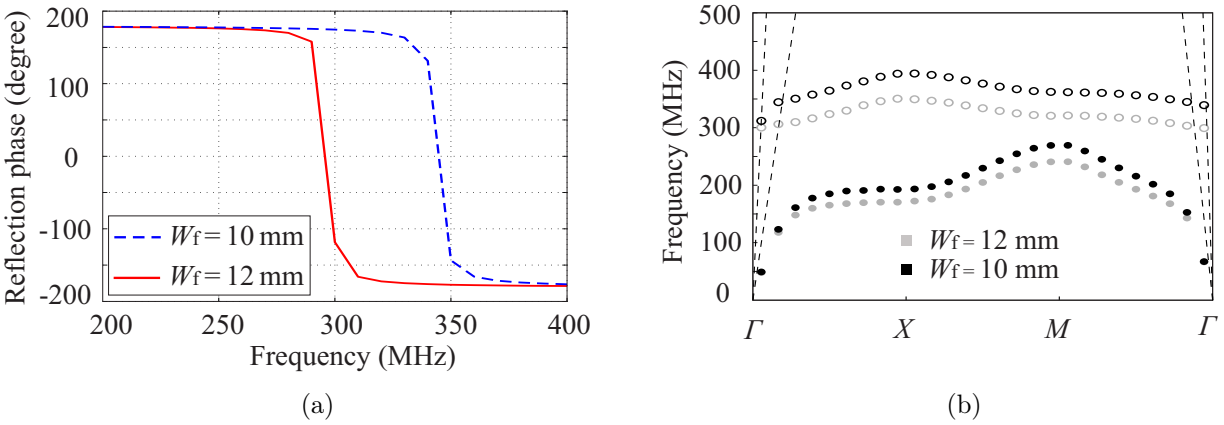

Figure 3.17: Simulated (a) reflection phase and (b) dispersion diagram of the compact uniplanar EBG surface with different floating patch dimensions (W_f = 10 mm and W_f = 12 mm).

3.3.1.3.2 Width of Gap between Patches: g

The gap between adjacent patches has a influence on the fringe capacitance. An increased resonance frequency is observed by enlarging the gap from the original size 0.5 mm to 2 mm. In comparison to the floating patch dimension W_f, the resonance frequency is less sensitive to the gap between adjacent patches g, indicating that the MIM capacitance is more prominent compared to the fringe capacitance. In order to achieve a more compact EBG design, the gap between the adjacent patches should be minimized. However, in practice this parameter is usually limited by the fabrication tolerance.

In the dispersion diagram we could barely see any difference of the dispersion curves for the two compared gap dimensions. In this sense the reflection phase is more sensitive to the geometry variation of the EBG structure compared to the dispersion characteristics.

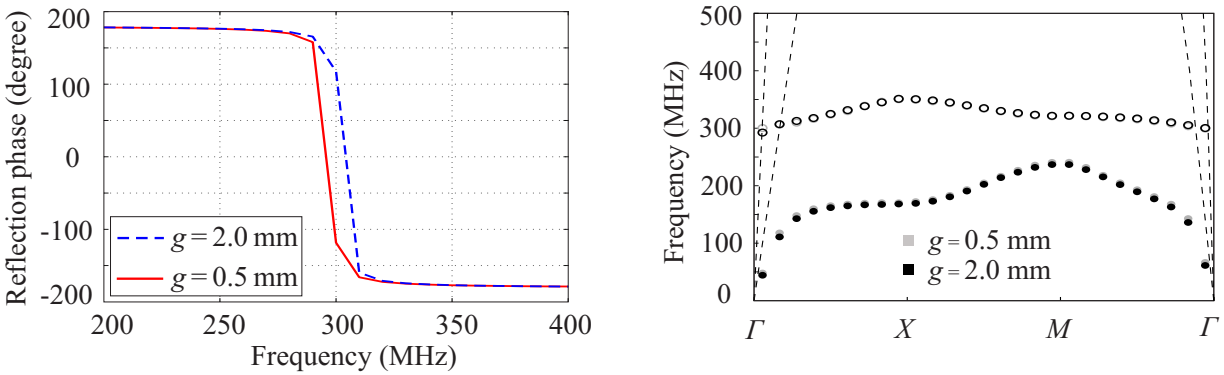

(a) (b)

Figure 3.18: Simulated (a) reflection phase and (b) dispersion diagram of the compact uniplanar EBG surface with different width of the gap between patches ($g = 2$ mm and $g = 0.5$ mm).

3.3.1.3.3 Width of Connection Line: w

The width of the inset connection line between adjacent patches w mainly affects the inductance. As shown in Fig. 3.19(a), a wider connection line leads to a decreased inductance, and hence to an increased resonance frequency. Specifically, by increasing the width of the connection line from $w = 0.5$ mm to $w = 1$ mm, the corresponding resonance frequency is shifted from 297 MHz to 313 MHz.

As displayed in Fig. 3.19(b), with an increased value of w the dispersion curve of the first mode is generally shifted to a higher frequency region, whereas the curve of the second mode is nearly identical to the one of the original design. As a reslut, the frequency band gap between the first and the second mode is reduced, which is caused by the decreased inductance.

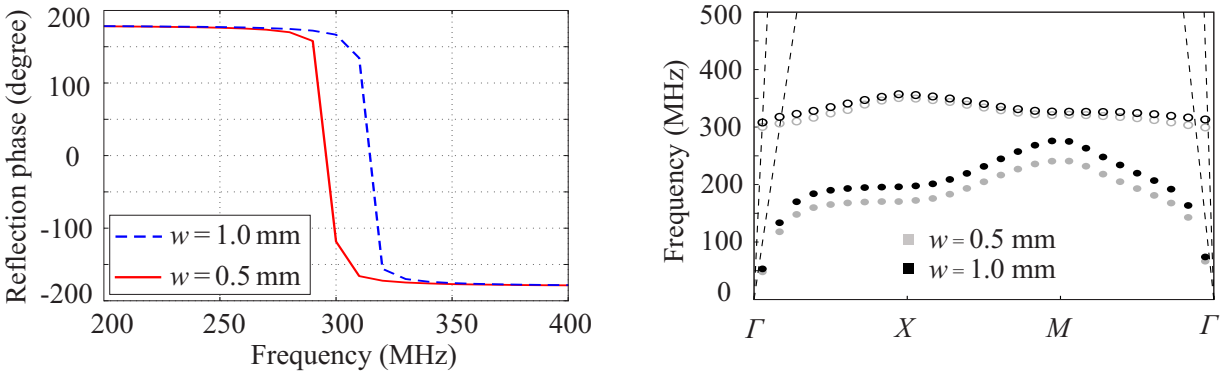

(a) (b)

Figure 3.19: Simulated (a) reflection phase and (b) dispersion diagram of the compact uniplanar EBG surface with different width of the connection line ($w = 1$ mm and $w = 0.5$ mm).

3.3.1.3.4 Width of Inset: W_i

The width of the inset on the patch has also an influence on the resonance frequency of the EBG structure. In principe, a larger W_i value provides an increased inductance, since more magnetic flux could be formed in the substrate due to the wider inset. On the other hand, the inset introduces a physical notch on the top patch, which in turn introduces a junction capacitance, and meanwhile reduces the fringe capacitance. Therefore, a larger W_i potentially decreases the total capacitance. Here an increased resonance frequency is observed by reducing the width of the inset (from 2.5 mm to 1.5 mm), which means the reduction on inductance by the narrower inset is more predominant in our case.

The dispersion diagram in Fig. 3.20(b) reveals a generally increased eigen-frequency of both modes for the EBG structure with a smaller inset width. The resulting band gap is very similar in comparison with the original design and no obvious variation is observed.

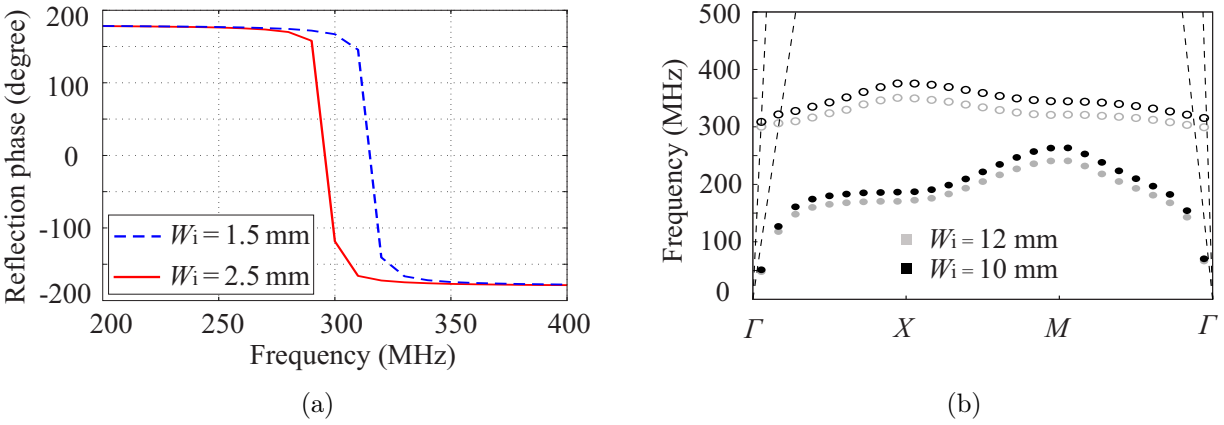

Figure 3.20: Simulated (a) reflection phase and (b) dispersion diagram of the compact uniplanar EBG surface with different width of the inset section (W_i = 1.5 mm and W_i = 2.5 mm).

3.3.1.3.5 Length of Connection Line: L_i

Similar to the width of inset W_i, the length of the inset connection line L_i has effects on both the inductance and the junction capacitance. A smaller L_i value would reduce the inductance and the capacitance, and hence increases the resulting resonance frequency. As shown in Fig. 3.21(a) a 5 mm reduction of the connection line leads to an increased resonance frequency.

In Fig. 3.21(b) the dispersion curves of the first and second mode are both shifted to higher frequencies for the case of a shorter connection line. Note that the band gap for a smaller L_i value is narrower compared to the one of the original design, indicating that the reduction of L_i has a more significant effect on the inductance than the junction capacitance.

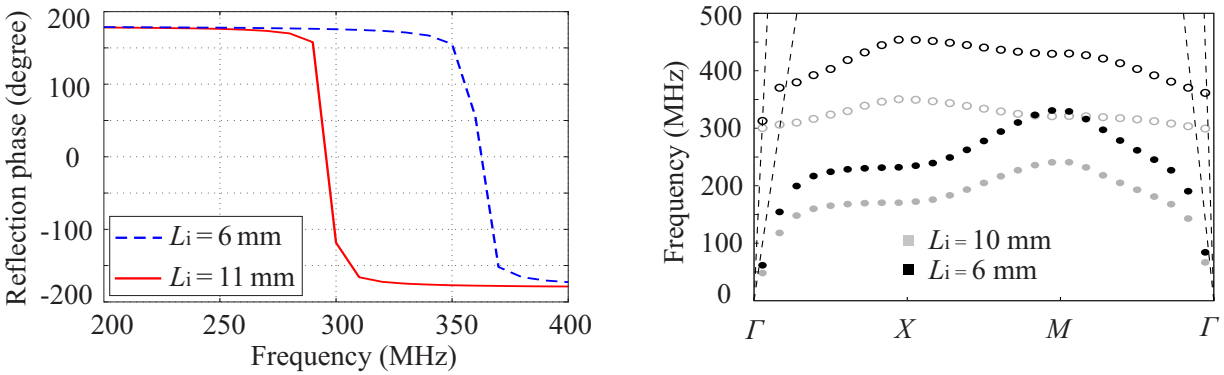

Figure 3.21: Simulated (a) reflection phase and (b) dispersion diagram of the compact uniplanar EBG surface with different length of the connection line (L_i = 6 mm and L_i = 11 mm).

3.3.1.3.6 Thickness of Top Substrate: h_1

Compared to the original design (h_1 = 0.15 mm), here we increase the thickness of the top core substrate (h_1) to 0.3 mm. Theoretically, this thickness should be kept as small as possible to create a large MIM capacitance, and thus achieve a compact EBG design. However, an increased capacitance tends to reduce the bandwidth (in-phase bandwidth of reflection phase diagram) of the EBG structure. Compared to the original design, a thicker top core substrate leads to an increase of the resonance frequency of the EBG structure from 297 MHz to 416 MHz [cf. Fig. 3.22(a)].

The dispersion diagram [cf. Fig. 3.22(b)] also indicates that the stop-band of the EBG structure is shifted to a higher frequency region, and the corresponding bandwidth is slightly increased for an increased thickness of the MIM structure due to the reduced capacitance.

3.3.1.3.7 Thickness of Bottom Substrate: h_2

The thickness of the bottom substrate mainly affects the inductance. A thinner bottom substrate tends to reduce the inductance, and hence to increase the resonance frequency. Here the thickness of the bottom substrate h_2 is set to 2 mm and compared with the original design. The resonance frequency of the EBG surface with a smaller h_2 value is shifted to a higher frequency by roughly 50 MHz. Additionally, the reflection phase curve in the case of a thicker bottom substrate reveals a slightly broader in-phase bandwidth in comparison with the original design, indicated by the less steep crossing through $\pi/2$ and $-\pi/2$.

The dispersion curve of the first mode remains almost unchanged compared to the one of the original design, while the curve of the second mode is shifted to a higher frequency region.

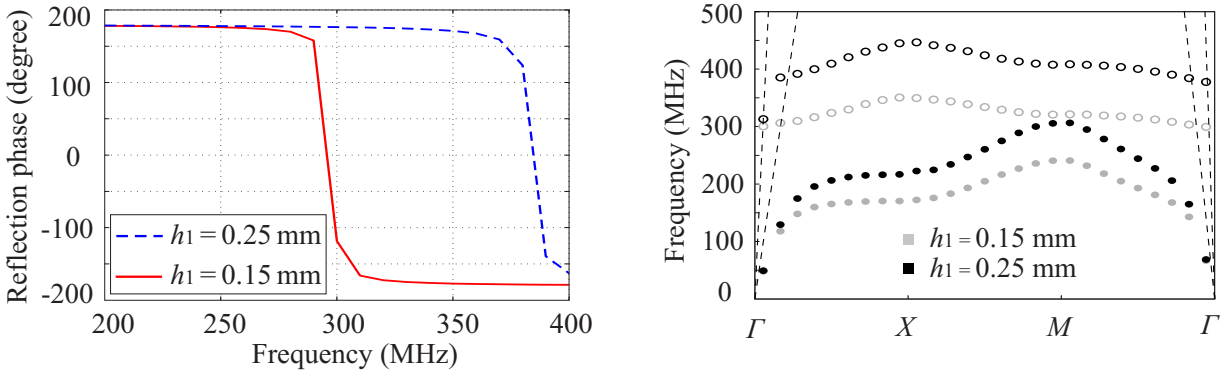

(a) (b)

Figure 3.22: Simulated (a) reflection phase and (b) dispersion diagram of the compact uniplanar EBG surface with different thickness of the upper substrate ($h_1 = 0.25$ mm and $h_1 = 0.15$ mm).

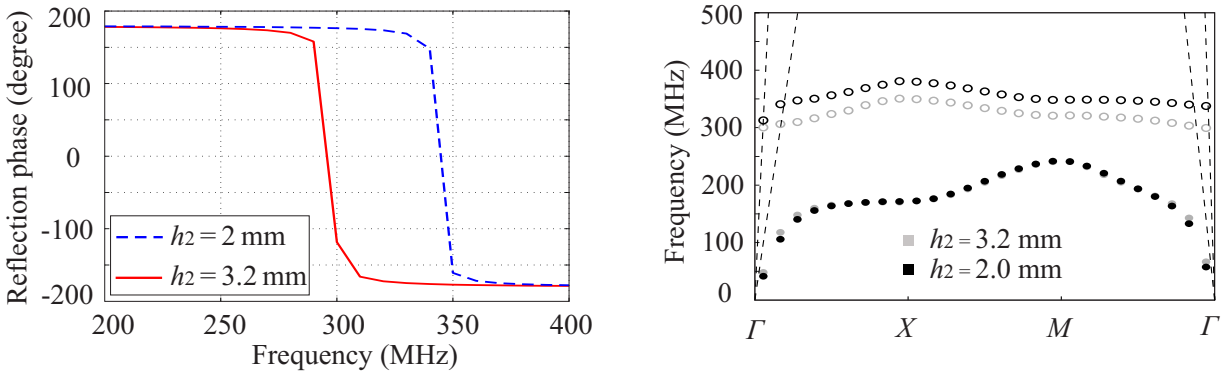

(a) (b)

Figure 3.23: Simulated (a) reflection phase and (b) dispersion diagram of the compact uniplanar EBG surface with different thickness of the lower substrate ($h_2 = 2$ mm and $h_2 = 3.2$ mm).

3.3.2 Mushroom-like Concept

In the previous subsection a compact uni-planar EBG structure based on multi-layer technology was presented. Here we propose a modified mushroom-like EBG structure with the similar topology as utilized in [67] and a same lattice dimension as the one based on uni-planar concept.

3.3.2.1 Multi-layer Mushroom-Like EBG Structure

Compared with the conventional mushroom EBG structure, the proposed compact EBG surface introduces additional floating metallic layers between the top patch layer and the ground plane, indicated by the white dashed lines in Fig. 3.24(a). The stack-up of the mushroom-like EBG remains unchanged as the one utilized for the uni-planar design, except that a vertical via with a diameter of d is located in the center of the patch and connects the top and the ground layers of the EBG lattice. With the geometry parameters given in Fig. 3.24(b), the proposed multi-layer EBG based on mushroom-like concept exhibits a resonance at 297 MHz.

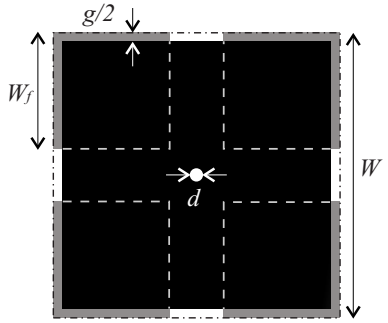

(a)

W	26.5 mm
W_f	12 mm
d	0.5 mm
g	0.5 mm

(b)

Figure 3.24: (a) Layout of the proposed compact mushroom-like EBG structure in top view, and (b) the corresponding geometry parameters.

3.3.2.2 Characterization of the Mushroom-Like EBG Design

Similar to the uni-planar concept, the proposed mushroom-like EBG structure is characterized by the reflection phase for plane wave incidence and the surface wave band gap.

3.3.2.2.1 Reflection Phase

The simulation model for the reflection phase investigation is identical to the one depicted in Fig. 3.5, except for the EBG lattice itself. TE and TM polarized plane waves with different incident angles are again considered. Fig. 3.25 shows the reflection phase at the top surface of the proposed EBG structure in the case of TM and TE polarization for

different incident angles. The proposed compact mushroom-like EBG structure exhibits a reflection phase close to 0° for a normal incidence at 297 MHz. As the incident angle increases, the resonant frequency of the mushroom-like EBG is slightly shifted to higher frequencies in the case of a TE polarization, whereas remains quite constant for a TM polarized incident wave. This can be explained by the fact that the variation of the tangential magnetic field component in the case of a TE polarized incident wave is more sensitive to the mushroom-like EBG due to its larger inductance, since its top patch, vertical vias and ground plane form a large current loop inside the substrate. The tangential magnetic field component decreases with an increased incident angle, and thus leads to a reduction of the induced inductance. As a result, the resonance frequency is shifted to a higher value, specifically, 298 MHz for a incident angle of 30° and 299 MHz for a incident angle of 60°. For a TM polarization the tangential electric field component is getting smaller with an increased incident angle. Thus, the charge accumulation across the gap between adjacent EBG lattices is less sufficient and provides a smaller capacitance, which results in a higher resonant frequency. However, an additional current on the vias of the mushroom-like EBG is induced by the normal electric field in the case of an oblique incidence. This induced current activates an additional inductance through the conducting path and tends to decrease the resonant frequency. Therefore, for the mushroom-like EBG the effect of the tangential and normal electric field is balanced and results in a quite constant resonant frequency against incident angles for a TM polarized incident wave.

Additionally, the mushroom-like EBG has a larger bandwidth over which the reflection phase falls between 180° to -180° compared to the uni-planar EBG. According to [47], this bandwidth is proportional to square root of the ratio of L and C from the LC model. Due to the through-plated vias, a longer conducting path, thus, a greater inductance is created by the mushroom-like EBG. Hence, a smoother transition from 180° to -180° of the reflection phase is observed with the mushroom-like EBG. Similar to the compact uni-planar EBG, as the incident angle increases the bandwidth of the EBG structure tends to decrease for a TE polarization, whereas increase for a TM polarization.

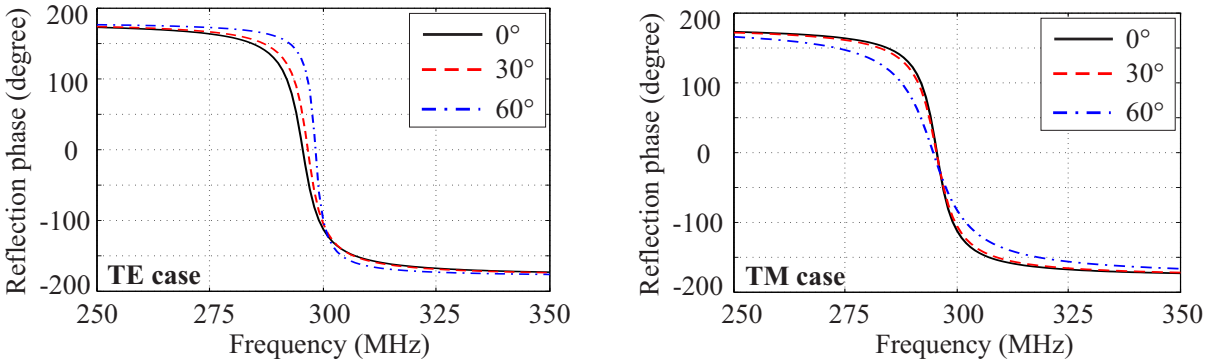

Figure 3.25: Simulated reflection phase of the multi-layer EBG structure in the case of (a) a TE polarization and (b) a TM polarization for different incident angles.

3.3.2.2.2 Band Gap — Dispersion Diagram

The dispersion diagram of the proposed mushroom-like EBG structure including the first two modes is given in Fig. 3.26. A surface wave stop-band between the first and second mode is observed and denoted by the grayly shaded frequency band. As we did for the uni-planar EBG, the polarization characteristics of the first two modes of the compact mushroom-like EBG are investigated. The first mode of the mushroom-like EBG structure is a TM-like mode indicated by the transversal magnetic field (red arrow) in the y-direction [cf. Fig. 3.27(a)]. Again, both transversal (y-direction) and longitudinal (x-direction) electric field components exist for the second mode. Due to the fact that the magnetic field aligns in the propagation direction [cf. Fig. 3.27(b)], here we suppose the second mode from the dispersion diagram to be a TE-like mode.

The dispersion curve of first mode is tightly bound to the light line in air till roughly 280 MHz, and then rapidly deviates from the light line into the slow wave region. The different behavior of the first mode between the uni-planar and mushroom-like can be explained in such a way that due to the absence of direct connection between the top layer and the ground plane, the electric field of the uni-planar EBG is more confined inside the substrate and, thus, the surface wave is mainly bound in the high permittivity region. For the mushroom-like EBG the electric field extends widely beyond the EBG surface and the surface waves are supported in the region above the EBG surface as well. In addition to the first mode, the dispersion curve of the second mode reveals a significant difference between the considered uni-planar and mushroom-like EBG surfaces. The second mode of the uniplanar EBG lies smoothly above the band gap (cf. Fig. 3.12), whereas the dispersion curve of the mushroom-like EBG raises up steeply (cf. Fig. 3.26). Note that the band gap of the mushroom-like EBG in our case is narrower than the one of the uni-planar EBG, and the resonance frequency is located more or less in the center of the band gap.

Basically, the dispersion curves of the considered uni-planar and mushroom-like EBG surfaces reveal similarities to the corresponding single-layer EBG designs [47, 50, 64]. Based on the dispersion diagram, the uni-planar EBG achieves a wider band gap between the first two modes than the mushroom-like EBG. However, a contrary trend was observed from the reflection phase analysis, where the mushroom-like EBG has a larger bandwidth over which the reflection phase falls between 90° and -90°. For both uni-planar and mushroom-like EBGs the band gap obtained from dispersion diagram does not match the frequency band with in-phase reflection.

3.3.2.2.3 Band Gap — Transmission Behavior

For a suspended TL model with 3 cm separation distance from the microstrip line to the EBG surface, the mushroom-like EBG exhibits a narrow stop-band for the transmission coefficient around 300 MHz, which conforms to the one predicted by the dispersion diagram (cf. Fig. 3.26). Different from the uni-planar EBG, the mushroom-like EBG consists of vertical vias and the electric field extends beyond the EBG surface. Therefore, the surface modes are not strictly confined on the surface of mushroom-like EBG, but are supported in the region above the EBG surfac. Hence, an approximate agreement of the band gaps

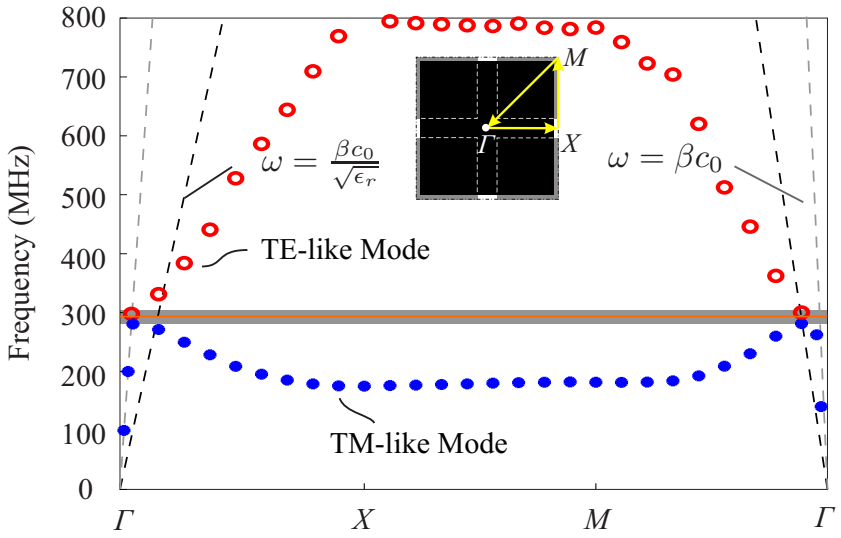

Figure 3.26: Simulated dispersion diagram of the multi-layer mushroom-like EBG structure including the first two modes. The stop-band between the first and second modes is denoted by the grayly shaded frequency band.

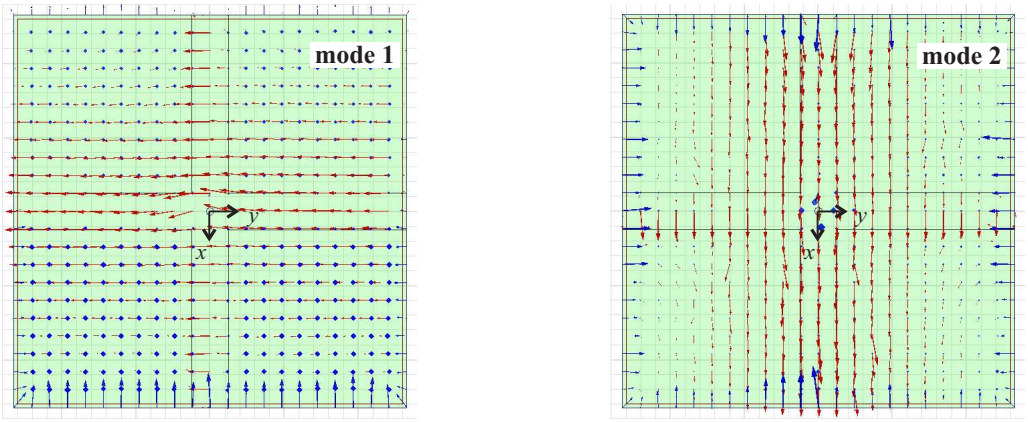

(a) (b)

Figure 3.27: Electric field (blue arrow) and magnetic field (red arrow) distribution on the top surface of the mushroom-like EBG at the spectral point of dispersion diagram $p_x = 10°$, $p_y = 0°$ (10° phase shift on x-direction).

from the transmission behavior and the dispersion diagram is observed. As the separation distance decreases, more parasitic resonances occur, since then the EBG lattice appears larger with respect to the stripline and the whole EBG surface exhibits less as homogeneous structure, but more as individual resonators. Generally, the suspended TL model could well predict the stop-band of the mushroom-like EBG.

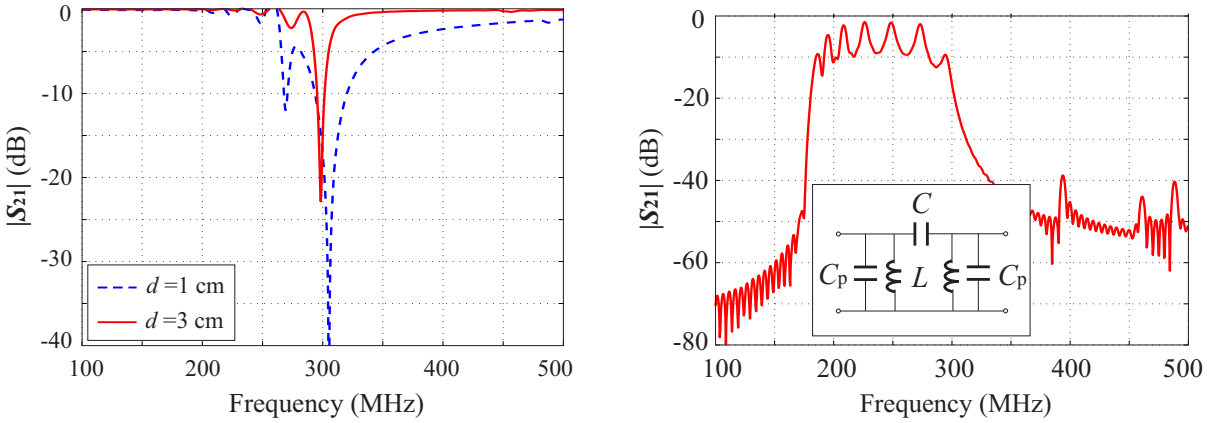

Figure 3.28: Simulated transmission coefficient of (a) a suspended TL model with a compact mushroom-like EBG placed between the air-filled microstrip transmission line, and (b) a co-planar TL model with a compact mushroom-like EBG embedded between two microstrip line sections.

In the case of a co-planar TL model the mushroom-like EBG can be represented by an equivalent lumped element circuit, which explains the band-pass filter-like transmission behavior [cf. Fig. 3.28(b)] [84, 104]. The shunt capacitor C_p is attributed to the parasitic capacitance between the metal patch and the ground plane. The ripples in the transmission curve within the frequency band from 200 MHz to 300 MHz are probably caused by the eigen-resonance of the metallic structures of EBG.

3.3.2.2.4 Prototype and Measurement

With the geometry parameters given in Fig. 3.24(b), a 5×9 EBG array based on the mushroom concept is fabricated and utilized for experimental investigation. Similar to the uni-planar EBG, the transmission behavior of the mushroom-like EBG structure is evaluated based on a suspended and a co-planar TL model.

With the suspended TL model ($d = 3$ cm), the mushroom-like EBG reveals a narrow stop-band around 297 MHz along with a parasitic resonance at 270 MHz, which shows an agreement to the simulation results (cf. 3.28(a)). With the co-planar TL model, the mushroom-like EBG reveals no typical stop-band but a band-pass filter-like transmission behavior with several ripples within the frequency range 200 MHz – 300 MHz, similar as the simulated results [cf. 3.28(b)].

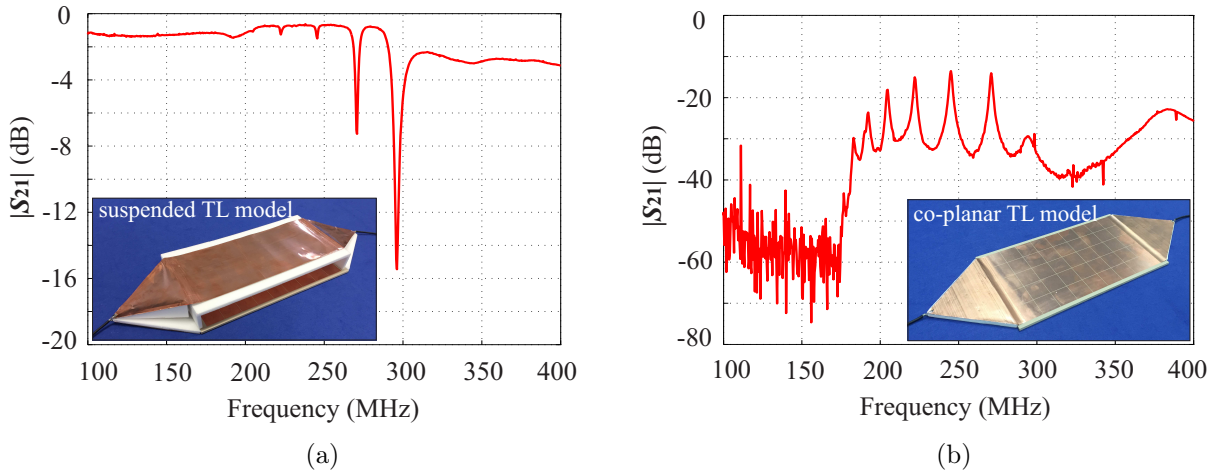

Figure 3.29: Measured transmission coefficient of (a) a suspended TL model with a compact mushroom-like EBG placed between the air-filled microstrip transmission line, and (b) a co-planar TL model with a compact mushroom-like EBG embedded between two microstrip line sections.

3.3.2.3 Parameter Study

Similar to the parameter study performed for the compact uni-planar EBG design, here we investigate the effect of the geometry parameters (cf. Fig. 3.24) of the mushroom-like EBG on the reflection phase and stop-band properties based on full-wave simulation.

3.3.2.3.1 Floating Patch Dimension: W_f

Similar to the uni-planar EBG design, by decreasing the dimension of the floating patch (from 12 mm to 10 mm) the MIM capacitance will be reduced, and thus results in a higher resonance frequency [cf. Fig. 3.30(a)]. Due to the decreased capacitance, the in-phase bandwidth is slightly increased, indicated by the less steep zero-crossing of the reflection phase curve.

With a smaller floating patch dimension, the dispersion curve of the first mode is shifted to a higher frequency. The second mode behaves a little bit more complicated: the eigen modes close to the Γ point are shifted to a higher frequency range, whereas the eigen frequencies of the modes away from the Γ point are slightly reduced [cf. Fig. 3.30(b)]. The resulting band gap is very similar to the one from the original design.

3.3.2.3.2 Diameter of Vertical Via: d

Theoretically, the diameter of the vertical via has also an impact on the resonance frequency, since the inductance decreases as the diameter increases. However, the reflection phase plot in Fig. 3.31(a) reveals no obvious change on resonance frequency for the case that the diameter of the via increases form 0.5 mm to 1.5 mm.

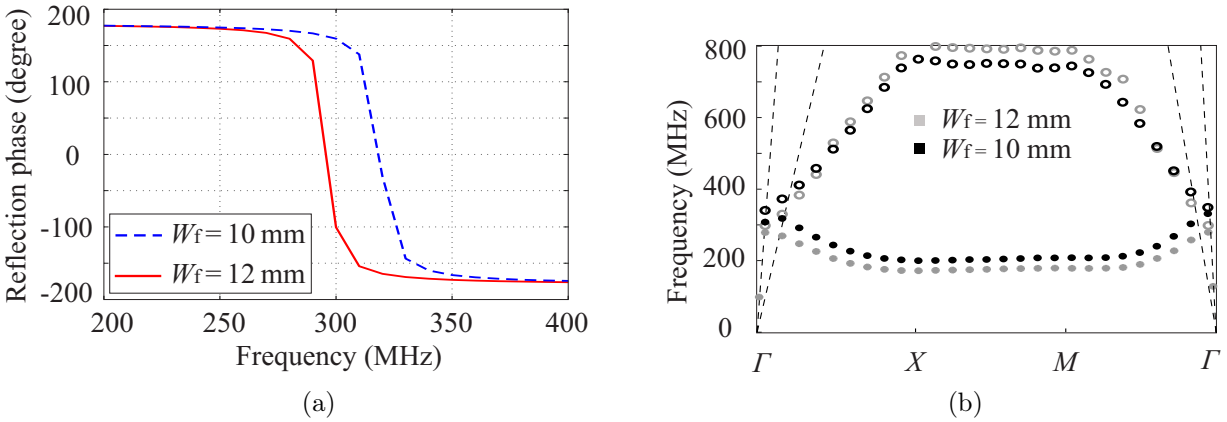

Figure 3.30: Simulated (a) reflection phase and (b) dispersion diagram of the compact uniplanar EBG surface with different floating patch dimensions (W_f = 10 mm and W_f = 12 mm).

From the dispersion diagram in Fig. 3.31(b) we can see that the dispersion curve of the first mode with a larger diameter of the vertical via (d = 1.5 mm) is slightly shifted to a higher frequency in comparison to the original case (d = 0.5 mm). The difference on the frequency band gap compared to the original design is negligible.

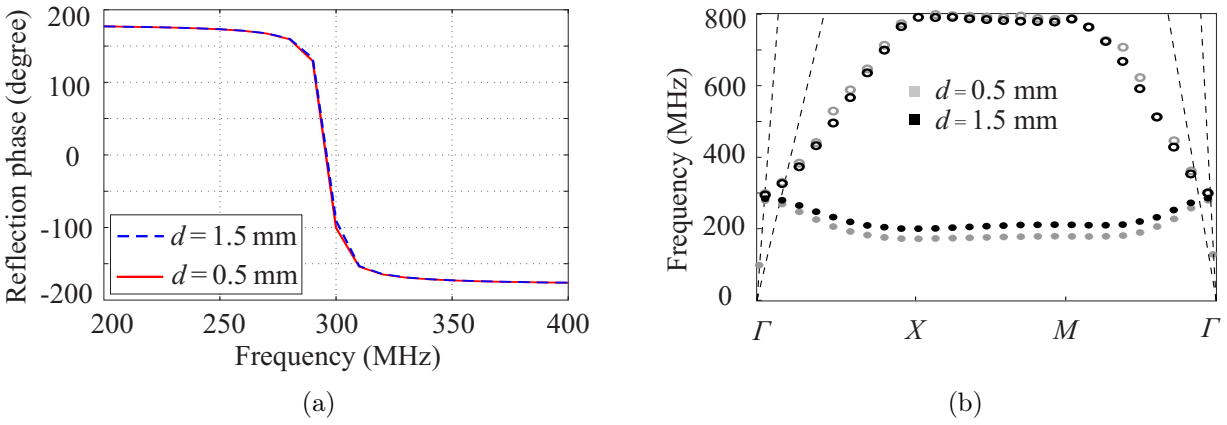

Figure 3.31: Simulated (a) reflection phase and (b) dispersion diagram of the compact uniplanar EBG surface with different diameter of the conducting vertical via (d = 1.5 mm, 0.5 mm).

3.3.2.3.3 Width of Gap between Patches: g

The gap between adjacent patches also has a influence on the fringe capacitance. An increased resonance frequency is observed by enlarging the gap from the original size 0.5 mm to 2 mm. The frequency band gap in the dispersion diagram is shifted to a higher frequency range, and the bandwidth is slightly increased due to the reduced fringe capacitance.

From the dispersion diagram we can see that the dispersion curve of the first mode with a larger gap dimension is almost identical to the one from the original design, whereas the dispersion curve of the second mode indicates that the modes are shifted to a lower frequency range, especially for the modes between point X and M [cf. Fig. 3.32(b)].

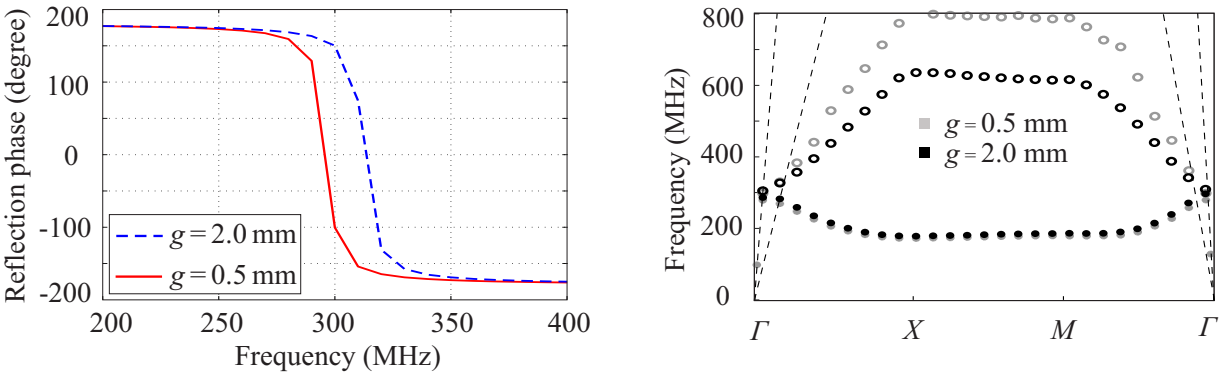

Figure 3.32: Simulated (a) reflection phase and (b) dispersion diagram of the compact mushroom-like EBG surface with different width of the gap between patches (g = 2 mm and g = 0.5 mm).

3.3.2.3.4 Thickness of Top Substrate: h_1

For a thicker top substrate, the MIM capacitance is reduced and an increased resonance frequency is obtained [cf. Fig. 3.33(a)]. Here we increase the thickness from 0.15 mm to 0.25 mm, and the corresponding resonance frequency is shifted from 297 MHz to 365 MHz. Compared to the original design, the reflection phase curve with a larger thickness of the top substrate reveals a smoother transition from π to -π, indicating a slightly increased in-phase bandwidth.

The dispersion diagram [cf. Fig. 3.33(b)] also indicates that the stop-band of the mushroom-like EBG structure is shifted to a higher frequency region, here close to 400 MHz.

3.3.2.3.5 Thickness of Bottom Substrate: h_2

Similar to the uni-planar EBG design, the thickness of the bottom substrate mainly affects the resonance frequency through the inductance. With a decreased h_2 value the resonance frequency for an in-phase reflection [cf. Fig. 3.34(a)] is shifted from 297 MHz to 365 MHz. The corresponding in-phase bandwidth is slightly reduced.

In Fig. 3.34(b) we also observe that the dispersion curves of the mushroom-like EBG with a smaller thickness of the lower substrate are shifted to a higher frequency region.

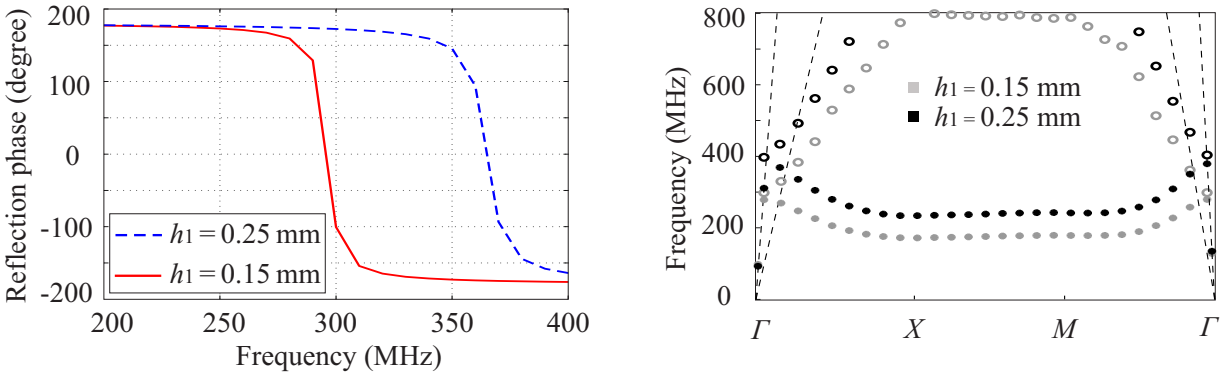

Figure 3.33: Simulated (a) reflection phase and (b) dispersion diagram of the compact uniplanar EBG surface with different top core substrate thickness (h_1 = 0.25 mm, 0.15 mm).

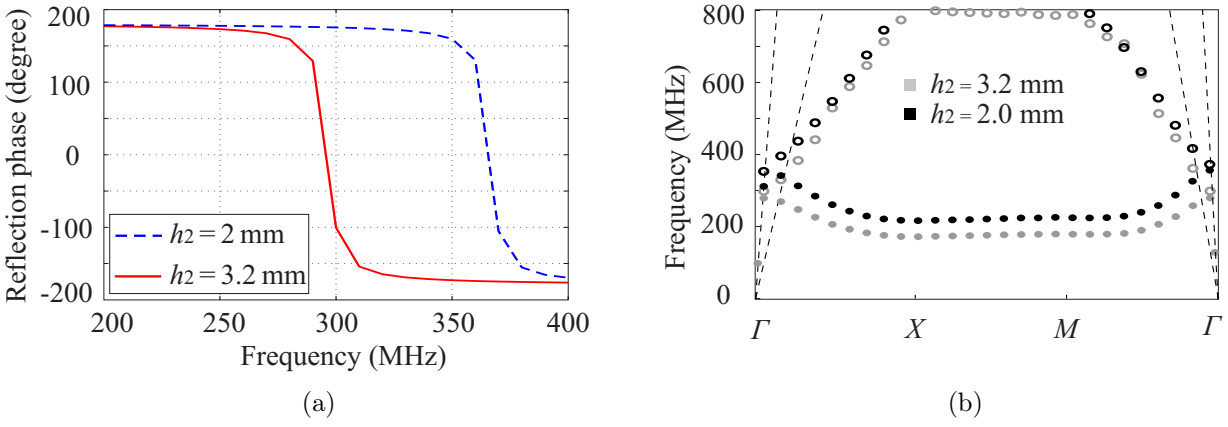

Figure 3.34: Simulated (a) reflection phase and (b) dispersion diagram of the compact mushroom-like EBG surface with different lower core substrate thickness (h_2 = 2 mm, 3.2 mm).

3.3.3 Summary of Compact EBG Designs

In this section two compact EBG structures based on uni-planar and mushroom-like designs have been presented. Both EBG structures achieve an in-phase reflection for a normal incidence at 297 MHz. The band gap property is evaluated based on the dispersion diagram of the lattice model (eigen-mode simulation) and the transmission behavior of finite-element model (driven-mode simulation). It seems that the lumped-element circuit model could better describe the reflection phase property of the EBG structure, while the band gap property for surface wave propagation is more complicated and a dispersion diagram is needed to indicate the corresponding band gap. It has been observed that the band gap does not necessarily coincide with the in-phase reflection frequency band. Additionally, the band gap for transmission coefficient based on finite-element model strongly depends on the transmission line model which is utilized for band gap evaluation. It has been shown that the suspended TL model could better describe the band gap of the mushroom-like EBG and reveals a good agreement to the band gap from dispersion diagram, whereas the co-planar TL model is more suitable for the uni-planar EBG to predict the band gap.

3.4 Summary of the Realized HIS Structure

In this chapter the RF shield with a large surface impedance, which is modeled by a SIBC in Chapter 2, is realized by a two-dimensional EBG structure. Considering that the dimension of the EBG lattice has to be small enough compared to the RF coil and the wavelength at the operation frequency, two compact multi-layer EBG structures based on uni-planar and mushroom-like designs have been presented. The obtained results have shown certain agreement to the classic single-layer EBGs in some respects, e.g., the mushroom-like EBG has a larger in-phase reflection bandwidth compared to the uni-planar EBG. On the other hand, distinct difference due to the specific designs, in our case the extremely thin MIM structure, have been observed in comparison to the classic single-layer EBGs [47, 50, 53]. Both EBG structures achieve a 0° reflection phase for a normal incidence at 297 MHz. In the case of an oblique incidence, the mushroom-like EBG and uni-planar exhibits a larger sensitivity to the incident angle in terms of the resonant frequency for a TE and TM polarization, respectively. Comparing to the uni-planar EBG, the mushroom-like EBG has a larger bandwidth over which the reflection phase falls between $\pi/2$ and $-\pi/2$. However, based on the dispersion diagrams, the uni-planar EBG achieves a wider band gap between the first two modes than the mushroom-like EBG. Therefore, we claim that the band gap does not necessarily coincide with the in-phase reflection frequency band. Additionally, by evaluating the electromagnetic field distribution, it has been confirmed that for both EBG designs the first mode of the dispersion curves is a TM-like mode, and the second mode is predominantly TE-like. The transmission behavior of the finite EBG array has been investigated based on suspended and co-planar TL models. The full-wave simulation and experimental results match well to each other and indicate that the mushroom-like EBG suppresses a surface wave and the corresponding stop-band can be evaluated by the suspended TL model, while the uni-planar EBG is more sufficient for surface current suppression and a co-planar TL model shall be utilized to detect the stop-band.

Chapter 4

RF Coils with HIS Shields

In Chapter 2 it has been demonstrated that the magnetic field distribution of an RF coil (dipole and loop) can be improved by using a shielding plate with high surface impedance. The proposed approach was investigated based on an artificial SIBC, which models the corresponding RF shield. In Chapter 3, two compact HIS structures based on different design concepts are presented. Due to the absence of the vertical conducting vias the fabrication of the compact uni-planar EBG is easier in comparison to the mushroom-like EBG. Here we utilize the realized HIS shield based on the uni-planar concept and investigate the coil performance of an RF coil backed by such a HIS shield. The field characteristics of the considered RF coils will be firstly investigated based on full-wave simulation, and further validated by experimental results.

4.1 Dipole Coil backed by HIS Shield

As demonstrated in Chapter 2, the dipole coil backed by an RF shield with high surface impedance exhibits an improved transverse magnetic field distribution compared to the conventional metallic plate. Instead of the artificial SIBC model, here a real HIS shield is utilized to investigate the effect of a HIS shield on the magnetic field distribution of a dipole coil.

4.1.1 Numerical FDTD-based Investigations

In this section we investigate the improvement on the B_1 distribution of a dipole coil by using a HIS as the RF shield based on numerical simulations.

4.1.1.1 Simulation Setup

The simulation model for the investigation of improving the B_1 homogeneity with a HIS shield is displayed in Fig. 4.1. The dipole element is the same as the one utilized in Chapter 2 for the investigation of the effect of different SIBCs. A two-dimensional HIS (EBG) structure which operates as the RF shield is placed below the dipole element with a separation distance of d. The HIS shield utilized here is based on the compact uni-planar design which is presented in Chapter 3. Additionally to the HIS case, two other shielding scenarios are considered here for the purpose of comparison: a perfect electric conductor (PEC), which models the conventional metallic shielding plate, and a perfect magnetic conductor (PMC), which exhibits an absolute surface current suppression (ideal case for a HIS shield). In order to model the human body at 297 MHz, a homogenous flat phantom ($\epsilon_\mathrm{r} = 58.2$, $\sigma = 0.92$ S/m) is placed 2 cm above the dipole element. The width, length and height of the phantom are set to 20 cm, 40 cm and 15 cm, respectively (cf. Fig. 4.1).

4.1.1.2 Improved B_1 Distribution

As explained in Chapter 2, for ultra-high-field MRI applications the maximum of the local specific absorption rate (peak SAR) is a critical parameter which restricts the power that can be applied to the RF coil, since exceeding the allowed value could cause RF safety issues [34, 88]. Here we continue to use the normalization for B_1 field as defined in (2.2.2), where the corresponding B_1 field is normalized to the square root of peak SAR.

The normalized B_1 field distributions in the transverse cut-plane of the phantom (cf. Fig. 4.1) for different shielding scenarios (PEC, HIS and PMC) are shown in Fig. 4.2. The effect of a variation of the separation distance from the dipole coil to the RF shields ($d = 5$ mm, 10 mm, 20 mm) is investigated here. In general, the HIS shield behaves quite similar to the PMC condition and provides an improved B_1 homogeneity due to the broader field distribution in comparison to the PEC condition (cf. Fig. 4.2). For a small separation

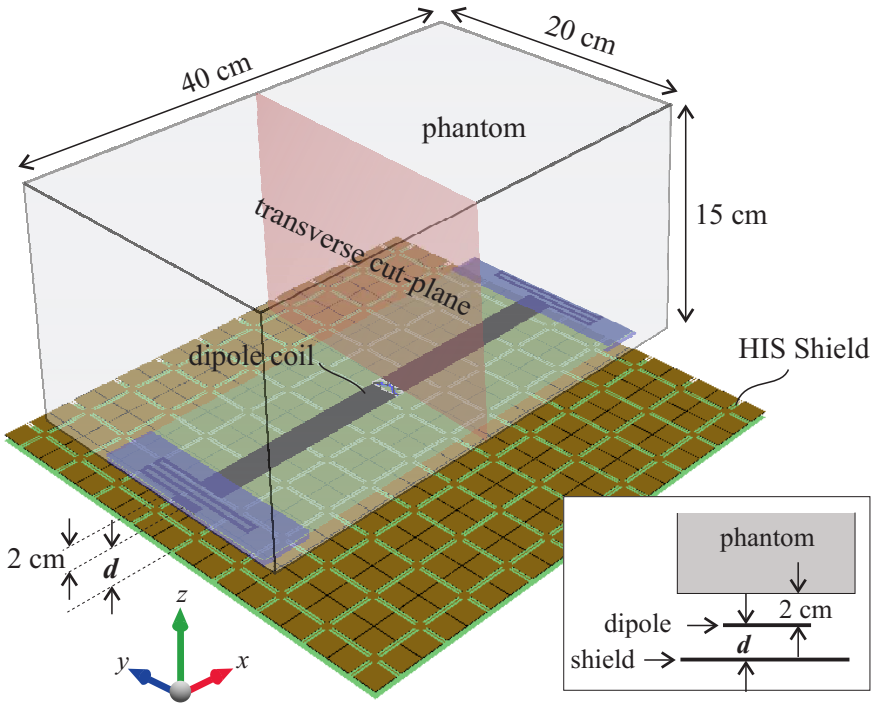

Figure 4.1: The simulation model in EMPIRE XPU for the investigation of improving the B_1 homogeneity with a HIS shield and the effect of different separation distance from the dipole coil to the shielding plate.

distance, the HIS has an advantage over the PEC shield considering the magnetic field distribution inside the phantom. The improvement can be explained by the fact that the induced current on the PEC shield considerably affects the B_1 field excited by the dipole coil due to proximity, whereas the surface current on the HIS shield is sufficiently suppressed. The current suppression effect can be clearly observed in Fig. 4.3, where the currents flow through the dipole coil and the surface of the shielding plate are calculated by integrating the magnetic field along an integration path which encloses the corresponding structure, here the dipole or the surface of the shielding plate. In this case the separation distance between the dipole coil and the shielding plate is set to 10 mm. As displayed in Fig. 4.3(a), in the frequency range from 200 MHz to 300 MHz the induced current on the PEC shield is similar in magnitude as the excitation current in the dipole coil. In contrast, for the same frequency range the current flowing on the surface of the HIS shield is effectively suppressed in comparison to the one in the dipole coil [cf. Fig. 4.3(b)].

For an increased separation distance, the impact of the induced current is weakened, and thus, changes on the field distribution with different shielding scenarios (HIS and PEC) are reduced. Additionally, the penetration depth is slightly enhanced by utilizing a HIS/PMC shield, indicating by the extended equipotential lines of the B_1 distribution (cf. Fig. 4.2). It has been observed that the HIS shield with the smallest separation to the dipole element reveals the most prominent difference on magnetic field distribution compared to the case with a PEC shield. In this sense, the separation distance from the

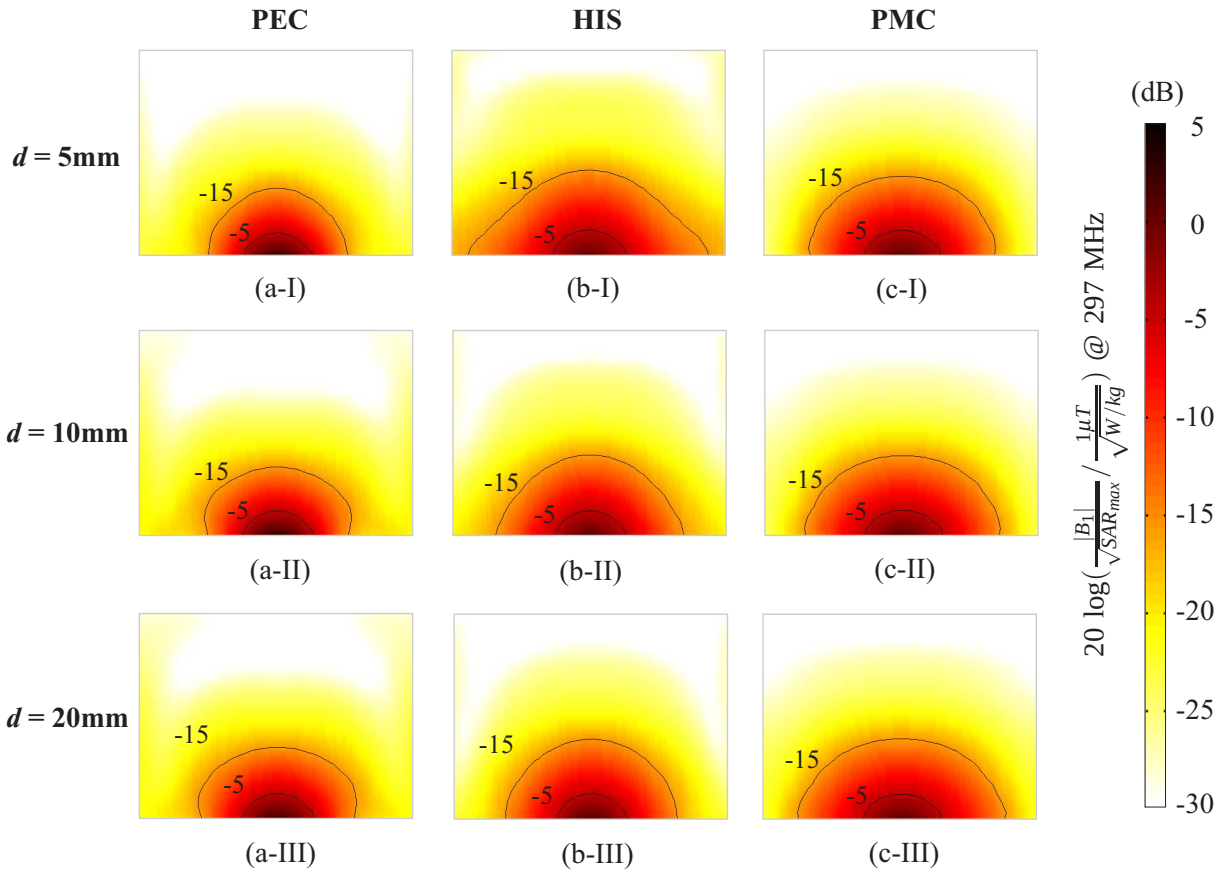

Figure 4.2: Simulated $|B_1|$ field distribution of the dipole coil in the transverse cut of the phantom for different shielding scenarios [(a) PEC, (b) HIS, and (c) PMC] and separation distances ($d = 5$ mm, 10 mm, 20 mm) at 297 MHz. The corresponding field distribution is normalized to the square root of the peak SAR inside the phantom and plotted in dB.

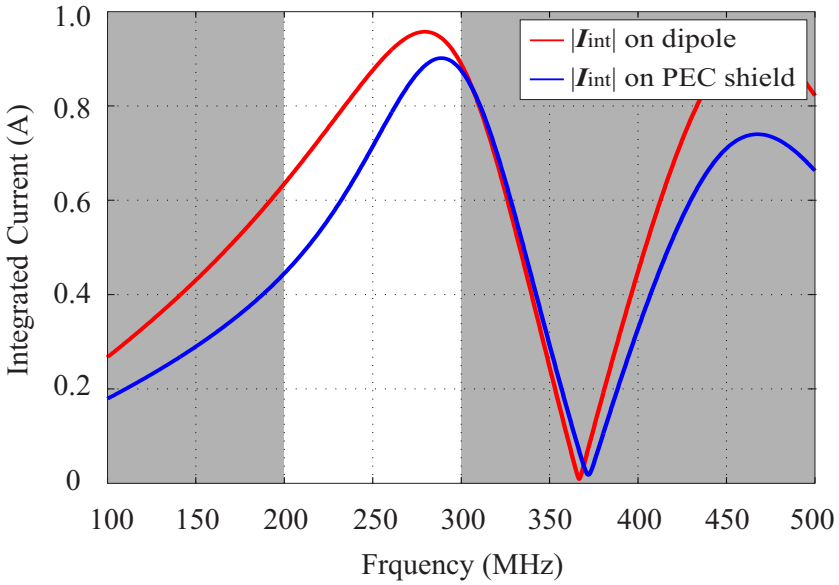

(a)

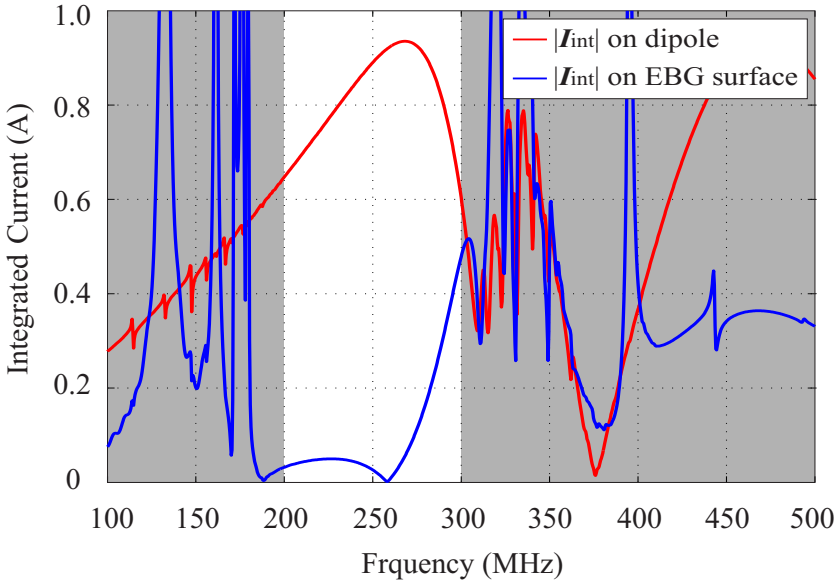

(b)

Figure 4.3: Integrated currents flow through the dipole coil (red line) and the surface of the shielding plate (blue line). The current is calculated by integrating the magnetic field along an integration path which encloses the corresponding structure, here the dipole or the surface of the shielding plate. The considered shielding plate — (a) a PEC shield and (b) a HIS shield — are placed underneath the dipole coil with a separation distance of 1 cm.

dipole coil to the HIS shield should be kept as small as possible in order to maximize the effect of the HIS shield. However, it also has to be pointed out that for a small separation distance the induced current on the metal structure of the HIS surface could disturb the field distribution excited by the dipole element. For this reason the lattice of the HIS surface has to be miniaturized, so that the HIS shield behaves as a "meta-surface", instead of several discrete metal structures.

4.1.2 Experimental Validation

In this section the improvement on the B_1 distribution of a dipole coil backed by a HIS surface is validated by near-field measurement.

4.1.2.1 Experimental Setup

The established near-field measurement setup for the experimental validation is shown in Fig. 4.4. The symmetrically fed dipole coil element is printed on Rogers RO4003 substrate (25 cm $\times$ 10 cm) with a thickness of 500 μm. The high-dielectric substrates (Rogers RO3010) enclosing the meanders are used to fine-tune the current distribution on the stripline [87]. The separation between the dipole coil element and the side wall of the phantom container is set to 2 cm. The absolute magnetic field distribution of the dipole coil backed by two types of shielding plates—a copper-clad substrate and a two-dimensional multi-layer HIS structure [101]—are compared. In order to eliminate the impact of the eigenmode current distribution on the shielding plate [71, 105], a relative large copper-plated substrate with respect to the dipole coil is used here. The dimension of the applied HIS shield is similar to the dipole coil due to in-house technological limitations.

For each case (a HIS shield and a copper-clad substrate), a more than 10 dB return loss for the dipole coil is achieved by employing an appropriate matching network. The employed matching network consists of a series and a shunt capacitors. A $\lambda/4$ coaxial balun is utilized to obtain a balanced current distribution on two arms of the dipole coil [106].

Firstly, the HIS surface is placed 2 cm behind the dipole coil, as we did for the initial investigation with the SIBC model in Chapter 2. Similar to the simulation model in Fig. 2.7, we define two evaluation planes inside the phantom, where the absolute magnetic field distributions are measured. The transverse cut has a width of 14 cm (z direction) and a height of 10 cm (x direction), starting from the side wall of the container. The coronal cut in the yz plane, which is located 3 cm inside the phantom, is 25 cm in length and 14 cm in width, as shown in Fig. 4.4.

Additionally, the effect of different separation distance (d = 5 mm, 10 mm, 20 mm) between the dipole coil and the RF shield is investigated [56]. The corresponding magnetic field distribution is measured along a transverse path which locates in the transverse cut and 4 cm away from the dipole coil.

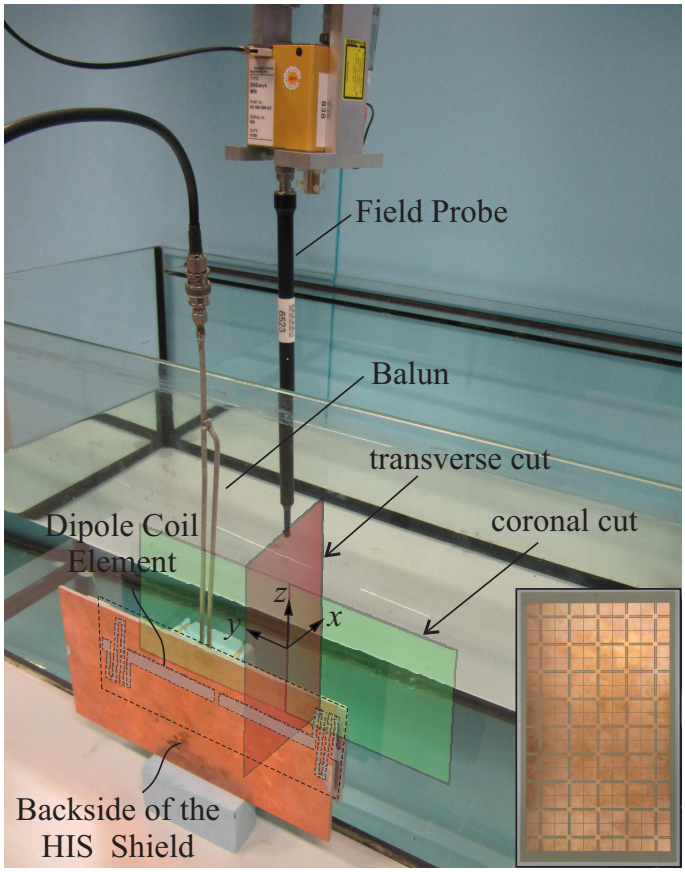

Figure 4.4: Experimental setup for near-field measurement with a liquid based phantom which emulates the human body around 297 MHz. The utilized HIS shield on top view is displayed in the bottom right corner. The separation between the dipole coil element and the side wall of the phantom container is set to 2 cm. The dipole coil is fed through a $\lambda/4$ coaxial balun in order to obtain a balanced current distribution on the two arms of the dipole coil.

4.1.2.2 Experimental Results

The measured field distributions with the two aforementioned shielding plates on the pre-defined evaluation planes are shown in Fig. 4.5. The corresponding magnetic field is normalized to the square root of peak SAR inside the phantom and plotted in dB. Knowing that the electric field decays with deeper penetration into the phantom and the dimension of the phantom is large enough to eliminate the reflection effect of electric field at the open end of the phantom, we measure the absolute electric field close to the side wall of the phantom container and use it for the SAR_{max} calculation.

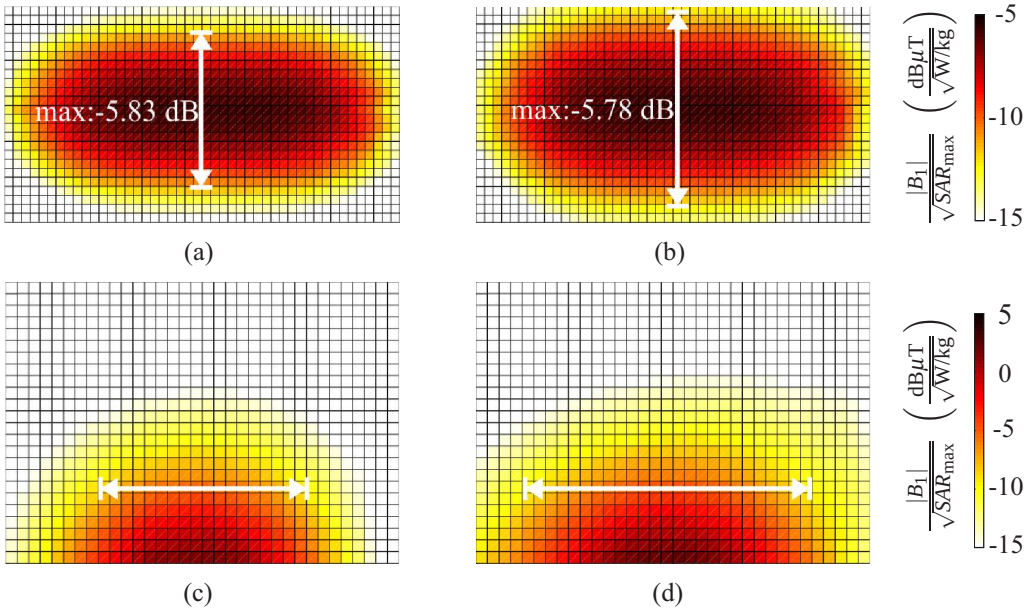

Figure 4.5: Measured absolute B_1 field distributions at 297 MHz on (a, b) the coronal cut and the (c, d) transverse cut for different shielding plate: (a, c) a copper-plated substrate and (b, d) a two-dimensional HIS structure.

Compared to the field distribution with the SIBC model (cf. Fig. 2.9), an excellent agreement of the field distribution between simulation and measurement is observed. The normalized magnetic field on the coronal cut produced by the dipole element backed with an EBG structure reveals an improvement in terms of homogeneity due to the broader field distribution and absolute penetration in comparison to a copper-plated substrate [cf. Fig 4.5(a, b)]. The transverse cuts in Fig. 4.5(c) and (d) also indicate that a broader magnetic field distribution in transversal direction can be achieved by using a shielding plate with large surface impedances, e.g. an EBG structure. Additionally, the absolute penetration of the magnetic field inside the phantom is slightly improved as well.

The measured magnetic field distributions of the dipole coil backed by a HIS shield and a copper-clad substrate for different separation distances are shown in Fig. 4.6. In general, the HIS shield provides an improved B_1 distribution in terms of penetration depth and homogeneity which is indicated by a broader field contour [cf. Fig. 4.6(a)]. As the separation distance increases, an increase in the B_1 field of the dipole coil with a copper-clad

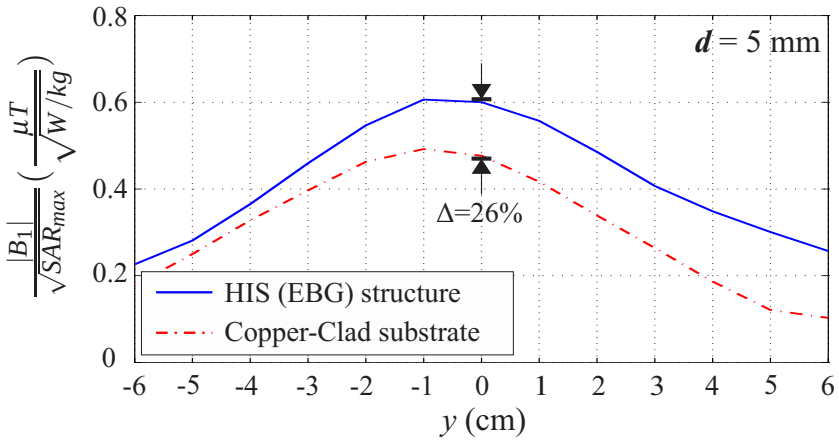

(a)

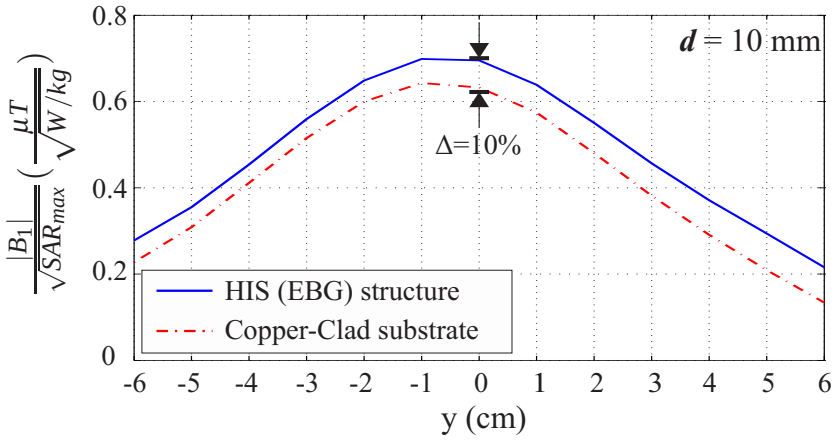

(b)

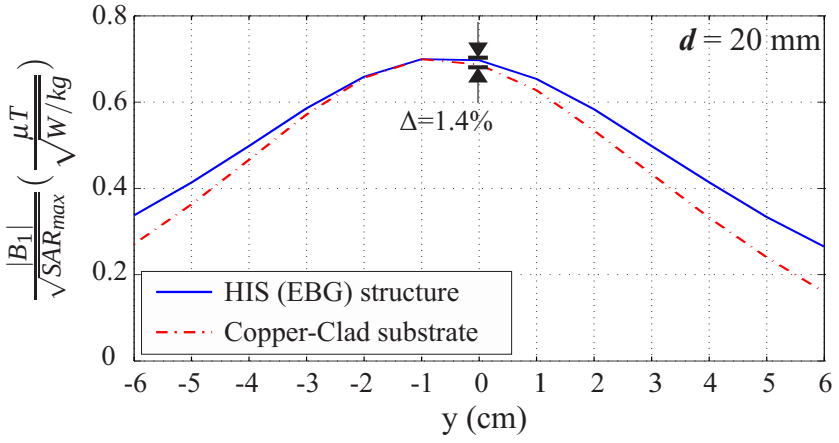

(c)

Figure 4.6: Measured magnetic field distribution of the dipole coil backed by an EBG structure and a copper-clad substrate for a separation distance of (a) 5 mm, (b) 10 mm and (c) 20 mm at 297 MHz. The corresponding field distribution is normalized to square root of the peak SAR.

substrate can be observed since the effect of the induced current on the copper surface is reduced. For a HIS shield, the B_1 distribution is quite constant for different separation distances [cf. Fig. 4.6(b) and Fig. 4.6(c)] due to the fact that the surface current on the HIS shield is efficiently suppressed. The slight decrease of the B_1 distribution for an extremely small separation distance ($d = 5$ mm) is probably caused by the residual surface current. As a result, the difference of utilizing a HIS shield and an ordinary metallic plate tends to be weakened as the separation distance increases. The slight asymmetry in the field distribution with respect to the center of the transverse path is due to the imperfect alignment of the experimental setup.

4.1.3 Summary of Dipole Coil backed by HIS Shield

In this section the field characteristics of a dipole coil backed by a real HIS shield has been evaluated based on full-wave simulation and experiments. Compared to a conventional metal plate (or a PEC boundary condition), a HIS shield behind a dipole coil provides an improved B_1 distribution inside the phantom, in terms of homogeneity and absolute penetration depth. The observed field characteristics reveals a good agreement in comparison to the ones obtained by the SIBC model in Chapter 2. Furthermore, the approach of improving the B_1 distribution of a dipole coil by using a HIS shield has been verified by the near-field measurement.

4.2 Eight-Channel Dipole Coil with HIS Shield

In the previous section we have demonstrated that the B_1 field of a dipole element could be improved by using an RF shield with high surface impedance. In this section an eight-channel dipole coil backed by a HIS shield is presented. The field distribution of the proposed coil will be evaluated based on full-wave simulation and experimental results.

4.2.1 Investigation based on Numerical Simulation

First, the magnetic field distribution of the proposed dipole coil backed by HIS shield is investigated based on full-wave simulation.

4.2.1.1 Simulation Setup

The simulation setup of the eight-channel dipole coil backed by a HIS shield is depicted in Fig. 4.7. The eight dipole elements are equally distributed around a homogeneous cylindrical phantom ($\epsilon_r = 45.3$, $\sigma = 0.87$ S/m, $\rho = 1000$ kg/m^3), which has a diameter of 20 cm. The symmetrically fed dipole element is printed on a 0.25 mm-thick Roger substrate (RO4003), and is terminated by two meanders. The geometry detail of the meander remains unchanged in comparison to the one presented in [70], but with an increased total length [cf. Fig. 4.7(d)]. The width of the meander line and the gap between two of them are both set to 2 mm. In this case the current distribution on the dipole is very similar to the one of the dipole with high-dielectric loadings (cf. Sec. 2.2). In principe, the increased meander length and the high-dielectric loading have the same functionality and both fine-tune the current distribution on the dipole. For fabrication convenience of the curved structure we prefer the longer meanders rather than the high-dielectric loadings.

The dipole elements are surrounded by a tube-like HIS shield based on the compact uniplanar design (cf. Sec. 3.3), which has a diameter of 25 cm. It has been found that the thickness of the lower substrate has a prominent impact on the resonance frequency of the HIS structure compared to its relative permittivity. Here a 5 mm-thick acrylic glass tube is used as the lower substrate, instead of the Arlon substrate (AD1000) in previous design. According to the new stack-up the a minor modification of geometry parameters of the HIS lattice is necessary to achieve a 297 MHz resonance frequency.

Here the simulation model is established in a cylindrical coordinate system in OpenEMS[1], since the extreme thin substrate of the HIS structure (between top and floating metal layers) challenges the mesh strategy of a FDTD simulator in cartesian coordinate system, whereas a cylindrical coordinate system naturally fits the tube-like HIS shield perfectly. The HIS shield consists of 32 and 12 unit cells in azimuth and longitudinal direction,

[1] OpenEMS is a free and open electromagnetic field solver using the FDTD method. Matlab or Octave are used as an easy and flexible scripting interface [107]. It features fully 3-D cartesian and cylindrical coordinates based graded meshes.

respectively. With this arrangement the radial separation between the dipole and the top surface of the HIS shield is roughly 10 mm, which is similar to the distance from the dipole element to the outside of the cylindrical phantom.

4.2.1.2 Simulation Result

The simulated transverse $|{B_1}^+|$ distribution of the eight-channel dipole coil backed by a HIS shield is displayed in Fig. 4.8. For comparison purpose the field distribution of the dipole coil in the case of a PEC and a PMC shield are considered as well. The corresponding field distribution is normalized to the square root of the overall accepted power by the coil and plotted in dB.

For the dipole coil backed by a PEC shield a clear separation between the excited magnetic field by the individual coil element in the regions close to the surface of the phantom can be observed. In other words, the field strength in the area between the adjacent coil elements is considerably lower in comparison to the dominating fields near the coil elements [cf. Fig. 4.8(a)]. With an increased penetration depth into the phantom the absolute ${B_1}^+$ field reveals a rapid decrease due to the lossy phantom. However, in the central region of the phantom a stronger field distribution, namely "central brightening", is observed due to the constructive summation of the magnetic field from opposite coil elements. This "central brightening" effect is more obvious for UHF MRI, since the electromagnetic wavelength is compressed due to the higher Larmor frequencies. It is worth mentioning that the null of the field distribution in the center of the phantom is attributed to the numerical singularity, since the transverse magnetic field component can not be defined in a single point.

If the dipole coil is surrounded by a PMC shield, the $|{B_1}^+|$ distribution is significantly improved, both in terms of field homogeneity and penetration depth. As explained previously, the dipole backed by a PMC shield exhibits a broader transverse magnetic field distribution due to the fact that the normal magnetic field component is supported at the PMC boundary. As a result, the $|{B_1}^+|$ distribution in the area between the adjacent coil elements is significantly enhanced [cf. Fig. 4.8(c)], showing a more homogeneous field distribution compared to case with a PEC shield. Additionally, the dipole coil surrounded by a PMC shield also reveals a stronger field penetration inside the phantom, indicated by an increased field strength in the central area of the phantom, i.e. stronger "central brightening" effect.

In general, the HIS shield behaves in a similar manner as the ideal PMC shield. Compared to the case with a PEC shield, the dipole coil surrounded by a HIS shield exhibits an improved $|{B_1}^+|$ distribution in terms of field homogeneity and penetration depth. The area between the adjacent coil elements is filled by stronger magnetic fields. The field penetration depth inside the phantom is increased as well, since the induced out-of-phase current on the HIS shield is suppressed by its large surface impedance. However, due to the small current induced on the metallic structure of the HIS shield, the improvement on field distribution is less significant compared to the case with a PMC shield.

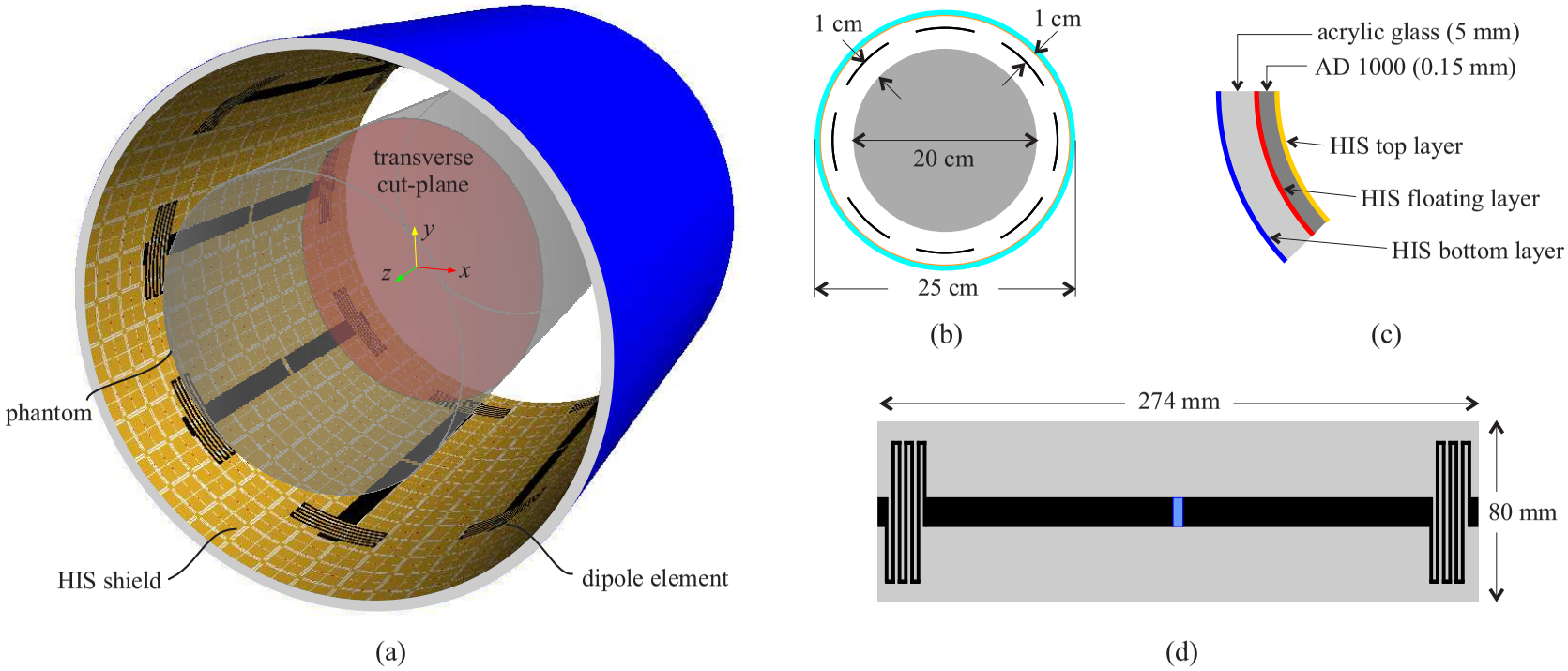

Figure 4.7: The simulation setup of the eight-channel dipole coil backed by a HIS shield in (a) the perspective view and (b) the top view. The eight dipole elements are equally distributed around a homogeneous cylindrical phantom, which has a diameter of 20 cm. The radial separation between the dipole and the HIS shield is roughly 10 mm. (c) The stack-up of the HIS shield: the top and floating layers of the HIS shield are printed on a 0.15 mm-thick Arlon substrate (AD1000), and the bottom layer of the HIS shield lies on the outer surface of an acrylic glass tube with a thickness of 5 mm. (d) The symmetrically fed dipole element is printed on a 0.25 mm-thick Roger substrate (RO4003), and is terminated by two meanders.

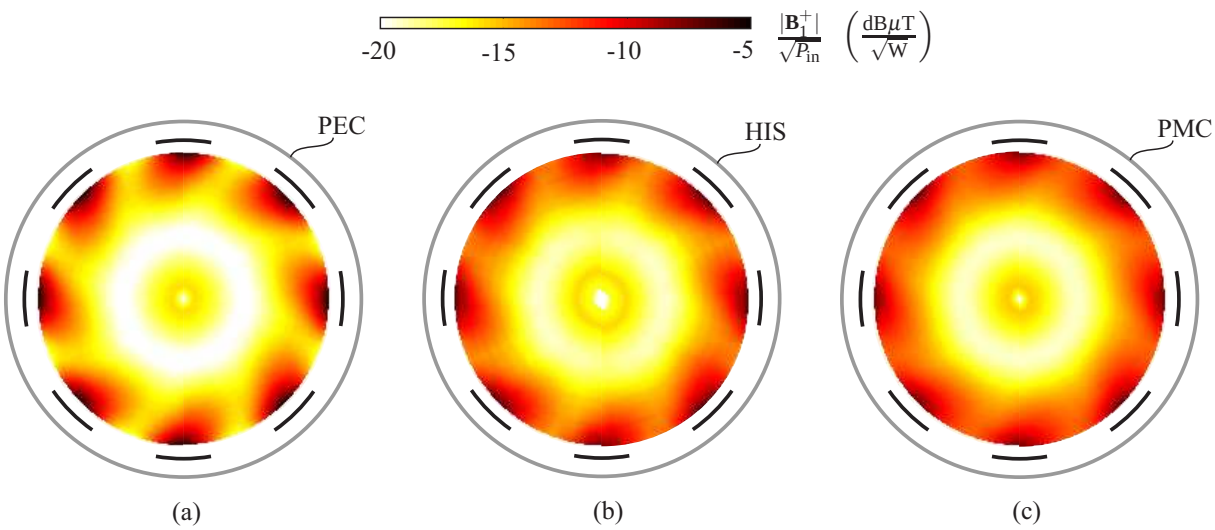

Figure 4.8: The simulated transverse $|B_1{}^+|$ distribution of the eight-channel dipole coil surrounded by (a) PEC, (b) HIS, and (c) PMC shield at 297 MHz. The corresponding field distribution is normalized to the square root of the overall accepted power by the coil and plotted in dB.

4.2.2 Investigation based on Experimental Result

Now the magnetic field distribution of the proposed dipole coil backed by HIS shield will be investigated based on near-field measurement.

4.2.2.1 Configuration of the Eight-Channel Dipole Coil with HIS Shield

Basically, the proposed eight-channel dipole coil backed by a HIS shield consists of two coaxial acrylic glass tubes: the dipole elements and the HIS shield are allocated on the inner and outer tube, respectively [cf. Fig. 4.9(a, c)].

The dipole coil elements are printed on Roger substrates (RO4003) with a thickness of 0.25 mm and stuck on the inner surface of the tube with a smaller diameter ($d_\mathrm{i} = 22.2$ cm). The dipole element is fed by two vertical conducting vias which go through the tube wall and connect the matching network. The corresponding matching network is printed on a piece of RO4350 material and placed on the outer surface of the tube. As shown in Fig. 4.9(f), the employed matching network consists of a shunt capacitance with the value of 3.3 pF and a series inductance which is roughly 75 nH, along with a coaxial cable used as 180° delay line. This 180° delay line forces the current at the feeding points of the two arms of the dipole to be equal in magnitude and opposite in phase, hence, eliminates the unbalanced current in the feeding cable [106].

The outer tube has an inner diameter of 24 cm. The top and floating layers of the HIS shield are printed on a 0.15 mm-thick Arlon substrate (AD1000) and tightly glued on the inner surface of the tube. The outer surface of the tube is wrapped up by a metal sheet,

which serves as the bottom layer of the HIS shield [cf. Fig. 4.9(e)]. The fabricated HIS shield has 32 and 12 unit cells in azimuth and longitudinal direction, respectively. Due to the technology limitation the upper layer of the HIS shield was fabricated in two pieces, each consisting of 16 unit cells in azimuth direction. This operation results in two tiny slits on the HIS shield and creates discontinuity and inhomogeneity on the HIS shield. We arrange the two slits in the position exactly in the middle of two dipole elements in order to minimize the impact on the coil performance. For stability consideration the inner and outer tubes are fixed by four screws on each end of the tube. The thickness of the inner and outer acrylic glass tube is 4 mm and 5 mm, respectively. Eventually, the radial separation from the dipole to the HIS shield, and from the dipole to the phantom are both roughly 10 mm.

Additionally, an eight-channel dipole coil backed by a simple metal shield is built and compared to the one with a HIS shield [cf. Fig. 4.9(b, d)]. A similar topology is utilized for the dipole coil with a metallic shield. The dipole element is printed on a 0.25 mm-thick RO4003 substrate and attached on the inner surface of the tube with a smaller diameter ($d_\mathrm{i} = 23$ cm), but with a different matching network, where the shunt capacitance is 1.2 pF and the series inductance is roughly 110 nH. The outer surface of the tube with a larger diameter ($d_\mathrm{i} = 25$ cm) is wrapped up by a copper foil and serves as the metallic shield.

4.2.2.2 Experimental Setup

As depicted in Fig. 4.10(c), the dipole coil is loaded by a cylindrical phantom container with a diameter of 20 cm, which is filled with tissue-mimicking liquid ($\epsilon_\mathrm{r} \approx 45$, $\sigma \approx 0.8$ S/m). The source power from the signal generator is firstly split into four equal parts with a 90° phase-shift using a Butler matrix. Each part is followed by a subsequent power amplifier and a modified *Wilkinson* power divider, which provides an additional 45° phase-shift between the two outputs. In total eight equal parts of power with a relative phase lag of 45° are generated and applied to the dipole elements. The schematic diagram and the realized feeding network for the eight-channel dipole coil is depicted in Fig. 4.10(a) and in Fig. 4.10(b), respectively. In our case the power assigned to each channel is roughly 2 W, and varies a little bit between elements due to the slightly different matching behaviors. Keeping the power per channel in a relative low level is under the consideration that the resisters utilized in the *Wilkinson* power divider are not high power components.

The magnetic field distribution in the transverse cut of the phantom [cf. Fig. 4.10(c)] is measured for the dipole coil backed by a HIS shield and a metallic shield. Due to the technological limitation of the field probe, instead of $|B_1^+|$, the absolute magnetic field distribution $|B_1|$ is measured.

4.2.2.3 Experimental Result

The measured absolute magnetic field distributions of the considered eight-channel dipole coil surrounded by a metallic shield and a HIS shield are displayed in Fig. 4.11. The

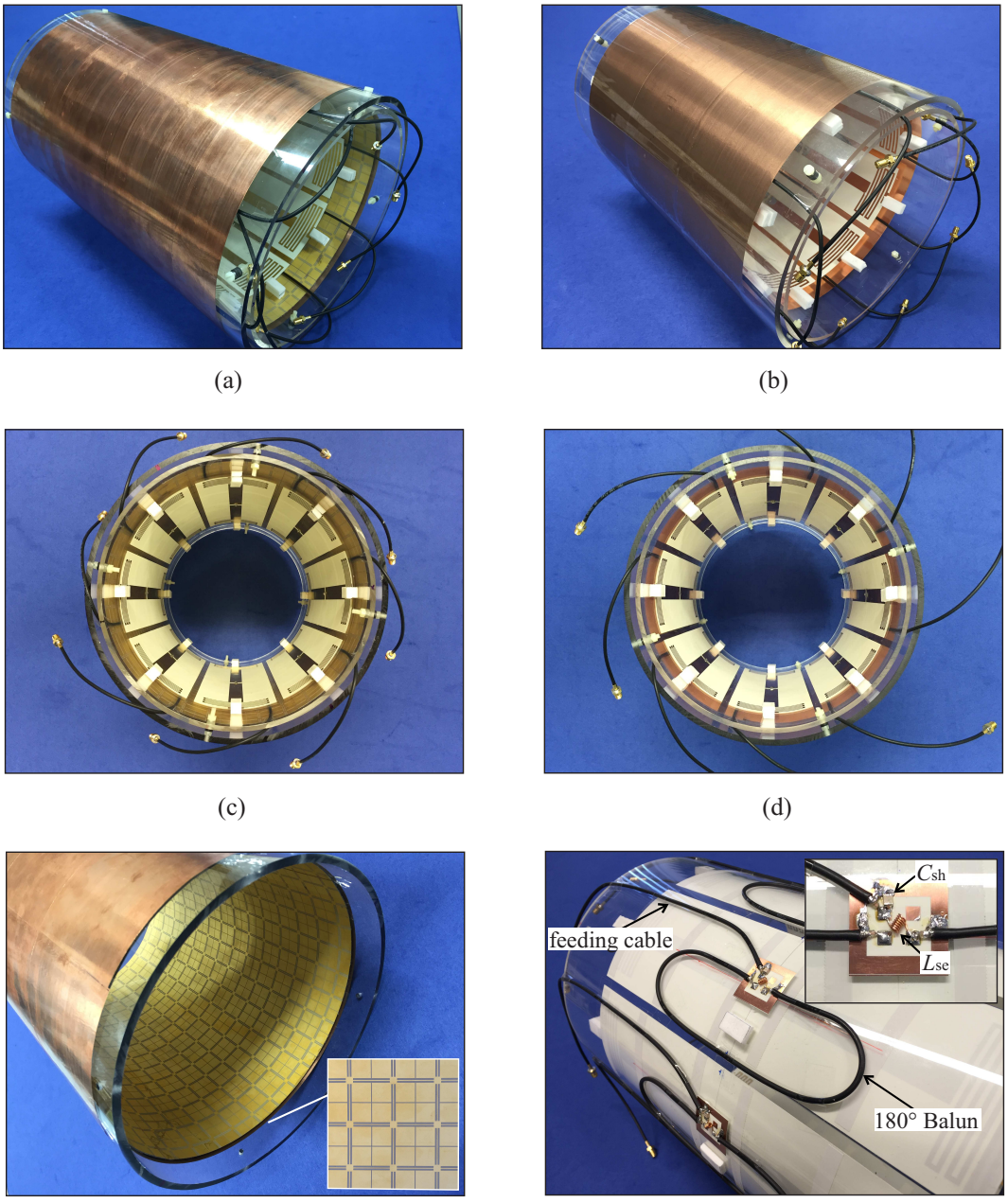

Figure 4.9: Fabricated prototypes of the eight-channel dipole coil surrounded by (a, c) a HIS shield and (b, d) a metallic shield in perspective and top view. (e) The HIS shield along with a zoomed view of its lattice structure in absence of the dipole coil elements. (f) The matching network of the dipole element consisting of a shunt capacitance and a series inductance, along with a coaxial cable used as 180° delay line.

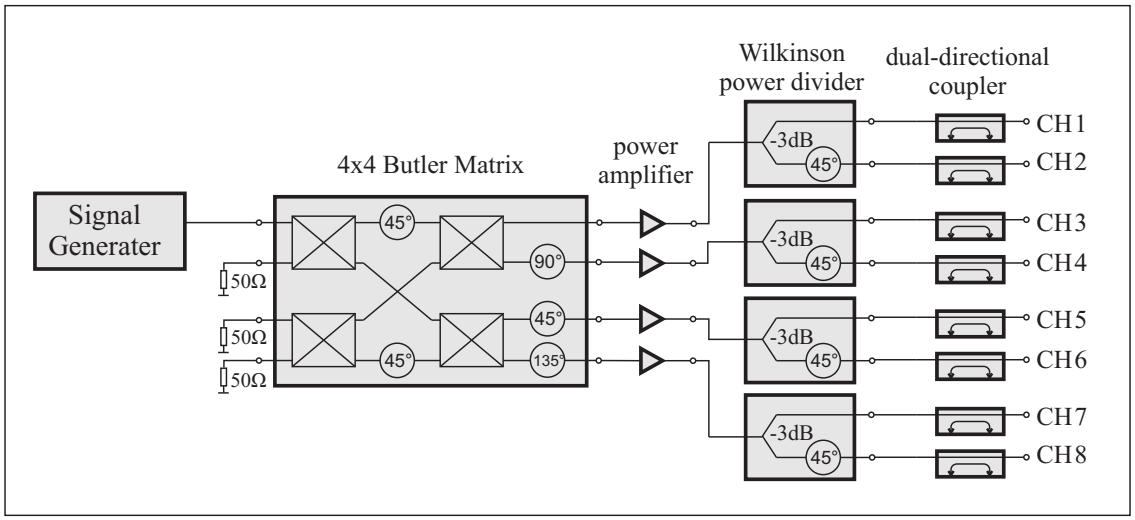

(a)

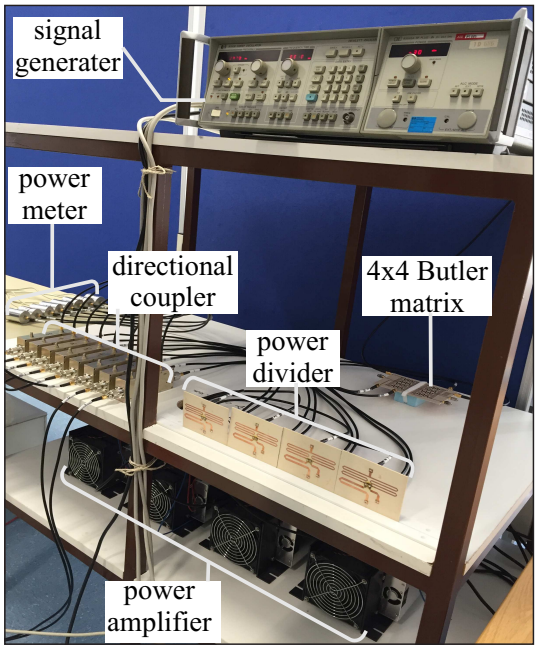

(b)

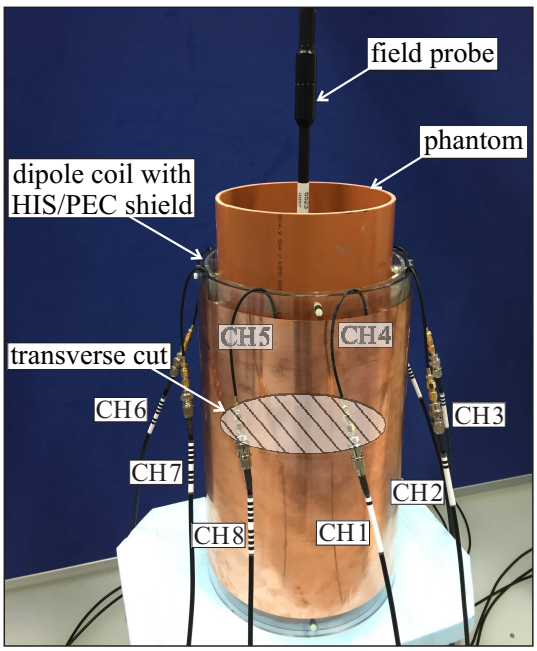

(c)

Figure 4.10: (a) The schematic diagram and (b) the realized feeding network for the eight-channel dipole coil. The source power from the signal generator is firstly split into four equal parts with a 90° phase-shift using a Butler matrix. Each part is followed by a subsequent power amplifier and a modified *Wilkinson* power divider, which provides an additional 45° phase-shift between the two outputs. In total eight equal parts of power with a relative phase lag of 45° are generated and applied to the dipole elements. (c) For field measurement the dipole coil is loaded by a cylindrical phantom container with a diameter of 20 cm, which is filled with tissue-simulating liquid ($\epsilon_r \approx 45$, $\sigma \approx 0.8$ S/m).

corresponding field distribution is acquired at 297 MHz and normalized to the square root of the overall accepted power by the coil. In general, the dipole coil with HIS shield provides a stronger and more homogeneous magnetic field distribution compared to the case where the metallic shield is utilized. Due to the fact that the out-of-phase surface current on the HIS shield is sufficiently suppressed, the excited B_1 field is significantly enhanced. As a result, the penetration depth of the magnetic field inside the phantom is increased by using the HIS shield, indicated by the more obvious "central-brightening" (cf. Fig. 4.11). Additionally, the magnetic field in the regions between the neighboring coil elements which are surrounded by a HIS shield is considerably stronger compared to the case of a metallic shield. Therefore, the overall B_1 field is distributed inside the phantom in a more homogeneous manner.

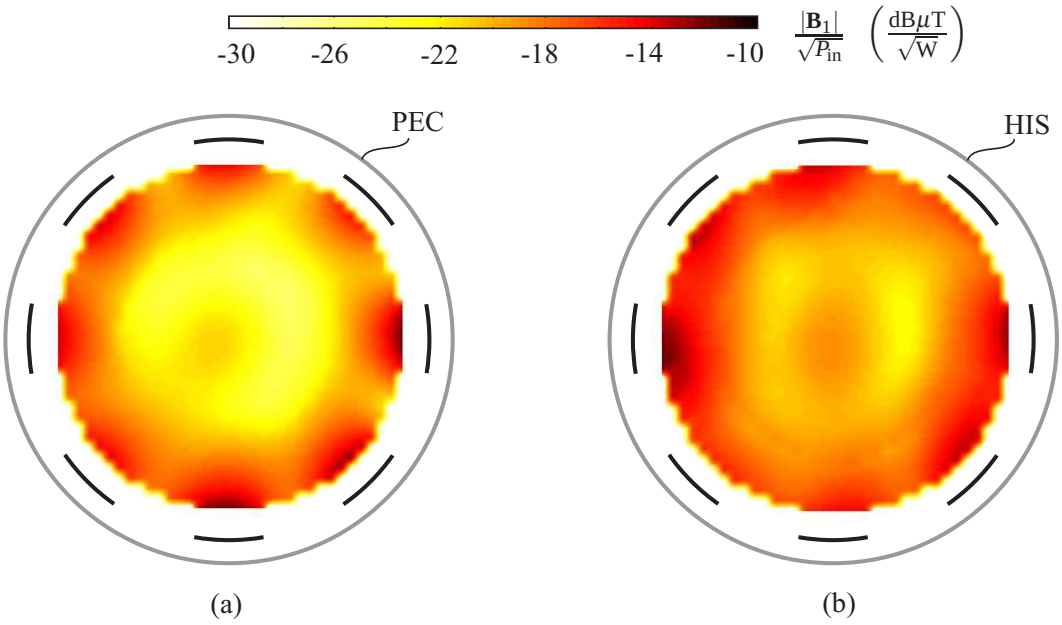

Figure 4.11: The measured transverse $|B_1|$ distribution of the eight-channel dipole coil surrounded by (a) a metallic shield, and (b) a HIS shield at 297 MHz. The corresponding field distribution is normalized to the square root of the overall accepted power by the coil and plotted in dB.

The slight asymmetry in field patterns for both cases – the HIS and the metallic shield – is mainly caused by the unequal excitation of the coil elements due to the imperfect power splitting by the Bulter matrix and the power dividers. Besides, the coil misalignment and slightly different matching levels between coil elements have also effects on the asymmetry. As mentioned previously, the upper layer of the HIS shield was fabricated in two pieces due to the technology limitation, which created two tiny slits was the HIS shield. The resulting discontinuity on the HIS shield has impact on the field pattern. Particularly, the B_1 field in the vicinity of the slit is weaker in comparison with the regular case where the HIS shield is continuous and homogeneous. For the field distribution obtained with a HIS shield, this additional effect could also aggravate the asymmetry of the field pattern.

Being another important parameter, the coupling between the coil elements under different

shielding scenarios (HIS and metallic shield) are investigated. The measured scattering parameters of the dipole coil surrounded by a HIS shield and a conventional metallic shield are plotted in Fig. 4.12(a) and Fig. 4.12(b), respectively. The corresponding scattering parameters are measured with a two-port vector network analyzer (VNA) with the remaining coil elements being terminated by 50 Ω loads. Around the operation frequency, here 297 MHz, the coupling between the coil elements which are surrounded by a HIS shield is generally stronger compared to the case where a metallic shield is used, especially between the nonadjacent elements (e.g. $|S_{31}|$, $|S_{41}|$, $|S_{51}|$). The increased coupling level is caused by the stronger and broader magnetic field excited by the dipole coil in the transverse cut-plane.

Another interesting phenomenon is that the bandwidth for 10 dB return loss of the dipole coil with a HIS shield is considerably larger compared to the one of the dipole coil with a metallic shield. This could be explained in such a way that for the metallic shield the imaged dipole with out-of-phase current reduces the radiation resistance, whereas for the HIS shield the imaged dipole with in-phase current enhances the radiation resistance.

4.2.3 Summary of Eight-Channel Dipole Coil with HIS Shield

In this section the approach to improve the B_1 distribution of an RF coil by using a HIS shield has been evaluated by a multi-channel dipole coil. According to the full-wave simulation and experimental results, it has been demonstrated that the dipole coil surrounded by a HIS shield provides a stronger and more homogeneous magnetic field distribution compared to the case where the metallic shield is utilized. However, the coupling between the coil elements which are surrounded by a HIS shield is also stronger compared to the case where a metallic shield is used, especially between the nonadjacent elements.

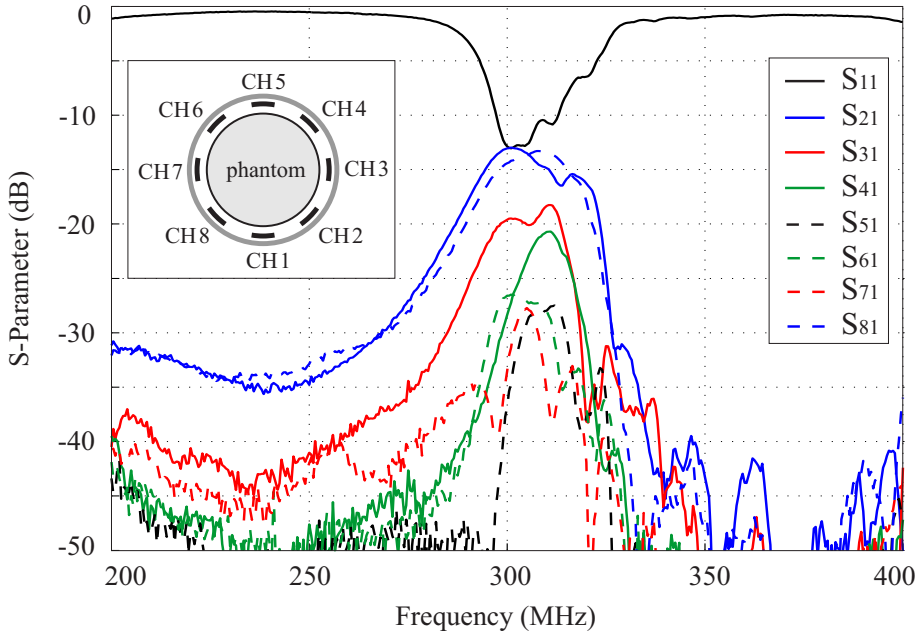

(a)

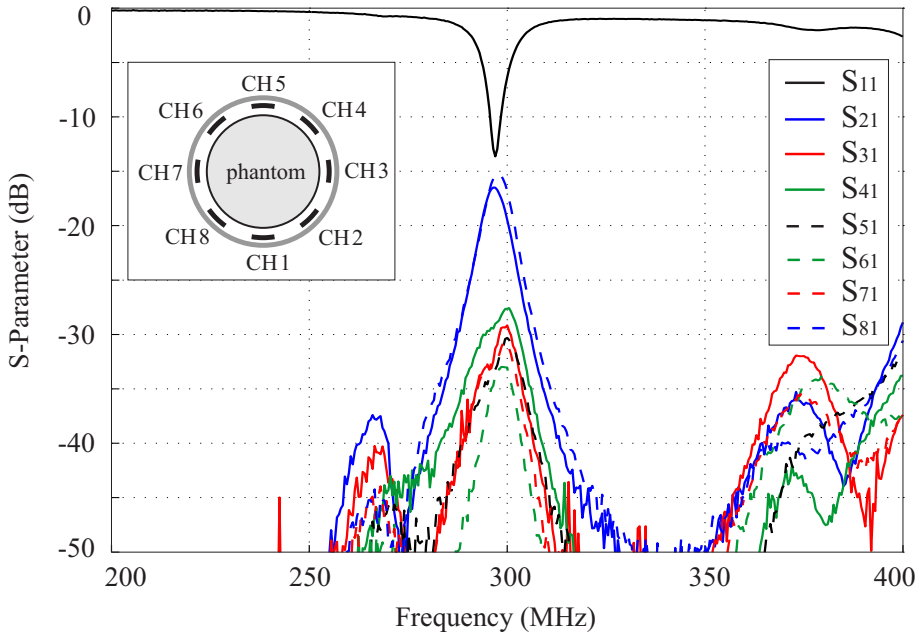

(b)

Figure 4.12: Measured scattering parameters of the dipole coil surrounded by (a) a HIS shield and (b) a conventional metallic shield. The corresponding scattering parameters are measured with a two-port vector network analyzer (VNA) with the remaining coil elements being terminated by 50 Ω loads.

4.3 Loop Coil backed by HIS Shield

Based on the investigation in Chapter 2 the surface loop coil backed by an RF shield with high surface impedance exhibits an improved SNR and B_1 efficiency. In this section we apply a real HIS as the RF shield of a surface loop, and evaluate the impact of this HIS shield on the coil performance. The investigation will be carried out based on full-wave simulation and experimental results.

4.3.1 Numerical FEM-based Investigations

In this section we investigate the improvement on the SNR and B_1 efficiency of a surface loop coil by using a HIS as the RF shield based on numerical simulations.

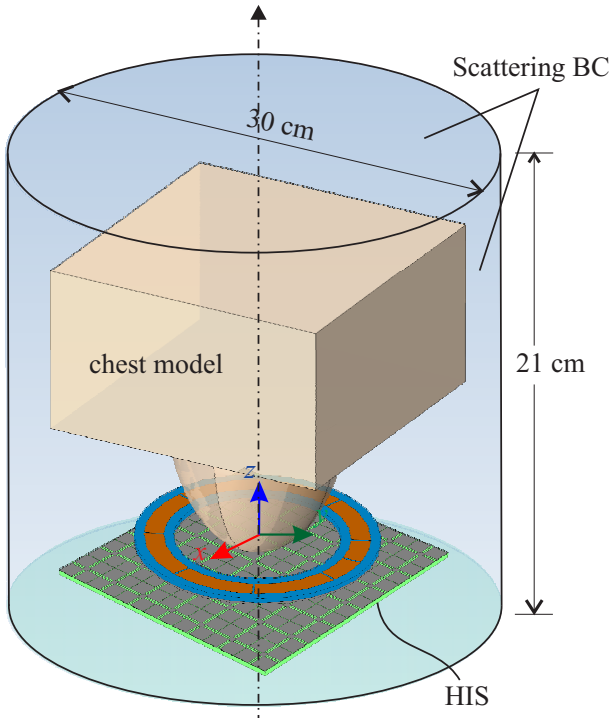

Figure 4.13: The simualtion setup of the series loop loaded by a homogeneous chest/breast model for the investigation on the effect of different shielding scenarios. For the PEC and PMC cases, the bottom boundary of the computational domain in -z direction serves as the RF shields. For the case of a HIS, a 7×7 EBG array is placed beneath the loop structure with the bottom boundary of the computational domain setting to scattering boundary condition.

4.3.1.1 Simulation Setup

The simulation setup for the investigation on the effect of different RF shields based on the series resonant loop structure is depicted in Fig. 4.13. Compare to the simulation setup in

Fig. 2.17, the cylindrical phantom is replaced by a simple chest/breast model. The simple chest/breast model is a combination of two parts: a half ellipsoid with the semi-axis a, b and c set to 45 mm, 45 mm and 80 mm, respectively, and a block with the dimension of 150 mm×150 mm×80 mm. The vertex of the ellipsoid is nested 5 mm inside the surface coil. For experimental convenience the material parameters of the chest/breast model (e.g. permittivity and electrical conductivity) are set to $\epsilon_r = 58.2$ and $\sigma = 0.92$ S/m, which are similar to the parameters of the available phantom utilized for experimental validation in our laboratory. For the case of a HIS, a 7×7 HIS array based on the design presented in Chapter 3 is placed underneath the loop structure with the bottom boundary of the computational domain placed below the HIS and set to a scattering boundary condition. Additionally to the HIS case, a perfect electric conductor (PEC) and a perfect magnetic conductor (PMC) shield are also considered for a comparison purpose. In this two cases the bottom boundary of the computational domain is assigned to a PEC or a PMC boundary condition, and serves as the RF shield.

The series loop has been tuned to achieve a resonance at 297 MHz (Larmor frequency for 7 T MRI) for the PEC, HIS and PMC shields separately with a separation distance of 10 mm to the top surface of the loop. The corresponding geometry parameters are given in table 4.1. From the imaginary part of input impedance (cf. Fig. 4.14) resonances at 297 MHz for different shielding scenarios are verified. It can be noticed that the input impedance for the PEC and PMC shields exhibit a monotone behavior, while the loop structure backed by a HIS shield reveals a fluctuation of the input impedance due to the frequency dependent surface impedance of the HIS shield. Additionally, the real part of the input impedance for HIS and PMC shields is comparably larger than the case of a PEC shield.

Table 4.1: Parameters of the Series Loop with PEC, HIS and PMC Shields

Type of Shield	Nr. of cells	R [mm]	W_l [mm]	W_s [mm]	θ_{unit} [deg]	θ_{bot} [deg]	θ_{gap} [deg]
PEC	8	53	10	20	45	43.2	1.08
HIS	8	53	10	20	45	24.8	2.16
PMC	8	53	10	20	45	20	2.16

4.3.1.2 Influence on B_1 Efficiency and *SNR*

The B_1 efficiency and the *SNR* of a series resonant loop in the transversal cut-plane of the homogeneous chest model are shown in Fig. 4.15 for different shielding scenarios (PEC, HIS and PMC). The HIS and PMC shields behave in a similar manner and provide an increased B_1 efficiency and *SNR*, especially for the ellipsoid region, where is also the most interesting areas for surface coils. Specifically, the B_1 efficiency and *SNR* distribution for the PEC case exhibit a girdle band with greater magnitude above the loop structure and a depression near the vertex of the ellipsoid, whereas for the HIS and PMC case a superior distribution which covers the lower part of the ellipsoid is observed, both in terms of strength and

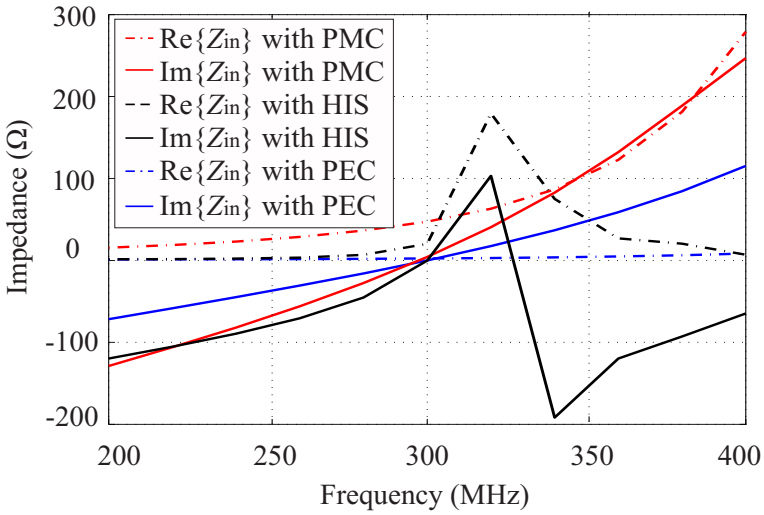

Figure 4.14: The port input impedance of surface coil model based on the series resonant loop structure for different shielding scenarios (PEC, HIS and PMC).

homogeneity. The arise of this variation on B_1 efficiency and *SNR* distribution is due to the stronger normal magnetic field near the HIS and PMC shield, whereas a suppressed normal component by the PEC shield (cf. Fig. 2.20). The improvement is more prominent for a small penetration depth, and fades away as going deeper inside the phantom. Since the fields decay rapidly as the penetration depth increases, the plots in Fig. 4.15 reveal scarcely any difference in the block region. Nevertheless, the proposed approach of utilizing a HIS (PMC) shield behind a surface coil shows promising results concerning the B_1 efficiency and the *SNR*.

4.3.2 Experimental Validation

In this section the improvement on the B_1 efficiency and *SNR* of a loop coil by utilizing a HIS shield is validated by the experiential results.

4.3.2.1 Experimental Setup

For the experimental validation two loop structures with the corresponding geometry for PEC and HIS shielding scenarios from Table 4.1 are built [cf. Fig. 4.16(a, b)]. The metal structures of the series resonant loop are printed on a 0.64 mm-thick Rogers RO3010 substrate and pasted on a structural foam ring with a thickness of 5 mm for mechanical stability. The matching network of the loop structure and the corresponding equivalent circuit are displayed in Fig. 4.16(c, d). The matching circuit consists of a shunt capacitor and a series inductor along with a coaxial cable used as 180° delay line. This 180° delay line forces the current at the feeding points of the loop to be equal in magnitude and opposite in phase, hence, eliminates the unbalanced current in the feeding cable [106]. With appropriately chosen capacitor and inductor values (PEC: $C_{\mathrm{sh}} = 47$ pF and $L_{\mathrm{se}} = 3.1$ nH,

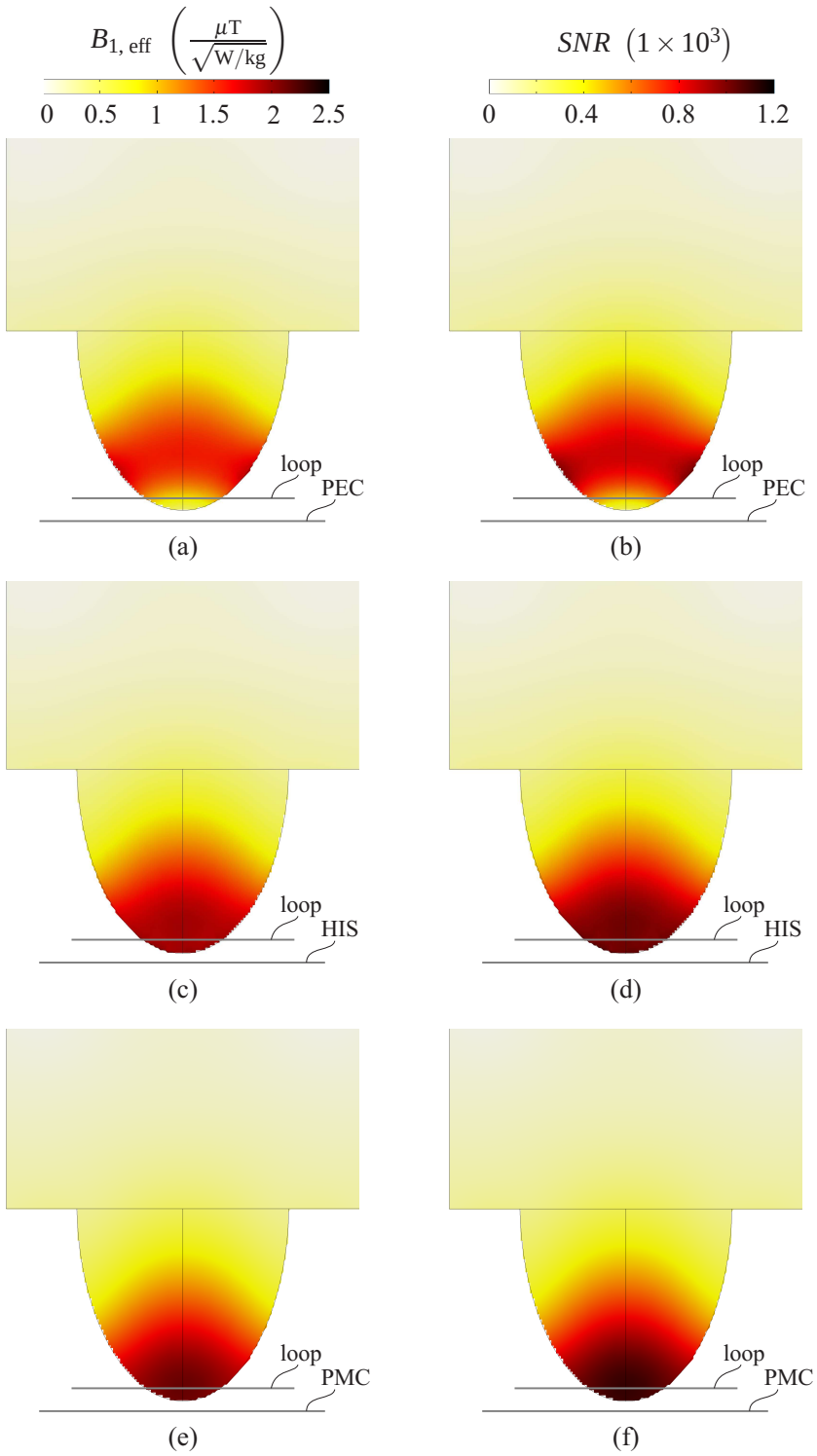

Figure 4.15: The B_1 efficiency (left column) and SNR (right column) on the yz cut of the simple chest model (cf. Fig. 4.13) for the cases that the series loop is shielded by (a, b) PEC, (c, d) HIS and (e, f) PMC shield at 297 MHz.

HIS: $C_{\mathrm{sh}} = 33$ pF and $L_{\mathrm{se}} = 6.2$ nH), a more than 10 dB return loss for each shielding scenario is achieved.

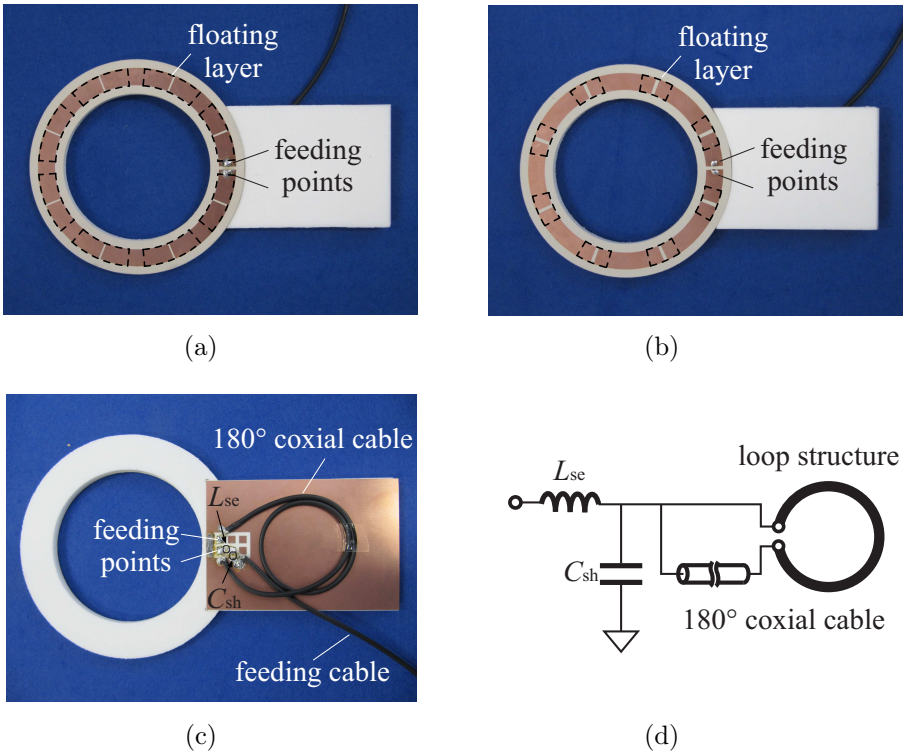

Figure 4.16: The prototypes of the proposed series resonant loop for (a) a PEC shield and (b) a HIS shield, together with (c) the additional board with matching network on the backside of the loop structure and (d) the corresponding equivalent circuit.

The experimental setup for the near-field measurement is shown in Fig. 5.9. The phantom container has a similar shape as the one used for simulation in Sec. 4.3.1 and is filled with tissue simulating liquid ($\epsilon_{\mathrm{r}} \approx 58$, $\sigma \approx 0.9$ S/m). The vertex of the ellipsoid part of the phantom container is nested roughly 5 mm below the top surface of the loop structure. The loop structure is placed 10 mm above the shielding plate, which is in our case a HIS structure and a copper-clad substrate for the PEC case. The sampling plane for the field measurement is defined vertical to the top surface of the loop coil and crossing its center axis (cf. Fig. 5.9).

4.3.2.2 Experimental Results

With the experimental setup depicted in Fig. 4.17 the absolute magnetic and electric field on the sampling plane are measured for the different shielding scenarios. Generally, the SAR and the dissipated power P_{L} inside a volume filled with tissue can be calculated based on the following equations:

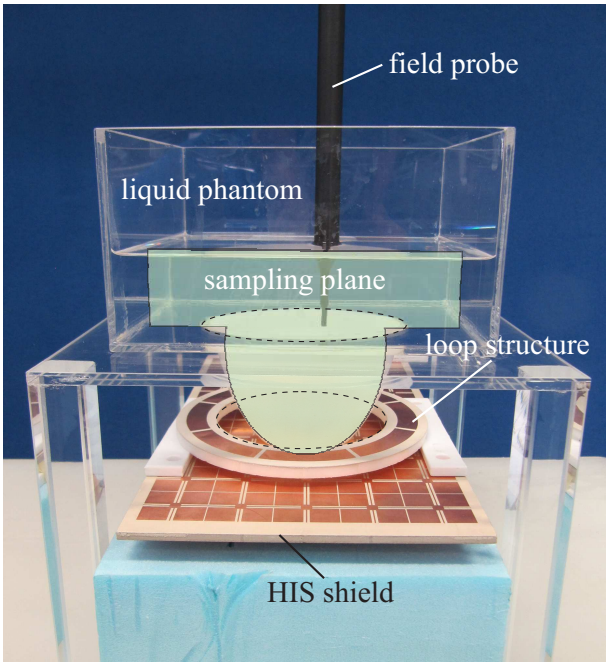

Figure 4.17: The experiential setup of near-field measurement for the series resonant loop structure with different shielding scenarios (a copper-clad substrate and a HIS structure).

$$SAR = \frac{\sigma |\mathbf{E}|^2}{2\rho}, \tag{4.3.1}$$

$$P_{\mathrm{L}} = \frac{\sigma}{2} \iiint_V |\mathbf{E}|^2 dV = \frac{\sigma}{2} \operatorname{avg}(|\mathbf{E}|^2)\, V, \tag{4.3.2}$$

where σ and ρ is the electrical conductivity and the mass density of the tissue, respectively. Since σ and ρ are constant for a homogeneous phantom, for experimental convenience we can map the B_1 efficiency defined in (2.3.2.1) to the ratio of the absolute magnetic field and the peak value of measured electric field. The SNR in (2.3.1) can be evaluated through the ratio of the absolute magnetic field and the average of measured electric field:

$$R_1 = \frac{|\mathbf{H}|}{\max(|\mathbf{E}|)} \propto B_{1,\,\mathrm{eff}}, \tag{4.3.3}$$

$$R_2 = \frac{|\mathbf{H}|}{\operatorname{avg}(|\mathbf{E}|)} \propto SNR. \tag{4.3.4}$$

Assuming that the electromagnetic field distribution inside the phantom is rotational symmetric, the field characteristic inside the phantom can be represented by the measured field distribution on a single sagittal sampling plane. The ratios defined in (4.3.3) and (4.3.4)

are plotted in Fig. 4.18 based on the measured magnetic and electric field distribution in the sampling plane. As shown in Fig. 4.18, the surface loop associated with a HIS shield reveals a superior magnetic field distribution for both normalization criterions, especially for the lower part of the ellipsoid phantom. As explained in Section 4.3.1, the normal component of magnetic field is supported at the surface of the HIS shield, whereas suppressed by the copper-clad substrate. As a result, the magnetic field in the vicinity of a HIS shield is considerably stronger in comparison with the case of a copper-clad substrate (cf. Fig. 4.18). The improvement on field distribution by using a HIS is more prominent for the regions near the surface coil, in our case, the ellipsoid part. As the penetration depth further increases, this improvement fades away. Additionally, note that if the field is normalized based on the maximum electric field, the difference on field distribution between HIS and PEC is more distinct than in the case where the field is normalized based on the averaged electric field. Compared to the full-wave simulation of Section 4.3.1, an excellent agreement can be observed between the simulated and measured results.

4.3.3 Summary of Loop Coil backed by HIS Shield

In this section the field characteristics of a surface loop coil backed by a real HIS shield have been evaluated based on full-wave simulation and experiments. Due to the fact that the normal component of magnetic field is enhanced at the surface of a HIS, whereas suppressed by a PEC surface, the B_1 field in vicinity of the HIS shield is enhanced compared to the case with a conventional metal plate (or a PEC boundary condition). Hence, the coil performance can be improved by applying a HIS shield compared to the case with a PEC shield, especially in the regions adjacent to the surface coil. The improvement degrades with larger penetration depth into the phantom. The proposed approach has been validated by the near-field measurement, which shows a good agreement with the full-wave simulations in terms of the field distribution. The investigation with a simple chest/breast model reveals potentials of the HIS RF shield for the ultra-high-field MRI applications, e.g., for breast imaging.

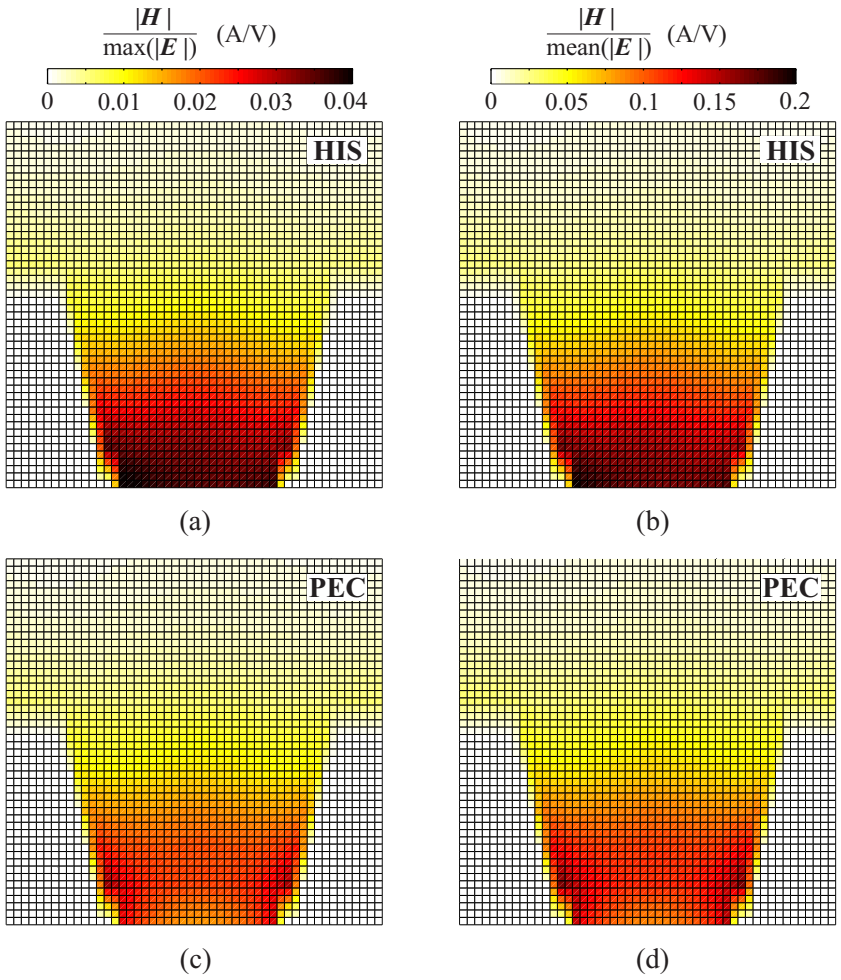

Figure 4.18: Measured absolute magnetic field distribution at 297 MHz on the sampling plane for different shielding scenarios: (a, b) a HIS structure and (c, d) a copper-clad substrate. The corresponding magnetic field is normalized to two bases—(a, c) the maximum and (b, d) the mean value of the measured electric field, which correlates to the B_1 efficiency and the *SNR*, respectively.

4.4 Summary of RF Coils with HIS Shields

The field characteristics of a dipole coil and a surface loop coil backed by a two-dimensional HIS surface have been investigated based on full-wave simulation and experimental results, which show an excellent agreement. For a dipole coil backed by a HIS shield the B_1 distribution inside the phantom is considerably improved, in terms of homogeneity and absolute penetration depth. For a surface loop coil backed by a HIS shield the B_1 efficiency and the *SNR* are significantly enhanced as well for the region in the vicinity of the surface coil. For both cases (dipole and loop), the improvement due to the HIS shield degrades with a larger penetration depth into the phantom, and a larger separation distance from the HIS shield to the coil. The presented investigation may inspire the design of a low-profile RF coil with improved coil performance compared to the conventional metal shield.

Additionally, an eight-channel dipole coil backed by a HIS shield is presented and compared to the case with a conventional metallic shield. Based on the simulated and measured magnetic field distribution, it can be noticed that the overall magnetic field inside the phantom is enhanced by the HIS shield and is distributed in a more homogeneous manner.

Chapter 5

Coupling Investigation of Multi-Channel RF Dipole Coils

For an RF coil array consisting of several array elements, the coupling characteristic of the coil array, especially between the neighboring elements, is of our great interest. Since the coupling characteristic of the coil has a significant influence on the coil performance, in this chapter we carry out a coupling investigation of the dipole coil for 7 Tesla MRI. Here we present an investigation of coupling mechanism of different dipole coil elements by applying a characteristic mode analysis. Based on the results from coupling investigation, a multi-channel dipole coil consisting of different dipole coil element is proposed, which achieves an optimal compromise between the field distribution and the coupling characteristic. Additionally, the effect of the RF shield, which is characterized by its surface impedance, on the coupling between the neighboring elements of a coil array is evaluated. This fundamental investigation reveals a new approach to modify the coupling characteristics of the dipole coil elements for UHF MRI.

5.1 Coupling Investigation of Dipole Coils based on Characteristic Mode Analysis (CMA)

In this section we propose an approach to investigate the coupling mechanism of different dipole coil elements based on characteristic mode analysis [108]. The conclusion obtained from characteristic mode analysis will be confirmed by FDTD simulation and experimental results.

5.1.1 Coil Elements Considered

Diverse dipole-like coil elements have been utilized to build RF coils for UHF MRI. Different from the direct lumped-element-connection between stripline and the shielding plate in [69] and [70], a field-based coupling which enables the shielding plate to resonate in its natural half-wavelength eigen-mode was initially introduced in [71]. This novel 41 cm-long coil has an increased coupling due to the magnetic field produced by the eigen-resonant current on the shielding plate edges. By shrinking the longitudinal dimension of the coil element, the coupling to the adjacent element can be diminished due to the suppressed eigen-resonant current.

Fig. 5.1 depicts the coil elements which will be specifically analyzed. In all cases, the coil element is 25 cm long and 10 cm wide. The stripline element and the corresponding shielding plate are printed on Rogers RO4003 substrates ($\epsilon_r = 3.55$) with a thickness of 0.5 mm, which are separated by 2 cm. For the cases of the ordinary stripline element and the element using meanders, a so-called end-capacitor with the value of 3.3 pF and 1 pF is applied to fine-tune the current distribution on the stripline, respectively. The geometry of the open-ended element in Fig. 5.1(c) remains unchanged in comparison to the standard meandered element, except that the end-capacitors and the corresponding metallic connections are removed.

5.1.2 Characteristic Mode Analysis

Characteristic Mode Analysis (CMA) is the numerical calculation of a weighted set of orthogonal current-modes that are supported on a conducting surface. The current density J on the surface S is related to the tangential components of electric field through a symmetric operator Z, which has the dimension of impedance [105]:

$$Z(\mathbf{J}) - \mathbf{E}_{\tan} = (R + jX)(\mathbf{J}) - \mathbf{E}_{\tan} = 0, \tag{5.1.1}$$

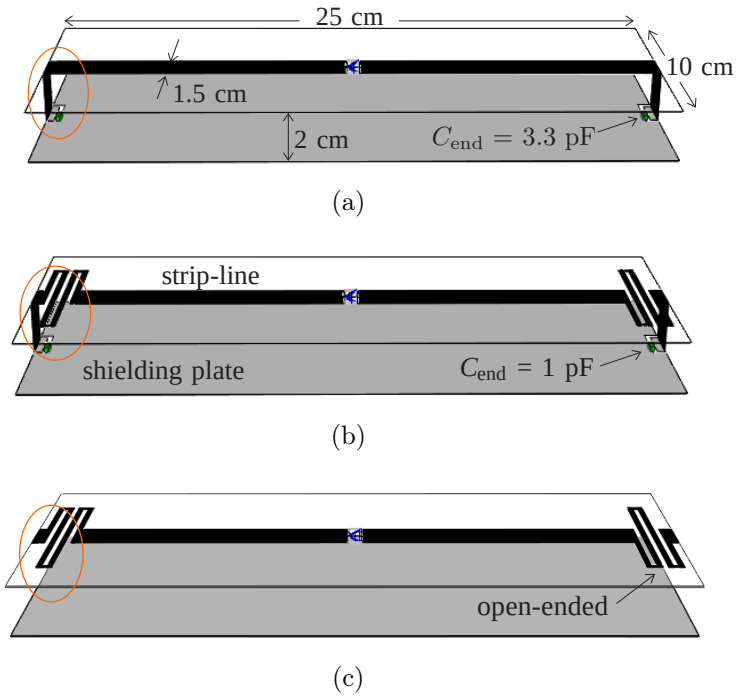

Figure 5.1: RF coil elements under consideration: (a) the ordinary stripline element with an end-capacitor of 3.3 pF, (b) the meandered stripline element with an end-capacitor of 1 pF and (c) the open-ended dipole element.

where the operators R and X represent the real and imaginary parts of Z, respectively. Z is symmetric from the reciprocity theorem [109] but not *Hermitian*, whereas R and X are real and symmetric. The generalized eigenvalue problem has a following formulation

$$X(\mathbf{J}_n) = \lambda_n R(\mathbf{J}_n), \tag{5.1.2}$$

where λ_n and J_n are the eigenvalue and characteristic current of the corresponding characteristic mode, respectively. The subscript n refers to the index of the characteristic mode. These characteristic currents can provide physical insight into the electromagnetic properties of structures.

Additionally, CMA can be used to synthesize the full-wave current on a structure by taking into account the excitation. This may be expressed as follows [105]:

$$\mathbf{J}_{tot} = \sum_n \frac{V_n^i}{(1+j\lambda_n)\langle \mathbf{J}_n,\, R\mathbf{J}_n\rangle}\mathbf{J}_n = \sum_n \frac{\langle \mathbf{J}_n,\, \mathbf{E}^i\rangle}{(1+j\lambda_n)\langle \mathbf{J}_n,\, R\mathbf{J}_n\rangle}\mathbf{J}_n, \tag{5.1.3}$$

where V_n^i is the so-called modal excitation coefficient (MEC) and λ_n is the eigenvalue associated with the nth characteristic mode. Here we define the symmetric product of two vector functions $\mathbf{A}$ and $\mathbf{B}$ on surface S as

$$\langle \mathbf{A}, \mathbf{B} \rangle = \oiint_S \mathbf{A} \cdot \mathbf{B} \, dS. \tag{5.1.4}$$

The MEC accounts for the coupling between the excitation and the nth mode, and determines if a particular mode is excited by the impressed electric field E^i in (5.1.3). For an effective excitation of the nth mode, we obtain a maximization of the nth modal excitation coefficient V_n^i and an eigenvalue λ_n which approaches zero.

The coil elements in Fig. 5.1 excited by lumped ports have been solved for the first seven modes at 300 MHz in FEKO, an EM simulation software based on method of moment (MoM). Without changing the substantial properties of the structure, the dielectric substrates are not included for the characteristic mode analysis in order to avoid out-of-memory simulation issues. The corresponding MECs of the solved modes for different coil elements are given in Fig. 5.2. Besides a dominant mode (mode index 4 in the case of the ordinary and meandered element, mode index 6 for the open-ended element), a secondary mode (mode index 1) with comparably small MEC is excited.

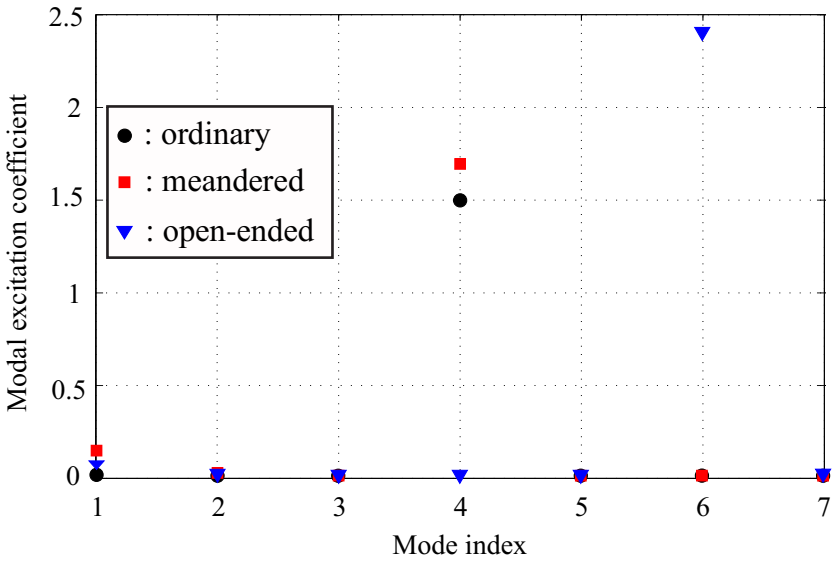

Figure 5.2: Modal excitation coefficients of the coil elements depicted in Fig. 5.1 for the first seven modes at 300 MHz.

Fig. 5.3 illustrates the current distributions at 300 MHz of the dominant and secondary mode for the three coil elements. The current distribution of the dominant modes will be discussed firstly. The dominant mode of the ordinary stripline element reveals a loop current which circulates through the stripline and the shielding plate via the end-capacitors. This loop current presents an inductive nature which is denoted by the positive eigenvalue of the corresponding mode in Fig. 5.3(a) [105]. The meandered element shows similar characteristics as the ordinary one: a loop-like current and a positive eigenvalue. In contrast, the dominant mode of the open-ended element exhibits a negative eigenvalue as shown in Fig. 5.3(e), which indicates the coil element behaves as an electric dipole. Under the stripline current an out-of-phase mirror current on the shielding plate is observed.

The secondary mode of the ordinary element in Fig. 5.3(b) shows a strong current on the shielding plate with respect to its stripline current, which intends to increase the overall shielding plate current in driven mode. Note that in Fig. 5.3(f) the open-ended element has an in-phase eigencurrent below the stripline, which leads to a reduced overall shielding plate current. For the meandered element, the current on the stripline and shielding plate are comparable, as shown in Fig. 5.3(d). Hence, the contribution of stripline and shielding plate current to the overall current from this mode is almost balanced. Consequently, a compromising current distribution for the meandered element between the two previous cases is expected.

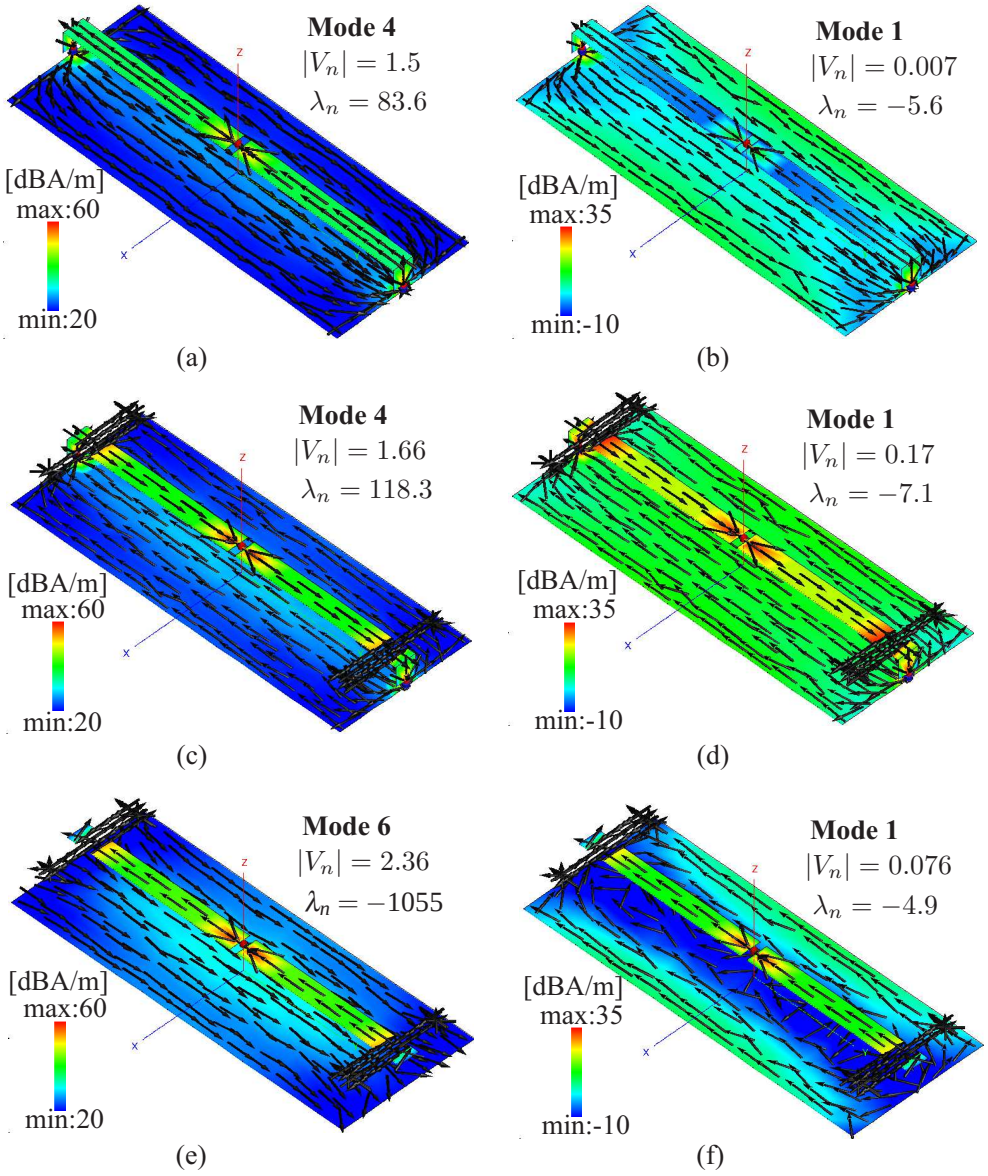

Figure 5.3: Current distribution for the dominant (left column) and secondary (right column) modes of the coil elements under consideration: (a, b) the ordinary stripline element with C_{end} = 3.3 pF, (c, d) the meandered stripline element with C_{end} = 1 pF and (e, f) the open-ended dipole element.

5.1.3 FDTD Simulation

Taken into account the effect of phantom, a driven-mode simulation has been carried out. A flat phantom ($\epsilon_r = 58.2$, $\sigma = 0.92$ S/m) is placed 2 cm above two coil elements which are aligned adjacent to each other with a 5 mm edge-to-edge separation. The scattering parameters for the three types of coil element at 300 MHz are listed in Tab. 5.1. The ordinary stripline element has the highest coupling around -10 dB compare to the other cases. The meandered element achieves a decoupling below -20 dB. The coupling of open-ended element is much lower than the ordinary stripline element but a little bit higher than the meandered element with end-capacitor.

Table 5.1: Simulated S-Parameters of Two Parallel Aligned Coil Elements Which are Placed Bellow a Flat Phantom

coil element	ordinary element (C_{end}=3.3 pF)	meandered element (C_{end}=1 pF)	open-ended element
S_{11} [dB]	-21.0	-20.3	-20.6
S_{21} [dB]	-10.1	-21.6	-18.9

Fig. 5.4 shows the absolute magnetic field on the central transversal and longitudinal cross-sections of the two parallel aligned coil elements. The corresponding magnetic field is normalized to the square-root of the accepted power and plotted in dB.

Due to the large loop current, the magnetic field is concentrated between the stripline and the shielding plate for the ordinary stripline element, as shown in Fig. 5.4(a). Hence, when two elements are aligned adjacent to each other, a relative strong magnetic field below the stripline is observed on the longitudinal plane in Fig. 5.4(b). This magnetic field results in an enhanced coupling between the two elements.

As already shown in the CMA previously, the open-ended element behaves as an electric dipole. Instead of concentrated between stripline and shielding plate, the magnetic field is distributed above the stripline in a broader manner, as depicted in Fig. 5.4(e). This magnetic field contributes mainly to the coupling in this case. Since the magnetic field under the stripline is considerably decreased compare to the ordinary element, an increase of isolation by approx 9 dB is achieved.

Neither concentrated below the stripline by the large shielding plate current, nor distributed above the stripline due to the small shielding plate current, the magnetic field of the meandered element is quite constant along the z-axis in Fig. 5.4(c). Hence, the coupling from the magnetic field below and above the stripline is diminished and an enhanced decoupling is achieved.

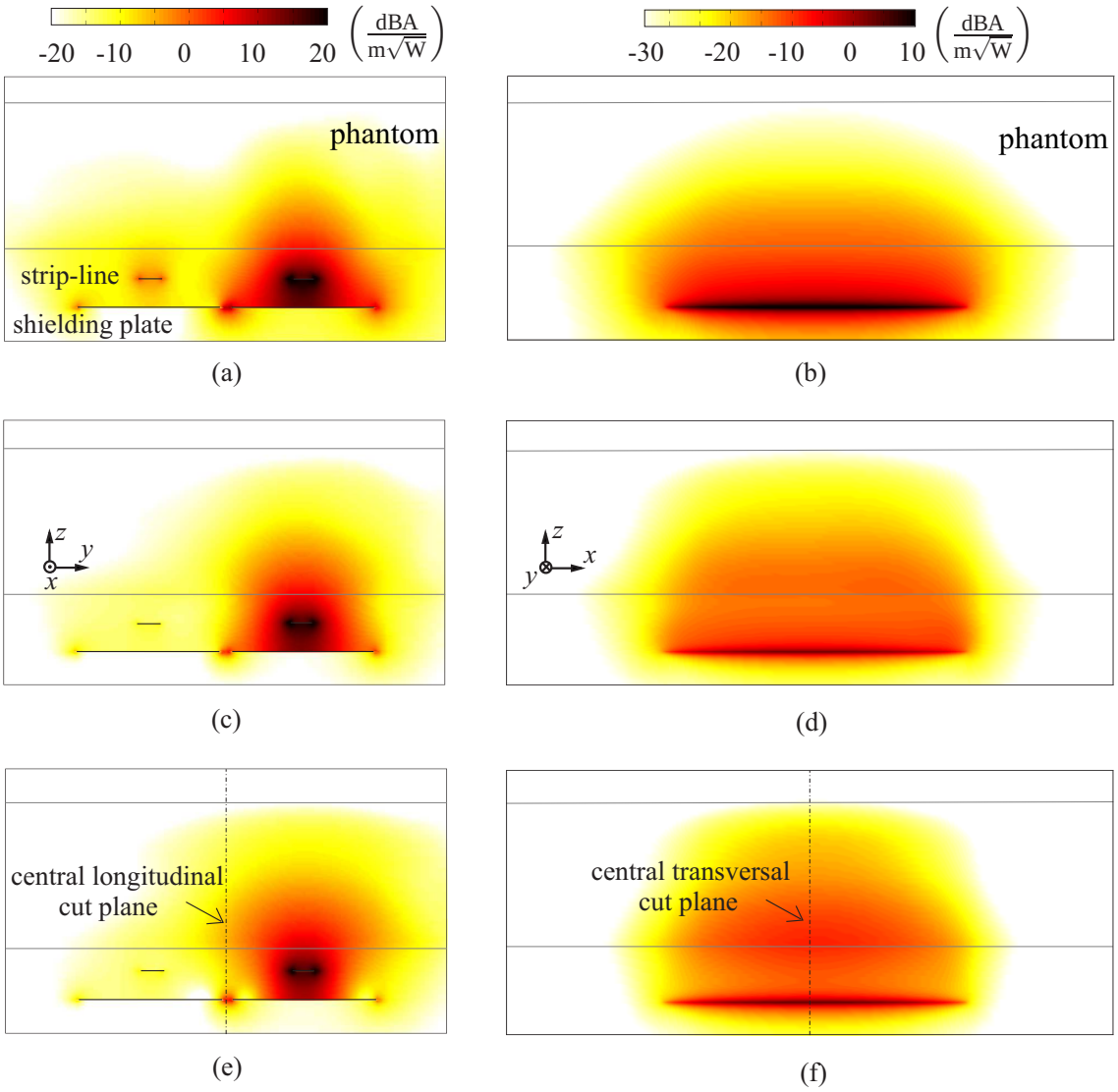

Figure 5.4: Simulated absolute magnetic field on the central transversal (left column) and longitudinal (right column) cross-section of two parallel aligned coil elements at 300 MHz: (a, b) the ordinary stripline element with an end-capacitor of 3.3 pF, (c, d) the meandered stripline element with an end-capacitor of 1 pF and (e, f) the open-ended dipole element.

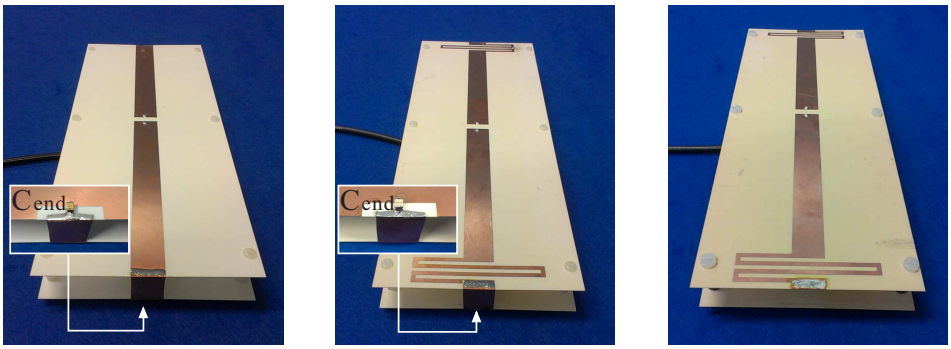

(a) (b) (c)

Figure 5.5: Fabricated prototypes: (a) the ordinary dipole element (C_{end}=1 pF), (b) the meandered dipole element (C_{end}=3.3 pF) and (c) the open-ended dipole element.

5.1.4 Prototypes and Measurement

The prototypes of the stripline elements to be compared are shown in Fig. 5.5. For the coupling measurement, two coil elements are placed 2 cm away from the phantom ($\epsilon_{\text{r}} \approx 58.2$, $\sigma \approx 0.92$ S/m) in parallel with a 5 mm edge-to-edge separation in between.

Fig. 5.6 shows the matching for all the considered coil elements is better than -10 dB around 300 MHz. The ordinary element has the highest coupling about -10 dB, whereas the meandered element exhibits a coupling lower than -28 dB. The open-ended element falls in between of the aforementioned two cases: a coupling around -20 dB is achieved. The measurements show a good agreement with the simulation except for the lower coupling of the meandered elements in comparison to simulation, which could be caused by the imperfect alignment during the measurement .

5.1.5 Summary of Coupling Investigation based on CMA

In this section a novel coupling investigation of different RF coil elements has been carried out based on characteristic mode analysis and FDTD simulation. The coil element with lumped-element connection to the shielding plate exhibits a loop-like current and focus the magnetic field below the stripline, which contributes mainly to the coupling to the neighboring element. The element without direct connection to the shielding plate behaves more like an electric dipole. Instead of being focused below the stripline, the magnetic field is distributed above the stripline in a broader manner, which is more considerable for the coupling. Specifically, the meandered coil element seems to find a compromise between the two aforementioned scenarios and achieves an optimal decoupling. The experimental results show a good agreement to the numerical simulations.

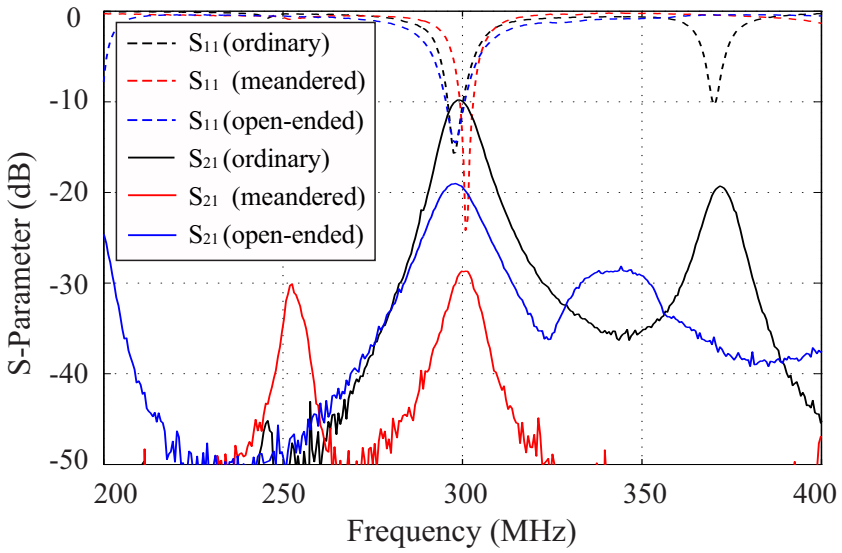

Figure 5.6: Measured scattering parameters of two parallel aligned coil elements in different loaded cases: the ordinary dipole element with C_{end}=1 pF, the meandered dipole element with C_{end}=3.3 pF, and the open-ended dipole element.

5.2 Dipole Coil with Combined Element

From the previous coupling investigation we have seen that different dipole elements exhibit various field and coupling characteristics. In this section we present an eight-channel dipole coil consisting of different dipole coil elements, and explore the feasibility to achieve an optimal compromise between field distribution and coupling characteristic by combining different coil elements.

5.2.1 Proposed Dipole Coils

Here we employ the symmetrically fed dipole element which was terminated by two meanders on each side. Different termination scenarios to the corresponding RF shield are considered: through a so-called end-capacitor with the value of 1 pF [70]; and in the absence of direct connection between the RF shield and the meanders, which are encompassed by high-dielectric substrates [87] to fine-tune the current distribution on the dipole. For both cases, the stripline dipole and the corresponding RF shield are printed on Rogers RO4003 substrates (25 cm × 8 cm) with a thickness of 0.5 mm, and separated by 2 cm of air.

Fig. 5.7 shows the absolute magnetic field of the considered dipole elementson the transverse cross-section of the simulation domain. A homogeneous flat phantom ($\epsilon_{\text{r}} = 45.3$, $\sigma = 0.87$ S/m) was placed 2 cm above the dipole element. The corresponding magnetic field is normalized to the square-root of the accepted power and plotted in dB. The dipole element with end-capacitors reveals a loop current which circulates through the stripline

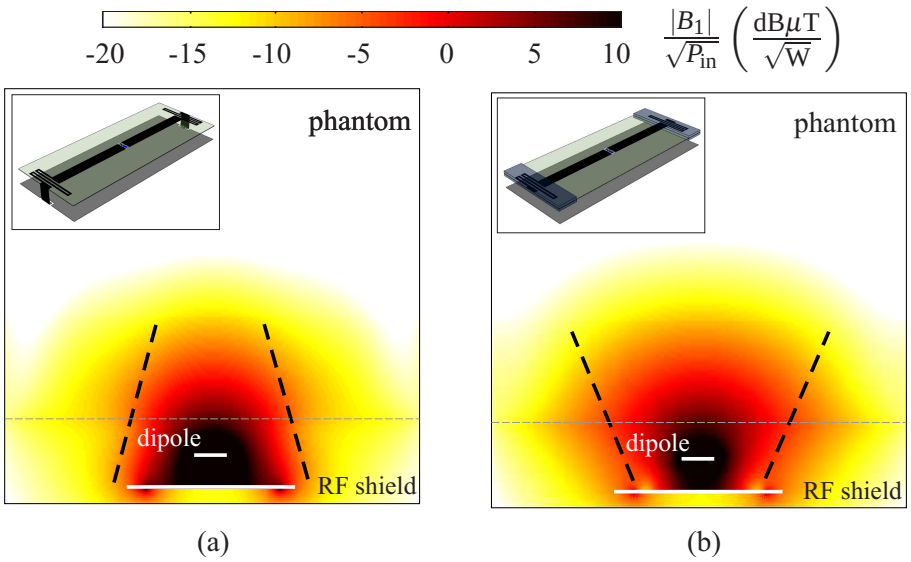

Figure 5.7: Simulated absolute magnetic field distribution on the transverse cross-section of the considered dipole elements: (a) dipole element with end-capacitors, (b) open-ended dipole element. The corresponding magnetic field is normalized to the square-root of the accepted power and plotted in dB.

and the RF shield via the end-capacitors. As a result, a relative strong magnetic field below the stripline is observed [cf. Fig. 5.7(a)]. Without the direct connection to the RF shield, the magnetic field of the open-ended dipole element could more "freely" propagates away from the stripline, and distribute above the stripline in a broader manner [cf. Fig. 5.7(b)]. The drawback is that this broader field distribution leads to a higher coupling between adjacent elements [108].

5.2.2 EM Model Validation

The EM model of the proposed RF coils with different dipole elements are validated through the comparison of full-wave simulation and near-field measurement.

5.2.2.1 Full-Wave Simulation

The transverse B_1 distributions of the proposed dipole coils are simulated with a full-wave simulator based on the *Finite Difference Time Domain* (FDTD) method, here EMPIRE XPU[1], and displayed in Fig. 5.8. For each coil setup the dipole elements are properly matched in such a way that the power delivered to each dipole element is identical. The corresponding field distributions are normalized to the total accepted power by the coil

[1]EMPIRE XPU is one of the leading 3D electromagnetic field simulators. It is based on the powerful Equivalent Circuit Finite Difference Time Domain method (EC-FDTD), which has become an industrial standard for RF and microwave component and antenna design.

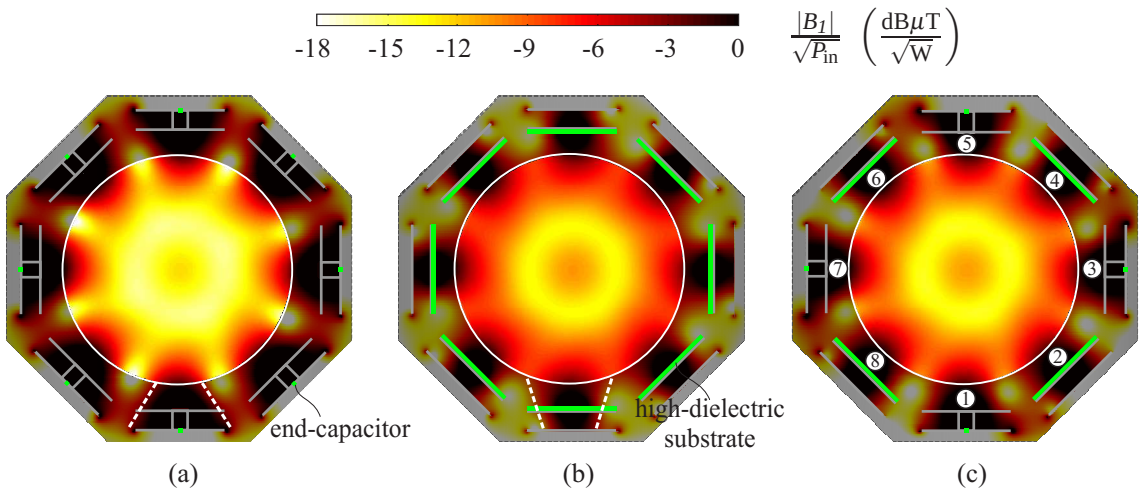

Figure 5.8: Simulated $|B_1|$ distributions on the transverse cut of the proposed dipole coils: (a) an eight-channel coil based on dipole elements with end-capacitors; (b) an eight-channel coil based on open-ended dipole elements; and (c) an eight-channel coil based on an alternate combination of the aforementioned two dipole elements. The corresponding $|B_1|$ distributions are normalized to the square root of total accepted power and plotted in dB. The field distribution outside the phantom (in the shaded area) is also displayed in order to indicate the unique field pattern of different coil elements.

elements. The coil based on dipole elements with end-capacitors reveals a strong concentration of magnetic field between the stripline and the RF shield, showing a triangle-shaped field distribution, where only the tip of the triangle is extended into the phantom [cf. Fig. 5.8(a)]. As a result, the degradation of the B_1 field in the regions between the adjacent elements is obvious. For the coil with open-ended elements, the field is not confined below the stripline, but spread out in a broader manner inside the phantom, which results in an inverted-triangle-shaped field distribution [cf. Fig. 5.8(b)]. Hence, the in-between areas with low field in Fig. 5.8(a) are covered by the broader field distributions, and an improved B_1 homogeneity is achieved. As mentioned previously, this broader field distribution leads to a stronger coupling between the neighboring elements. Therefore, we present a new setup which achieves a compensation of the triangle- and inverted-triangle-shaped field distribution [cf. Fig. 5.8(c)]. In this case, the gaps between the elements with end-capacitors will be compensated by the open-ended elements, and thus, a more uniform B_1 field is observed. On the other hand, the coil will not suffer from the strong coupling between the neighboring elements, since the field generated by the elements with end-capacitors and the open-ended elements do not deeply overlap with each other as in Fig. 5.8(b).

Here a numerical analysis of the field parameters is performed and compared for different coils in Tab. 5.4. To some extent, the averaged penetrating ability of magnetic field can be correlated to the mean value of $|B_1|$, and the homogeneity of $|B_1|$ field is then represented by the coefficient of variation (CoV) of $|B_1|$:

Table 5.2: Simulated Field Parameters of the Considered Dipole Coils

Type of Coil	mean($\frac{\lvert B_1\rvert}{\sqrt{P_{\text{in}}}}$)	CoV($\frac{\lvert B_1\rvert}{\sqrt{P_{\text{in}}}}$)
CASE 1: End-Capacitor Element	0.334 $[\frac{\mu\text{T}}{\sqrt{\text{W/kg}}}]$	0.479
CASE 2: Open-Ended Element	0.415 $[\frac{\mu\text{T}}{\sqrt{\text{W/kg}}}]$	0.321
CASE 3: Combination of 1 and 2	0.398 $[\frac{\mu\text{T}}{\sqrt{\text{W/kg}}}]$	0.369

$$\text{CoV}\left(|\mathbf{B}_1|\right) = \frac{\text{std}\left(|\mathbf{B}_1|\right)}{\text{mean}\left(|\mathbf{B}_1|\right)}, \tag{5.2.1}$$

where std(·) stands for the standard deviation. A small CoV indicates a low variance of the examined variable, and thus, a better homogeneity. In comparison to the coil with end-capacitors, due to the better radiation ability the open-ended dipole element provides a superior B_1 field (larger mean($|B_1|$) and smaller CoV($|B_1|$). The field parameters of the coil with combined dipole elements fall between the other two cases. Compared to the coil with end-capacitors, the combined dipole arrangement exhibits an increase of 19 % on mean($|B_1|$), and a reduction of 23 % on CoV($|B_1|$).

5.2.2.2 Experimental Validation

Besides the FDTD full-wave simulation, the magnetic field distributions of different coil setups are also investigated by near-field measurement. The experimental setup for near-field measurement is depicted in Fig. 5.9. The dipole elements are equably arranged around a cylindrical phantom ($\epsilon_r \approx 45.3$, $\sigma \approx 0.87$ S/m) with a diameter of 20.5 cm. Fig. 5.9 displays the particular case with combined coil elements, it should be noted that the other two cases share the same measurement setup. The geometry parameters of the coil elements are in accordance with the ones utilized in simulation. The source power is firstly split into four equal parts with a 90° phase-shift using a Butler matrix. Each output signal is followed by a subsequent power amplifier and a Wilkinson power divider, which provides an additional 45° phase-shift between the two outputs. In total eight equal signals with a relative phase lag of 45° are generated and applied to the dipole elements. In our case the power accepted for each channel is roughly 5 W, and varies a little bit between elements due to the slightly different matching behaviors.

Fig. 5.10 shows the measured absolute magnetic field distribution on the transverse cut inside the phantom (cf. Fig. 5.9) for different dipole coils. The corresponding field distributions are normalized to the square root of the total accepted power by the coil elements. The slight asymmetry of the field pattern is mainly caused by the unequal excitation of the coil elements due to the imperfect power splitting by the Bulter matrix and the power

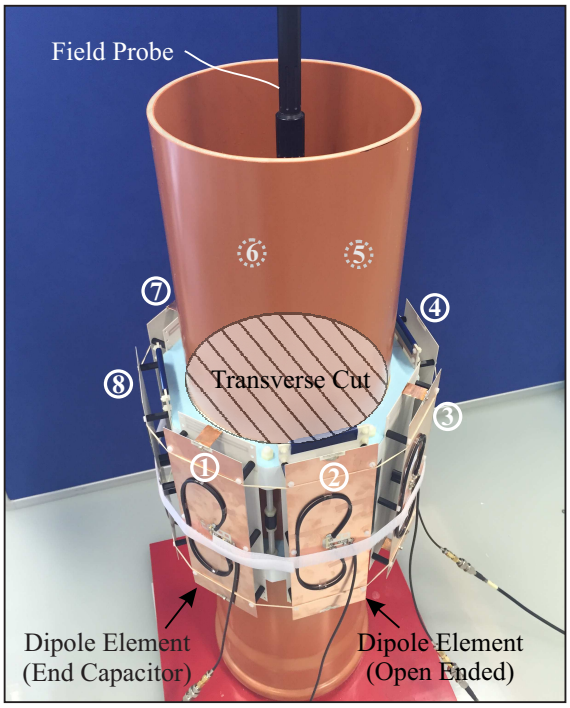

Figure 5.9: Experimental setup for near-field measurement. The dipole elements are arranged quadripartitely around a cylindrical phantom ($\epsilon_r \approx 45.3$, $\sigma \approx 0.87$ S/m) with a diameter of 20 cm.

dividers. Besides, the coil misalignment and slightly different matching levels between coil elements could also aggravate the asymmetry. Due to the finite thickness of the side wall of the phantom container and the radius of the field probe, the measurable field region ($D = 16$ cm) is smaller than the actual cross section of the phantom ($D = 20$ cm). This smaller field of view (FoV) weakens the difference on field distribution between the dipole coils under comparison, since in the outer region of the phantom the field difference is more prominent. Nevertheless, the coil with open-ended elements reveals the most promising $|B_1|$ distribution, in terms of mean value and CoV of $|B_1|$. Compared to the case with end-capacitors, the combination of two different dipole elements exhibits a more homogeneous and strengthened $|B_1|$ distribution, especially in the regions between the neighboring elements.

Similarly, a numerical analysis of the field parameters is carried out based on the measured data (cf. Tab. 5.3). In general, the field parameters of the measured magnetic field shows the same tendency as the ones based on full-wave simulation in Tab. 5.4. The coil with open-ended dipole elements reveals the largest mean value and the smallest coefficient of variation of the absolute magnetic field, indicating a superior field distribution. The coil with end-capacitors exhibits a comparatively inferior field distribution, denoted by the smallest mean value and the largest CoV of the absolute magnetic field. The field parameters of the coil with combined dipole elements again fall in between the other two cases, suggesting an intermediate magnetic field distribution. Since the accessible field region for measurement is smaller than the phantom cross section in full-wave model (due

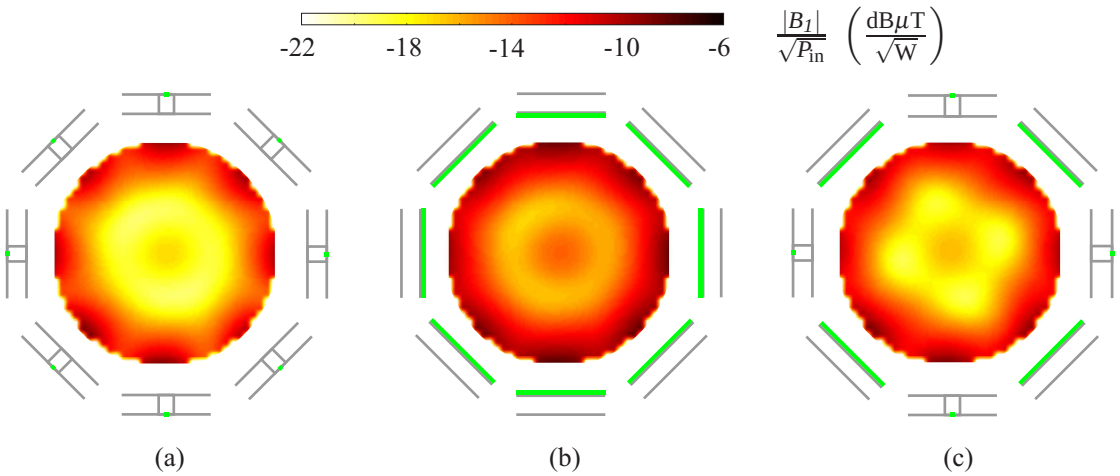

Figure 5.10: Measured $|B_1|$ distributions on the transverse cut of the proposed dipole coils: (a) an eight-channel coil based on dipole elements with end-capacitors; (b) an eight-channel coil based on open-ended dipole elements; and (c) an eight-channel coil based on an alternate combination of the aforementioned two dipole elements. The corresponding $|B_1|$ distributions are normalized to the square root of total accepted power and plotted in dB.

Table 5.3: Measured Field Parameters of the Considered Dipole Coils

Type of Coil	mean($\frac{\lvert B_1\rvert}{\sqrt{P_{in}}}$)	CoV($\frac{\lvert B_1\rvert}{\sqrt{P_{in}}}$)
CASE 1: End-Capacitor Element	0.143 $[\frac{\mu T}{\sqrt{W/kg}}]$	0.574
CASE 2: Open-Ended Element	0.186 $[\frac{\mu T}{\sqrt{W/kg}}]$	0.548
CASE 3: Combination of 1 and 2	0.159 $[\frac{\mu T}{\sqrt{W/kg}}]$	0.566

to the sidewall of the phantom container and the diameter of the field probe), the measured field magnitude is smaller than the simulation results [cf. Fig. 5.8(a-c)]. As mentioned earlier, this smaller FoV weakens the difference on field distribution between the three compared coil arrangements and leads to a less different CoV in Table 5.3. We can notice that due to the smaller mean values, the CoV of the measured magnetic field in Table 5.3 are larger than the ones computed based on the simulation results (cf. Table 5.4).

Basically, the full-wave simulation and near-field measurement reveal a very similar magnetic field distribution inside the phantom, which is also confirmed by the numerical analysis. Through the comparison of simulated and measured results, the numerical models of the considered coil arrangements are effectively validated.

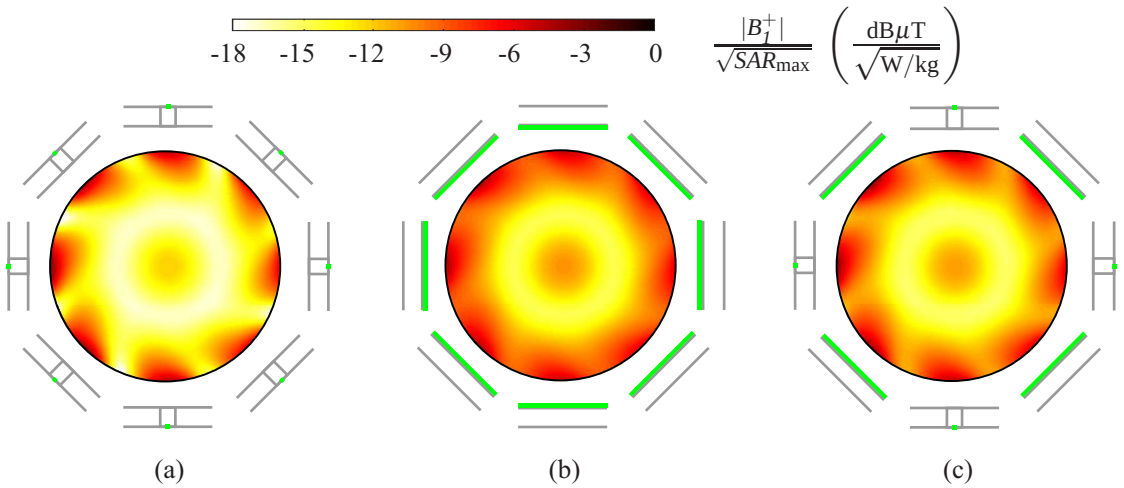

Figure 5.11: Simulated $|B_1^+|$ distributions on the transverse cut of the proposed dipole coils: an eight-channel coil based on dipole elements with end-capacitors (a); an eight-channel coil based on open-ended dipole elements (b); and an eight-channel coil based on an alternate combination of the aforementioned two dipole elements (c). The corresponding $|B_1^+|$ distributions are normalized to square root of the peak SAR inside phantom and plotted in dB.

5.2.3 B_1^+ Distribution

For a multi-channel RF coil, the circularly polarized magnetic field, namely the B_1^+ field, inside the phantom is mostly considered [91, 92]. In our case the coil elements are fed equally in magnitude and with a relative phase lag of 45° to excite the first-order CP+ mode. For the UHF MRI application, the local peak SAR is a critical limitation which should be minimized. In addition to the absolute field distribution, here we also investigate the circularly polarized B_1^+ field inside the phantom, and normalize it to the square root of peak SAR (cf. Fig. 5.11). In general, the $|B_1^+|$ distributions show a similar tendency as the absolute B_1 distribution in Fig. 5.8, except for the slightly rotated field patterns due to the circular polarization.

Table 5.4: Simulated Field Parameters of the Considered Dipole Coils

Type of Coil	mean($\frac{|B_1^+|}{\sqrt{SAR_{\max}}}$)	CoV($\frac{|B_1^+|}{\sqrt{SAR_{\max}}}$)
CASE 1: End-Capacitor Element	0.255 $[\frac{\mu\mathrm{T}}{\sqrt{\mathrm{W/kg}}}]$	0.390
CASE 2: Open-Ended Element	0.321 $[\frac{\mu\mathrm{T}}{\sqrt{\mathrm{W/kg}}}]$	0.273
CASE 3: Combination of 1 and 2	0.275 $[\frac{\mu\mathrm{T}}{\sqrt{\mathrm{W/kg}}}]$	0.307

The numerical analysis of the $|B_1^+|$ distribution reveal a similar tendency as the $|B_1|$

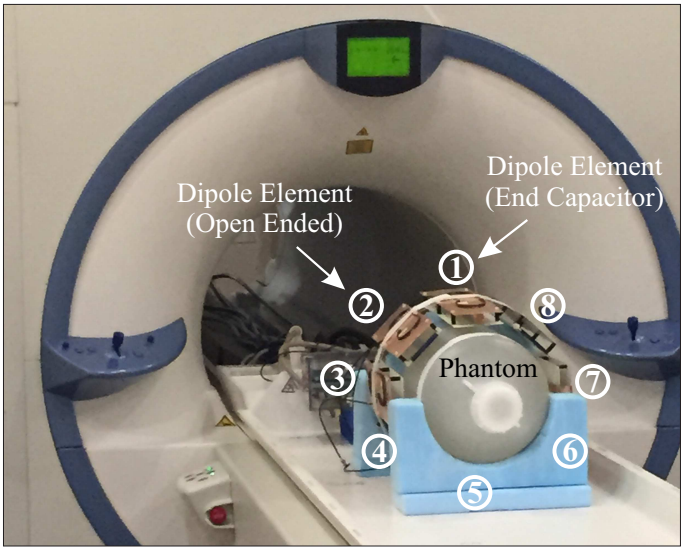

Figure 5.12: Eight-channel dipole coil with combined elements loaded with a cylindrical phantom positioned on the patient table of a MRI scanner.

distribution. The dipole coil with end-capacitors is of the smallest mean value and the largest CoV of the B_1^+ distribution, whereas the open-ended dipole coil exhibits the largest mean($|B_1^+|$) and the smallest CoV($|B_1^+|$) of the three considered cases. The field parameters of the coil with combined dipole elements fall between the other two cases.

5.2.4 Absolute B_1^+ Maps

In addition to the near-field measurement, the absolute B_1^+ maps of the proposed multi-channel coils with different dipole elements are acquired with the method presented in [110] in a 7 T MRI scanner (Magnetom 7 T, Siemens Healthcare).

5.2.4.1 Measurement Setup

As shown in Fig. 5.12, the eight-channel dipole coil with combined elements is loaded with a cylindrical phantom ($\epsilon_r \approx 45$, $\sigma \approx 0.8$ S/m, $d = 21$ cm) and positioned on the patient table of a 7 T MRI scanner. The coil elements are fed with 45° phase lag to each other in order to excite the first-order CP+ mode. The peak power applied on each channel is 40 W with 1 ms duration. Including the losses in the RF cables, coil matching network, Tx/Rx switches, etc., the available power that reaches the coil element is less than the applied power. Fig. 5.12 displays the particular case with combined coil elements, it should be noted that the same measurement setup is applied for the other two cases.

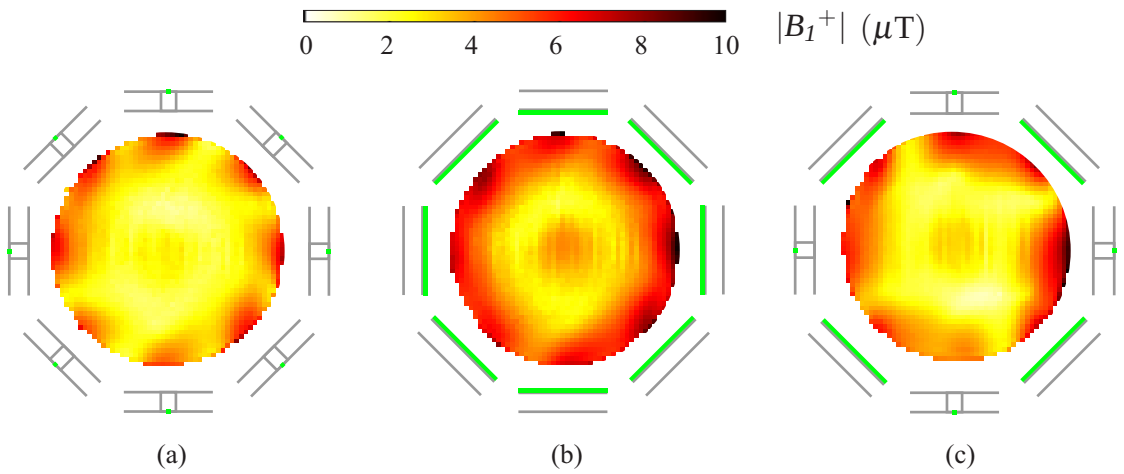

Figure 5.13: Acquired absolute transverse B_1^+ maps for different dipole coils: (a) an eight-channel coil based on dipole elements with end-capacitors; (b) an eight-channel coil based on open-ended dipole elements; and (c) an eight-channel coil based on an alternate combination of the aforementioned two dipole elements.

5.2.4.2 Results and Discussion

The absolute B_1^+ maps on the transverse plane of the phantom are compared for different dipole coil arrangements: a) an eight-channel coil based on dipole elements with end-capacitors, b) an eight-channel coil based on open-ended dipole elements, and c) an eight-channel coil based on an alternating combination of the aforementioned two dipole elements. From Fig. 5.13(b) it can be seen that the field strength in the region between the coil elements with end-capacitors is considerably lower compared to the primary field excited by the dipole coil, whereas the coil with open-ended elements exhibits an extended field distribution, which significantly improves the field strength in the regions between the neighboring elements. Additionally, the overall field penetration depth of the open-ended scenario is slightly increased as well, indicated by the more obvious "central-brightening" [cf. Fig. 5.13(b)]. The dipole coil with combined elements reveals an "intermediate" B_1^+ distribution, which falls between the aforementioned two cases. Compared to the end-capacitor scenario, the field strength between the coil elements as well as the field penetration are enhanced for the case using alternating combination of dipole elements. However, the improvement is not as significant as the one achieved with open-ended scenario. The asymmetry of the absolute B_1^+ maps is probably caused by the impurity of the CP+ mode due to the inaccurate relative phase lag between the coil elements. Different matching levels for individual elements and imperfect alignment around the phantom could also aggravate the asymmetry of the B_1^+ distributions.

In order to illustrate the difference in field distribution of different dipole elements (coil element with end-capacitors and coil element with open-ends), the relative B_1^+ maps on the transverse plane of the dipole coil with combined elements are shown in Fig. 5.14. The meander sections of dipole elements 1, 3, 5, 7 are terminated by open ends, while dipole elements 2, 4, 6, 8 are with end-capacitors. From Fig. 5.14 we can see that the open-ended

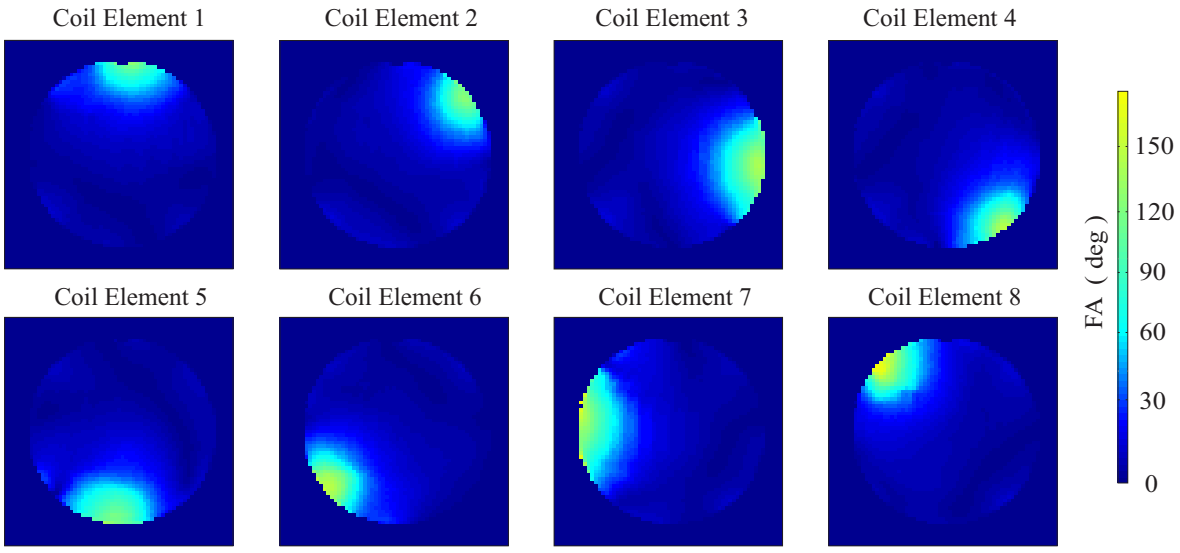

Figure 5.14: Absolute B_1^+ maps scaled to flip angle on the transverse plane of the dipole coil with combined elements for individual elements. Coil Element 1, 3, 5, 7 are open-ended, coil element 2, 4, 6, 8 are with end-capacitors.

elements reveal a more widely spread field distribution along with a stronger penetration into the phantom, in comparison to the elements with end-capacitors.

5.2.5 Scattering Parameters

The coupling characteristics of the proposed RF coils with different dipole elements are compared based on full-wave simulation and S-parameter measurement.

5.2.5.1 Full-Wave Simulation

The coil arrangement for the investigation of coupling characteristics of different coil setups remains unchanged as depicted in Fig. 5.8. For each case one of the dipole elements with the port number 1 [cf. Fig. 5.8(f)] is excited with the remaining adjacent elements being terminated by 50 Ω loads. Normally, the neighboring elements present the "worst-case" coupling due to proximity. Fig. 5.16 compares the S-parameters of two directly adjacent elements (with port numbers 1 and 2) for different coil setups. With appropriate matching networks a more than 35 dB return loss is achieved for all the dipole coils. As expected the dipole element with end-capacitors achieves an optimal decoupling around 38 dB to the neighboring element at 300 MHz. Through the extended field distribution the open-ended dipole element could more easily couple to the adjacent element [cf. Fig. 5.8(b)], and thus leading to the highest coupling level in the three considered cases ($|S_{21}|$ = -21 dB). As a compromise of the other two scenarios the dipole coil with combined elements reveals an intermediate $|S_{21}|$ with a value of -28 dB, which falls between the other two cases.

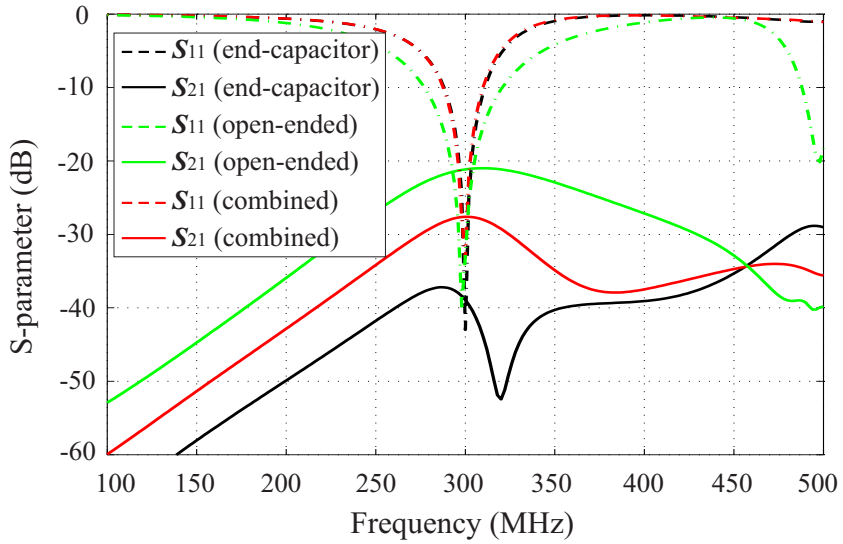

Figure 5.15: Simulated S-parameters for different coil setups as depicted in Fig. 5.8. For each case one of the dipole elements with the port number 1 is excited with the remaining adjacent elements being terminated by 50 Ω loads.

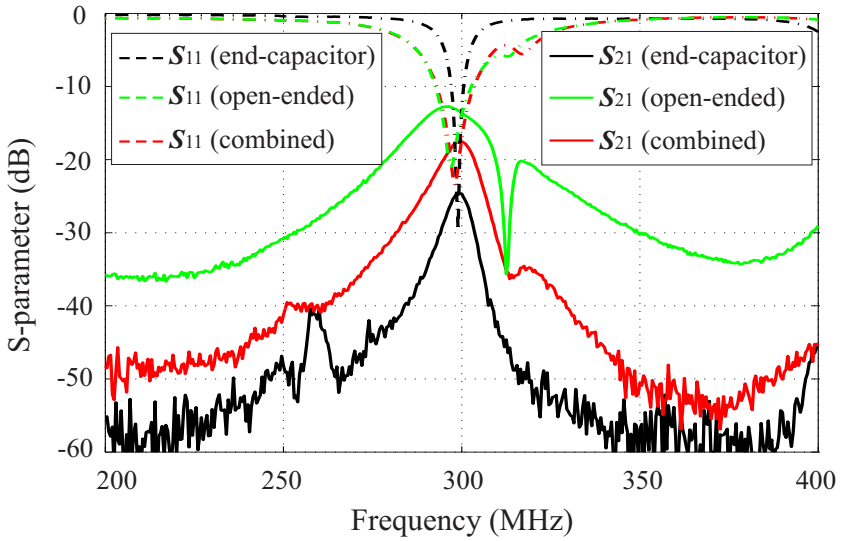

Figure 5.16: Measured S-parameters for different coil setups as depicted in Fig. 5.8. For each case the reflection coefficient of the dipole element with the port number 1, as well as the transmission coefficient between port 1 and 2, are measured with the remaining adjacent elements being terminated by 50 Ω loads.

5.2.5.2 Experimental Validation

The S-parameters of two directly adjacent elements in Fig. 5.9 are measured with a two-port network analyzer for different coil setups. The matching network of the coil element with end-capacitors consists of a shunt capacitor of 14 pF and a series capacitor of 3.9 pF. The open-ended coil element is matched to 300 MHz with a shunt capacitor of 30 pF and a series inductor of 2.1 nH. With the proper matching networks a more than 20 dB return loss is achieved for all the coil elements. As shown in Fig. 5.16, the coil with end-capacitors reveals a most promising decoupling between the neighboring elements, indicated by the smallest $|S_{21}|$ of 25 dB at 300 MHz. The coil consisting of open-ended elements exhibits the highest coupling level around 14 dB due to the broader field distribution inside phantom. The coupling level of the coil with combined elements falls in between the aforementioned two scenarios, showing an intermediate $|S_{21}|$ with a value of 18 dB.

5.2.6 Summary of Dipole Coil with Combined Elements

In this section the magnetic field distribution and coupling characteristics of a multi-channel RF coil consisting of different dipole elements for 7 T MRI have been investigated. It has been shown that the open-ended dipole coil exhibits a superior magnetic field distribution, whereas the dipole coil with endcapacitors achieves a sufficient decoupling between the neighboring elements. Hence, a coil setup which combines the aforementioned two types of dipole elements is proposed. By nesting the open-ended dipole elements in between the ones with end-capacitors, the magnetic field distribution is improved in comparison to the dipole coil consisting only of the elements with end-capacitors, and additionally, the adjacent element are less coupled to each other in comparison to the dipole coil consisting only of the open-ended elements. Here we demonstrated the feasibility to achieve a compromise between field distribution and coupling behavior by combining different dipole coil elements. The presented investigation is based on full-wave simulations and corresponding measurements, which match to each other very well. In addition to the near-field measurement, the eight-channel coil with combined dipole elements is tested in a 7 T MRI scanner, which validated the proposed approach.

5.3 Coupling Investigation of Dipole Coils backed by Surface Impedance Characterized Shields

In this section we present a coupling investigation of RF coil array elements which are backed by surface impedance characterized RF shields for 7 Tesla MRI [111]. Two simulation models for the dipole coil element are considered here: an ideal impressed current model for an initial 2-D investigation, and a symmetrically fed dipole with meander terminals for the 3-D investigation. The RF shield, which is placed behind the coil element, is characterized by a surface impedance boundary condition (SIBC), where different surface impedances are defined. An optimal surface impedance of the RF shield can be found to achieve minimum coupling between neighboring coil elements. Different spatial arrangements (e.g., the shape of the phantom, the edge-to-edge separation between coupled coil elements, the separation from coil element to RF shield) are considered.

5.3.1 Coupling Investigation based on 2-D Models

In this section we investigate the coupling characteristics of stripline dipole coil elements with surface impedance characterized RF shields based on a two-dimensional model.

5.3.1.1 Simulation Setup

The two-dimensional simulation model in COMSOL Multiphysics for the coupling investigation of dipole elements is depicted in Fig. 5.17. Here we consider two different coil arrangements: two parallel aligned dipole elements loaded with a flat homogeneous phantom, and two dipole elements offset by an azimuthal angle around a cylindrical phantom. Same phantom parameters ($\epsilon_\mathrm{r} = 58.2$, $\sigma = 0.92$ S/m, $\rho = 1000$ kg/m^3) are utilized for the two aforementioned arrangements to emulate the human body for 7 T MRI.

For the flat phantom arrangement, the coordinate system is placed in such a way that the x and y axis coincide with the horizontal and vertical direction, respectively, and the z axis points outward the figure. The SIBC normal to the y direction, which models the RF shield, is located below the dipole element with a separation of h. The remaining boundaries of the simulation domain are assigned to a scattering boundary condition, which provides a sufficiently low reflection. Here, a 1.5 cm wide stripline shaped current sheet with an impressed surface current density J_s of 1 A/m in z-direction is used as the excitation of the electromagnetic field. The input power per unit length of this active element is calculated by

$$P_1{}' = -\frac{1}{2}\Re\{\int_S \mathbf{E}\cdot\mathbf{J}_\mathrm{s}^*\, ds\}, \tag{5.3.1}$$

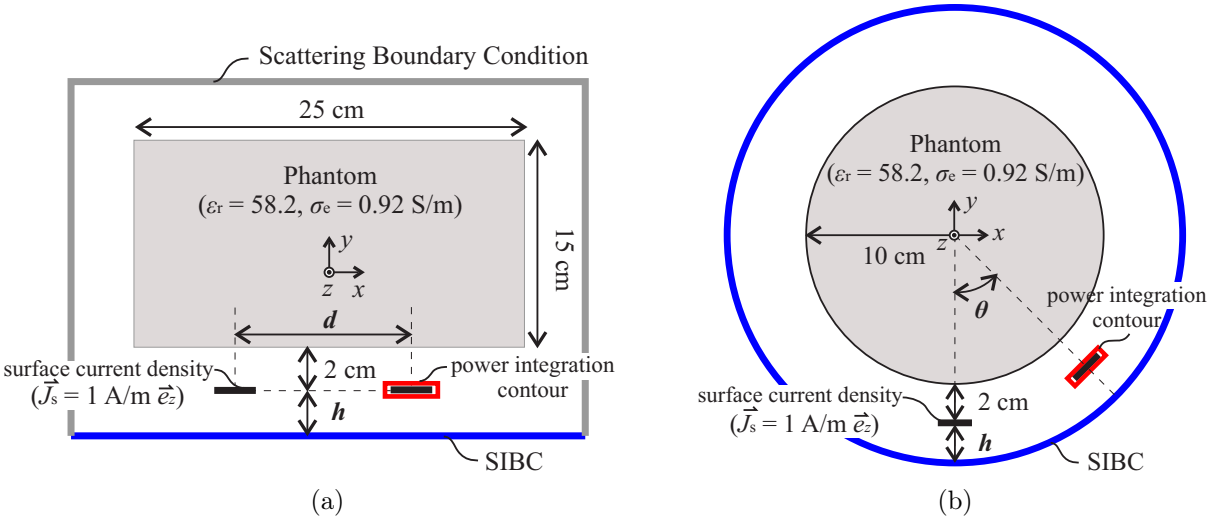

Figure 5.17: Two-dimensional simulation models for the coupling investigation of dipole elements with surface impedance characterized RF shields: (a) two parallel aligned dipole elements loaded by a flat phantom, (b) two dipole elements azimuthally offset by angle θ around a cylindrical phantom.

where $\mathbf{J}_s$ and $\mathbf{E}$ is the impressed electric surface current density and the resulting electric field on the stripline [cf. Fig. 5.17(a)], respectively. A passive element is aligned parallel to the active element with a center-to-center separation of d. The received power per unit length by this passive element can be computed by integrating the time averaged energy flux density through the integration contour [cf. Fig. 5.17(a)], which encloses the passive element with a surface impedance of 50 Ω[2]:

$$P_2' = \frac{1}{2}\Re\{\int_S (\mathbf{E} \times \mathbf{H}^*) \cdot \mathrm{d}\mathbf{s}\}. \tag{5.3.2}$$

The coupling between the active and passive elements then can be evaluated by the ratio of P_2' (5.3.2) and P_1' (5.3.1).

For the cylindrical phantom arrangement, the passive element is rotated by an azimuthal angle θ with respect to the phantom center. Angle θ (24°, 36°, 48°) is chosen in such a way that the azimuthal arc between the elements has the same length as the horizontal separation d (5 cm, 7.5 cm, 10 cm) for the flat phantom arrangement. The outer boundary of simulation domain is assigned to SIBC, which models the RF shield. The power calculation for the active and passive elements remains unchanged in comparison to the case for a flat phantom.

[2]The surface impedance of the passive element is set to 50 Ω in order to model the 50 Ω port impedance in reality.

5.3.1.2 Simulation Results

The power ratio P_2'/P_1' for the coil arrangement (cf. Fig. 5.17) is plotted versus surface impedance of the RF shield in Fig. 5.18. The effect of different separation distance from element to element, and from element to RF shield are investigated. In general, a large surface impedance provides a higher coupling level than a small surface impedance. Obviously, the coupling is stronger for a smaller separation between adjacent elements (d, θ). As the separation distance from the coil element to the RF shield (h) increases, a slightly reduced surface impedance selectivity of the coupling behavior is observed, indicated by a flatter curve for the power ratio. With the coil arrangement in Fig. 5.17, the minimum coupling between dipole elements appears when the surface impedance of the RF shield approaches 10 Ω. For extremely small and large surface impedance, the power ratio versus surface impedance is quite constant, showing a nearly flat curve. In comparison, the power ratio is more sensitive to the surface impedance in the range $0.1\ \Omega \leq Z_s \leq 10^3\ \Omega$. Basically, the optimal surface impedance behaves in a similar manner for different coil arrangement, except that for a larger element-to-element separation (d, θ), the coupling for the flat phantom arrangement is stronger than the one for the cylindrical phantom arrangement. This phenomenon can be explained by the more constructively superimposed electromagnetic field of the dipole elements due to the azimuthal offset.

5.3.2 Coupling Investigation based on 3-D Models

In this the coupling characteristics of stripline dipole coil elements with surface impedance characterized RF shields is investigated based on a three-dimensional model.

5.3.2.1 Simulation Setup

The three-dimensional simulation model for the coupling investigation of dipole elements is depicted in Fig. 5.19, where a symmetrically fed dipole coil element with meander terminals is utilized. The total length of the coil element is 25 cm. The geometry of the meander remains unchanged in comparison to the structure in [70]. In order to fine-tune the current distribution on the strip line, high-dielectric substrates have been placed around the meander sections to increase their electrical length [87]. Similar to the two-dimensional investigation, a flat and a cylindrical phantom arrangement are considered. Phantom parameters are kept unchanged compared to Section 5.3.1. The separation between neighboring elements for the flat and cylindrical phantom arrangement is set to $d = 10$ cm and $\theta = 48$ deg, respectively. The separation between the element and the RF shield is fixed to 1 cm for the three-dimensional investigations.

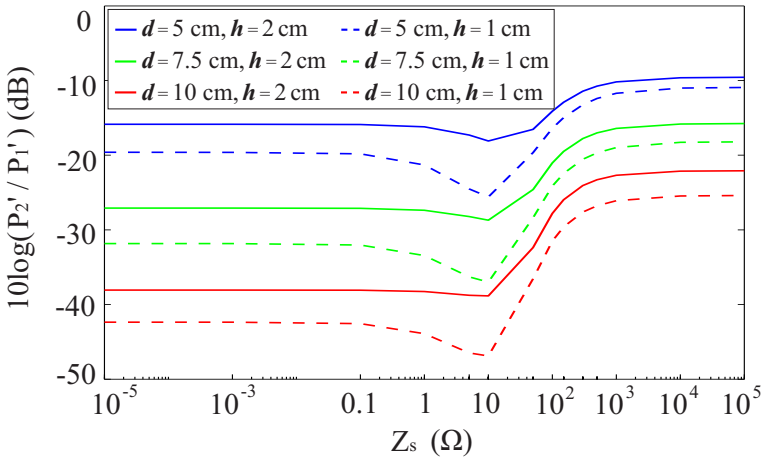

(a)

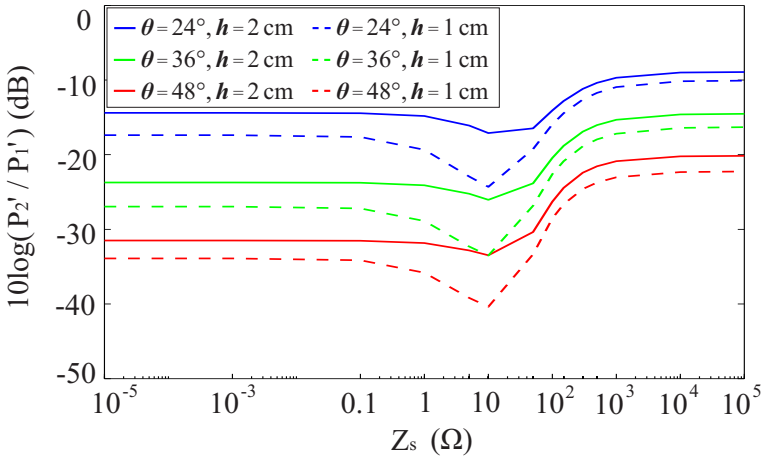

(b)

Figure 5.18: Calculated power ratio P_2'/P_1' for (a) the flat phantom arrangement and (b) the cylindrical phantom arrangement. P_1' and P_2' is the input power at the active element and the received power at the passive element, respectively. The effect of different separation distance from element to element (d, θ), and from element to RF shield (h) are investigated.

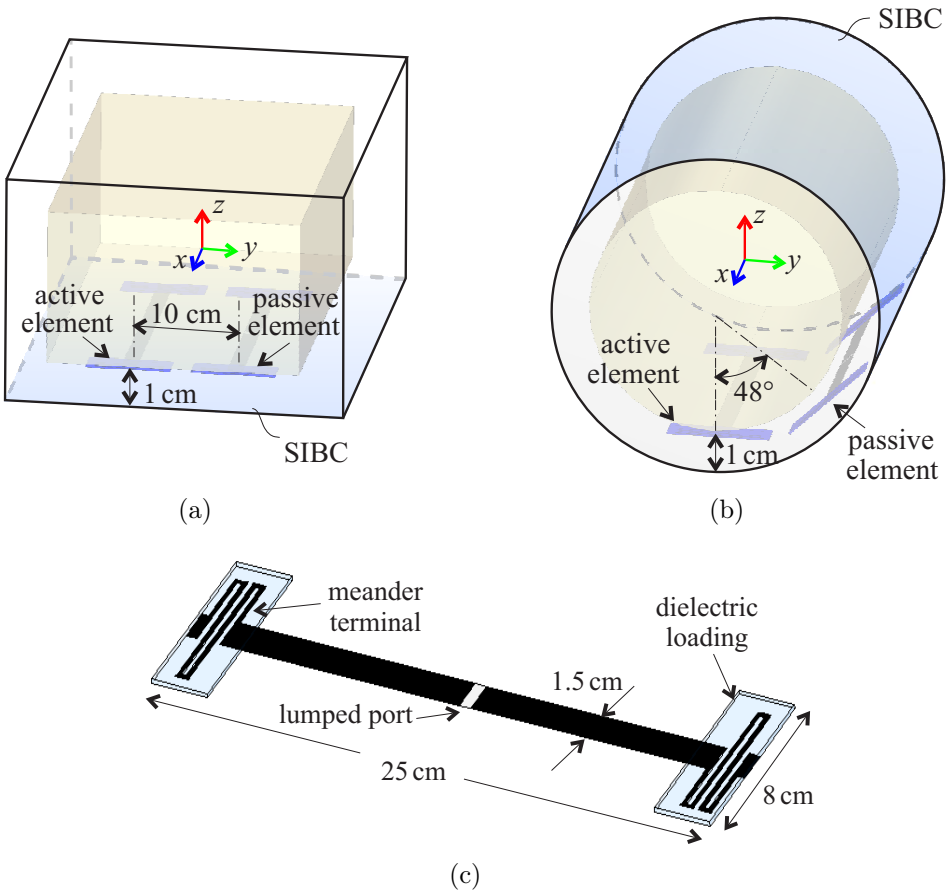

Figure 5.19: Three-dimensional simulation models for the coupling investigation of dipole elements with surface impedance characterized RF shields. (a) Two parallel aligned dipole elements below a flat phantom. (b) Two azimuthally offset dipole elements around a cylindrical phantom. (c) Symmetrically fed dipole element with meander terminals, which are covered by high-dielectric material.

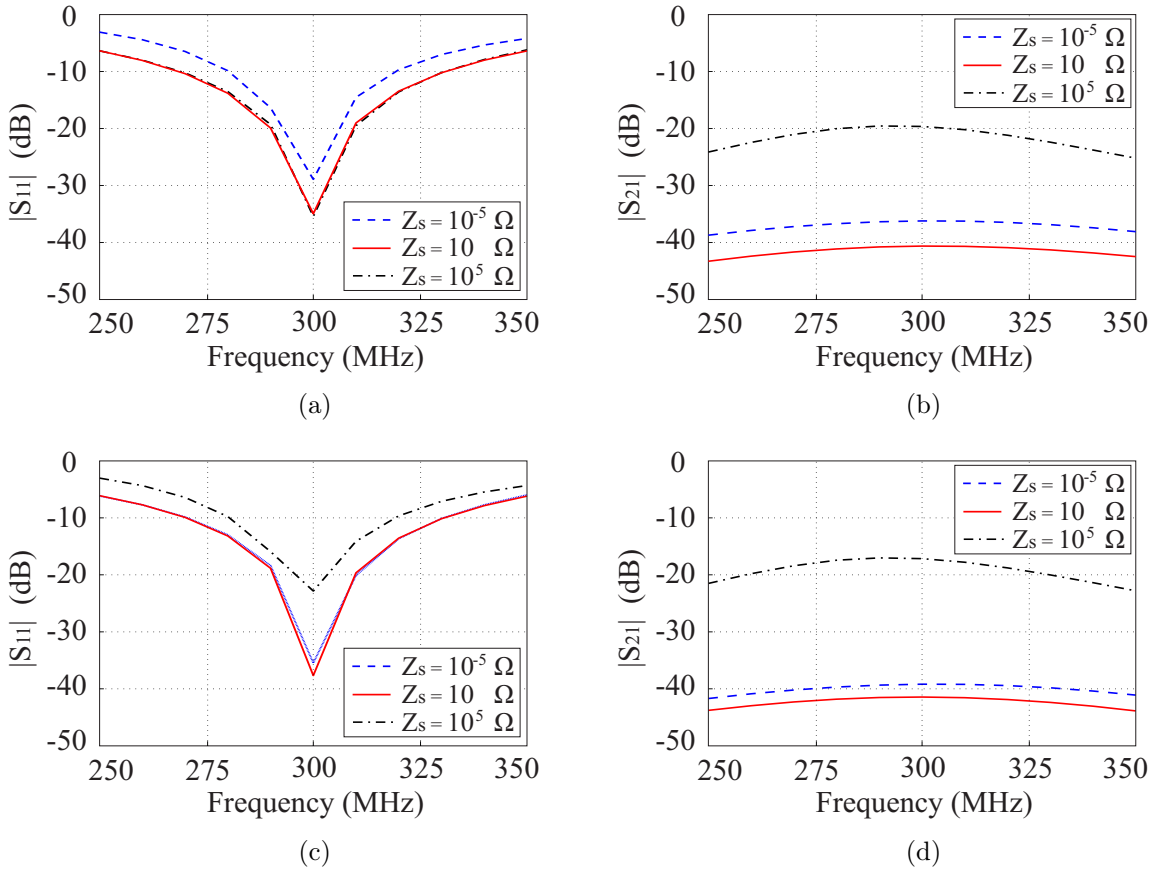

Figure 5.20: Simulated scattering parameters for (a, b) two parallel aligned dipole elements below a flat phantom, and (c, d) two azimuthally offset dipole elements around a cylindrical phantom.

5.3.2.2 Simulation Results

The simulated transmission coefficient $|S_{21}|$ of the coil arrangement (cf. Fig. 5.19) for different surface impedance of RF shield are plotted in Fig. 5.20. For each surface impedance a sufficient matching ($|S_{11}| \leq$ -25 dB) is achieved. The RF shield with large surface impedance ($Z_S = 10^5\ \Omega$) provides the highest coupling in the three compared cases. The coil elements with optimal surface impedance ($Z_S = 10\ \Omega$) from the two-dimensional investigation (cf. Fig. 5.18) reveal a minimum coupling at 300 MHz. The surface impedance $Z_S = 10^{-5}\ \Omega$ behaves in a quite similar manner as the optimal case, but with a slightly higher coupling level. The minor difference between $Z_S = 10\ \Omega$ and $Z_S = 10^{-5}\ \Omega$ is in accordance with the flat curve for low surface impedance values in Fig. 5.18.

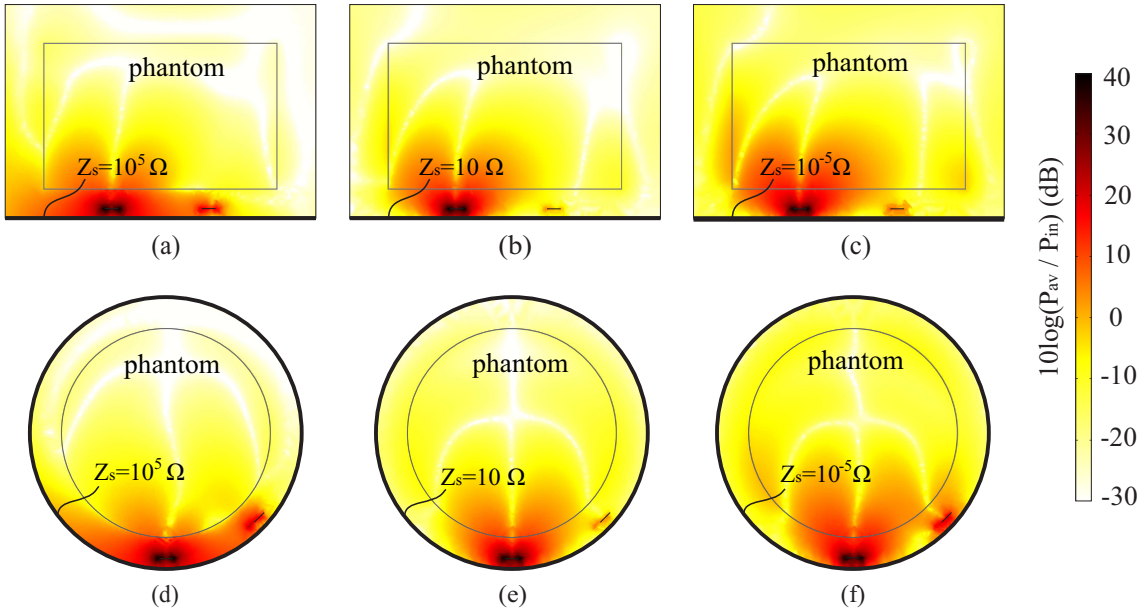

Figure 5.21: Time-averaged energy flux density in the transverse cut of the simulation domain for two parallel aligned dipole elements loaded by (a, b, c) a flat phantom [cf. Fig.5.19(a)], and (d, e, f) two azimuthally offset dipole elements loaded by a cylindrical phantom [cf. Fig.5.19(b)]. The surface impedance of the RF shield for (a, d), (b, e) and (c, f) is assigned to $10^5\ \Omega$, $10\ \Omega$ and $10^{-5}\ \Omega$, respectively. $Z_S = 10\ \Omega$ refers to the case with the optimal decoupling.

In order to understand the obtained coupling characteristics of the coil elements for different surface impedances, the time-averaged energy flux density P_{av} (i.e. Poyinting vector), which is normalized to the input power of the excited dipole element, in transverse cut ($z = 0$) of the simulation domain (cf. Fig. 5.21) was investigated. For a large surface impedance the energy flux density is focused in the vicinity of the coil element (outside the phantom) and extends to the neighboring element, resulting in a high coupling level. For a small surface impedance the coupling is mainly supported by the power flow inside the phantom. The different energy flux densities near the RF shield are due to the fact that the tangential electric field and normal magnetic field are supported by the boundary with large surface impedance, which is similar to a perfect magnetic conductor; whereas

they are suppressed by the boundary with small surface impedance, which is similar to a perfect electric conductor. The minimum coupling is achieved with the optimal surface impedance, where the energy flux density in- and outside the phantom are moderately balanced.

5.3.3 Summary of Coupling Investigation of Dipole Coils with SIBC Characterized Shields

In this section we presented a coupling investigation of dipole elements with surface impedance characterized RF shield. Two simulation models for the dipole coil element have been considered here: an ideal impressed current model for 2-D analysis, and a symmetrically fed dipole with meander terminals for the 3-D case. Depending on the spatial arrangement (e.g. the shape of the phantom, the edge-to-edge separation between coupled coil elements, the separation from coil element to RF shield), an optimal surface impedance of the RF shield could be found for a minimum coupling between neighboring coil elements. The optimal surface impedance can be realized by a frequency selective surface (FSS) [65]. Our investigation reveals a new approach to modify the coupling characteristics of the dipole coil elements for 7 T MRI. The dipole elements utilized here are designed for 7 T MRI, however, the proposed approach is very general and can be applied to other MRI settings with different magnetic field strengths as well.

5.4 Summary of Coupling Investigation of Multi-Channel RF Dipole Coils

In this chapter we carried out a coupling investigation of different RF dipole coil for 7 T MRI based on characteristic mode analysis. The coil element with lumped-element-connection to the shielding plate exhibits a loop-like current and focus the magnetic field below the stripline, which contributes mainly to the coupling to the neighboring element. The element without direct connection to the shielding plate behaves more like an electric dipole. Instead of being focused below the stripline, the magnetic field is distributed above the stripline in a broader manner, which is more considerable for the coupling. Specifically, the coil element presented in [70] seems to find a compromise between the two aforementioned scenarios and achieves an optimal decoupling.

Inspired by the results obtained from coupling investigation, we presented an eight-channel dipole coil consisting of different dipole coil elements, and explore the feasibility to achieve an optimal compromise between field distribution and coupling characteristic by combining different coil elements. Two types of dipole elements are considered here: the meandered dipole element with lumped-element connection to the RF shield (end-capacitor scenario), and in the absence of direct connection to the RF shield (open-ended scenario). It has been shown that the open-ended dipole coil exhibits a superior magnetic field distribution, whereas the dipole coil with end-capacitors achieves a sufficient decoupling between the neighboring elements. By nesting the open-ended dipole elements in between the ones with end-capacitors, the magnetic field distribution is improved in comparison to the dipole coil consisting only of the elements with end-capacitors, and meanwhile, the adjacent element are less coupled to each other in comparison to the dipole coil consisting only of the open-ended elements. Here we simply demonstrated the feasibility to improve the coil performance by combining different coil elements. According to specific applications, the combination strategy of dipole elements could be optimized. The presented investigation is based on full-wave simulation and experimental measurement, which match to each other very well. In addition to the near-field measurement, the eight-channel coil with combined dipole elements is applied to a 7 T MRI scanner to carry out an imaging test, which validated the proposed approach.

Additionally, a coupling investigation of dipole elements with surface impedance characterized RF shield is performed. Depending on the spatial arrangement (e.g. the shape of the phantom, the edge-to-edge separation between coupled coil elements, the separation from coil element to RF shield), an optimal surface impedance of the RF shield could be found for a minimum coupling between neighboring coil elements. The optimal surface impedance can be realized by a frequency selective surface (FSS) [65]. This investigation reveals a new approach to modify the coupling characteristics of the dipole coil elements for 7 T MRI. The dipole elements utilized here are designed for 7 T MRI, however, the proposed approach is very general and can be applied to other MRI settings with different magnetic field strengths as well.

Chapter 6

Conclusion and Outlook

In this chapter, the main research results of each chapter are summarized. Finally, a conclusion and an outlook on future works is presented.

6.1 Summary and Conclusion

In this thesis the feasibility to improve the radio frequency (RF) coil performance for 7 T magnetic resonance imaging (MRI) applications by using a high-impedance-surface (HIS) RF shield is investigated. It has been demonstrated, that the RF shield with high surface impedance provides an improved magnetic field distribution of dipole and loop coils compared to the conventional metal shield. It is worth mentioning that the presented investigation is performed for 7 T MRI, however, the proposed approach is very general and can be applied to other MRI settings with different magnetic field strengths as well.

Firstly, the RF shield is modeled by a surface impedance boundary condition (SIBC), which is characterized by the corresponding surface impedance on it. With this SIBC model, a fundamental investigation of the effect of different shields on the electromagnetic (EM) fields generated by the RF coils was carried out in a systematic manner. For each coil type (dipole and loop) two simulation models are considered: an ideal impressed current model for two-dimensional analysis and a real dipole/loop structure for three-dimensional analysis. We have observed that if the absolute electromagnetic field distribution is considered, the SIBC can be approximately characterized by the magnitude of a complex surface impedance. An increase of the surface impedance on the shielding plate leads to an improved homogeneity of the B_1 field distribution on the transversal plane, in terms of the field homogeneity and the absolute penetration depth. This approach was further verified by a multi-channel coil array arrangement, which consists of eight dipole elements equally distributed in azimuthal direction. For this eight-channel RF dipole coil, a 10% reduction on coefficient of variation of the transverse $|B_1^+|$ distribution, and a 7% increase on the averaged transverse $|B_1^+|$ can be achieved by using an RF shield with a high surface impedance ($1.2{\cdot}10^5$ Ω) comparing to the case with a small one (1.2 Ω). For a surface loop

coil, the B_1 field in vicinity of the RF shield with a large surface impedance is significantly enhanced compared to the case with a small surface impedance. As a result, the coil performance (SNR and B_1 efficiency) of a surface loop is considerably improved by the RF shield with a large surface impedance. The result obtained here may inspire the design of a low-profile surface coil with an artificial magnetic conductor (AMC) as the RF shield in order to achieve an enhanced B_1 distribution.

To realize the RF shield with a high surface impedance, which was modeled by a SIBC boundary previously, two compact HIS/EBG designs based on uni-planar and mushroom-like concepts for 7 T MRI application (297 MHz) were presented. In antenna applications the terminology of electromagnetic bandgap (EBG) structure is perhaps more widely and well known. In certain frequency bands EBG structures prevent the propagation of electromagnetic waves and exhibit a high surface impedance, hence they can be functionality considered as a HIS. In Chapter 3 we firstly provide a brief introduction to the HIS/EBG structure, including the definition, characterization, and well-known examples of a HIS/EBG structure. According to full-wave simulation, the proposed EBG structures exhibit a 0° reflection phase for a normal incidence at 297 MHz. Comparing to the uni-planar EBG, the mushroom-like EBG has a larger bandwidth over which the reflection phase falls between $\pi/2$ and $-\pi/2$. In the case of an oblique incidence, the mushroom-like EBG and uni-planar exhibits a larger sensitivity to the incident angle in terms of the resonant frequency for a TE and TM polarization, respectively. Based on dispersion diagram, both EBGs exhibit a frequency bandgap for surface wave propagation which includes the Larmor frequency for 7 T MRI (297 MHz). The uni-planar EBG achieves a wider band gap between the first two modes than the mushroom-like EBG. Additionally, the bandgap property of a finite-element EBG array based on the presented EBG designs were evaluated via two transmission line (TL) models. The full-wave simulation and experimental results match well to each other and indicate that the mushroom-like EBG suppresses a surface wave and the corresponding stop-band can be evaluated by the suspended TL model, while the uni-planar EBG is more sufficient for surface current suppression and a co-planar TL model shall be utilized to detect the stop-band.

Due to the absence of the vertical conducting vias the fabrication of the compact uni-planar EBG is easier to fabricate in comparison to the mushroom-like EBG, and hence, is utilized to realize the HIS shield. The field characteristics of the considered RF coils (dipole and loop) backed by the realized HIS shield and a conventional metal shield were investigated based on full-wave simulation, and further validated by experimental results. We have seen that, compared to the conventional metal shield, the B_1 distribution of the considered coils is significantly improved by the HIS shield, both in terms of field homogeneity and penetration depth. Additionally, the improvement due to the HIS shield degrades with a larger penetration depth into the phantom, and a larger separation distance from the HIS shield to the coil. Nevertheless, the presented investigation may inspire the design of a low-profile RF coil with improved coil performance compared to the conventional metal shield.

Besides the field based investigation, we presented an investigation of coupling mechanism of several well-established dipole coil elements by applying a characteristic mode analysis

and full-wave simulation. Two types of dipole elements were considered here: the meandered dipole element with lumped-element connection to the RF shield (end-capacitor scenario), and in the absence of direct connection to the RF shield (open-ended scenario). It has been shown that the open-ended dipole coil exhibits a superior magnetic field distribution, whereas the dipole coil with end-capacitors achieves a sufficient decoupling between the neighboring elements. Based on these results from coupling investigation, a multi-channel dipole coil which combined the aforementioned two dipole types was proposed. An compromise between the field distribution and the coupling characteristic was achieved. Additionally, a fundamental investigation was carried out to evaluate how the coupling mechanism is affected by the RF shield which is characterized by its surface impedance. Depending on the spatial arrangement (e.g. the shape of the phantom, the edge-to-edge separation between coupled coil elements, the separation from coil element to RF shield), an optimal surface impedance of the RF shield could be found for a minimum coupling between neighboring coil elements. This fundamental investigation has shown a new approach to modify the coupling characteristics of the dipole coil elements for UHF MRI.

In summary, this work demonstrated the possibility to enhance the RF coil performance by using HIS shield instead of the conventional metal shield. The utilized HIS shield is realized by a two-dimensional compact uni-planar EBG structure. The HIS shield approach was validated through full-wave simulation and near-field measurement, as well as test in a 7 T MRI scanner.

6.2 Outlook

The approach to improve the B_1 distribution of the RF coils has been systematically investigated through full-wave simulation and near-field measurement. Before carrying out the final *in-vivo* imaging test, the SAR evaluation based on heterogeneous body models should be performed, which has not been accomplished yet due to the extreme time consumption for simulation. The utilized HIS structure has an extremely thin substrate layer, where the top and floating metal layers are printed and create a metal-insulator-metal (MIM) capacitance. Hence, a more compact lattice design can be achieved due to the enhanced total capacitance (cf. Chapter 3). However, this extremely thin layer requires an extremely fine mesh grid to appropriately describe its geometry, which leads to an over-long simulation time.

In order to avoid the aforementioned issue concerning the simulation time, some alternative lattice designs of the HIS structure, which have a larger thickness of the top substrate, should be investigated. As a result, more complicated metal structures on the top surface might be needed to compensate the reduction on MIM capacitance due to the increased thickness of the top substrate.

The first prototype of the multi-channel dipole surrounded by a HIS shield is constructed on a “hard” acrylic glass tube, which causes inconvenience during the construction process,

especially for the gluing of the MIM layer on the inner side of the acrylic glass tube. Alternatively, "soft" materials with similar parameters (ϵ_r, tanδ) can be utilized to achieve a more flexible HIS shield, which is considerably lighter and easier to handle. Another advantage of such a flexible HIS shield is that it can be better accommodated to patient's contour for whole-body imaging.

Finally, the proposed approach to improve the RF coil performance by HIS shields is very general and can be applied to other MRI settings with different magnetic field strengths as well. Recently, this approach has been applied to MRI systems with lower field strength, and revealed promising results [112, 113]. Part of the future work could be further investigate the application of the HIS shield approach in other magnetic field strengths, e.g. 1.5 T, 3 T, 9.4 T.

Bibliography

[1] H. E. Martz, C. M. Logan, D. J. Schneberk, and P. J. Shull, *X-Ray Imaging: Fundamentals, Industrial Techniques, and Applications*. CRC Press, August 2016.

[2] W. Gerlach and O. Stern, "Das magnetische Moment des Silberatoms," *Zeitschrift für Physik*, vol. 9, no. 1, pp. 353–355, 1922.

[3] J. M. B. Kellogg, I. I. Rabi, N. F. Ramsey, and J. R. Zacharias, "The Magnetic Moments of the Proton and the Deuteron. The Radiofrequency Spectrum of H $_2$ in Various Magnetic Fields," *Phys. Rev.*, vol. 56, pp. 728–743, 1939.

[4] I. I. Rabi, S. Millman, P. Kusch, and J. R. Zacharias, "The Molecular Beam Resonance Method for Measuring Nuclear Magnetic Moments. The Magnetic Moments of $_3\mathrm{Li}^6$, $_3\mathrm{Li}^7$ and $_9\mathrm{F}^{19}$," *Phys. Rev.*, vol. 55, pp. 526–535, 1939.

[5] P. V. Prasad, Ed., *Magnetic Resonance Imaging: Methods and Biologic Applications*, ser. Methods in Molecular Medicine. Humana Press, 2006.

[6] F. Bloch, W. W. Hansen, and M. Packard, "Nuclear Induction," *Phys. Rev.*, vol. 69, p. 127, 1946.

[7] E. M. Purcell, H. C. Torrey, and R. Pound, "Resonance absorption by nuclear magnetic moments in a solid," *Phys. Rev.*, vol. 69, p. 37, 1946.

[8] E. D. Becker, "A Brief History of Nuclear Magnetic Resonance," *Anal. Chem.*, vol. 65, no. 6, pp. 295A–302A, March 1993.

[9] R. Damadian, "Tumor Detection by Nuclear Magnetic Resonance," *Science.*, vol. 171, no. 3976, pp. 1151–3, 1971.

[10] P. C. Lauterbur, "Image Formation by Induced Local Interactions: Examples Employing Nuclear Magnetic Resonance," *Nature*, vol. 242, no. 5394, pp. 190–191, 1973.

[11] P. C. Lauterbur, "Magnetic Resonance Zeugmatography," *Pure and Applied Chemistry*, vol. 40, pp. 149–157, 1974.

[12] A. Kumar, D. Welti, and R. R. Ernst, "NMR Fourier zeugmatography," *J. Magn. Reson.*, vol. 18, pp. 69–83, 1975.

[13] P. Mansfield, "Multi-planar image formation using NMR spin echoes," *J. Phys. C: Solid State Phys.*, vol. 10, pp. L55–L58, 1977.

[14] P. A. Bottomley, H. R. Hart, W. A. Edelstein, J. F. Schenck, L. S. Smith, W. M. Leue, O. M. Mueller, and R. W. Redington, "NMR Imaging/spectroscopy System To Study Both Anatomy And Metabolism," *Lancet.*, vol. 2, no. 8344, pp. 273–274, 1983.

[15] P. Mansfield, "Real-Time Echo-Planar Imaging By NMR," *Br. Med. Bull.*, vol. 40, no. 2, pp. 187–190, 1984.

[16] A. Haase, J. Frahm, D. Matthaei, W. Hanicke, and K.-D. Merboldt, "FLASH imaging: Rapid NMR Imaging Using Low Flip-Angle Pulses," *J. Magn. Reson.*, vol. 67, no. 2, pp. 258–266, 1986.

[17] D. K. Sodickson and W. J. Manning, "Simultaneous acquisition of spatial harmonics (SMASH): Fast imaging with radiofrequency coil arrays," *Magn. Reson. Med.*, vol. 38, no. 4, pp. 591–603, 1997.

[18] K. P. Pruessmann, M. Weiger, M. B. Scheidegger, and P. Boesiger, "SENSE: sensitivity encoding for fast MRI," *Magn. Reson. Med.*, vol. 42, no. 5, pp. 952–962, September 1999.

[19] M. A. Griswold, P. A. Jakob, R. M. Heidemann, M. Nittka, V. Jellus, J. Wang, B. Kiefer, and A. Haase, "Generalized Autocalibrating Partially Parallel Acquisitions (GRAPPA)," *Magn. Reson. Med.*, vol. 47, pp. 1202–10, 2002.

[20] J. T. Vaughan, M. Garwood, C. M. Collins, W. Liu, L. DelaBarre, G. Adriany, P. Andersen, H. Merkle, R. Goebel, M. B. Smith, and K. Ugurbil, "7T vs. 4T: RF power, homogeneity, and signal-to-noise comparison in head images," *Magn. Reson. Med.*, vol. 46, no. 1, pp. 24–30, 2001.

[21] T. Vaughan, L. DelaBarre, C. Snyder, J. Tian, C. Akgun, D. Shrivastava, W. Liu, C. Olson, G. Adriany, J. Strupp, P. Andersen, P.-F. van de Moortele, M. Garwood, and K. Ugurbil, "9.4T human MRI: preliminary results," *Magn. Reson. Med.*, vol. 56, no. 6, pp. 1274–82, 2006.

[22] C. Qian, I. S. Masad, J. T. Rosenberg, M. Elumalai, W. W. Brey, S. C. Grant, and P. L. Gor'kov, "A volume birdcage coil with an adjustable sliding tuner ring for neuroimaging in high field vertical magnets: ex and in vivo applications at 21.1T," *J. Magn. Reson.*, vol. 221, pp. 110–116, 2012.

[23] J. T. Vaughan, C. J. Snyder, L. J. DelaBarre, P. J. Bolan, J. Tian, L. Bolinger, G. Adriany, P. Andersen, J. Strupp, and K. Ugurbil, "Whole-body imaging at 7T: Preliminary results," *Magn. Reson. Med.*, vol. 61, no. 1, pp. 244–248, 2009.

[24] S. G. van Elderen, M. J. Versluis, A. G. Webb, J. J. Westenberg, J. Doornbos, N. B. Smith, A. de Roos, and M. Stuber, "Initial Results on In Vivo Human Coronary MR Angiography at 7 T," *Magn. Reson. Med.*, vol. 62, pp. 1379–84, 2009.

[25] C. J. Snyder, L. DelaBarre, G. J. Metzger, P.-F. van de Moortele, K. Akgun, C. Ugurbil, and J. T. Vaughan, "Initial Results of Cardiac Imaging at 7 Tesla," *Magn. Reson. Med.*, vol. 61, pp. 517–524, 2009.

[26] O. Kraff, A. K. Bitz, P. Dammann, M. E. Ladd, and H. H. Quick, "An eight-channel transmit/receive multipurpose coil for musculoskeletal MR imaging at 7 T," *Med. Phys.*, vol. 37, no. 12, pp. 6368–76, 2010.

[27] M. A. Korteweg, W. B. Veldhuis, F. Visser, P. R. Luijten, W. P. Mali, P. J. van Diest, M. A. van den Bosch, and D. J. Klomp, "Feasibility of 7 Tesla breast magnetic resonance imaging determination of intrinsic sensitivity and high-resolution magnetic resonance imaging, diffusion-weighted imaging, and (1)H-magnetic resonance spectroscopy of breast cancer patients receiving neoadjuvant therapy," *Invest. Radiol.*, vol. 46, pp. 370–376, 2011.

[28] D. Weishaupt, J. Froehlich, D. Nanz, V. Koechli, K. Pruessmann, and B. Marincek, *How does MRI work?: An Introduction to the Physics and Function of Magnetic Resonance Imaging*, 2nd ed. Springer, 2008.

[29] R. H. Hashemi, W. G. Bradley Jr, and C. J. Lisanti, *MRI: The Basics*, 3rd ed. Lippincott Williams&Wilki, 2010.

[30] R. W. Brown, Y.-C. N. Cheng, E. M. Haacke, M. R. Thompson, and R. Venkatesan, *Magnetic Resonance Imaging: Physical Principles and Sequence Design*, 2nd ed. Wiley-Blackwell, June 2014.

[31] M. A. Bernstein, K. F. King, and X. J. Zhou, Eds., *Handbook of MRI Pulse Sequences*. Elsevier Academic Press, 2004.

[32] C. Westbrook, *MRI at a Glance*, 2nd ed. Wiley-Blackwell, 2009.

[33] J. R. McFall, *Hardware and coils for MR imaging*, In: Riederer SJ, Wood ML (eds) Categorical course in physics: The basic physics of MR imaging. RSNA Publications no 41, Oak Brook Std., 1997.

[34] J. T. Vaughan and J. R. Griffiths, Eds., *RF Coils for MRI*. Wiley, August 2012.

[35] J. Mispelter, M. Lupu, and A. Briguet, *NMR Probeheads for Biophysical and Biomedical Experiments: Theoretical Principles and Practical Guidelines*, 2nd ed. Imperial College Press, 2013.

[36] J. Hennig and O. Speck, Eds., *High-Field MR Imaging*, ser. Medical Radiology. Springer, 2011.

[37] D. O. Brunner, N. De Zanche, J. Fröhlich, J. Paska, and K. P. Pruessmann, "Travelling wave nuclear magnetic resonance," *Nature*, vol. 457, pp. 994–998, Feb. 2009.

[38] D. O. Brunner, N. De Zanche, J. Paska, J. Fröhlich, and K. P. Pruessmann, "Travelling wave MR: Comparison with a volume resonator at 7T," in *25th Annual Sci. Meeting of Europ. Soc. for Magn. Reson. in Med. and Biol.*, Valencia, Spain, Oct. 2-4, 2009, pp. 61–62.

[39] D. Erni, T. Liebig, N. H. L. Koster, and A. Rennings, "Meta-MRT-Antennenvorrichtungen für die Wanderwellen-Magnetresonanztomographie," Universität Duisburg-Essen, Allgemeine und Theoretische Elektrotechnik (ATE), Dec. 13, 2012, (German patent, reference number 10 2011 111 996).

[40] A. Rennings, J. Mosig, A. Bahr, C. Caloz, M. E. Ladd, and D. Erni, "A CRLH Metamaterial based RF Coil Element for Magnetic Resonance Imaging at 7 Tesla," in *3rd Eur. Antennas Propag. Conf*, Berlin, Germany, March 23-27, 2009, pp. 3231–3234.

[41] J. F. Schenck, "Health and Physiological Effects of Human Exposure to Whole-Body Four-Tesla Magnetic Fields during MRI," *Ann N Y Acad Sci*, vol. 649, pp. 285–301, 1992.

[42] J. F. Schenck, C. L. Dumoulin, R. W. Redington, H. Y. Kressel, R. T. Elliott, and I. L. McDougall, "Human exposure to 4.0-Tesla magnetic fields in a whole-body scanner," *Med. Phys.*, vol. 19, pp. 1089–1098, 1992.

[43] M. J. P. van Osch and A. G. Webb, "Safety of Ultra-High Field MRI: What are the Specific Risks?" *Curr. Radiol. Rep.*, vol. 2:61, 2014.

[44] J. D. Joannopoulos, S. G. Johnson, J. N. Winn, and R. D. Meade, *Photonic Crystals: Molding the Flow of Light*, 2nd ed. Princeton University Press, Februar 2008.

[45] B. A. Munk, *Frequency Selective Surfaces: Theory and Design*. John Wiley & Sons, Inc., Mai 2000.

[46] E. Yablonovitch, "Inhibited Spontaneous Emission in Solid-State Physics and Electronics," *Phys. Rev. Lett.*, vol. 58, pp. 2059–2062, 1987.

[47] D. Sievenpiper, L. Zhang, F. J. Broas, N. G. Alexopolous, and E. Yablonovitch, "High-Impedance Electromagnetic Surfaces with a Forbidden Frequency Band," *IEEE Trans. Microw. Theory Techn.*, vol. 47, no. 11, pp. 2059–74, November 1999.

[48] Y. Rahmat-Samii and H. Mosallaei, "Electromagnetic band-gap structures: Classification, characterization and applications," in *Proc. Inst. Elect. Eng.-ICAP Symp.*, April 17-20, 2001, pp. 560–564.

[49] L. Brillouin, *Wave Propagation in Periodic Structures: Electric Filters and Crystal Lattices*, 1st ed. McGraw-Hill, 1946.

[50] F. Yang and Y. Rahmat-Samii, *Electromagnetic Band Gap Structures in Antenna Engineering*. Cambridge University Press, 2008.

[51] R. Gonzalo, P. Maagt, and M. Sorolla, "Enhanced Patch-Antenna Performance by Suppressing Surface Waves Using Photonic-Bandgap Substrates," *IEEE Trans. Microw. Theory Techn.*, vol. 47, no. 11, pp. 2131–8, November 1999.

[52] R. Coccioli, F.-R. Yang, K.-P. Ma, and T. Itoh, "Aperture-Coupled Patch Antenna on UC-PBG Substrate," *IEEE Trans. Microw. Theory Techn.*, vol. 47, no. 11, pp. 2123–2130, November 1999.

[53] F.-R. Yang, K.-P. Ma, Y. Qian, and T. Itoh, "A Uniplanar Compact Photonic-Bandgap (UC-PBG) Structure and Its Applications for Microwave Circuits," *IEEE Trans. Microw. Theory Techn.*, vol. 47, no. 8, pp. 1509–1514, August 1999.

[54] F. Yang and Y. Rahmat-Samii, "Microstrip Antennas Integrated With Electromagnetic Band-Gap (EBG) Structures: A Low Mutual Coupling Design for Array Applications," *IEEE Trans. Antennas Propag.*, vol. 51, no. 10, pp. 2936–46, October 2003.

[55] D. Sievenpiper, J. H. Schaffner, H. J. Song, R. Y. Loo, and G. Tangonan, "Two-Dimensional Beam Steering Using an Electrically Tunable Impedance Surface," *IEEE Trans. Antennas Propag.*, vol. 51, no. 10, pp. 2713–2722, October 2003.

[56] Z. Chen, K. Solbach, D. Erni, and A. Rennings, "Improved B1 Homogeneity of an MRI RF Coil Element using a High-Impedance-Surface Shield," in *9th German Microw. Conf.*, Nürnberg, Germany, March16-18, 2015, pp. 111–114.

[57] A. F. Harvey, "Periodic and Guiding Structures at Microwave Frequencies," *IRE Trans. Microw. Theory Tech.*, vol. 8, pp. 30–61, 1960.

[58] V. Radisic, Y. Qian, R. Coccioli, and T. Itoh, "Novel 2-D Photonic Bandgap Structure for Microstrip Lines," *IEEE Microw. Guided Wave Lett.*, vol. 8, no. 2, pp. 69–71, Feb 1998.

[59] E. Yablonovitch, T. J. Gmitter, and K. M. Leung, "Photonic band structure: The face-centered-cubic case employing nonspherical atoms," *Phys. Rev. Lett.*, vol. 67, no. 17, pp. 2295–2298, Oct 1991.

[60] E. Özbay, E. Michel, G. Tuttle, R. Biswas, M. Sigalas, and K.-M. Ho, "Micromachined millimeter-wave photonic band-gap crystals," *Appl. Phys. Lett.*, vol. 64, no. 16, pp. 2059–2061, Apr 1994.

[61] R. E. Collin, *Field Theory of Guided Waves*, 2nd ed. Wiley-IEEE Press, December 1990.

[62] C. S. Kim, J. S. Park, D. Ahn, and J. B. Lim, "A novel 1-D periodic defected ground structure for planar circuits," *IEEE Microw. Guided Wave Lett.*, vol. 10, no. 4, pp. 131–133, Apr 2000.

[63] D. Ahn, J.-S. Park, C.-S. Kim, J. Kim, Y. Qian, and T. Itoh, "A Design of the Low-Pass Filter Using the Novel Microstrip Defected Ground Structure," *IEEE Trans. Microw. Theory Tech.*, vol. 49, no. 1, pp. 86–93, Jan 2001.

[64] C. Chang, Y. Qian, and T. Itoh, "Analysis and Applications of Uniplanar Compact Photonic Bandgap Structures," *Progress In Electromagnetics Research*, vol. 41, pp. 211–235, 2003.

[65] N. Engheta and R. W. Ziolkowski, Eds., *Metamaterials: Physics and Engineering Explorations* . Wiley-IEEE Press, August 2006.

[66] T. J. Shepherd, C. R. Brewitt-Taylor, P. Dimond, G. Fixter, A. Laight, P. Lederer, P. J. Roberts, P. R. Tapster, and I. J. Youngs, "3D microwave photonic crystals: Novel fabrication and structures," *Electron Lett.*, vol. 34, no. 8, pp. 787–789, Apr 1998.

[67] G. Saleh, K. Solbach, and A. Rennings, "EBG Structure to Improve the B1 Efficiency of Stripline Coil for 7 Tesla MRI," in *6th Eur. Antennas Propag. Conf*, Prague, Czech Republik, March 26-30, 2012, pp. 1399–1401.

[68] G. Saleh, K. Solbach, D. Erni, and A. Rennings, "Four-Leaf-Clover-Shaped EBG Structure to Improve the H/E Field Ratio of Stripline Coil for 7 Tesla MRI," in *7th Eur. Antennas Propag. Conf*, Gothenburg, Sweden, April 8-12, 2013, pp. 1088–1090.

[69] D. O. Brunner, N. De Zanche, J. Froehlich, D. Baumann, and K. Pruessmann, "A symmetrically fed microstrip coil array for 7T," in *15th Proc. Intl. Soc. MRM*, 2007, p. 448.

[70] S. Orzada, A. Bahr, and T. Bolz, "A novel 7 T microstrip element using meanders to enhance decoupling," in *16th Proc. Intl. Soc. MRM*, Toronto, Ontario, Canada, May 3-9, 2008, p. 2979.

[71] Z. Chen, K. Solbach, D. Erni, and A. Rennings, "RF Coil Element with Longitudinal and Transversal Two-Peak Field Distribution for Low SAR 7-Tesla Magnetic Resonance Imaging," in *IEEE MTT-S Int. Microw. Symp. Dig.*, Seattle, WA, USA, June 2-7, 2013, pp. 1–4.

[72] P.-F. Van de Moortele, C. Akgun, G. Adriany, S. Moeller, J. Ritter, C. Collin, M. Smith, J. Vaughan, and K. Ugurbil, "B_1 destructive to interferences and spatial phase patterns at 7 T with head transceiver array coil," *Magn. Reson. Med.*, vol. 54, pp. 1503–1518, 2005.

[73] J. T. Vaughan, G. Adriany, G. Snyder, J. Tian, T. Thiel, L. Bolinger, H. Liu, L. DelaBarre, and K. Ugurbil, "Efficient High-Frequency Body Coil for High-Field MRI," *Magn. Reson. Med.*, vol. 52, pp. 851–859, 2004.

[74] G. Adriany, P.-F. Van de Moortele, F. Wiesinger, S. Moeller, J. P. Strupp, P. Andersen, C. Snyder, X. Zhang, W. Chen, K. P. Pruessmann, P. Boesiger, T. Vaughan, and K. Ugurbil, "Transmit and receive transmission line arrays for 7 Tesla parallel imaging," *Magn. Reson. Med.*, vol. 53, pp. 434–445, 2005.

[75] G. Adriany, P.-F. Van de Moortele, J. Ritter, S. Moeller, E. J. Auerbach, C. Akgün, C. J. Snyder, T. Vaughan, and K. Ugurbil, "A geometrically adjustable 16-channel transmit/receive transmission line array for improved RF efficiency and parallel imaging performance at 7 Tesla," *Magn. Reson. Med.*, vol. 59, pp. 590–597, 2008.

[76] S. Orzada, S. Maderwald, O. Kraff, I. Brote, M. E. Ladd, K. Solbach, P. Yazdanbakhsh, A. Bahr, H. P. Fautz, and A. K. Bitz, "16-Channel Tx/Rx Body Coil for RF Shimming with Selected Cp Modes at 7T," in *18th Proc. Intl. Soc. MRM*, Stockholm, Sweden, May 1-7, 2010, p. 50.

[77] A. J. E. Raaijmakers, O. Ipek, D. W. J. Klomp, C. Possanzini, P. R. Harvey, J. J. W. Lagendijk, and C. A. T. van den Berg, "Design of a Radiative Surface Coil Array Element at 7 T: The Single-Side Adapted Dipole Antenna," *Magn. Reson. Med.*, vol. 66, pp. 1488–1497, 2011.

[78] A. Raaijmakers, P. R. Luijten, and C. A. van den Berg, "Why do dipole antennas work? A comparison to loop coils as a function of element size," in *22nd Proc. Intl. Soc. MRM*, Milan, Italy, May 10-16, 2014, p. 4887.

[79] F. D. Doty, G. Entzminger, J. Kulkarni, K. Pamarthy, and J. P. Staab, "Radio frequency coil technology for small-animal MRI," *NMR Biomed.*, vol. 20, pp. 304–325, 2007.

[80] S. Tretyakov, *Analytical Modeling in Applied Electromagnetics*. Artech House, 2003.

[81] S. V. Yuferev and N. Ida, *Surface Impedance Boundary Conditions: A Comprehensive Approach*. CRC Pressr, 2009.

[82] Z. Chen, K. Solbach, D. Erni, and A. Rennings, "Electromagnetic Field Analysis of a Dipole Coil Element with Surface Impedance Characterized Shielding Plate for 7-Tesla MRI," *IEEE Trans. Microw. Theory Techn.*, vol. 64, no. 3, pp. 972–981, March 2016.

[83] T. B. A. Senior, "Approximation boundary conditions, part 1," University of Michigan Radiation Laboratory Report RL-861, Ann Arbor, MI, Tech. Rep., 1990.

[84] D. M. Pozar, *Microwave Engineering*, 4th ed. John Wiley & Sons, 2004.

[85] H. Raether, *Surface Plasmons on Smooth and Rough Surfaces and on Gratings*. New York: Springer-Verlag, 1988.

[86] S. A. Maier, *Plasmonics: Fundamentals and Applications*. Springer, 2007.

[87] Z. Chen, K. Solbach, D. Erni, and A. Rennings, "Dipole RF Element for 7 Tesla magnetic resonance imaging with minimized SAR," in *7th Eur. Antennas Propag. Conf*, Gothenburg, Sweden, April 8-12, 2013., pp. 1775–1778.

[88] F. G. Shellock, "Radiofrequency Energy-Induced Heating During MR Procedures: A Review," *J. Magn. Reson. Imaging*, vol. 12, pp. 30–36, 2000.

[89] B. M. Dawant, A. P. Zijdenbos, and R. A. Margolin, "Correction of Intensity Variations in MR Images for Computer-Aided Tissue Classification," *IEEE Trans. Med. Imaging*, vol. 12, no. 4, pp. 770–781, 1993.

[90] D. Wicks, G. J. Barker, and P. S. Tofts, "Correction of Intensity Nonuniformity in MR Images of any Orientation," *Magn. Reson. Imaging*, vol. 11, no. 2, pp. 183–196, 1993.

[91] D. I. Hoult, C.-N. Chen, and V. J. Sank, "Quadrature Detection in the Laboratory Frame," *Magn. Reson. Med.*, vol. 1, no. 3, pp. 339–353, September 1984.

[92] G. H. Glover, C. E. Hayes, N. J. Pelc, W. A. Edelstein, O. M. Mueller, H. R. Hart, C. J. Hardy, M. O'Donnell, and W. D. Barber, "Comparison of linear and circular polarization for magnetic resonance imaging," *J. Magn. Reson.*, vol. 64, pp. 255–270, 1985.

[93] H. Homann, *SAR Prediction and SAR Management for Parallel Transmit MRI*, ser. Karlsruhe transactions on biomedical engineering. KIT Scientific Publishing, 2012.

[94] W. Schnell, W. Renz, M. Vester, and H. Ermert, "Ultimate Signal-to-Noise-Ratio of Surface and Body Antennas for Magnetic Resonance Imaging," *IEEE Trans. Antennas Propag.*, vol. 48, no. 3, pp. 418–428, March 2000.

[95] D. F. Sievenpiper, "High-Impedance Electromagnetic Surfaces," Ph.D. dissertation, Ph.D. dissertation at University of California, Los Angeles, 1999.

[96] C. Kittel, *Introduction to Solid State Physics*, 7th ed. John Wiley & Sons, Oct. 1995.

[97] C. Kittel, *Introduction to Solid State Physics*, 7th ed. New York: Wiley Text Books, 1964.

[98] B.-Q. Lin, J. Liang, Y.-S. Zeng, and H.-M. Zhang, "A Novel Compact and Wide-Band Uni-Planar EBG Structure," *Progress In Electromagnetics Research C*, vol. 1, pp. 37–43, 2008.

[99] L. Peng, C.-l. Ruan, and J. Xiong, "Compact EBG for Multi-Band Applications," *IEEE Trans. Antennas Propag.*, vol. 60, no. 9, pp. 4440–4444, 2012.

[100] L. Kurra, M. P. Abegaonkar, A. Basu, and S. Koul, "A compact uniplanar EBG structure and its application in band-notched UWB filter," *Int. J. Microwave and Wireless Tech.*, vol. 5, pp. 491–498, 2013.

[101] Z. Chen, K. Solbach, D. Erni, and A. Rennings, "A Compact Electromagnetic Bandgap Structure based on Multi-layer Technology for 7-Tesla Magnetic Resonance Imaging Applications," in *44th Eur. Microw. Conf.*, Rome, Italy, Oct. 6-9, 2014, pp. 1576–1579.

[102] M. Y. Fan, R. Hu, Q. Hao, X. Zhang, and Z. Feng, "Advance in 2D-EBG research," *J. Infrared Millim. Waves*, vol. 22, no. 2, 2003.

[103] A. Aminian, F. Yang, and Y. Rahmat-Samii, "In-phase Reflection and EM Wave Suppression Characteristics of Electromagnetic Band Gap Ground Planes," in *2003 IEEE AP-S Dig.*, vol. 4, pp. 430-433, June 2003.

[104] R. J. Cameron, R. Mansour, and C. M. Kudsia, *Microwave Filters for Communication Systems : Fundamentals, Design and Applications*, 1st ed. John Wiley & Sons, 2007.

[105] R. F. Harrington and J. R. Mautz, "Theory of Characteristic Modes for Conducting Bodies," *IEEE Trans. Antennas Propag.*, vol. AP-19, no. 5, pp. 622–628, September 1971.

[106] C. A. Balanis, *Antenna Theory: Analysis and Design*, 3rd ed. John Wiley & Sons, May 2005.

[107] T. Liebig. openEMS - Open Electromagnetic Field Solver. General and Theoretical Electrical Engineering (ATE), University of Duisburg-Essen. [Online]. Available: http://openEMS.de

[108] Z. Chen, K. Solbach, D. Erni, and A. Rennings, "Coupling Investigation of Different RF Coil Elements for 7-Tesla Magnetic Resonance Imaging based on Characteristic Mode Analysis," in *IEEE MTT-S Int. Microw. Symp. Dig.*, Tampa Bay, FL, USA, June 1-6, 2014, pp. 1–4.

[109] R. F. Harrington, *Time-Harmonic Electromagnetic Fields*. Wiley-IEEE Press, September 2001.

[110] S. Brunheim, S. Orzada, S. Johst, M. Gratz, M. N. Voelker, O. Kraff, M. Floeser, A. K. Bitz, M. E. Ladd, and H. H. Quick, "Combining B1 mapping with TIAMO for fast and accurate multi-channel RF shimming in 7 Tesla body MRI," in *24th Proc. Intl. Soc. MRM*, Singapore, May 7-13, 2016, p. 0936.

[111] Z. Chen, K. Solbach, D. Erni, and A. Rennings, "Coupling Investigation between RF Coil Array Elements backed by Surface Impedance Characterized Shields for 7 Tesla MRI," in *10th German Microw. Conf.*, Bochum, Germany, March14-16, 2016, pp. 112–115.

[112] J. M. Algarín, M. J. Freire, F. Breuer, and V. C. Behr, "Metamaterial magnetoinductive lens performance as a function of field strength," *J. Magn. Reson.*, vol. 247, pp. 9–14, Oct. 2014.

[113] A. P. Slobozhanyuk, A. N. Poddubny, A. J. Raaijmakers, C. A. van den Berg, I. A. Kozachenko, A. V. Dubrovina, I. V. Melchakova, Y. Kivshar, and P. Belov, "Enhancement of Magnetic Resonance Imaging with Metasurfaces," *Adv. Mater.*, vol. 28, no. 9, pp. 1832–8, March 2016.

List of Figures

List of Tables

Appendix

A List of Acronyms

1D	One-Dimensional
2D	Two-Dimensional
3D	Three-Dimensional
CMA	Characteristic Mode Analysis
CoV	Coefficient of Variation
CP	Circular Polarization
EBG	Electromagnetic Band Gap
EM	Electromagnetic
FoV	Field of View
GRE Image	Gradient Echo Image
FDTD	Finite Difference Time Domain
FEM	Finite Element Method
FSS	Frequency Selective Surface
HFSS	High Frequency Structure Simulator
HIS	High Impedance Surface
MEC	Mode Excitation Coefficient
MIM	Metal-Insulator-Metal
MoM	Method of Moment
MRI	Magnetic Resonance Imaging
NMR	Nuclear Magnetic Resonance
NMV	Net Magnetization Vector

PEC	Perfect Electrical Conductor
PMC	Perfect Magnetic Conductor
PML	Perfect Matched Layer
RF	Radio Frequency
SAR	Specific Absorption Rate
SIBC	Surface Impedance Boundary Condition
SNR	Signal to Noise Ratio
TE	Transverse Electric
TM	Transverse Magnetic
TEM	Transverse Electromagnetic
TL	Transmission Line
TE for GRE	Echo Time
TR for GRE	Repetition Time
UHF	Ultra High Field
VNA	Vector Network Analyzer

B List of Symbols

Symbol	Quantity	Unit
$\mathbf{E}$	Electric field	V/m
$\mathbf{H}$	Magnetic field	A/m
$\mathbf{B}$	Magnetic flux density	T
$\mathbf{J}$	Current density	A/m^2
$\mathbf{J_s}$	Surface current density	A/m
Z_S	Surface impedance	Ω
S_{ij}	i, j element of the scattering matrix	
ϵ	Permittivity	F/m
ϵ_r	Relative permittivity	
μ	Permeability	H/m
σ	Electrical conductivity	S/m
ρ	Mass density	kg/m^3

C List of Publications

Z. Chen, K. Solbach, D. Erni, and A. Rennings, "Electromagnetic Field Analysis of a Dipole Coil Element with Surface Impedance Characterized Shielding Plate for 7-Tesla MRI," *IEEE Trans. Microw. Theory Techn.*, vol. 64, no. 3, pp. 972-981, March 2016.

Z. Chen, K. Solbach, D. Erni, and A. Rennings, "Improving B1 Efficiency and Signal-to-Noise-Ratio of a Surface Coil by a High-Impedance-Surface RF Shield for 7 T Magnetic Resonance Imaging," *IEEE Trans. Microw. Theory Techn.*, vol. 65, no. 3, pp. 988-997, March 2017.

Z. Chen, K. Solbach, D. Erni, and A. Rennings, "Field Distribution and Coupling Investigation of an 8-Channel RF Coil Consisting of Different Dipole Coil Elements for 7-Tesla MRI," *IEEE Trans. Biomed. Eng.*, DOI: 10.1109/TBME.2016.2602441, Aug. 2016.

S. Otto, **Z. Chen**, A. Al-Bassam, A. Rennings, K. Solbach, and C. Caloz, "Circular polarization of periodic leaky-wave antennas with axial asymmetry: Theoretical proof and experimental demonstration," *IEEE Trans. Antennas Propagat.*, vol. 62, pp. 1817-1829, April 2014.

Z. Chen, S. Otto, "A Taper Optimization for Pattern Synthesis of Microstrip Series-Fed Patch Array Antennas," in *39th European Microwave Conference (EuMC 2009)*, Sep. 28-Oct.2, Rome, Italy, pp. 160-163, 2009.

Z. Chen, K. Solbach, D. Erni, and A. Rennings, "Dipole RF Element for 7 Tesla magnetic resonance imaging with minimized SAR," in *7th European Conference on Antennas and Propagation (EuCAP 2013)*, April 8-12, Gothenburg, Sweden, pp. 1775-1778, 2013.

Z. Chen, K. Solbach, D. Erni, and A. Rennings, "RF Coil Element with Longitudinal and Transversal Two-Peak Field Distribution for Low SAR 7-Tesla Magnetic Resonance Imaging," in *IEEE Int. Microwave Symposium (IMS 2013)*, June 2-7, Seattle, USA, paper WE1E-2, 2013.

Z. Chen, A. Rennings, K. Solbach, and D. Erni, "A 4-channel RF coil with large longitudinal field-of-view for 7-T-MRI," in *30th Annual Sci. Meeting of Europ. Soc. for Magn. Reson. in Med. and Biol. (ESMRMB 2013)*, Oct. 3-5, Toulouse, France, p. 241, 2013.

Z. Chen, K. Solbach, D. Erni, and A. Rennings, "Coupling Investigation of Different RF Coil Elements for 7-Tesla Magnetic Resonance Imaging based on Characteristic Mode Analysis," in *IEEE Int. Microwave Symposium (IMS 2014)*, June 1-6, Tampa Bay, USA, paper TH2E-3, 2014.

Z. Chen, O. Kraff, K. Solbach, D. Erni, and A. Rennings, "A 4-Channel RF coil based on Novel Dipole-Element with Eigen-resonant Shielding Plate for 7-Tesla Magnetic Resonance Imaging," in *44th European Microwave Conference (EuMC 2014)*, Oct. 6-9, Rome, Italy, pp. 476-479, 2014.

Z. Chen, K. Solbach, D. Erni, and A. Rennings, "A Compact Electromagnetic Bandgap Structure based on Multi-layer Technology for 7-Tesla Magnetic Resonance Imaging Applications," in *44th European Microwave Conference (EuMC 2014)*, Oct. 6-9, Rome, Italy, pp. 1576-1579, 2014.

Z. Chen, K. Solbach, D. Erni, and A. Rennings, "Improved B1 Distribution of an MRI RF Coil Element using a High-Impedance-Surface Shield," in *9th German Microwave Conference (GeMiC 2015)*, March 16-18, Nürnberg, Germany, pp.111-114, 2015.

Z. Chen, M. Abbasi, K. Solbach, D. Erni, and A. Rennings, "RF Dipole Coil with Novel Slotted Shielding Plate Achieving an Improved B1 Distribution for 7 T MRI," in *23rd Proc. Intl. Soc. MRM (ISMRM 2015)*, May 30-June 5, Toronto, Canada, p. 3092, 2015.

Z. Chen, K. Solbach, D. Erni, and A. Rennings, "Coupling Investigation between RF Coil Array Elements backed by Surface Impedance Characterized Shields for 7 Tesla MRI," in *10th German Microwave Conference (GeMiC 2016)*, March 14-16, Bochum, Germany, pp.112-115, 2016.

Z. Chen, K. Solbach, D. Erni, and A. Rennings, "RF Dipole Coil backed by a High-Impedance-Surface Shield," in *1st YRA MedTech Symposium*, April 8, Duisburg, Germany, pp.16-17, 2016.

Z. Chen, J. T. Svejda, K. Solbach, D. Erni, and A. Rennings, "Simulation of an RF dipole coil with a high-impedance-surface (HIS) shield," in *EDUHF-LAB MRI Workshop 2016, BioEM Simulation for UHF MRI*, May 19, Medical Campus, Otto-von-Guericke University Magdeburg, 2016 (invited talk).

Q. Yuan, **Z. Chen**, S. Otto, S. Held, K. Solbach, D. Erni, and A. Rennings, "MetaBeam: Multi-layer CRLH antennas for 24 GHz sensor applications based on low-cost PCBs," in *6th German Microwave Conference (GeMiC 2011)*, March 14-16, Darmstadt, Germany, pp. 1-4, 2011.

A. Al-Bassam, S. Otto, **Z. Chen**, A. Rennings, and K. Solbach, "A capacitively-coupled series-fed patch leaky-wave antenna and optimization concepts for efficient broadside radiation," in *7th German Microwave Conference (GeMiC 2012)*, March 12-14, Ilmenau, Germany, pp. 1-4, 2012.

S. Otto, A. Al-Bassam, **Z. Chen**, A. Rennings, K. Solbach, and C. Caloz, "Q-Balancing in periodic leaky-wave antennas to mitigate broadside radiation issues," in *7th German Microwave Conference (GeMiC 2012)*, March 12-14, Ilmenau, Germany, pp. 1-4, 2012.

A. Rennings, B. Zhou, A. Al-Bassam, **Z. Chen**, S. Otto, K. Solbach, and D. Erni, "MetaBeam: A high-gain pencil-beam array antenna based on corporately fed CRLH meta-lines for the 24 GHz ISM band," in *7th German Microwave Conference (GeMiC 2012)*, March 12-14, Ilmenau, Germany, pp. 1-4, 2012.

J. T. Svejda, A. Rennings, **Z. Chen**, and D. Erni "Congener dual resonant antennas (CDRA) and zeroth order resonant antennas (ZORA)," RF Meeting 2014, Topical Meeting on RF Systems and Hardware, RF Coils, RF Safety, and Parallel Transmit in High-Field MRI, Oct. 15, Leiden University Medical Center, Leiden, The Netherlands, 2014.